IMPERIAL COLLEGE OF SCIENCE, TECHNOLOGY AND MEDICINE

UNIVERSITY OF LONDON

THE INTERACTION OF GUIDED WAVES WITH DISCONTINUITIES IN STRUCTURES

by

Alessandro Demma

A thesis submitted to the University of London for the degree of

Doctor of Philosophy

January 2003

Department of Mechanical Engineering

Imperial College of Science, Technology and Medicine

London SW7 2BX

Abstract

The thesis investigates the effect of geometrical discontinuities in plates and pipes on the propagation of guided waves. The discontinuities studied are both defects in the structure and features of the structure.

Firstly the scattering of the SH0 mode from discontinuities in the geometry of a plate is presented. Both Finite Element and modal decomposition methods have been used to study the reflection and transmission characteristics from a thickness step in a plate, very good agreement being obtained. A method to approximate the reflection from rectangular notches by superimposing the reflection from a step down (start of the notch) and a step up (end of the notch) is proposed. The limits of this method in approximating crack-like defects are discussed.

The second part of this thesis reports an experimental and numerical (Finite Element method) study of the reflection of the T(0,1) mode from defects in pipes. Both crack-like defects with zero axial extent and notches with varying axial extents are considered in this study. An interpretation of the crack-like reflection coefficients in terms of the wavenumber-defect size product is proposed.

The third part focuses on the reflection from notches in pipes. A systematic numerical analysis (Finite Element) of the effect of pipe size, defect size, guided wave mode and frequency on the reflection from notches is presented. A generalization of the results obtained for different test configurations is proposed. As a result, maps of reflection coefficient depending on the circumferential extent and depth of the defect are shown for a particular pipe size and an approximate formula for extrapolation to other pipe sizes is proposed. This study addresses problems encountered in practical testing and offers guidance for the interpretation of measurements.

The last part of the thesis studies guided wave propagation in pipes with bends. The dispersion curves for toroidal structures are derived using a Finite Element modal solution and the main characteristics of the modes of a curved pipe are described. A series of pipes with different bend radii were investigated experimentally and with numerical simulation (Finite Element). The influence of both bend radius and bend length on the transmission of the incident wave is shown. The modes travelling after the interaction with a bend are identified.

Acknowledgements

Firstly, I would like to thank my supervisor, Professor Peter Cawley, for his guidance, support and patience.

I would also like to thank Prof. A. Ajovalasit, Prof. F. Lanza di Scalea, Prof. R. Green and Dr. B. Djordjevic for introducing me to the world of scientific research.

My sincere thanks is also extended to all the members of the NDT Lab and Guided Ultrasonics Limited for their friendship and advice and to Dr. A.G. Roosenbrand of Shell Global solutions for interesting discussions.

This work was funded by the NDT lab, Guided Ultrasonics Limited and Shell Global Solutions.

Finally I would like to thank my family and my friends who supported me from far away and in particular Fumiko for her encouragement and infinite patience.

Contents

List of Figures

List of Tables

Chapter 1

Introduction

1.1 Motivation

The testing of pipes and pressure vessels used in the petro-chemical industry is a major issue for both safety reasons and environmental impact control. Tens of millions of kilometres of pipes and thousands of pressure vessels are used worldwide and these need to be monitored regularly. Routine maintenance of structures in service usually requires the implementation of NDT techniques. The use of conventional point-by-point NDT methods such as ultrasonic thickness gauging implies a slow inspection process which becomes very expensive when full inspection coverage is needed. Other NDT inspection methods such as radiography [1], eddy current [2, 3, 4] and Magnetic Flux [5, 6] are commonly used in plate and pipe testing. These methods require only external access but, for complete coverage of the pipe, they also tend to be relatively slow. It is therefore useful to introduce at the very first stage of an inspection process a screening procedure which is fast and sufficiently accurate to identify the areas where there is significant corrosion. When a preliminary fast screening test is performed, the use of conventional NDT techniques can focus on the classification of the severity of corrosion in the areas previously identified by the screening technique. Effectively, the implementation of a complementary fast screening technique enables the achievement of the conflicting goals of the reliable detection and sizing of corrosion and the reduction of the overall inspection costs.

A fast screening technique for pipe testing using classical ultrasonic bulk wave propagation is the pig method [7, 8] where an ultrasonic probe is sent inside the pipe

and this collects ultrasonic signals along the pipe length. This technique is quite expensive in terms of instrumentation and it also requires access to introduce and remove the pig. It is therefore suitable only for very long lengths of large diameter pipes.

Another screening technique for pipe testing is a guided wave inspection method developed in the NDT Lab at Imperial College [9, 10, 11]. This is capable of screening long lengths of pipes for corrosion (the typical range is 15-50 meters of pipe from a single location). The range for this type of testing is much shorter than with the pig but it is non-invasive and it is also relatively cheap. Cylindrically guided waves are excited at one axial location using an array of transducers distributed around the circumference of the pipe. These waves stress the whole pipe wall and propagate along the length of the pipe; they are partially reflected when they encounter features (such as welds, branches, drains, corrosion patches, etc...) that locally change the geometry of the pipe. The technique seeks to detect corrosion defects removing 5-10% of the total cross sectional area at any axial location. It was originally designed to test pipes in the 2-24 inch diameter range, but both smaller and larger pipe sizes can be tested.

Guided waves can also potentially be used for plate inspection. A medium-range plate inspection technique for detection of corrosion in large areas of thick plates (5-25 mm) has been developed at Imperial College [12]. The target application for this device is testing the floors and walls of steel plate structures in the petrochemical industry, such as storage tanks and pressure vessels.

The interaction of guided waves with discontinuities in the structure is a complex physical phenomenon which has not been explained for all of the possible cases encountered in real life. Discontinuities in structures can be either geometrical discontinuities such as welds connecting two parts together, curved parts attached to the main structure, free ends and of course corrosion defects or discontinuities due to material property changes such as two different materials welded together or a structure partly embedded in a surrounding medium. There are numerous practical applications where the effect of a discontinuity in the structure has to be understood in order to develop an effective testing strategy. In this thesis we deal with understanding the effect of geometrical discontinuities on guided wave

propagation in plates and pipes. The background literature on the different issues is presented in the relevant chapter rather than in this introduction chapter.

1.2 Outline of Thesis

The next chapter presents a general introduction to guided waves. A brief overview of the theoretical fundamentals of wave propagation is presented; guided waves in plates are then introduced with emphasis on SH waves which are used in this work. Guided waves in cylindrical structures are then described and the strategies used for the inspection of large structures are explained.

Chapter 3 presents an analysis of the scattering of the SH0 mode from discontinuities in the geometry of a plate. Both Finite Element and modal decomposition methods have been used to study the reflection and transmission characteristics from a thickness step in a plate. The significance of non-propagating modes in the scattering from steps in plates has been specifically investigated. A method to approximate the reflection from rectangular notches by superimposing the reflection from a step down (start of the notch) and a step up (end of the notch) has been proposed. The effect of frequency on the reflection from notches has been examined. The limits of this method in approximating crack-like defects have also been studied.

Chapter 4 examines the potential of the Torsional T(0,1) mode for pipe testing. The advantages of using T(0,1) over the use of longitudinal wave are explained. A quantitative study of the reflection of the T(0,1) mode from defects in pipes in the frequency range 10-300 kHz has been carried out, finite element predictions being validated by experiments on selected cases. Both crack-like defects with zero axial extent and notches with varying axial extents have been considered. The effect of defect size and frequency on the reflection of the T(0,1) mode and its mode conversion has been investigated. The results for cracks have been explained in terms of the wavenumber-defect size product, ka.

In Chapter 5 a generalization of the reflection coefficient from corrosion in pipes depending on the defect size, pipe size, frequency and mode used is attempted. The frequency limits of this generalization procedure are defined. Maps of reflection coefficient as a function of the circumferential extent and depth of the defect are

presented for a 3 inch schedule 40 pipe and an approximate formula for extrapolating to other pipe sizes is proposed and evaluated. The generalization procedure is proposed for a rectangular notch shape but a study on the effect of shape was initiated and is reported.

Chapter 6 deals with the understanding of the effect of a bend in a pipe network. The dispersion curves and mode shapes for curved pipes are found using a Finite Element procedure. A verification of this solution using a modal decomposition procedure is also shown. Then the straight-curved-straight transition is studied in terms of its effect on the propagation of the guided wave. The influence of both the bend radius and the bend length on the transmission of the incident wave is shown both with Finite Element analysis and experimentally.

In the last Chapter conclusions on the interaction of guided waves with geometrical discontinuities are drawn and future work is proposed.

Chapter 2

Guided Waves

2.1 Background

This chapter introduces the basic concepts of ultrasonic guided wave propagation in structures such as plates and pipes. In general the use of ultrasonic waves is well established in the NDT industry. Most standard tests for locating defects involve the excitation of a bulk wave in the material. Bulk waves are used more than guided waves in industry because they offer the advantage of being easy to understand and easy to use. Only two types of waves can propagate in the bulk of the material (shear and longitudinal), their velocity being constant with frequency. The measurements are performed by using transducers in two possible configurations, pulse echo when the emitter is used to receive the ultrasonic signal, and pitch and catch when the receiver and the emitter are two different units. Simple velocity and attenuation measurements can give accurate analysis of the health of the structure monitored. The use of bulk stress waves in NDT is a well documented subject [13, 14].

Although bulk wave techniques enable accurate and reliable inspection, guided waves are preferred when inspecting large structures where access is limited. The main difference between bulk and guided waves is that bulk waves travel in the bulk of the material (away from the boundaries) and guided waves travel either at the boundaries (surface waves) or between the boundaries (Lamb waves). Bulk and guided waves behave differently but they are actually governed by the same set of partial differential wave equations. The difference in the mathematical solution of the two types of waves is due to the boundary conditions. In the case of bulk waves

there is no need for boundary conditions because the wave is assumed to travel inside the bulk of the material (see Figure 2.1a). In contrast guided waves are the result of the interaction occurring at the interface between two different materials (see Figure 2.1b). This interaction produces reflection, refraction and mode conversion between longitudinal and shear waves which can be predicted using appropriate boundary conditions.

The difficulty in the application of guided waves arises from the complexity of solution. Guided waves are characterized by an infinite number of modes associated with a given partial differential equation solution whereas, as already mentioned, only longitudinal and shear modes are present in a bulk wave problem. As a result guided waves are highly dependent on wavelength and frequency, and propagating guided waves can only exist at specific combinations of frequency, wavenumber and attenuation.

2.1.1 Equations of motion in isotropic media

As mentioned above, both bulk waves and guided waves are governed by the same set of differential equations. In the following the equations of motion for an isotropic medium are derived.

Applying Newton's second law and the conservation of the mass within an arbitrary volume in an elastic solid it is possible to derive Euler's equation of motion [15]. When the material has constant density (ρ), is linearly elastic and the body forces applied to it are neglected, Euler's equation can be written as follows:

$$\rho \cdot (\frac{\partial^2 \mathbf{u}}{\partial t^2}) = \nabla \cdot \overrightarrow{\overrightarrow{\sigma}} \tag{2.1}$$

where $\mathbf{u}$ is the displacement field and $\overrightarrow{\overrightarrow{\sigma}}$ is the stress tensor. $\overrightarrow{\overrightarrow{\sigma}}$ can also be expressed in terms of the strain tensor $\overrightarrow{\overrightarrow{\varepsilon}}$ using Hooke's law:

$$\overrightarrow{\overrightarrow{\sigma}} = C \cdot \overrightarrow{\overrightarrow{\varepsilon}} \tag{2.2}$$

where C is the stiffness tensor (rank four). For an isotropic, homogeneous, linearly elastic material the theory of elasticity demonstrates that it is possible to reduce

the 21 possible components of the C tensor to two material constants (λ, μ) which are called the *Lamé* constants [16]. If the strain tensor is expressed in terms of displacement, Hooke's law simplifies to:

$$\overrightarrow{\overrightarrow{\sigma}} = \lambda \mathbf{I} \nabla \cdot \mathbf{u} + \mu(\nabla \mathbf{u} + \mathbf{u}\nabla^T) \tag{2.3}$$

Combining equation 2.1 and 2.3 yields Navier's differential equation of motion for isotropic elastic medium:

$$\mu \nabla^2 \mathbf{u} + (\lambda + \mu)\nabla\nabla \cdot \mathbf{u} = \rho(\frac{\partial^2 \mathbf{u}}{\partial t^2}) \tag{2.4}$$

Equation 2.4 is a compact expression which can be expanded in its three spatial components x,y,z:

$$\begin{aligned}
\mu(\frac{\partial^2}{\partial x^2} + \frac{\partial^2}{\partial y^2} + \frac{\partial^2}{\partial z^2})u_x + (\lambda + \mu)\frac{\partial}{\partial x}(\frac{\partial u_x}{\partial x} + \frac{\partial u_y}{\partial y} + \frac{\partial u_z}{\partial z}) &= \rho \frac{\partial^2 u_x}{\partial t^2} \\
\mu(\frac{\partial^2}{\partial x^2} + \frac{\partial^2}{\partial y^2} + \frac{\partial^2}{\partial z^2})u_y + (\lambda + \mu)\frac{\partial}{\partial x}(\frac{\partial u_x}{\partial x} + \frac{\partial u_y}{\partial y} + \frac{\partial u_z}{\partial z}) &= \rho \frac{\partial^2 u_y}{\partial t^2} \\
\mu(\frac{\partial^2}{\partial x^2} + \frac{\partial^2}{\partial y^2} + \frac{\partial^2}{\partial z^2})u_z + (\lambda + \mu)\frac{\partial}{\partial x}(\frac{\partial u_x}{\partial x} + \frac{\partial u_y}{\partial y} + \frac{\partial u_z}{\partial z}) &= \rho \frac{\partial^2 u_z}{\partial t^2}
\end{aligned} \tag{2.5}$$

These equations of motion must be satisfied by all elastic waves propagating in the material and will be referred to as the wave equations. Since the wave equations are linear, the superposition of two or more valid solutions will still provide a valid solution. The wave equations 2.5 cannot be integrated directly. Therefore, depending on the application, an appropriate solution must be assumed [16].

A neat way of manipulating the wave equation 2.4 is to use Helmholtz decomposition [17] to split the displacement field $\mathbf{u}$ into a rotational component $\nabla \times \mathbf{H}$ and an irrotational component $\nabla\phi$:

$$u = \nabla\phi + \nabla \times \mathbf{H} \tag{2.6}$$

where ϕ is a compressional scalar potential and $\mathbf{H}$ is an equivoluminal vector potential. Provided that the potentials are analytic functions, the displacement field will be continuous therefore satisfying the compatibility. It can also be shown that the vector field decomposition in 2.6 is always possible [18].

Substituting expression 2.6 into Navier's equation of motion 2.4 yields:

$$\nabla[(\lambda+2\mu)\nabla^2\phi-\rho(\frac{\partial^2\phi}{\partial t^2})]+\nabla\times[\mu\nabla^2\mathbf{H}-\rho(\frac{\partial^2\mathbf{H}}{\partial t^2})] \tag{2.7}$$

Equation 2.7 is satisfied if either of the two expressions in square brackets is equal to zero, therefore it can be substituted by for a set of two equations:

$$\begin{aligned} c_L\nabla^2\phi &= \frac{\partial^2\phi}{\partial t^2} \\ c_T\nabla^2\mathbf{H} &= \frac{\partial^2\mathbf{H}}{\partial t^2} \end{aligned} \tag{2.8}$$

where c_L and c_T are the phase velocity of the longitudinal and shear waves respectively:

$$\begin{aligned} c_L &= (\frac{\lambda+2\mu}{\rho})^{1/2} \\ c_T &= (\frac{\mu}{\rho})^{1/2} \end{aligned} \tag{2.9}$$

The equations 2.8 are conventionally called the Helmholtz differential equations.

2.2 Guided waves in plates

2.2.1 Background

Guided waves are acoustic waves travelling in the vicinity of the material boundaries. The boundaries not only influence the propagation but they actually guide the wave along the structure. The simplest of all acoustic waveguide structures is an unbounded plate with stress-free surfaces. The propagation of waves in plates was first studied by Lamb [19] in 1917 after whom the guided waves in free plates are named. His study analyzed symmetric and anti-symmetric modes separately. However, it was only after the experimental work of Worlton [20] that the possibility of using Lamb waves for non-destructive testing was demonstrated. Viktorov [21] also gave a considerable contribution to the understanding of guided waves in plates. Subsequently a series of authors reported on the use of guided waves in plates. The applications proposed were focusing either on the determination of the material

properties [22, 23, 24, 25] (typically short range applications) or flaw detection (typically medium to long range applications). Due to the complexity of the guided wave propagation the practical testing of plates needs to be optimized depending on the specific guided wave application. Many authors have reported on the optimization of the use of plate waves for detecting defects [26, 27, 28, 29]. A large number of workers have recognized the advantage of using guided waves for rapid inspection of plates in applications where it was possible to tolerate some reduction in sensitivity and resolution [30, 31, 32]. More recently a rapid plate inspection technique using an EMAT transducer array has been developed [12]. A variation to this technique using piezoelectric transducers permanently attached to the structure is also under investigation [33].

2.2.2 The free plate problem

A schematic diagram of a plate in a cartesian coordinate system is shown in Figure 2.2. The plate is assumed to extend to infinity in the y and z directions, and the origin of the x axis is located at the bottom of the plate. The propagation is along the z direction and the fields are assumed to be uniform in the y direction. This problem is governed by the equation of motion (2.8). Since the domain is finite, boundary conditions are needed to construct a well posed problem. The boundary conditions can in general be imposed as known tractions and/or displacements at the boundaries. In the case of a free plate the surfaces at the coordinates x=0 and x=t (where t is the thickness of the plate) are considered traction free.

The exact solution of the free plate problem has been obtained using different approaches. The most popular methods of solution are the displacement potentials introduced above (see [34] for more details) and the partial wave technique (see [16] for more details). Using the displacement potential method and assuming that the particle displacement is zero in the y direction ($u_y = 0$) and the only rotation is about the y axis ($H_x = H_z = 0$), the wave equation 2.8 reduces to:

$$\begin{aligned} c_L\left(\frac{\partial^2\phi}{\partial x^2} + \frac{\partial^2\phi}{\partial z^2}\right) &= \frac{\partial^2\phi}{\partial t^2} \\ c_T\left(\frac{\partial^2\mathbf{H_y}}{\partial x^2} + \frac{\partial^2\mathbf{H_y}}{\partial z^2}\right) &= \frac{\partial^2\mathbf{H_y}}{\partial t^2} \end{aligned} \tag{2.10}$$

the solution of which are the famous Lamb waves. Alternatively, assuming that the only component of displacement is in the y direction, and considering the solution for which the scalar potential vanishes (see [16] for more details), the wave equation 2.8 reduces to:

$$c_T(\frac{\partial^2 \mathbf{H}}{\partial x^2}) = \frac{\partial^2 \mathbf{H}}{\partial t^2} \tag{2.11}$$

where $\mathbf{H_y} = 0$ (because $u_x = u_z = 0$). The solution of equation 2.11 are the SH (Shear Horizontal) waves.

2.2.3 SH waves

The shear horizontal waves defined in equation 2.11 can be obtained by assuming a simple expression for the displacement u:

$$\mathbf{u} = u_y = A_y e^{i(k_{real}z - \omega t)} e^{-k_{imag}z} \tag{2.12}$$

where A_y is the amplitude of the displacement, i is the imaginary unit ($i = \sqrt{-1}$), k_{real} and k_{imag} are respectively the real and imaginary part of the wavenumber, ω is the circular frequency, z is the direction of propagation and t is the time. Derivation of the SH dispersion relation can be found in Auld [15].

The dispersion relation can easily be visualized using the dispersion curves. Figure 2.3 shows the phase velocity dispersion curves for a steel plate in vacuum. The curves scale linearly with frequency and thickness so that the use of the frequency-thickness scale on the abscissa allows these curves to be used for a plate of any thickness. They were calculated using the program Disperse [35], developed at Imperial College. SH waves can be either symmetric or antisymmetric but we do not differentiate the two families of SH modes here and simply use a counter variable to distinguish the different modes. The modes with even counter variable are symmetric and the modes with odd counter variable are antisymmetric. The fundamental SH mode, existing at zero frequency, is the SH0 (symmetric) mode. The properties of this mode are not frequency dependent: it is completely non-dispersive at all frequencies and its phase velocity is the bulk shear velocity. The next mode appearing is the SH1 (anti-symmetric) mode and its cut-off frequency is at about 1.6 MHz-mm.

From the dispersion relation it can be deduced that SH modes exist at all frequencies but they propagate only at frequencies higher than the cut-off frequency,

the only exception being SH0 which propagates at all frequencies. At frequencies lower than the cut-off there is a non-propagating solution for the mode. Partial wave theory gives extra physical insight on how to relate the phenomenon of non-propagating modes to the frequency of the wave [15]. In the partial wave technique, the solution to the free plate problem is first constructed from simple exponential-type waves (Equation 2.12) that are reflected back and forth between the boundaries of the plate (up and down waves schematized in Figure 2.4), the reflection at the boundaries being governed by Snell's law [15]. The superposition of the up and down waves in Figure 2.4 is a solution to the guided wave problem. In the example in Figure 2.4, as the frequency decreases, the angle of incidence θ of the partial wave decreases, becoming zero at the cut-off frequency. At the cut-off frequency, the partial waves simply reflect back and forth across the thickness of the waveguide and there is no variation of the stress and displacement field along the direction of propagation. The wavenumber, which is real in a propagating SH mode, is zero at the cut-off and becomes a purely imaginary number at lower frequencies. Consequently the displacement field will be different below and above the cut-off frequency.

From (2.12) it is clear that the displacement, which is a sinusoidal wave when the wavenumber is real, becomes a decreasing exponential curve for a non-propagating SH mode [15] so its effect decreases exponentially with distance from the point where the non-propagating mode is localized. The non propagating modes only involve a local disturbance and they do not carry any energy. Therefore a change in amplitude of the non-propagating modes does not cause any energy loss.

Figure 2.5 shows the attenuation curves for the non-propagating modes in a plate in a vacuum. An infinite number of non-propagating modes exist at any given frequency, but only the first five of them are plotted in Figure 2.5. The ordinate is the attenuation (in dB-mm/m) of the decay function and it is given by:

$$attn = t \cdot 20 \log \frac{1}{e^{-k_{imag}}} \tag{2.13}$$

where t is the thickness of the plate and k_{imag} is the imaginary wavenumber in equation (2.12). The attenuation of each mode decreases as the frequency increases and it becomes zero at the cut-off frequency. Moreover at any frequency value the attenuation increases with the counter variable of the SH mode. The SH0 mode is not traced in Figure 2.5 because it is the only mode which has real wavenumber

at all frequencies. Another important characteristic of the SH0 mode is that its displacement is constant through the thickness (see Figure 2.6a). Figure 2.6b shows the mode shape of the antisymmetric SH1 mode. The mode shapes of the higher order modes are characterized by an increasing number of zero crossings through the thickness (zero for SH0, one for SH1 and so on).

The stress field of SH modes is also relatively simple. This is characterized by two components of stress:

$$\begin{aligned} \tau_{yz} &= c_{44}\frac{\partial u_y}{\partial z} \\ \tau_{xy} &= c_{44}\frac{\partial u_y}{\partial x} \end{aligned} \tag{2.14}$$

where c_{44} is the shear modulus. The τ_{yz} stress component is directly proportional to the u_y displacement so its mode shape is the same as the mode shape for u_y.

2.3 Guided waves in hollow cylinders

2.3.1 Background

The current understanding of guided waves in hollow cylinders is based on studies carried out on cylindrical wave propagation in the late nineteenth century. Pochammer [36] (1876) and Chree [37] (1889) first investigated the propagation of guided waves in a free bar. In the mid twentieth century their work was revived and improved. The longitudinal modes of a bar were examined by Davies [38]. Later work by many researchers such as Pao and Mindlin [39], Onoe et al [40] and Meeker and Meitzler [41] developed the three-dimensional problem of a solid circular cylinder in a vacuum. The analytical foundation for the investigation of harmonic waves in a hollow circular cylinder of infinite extent was built by Gazis [42, 43]. Confirmation of the analytical predictions given by Gazis was presented by Fitch [44] who carried out experiments using both axially symmetric and non-symmetric modes in hollow cylinders.

2.3.2 The hollow cylinder problem

A schematic diagram of a hollow cylinder and the axis definition are shown in Figure 2.7: z is along the length of the cylinder, r is the radial direction and θ is the angle coordinate.

Since the Helmholtz differential equations 2.8 are separable in cylindrical coordinates (see Morse and Feshbach [17]), the solution may be divided into the product of functions of each of the spatial dimensions.

Assuming a harmonically oscillating source the solutions for the equations 2.8 will be:

$$\phi, \mathbf{H} = \Gamma_1(r)\Gamma_2(\theta)\Gamma_3(z)e^{i(\mathbf{kr}-\omega t)} \tag{2.15}$$

where $\mathbf{k}$ is the wavenumber (vector), and $\Gamma_1(r)$, $\Gamma_2(\theta)$ and $\Gamma_3(z)$ describe the field variation in each spatial coordinate. Assuming that the wave does not propagate in the radial direction (r) and that the displacement field varies harmonically in the axial (z) and circumferential (θ) directions, equation 2.15 can be written as:

$$\phi, \mathbf{H} = \Gamma_1(r)e^{i(k_\theta\theta+\xi z-\omega t)} \tag{2.16}$$

where k_θ is the angular wavenumber component and ξ is the component in the z direction.

Substituting these expressions for the potential into equation 2.8 it is possible to derive a system of differential equations which can be solved numerically (see Pavlakovic [45] for more details on this subject). It is then possible to obtain the dispersion curves describing the wave propagating in hollow cylinders.

2.3.3 Naming

In order to refer to different modes in cylindrical systems consistently, we will use a modified version of the system used by Silk and Bainton [46], which tracks the modes by their type, their circumferential order and their consecutive order. The labelling assigns each mode to one of three types: Longitudinal (L) modes, which are longitudinal axially symmetric modes Torsional (T) modes, which are rotational axially symmetric modes whose displacement is primarily in the circumferential direction, and Flexural (F) modes, which are non axially-symmetric modes.

In addition to the type of mode, a dual index system identifies the modes uniquely. The first index gives the harmonic order of circumferential variation. Consequently all modes whose first integer is zero are axially symmetric, all modes whose first integer is one have one cycle of variation of displacement and stresses around the circumference, and so on. The second index is a counter variable. The value 1 is associated with the fundamental modes; the higher order modes are numbered consecutively.

2.3.4 Nature of the modes in hollow cylinders

The dispersion curves for a system describe the solutions to the modal wave propagation equations and give the properties of guided waves (phase velocity, energy velocity, attenuation and mode shape). In general this information enables the prediction of the optimum test conditions and helps the understanding of the experimental results. The software 'Disperse' [35] has been used to model the studied cases. Figure 2.8 shows the phase velocity dispersion curves for a 3-inch diameter schedule 40 steel pipe with 5.5mm wall thickness in vacuum. In the frequency range 0-100 kHz 22 modes are physically possible in this case. In most non-destructive testing situations only the lower circumferential order modes are used since practical measurement systems usually do not have enough resolution around the circumference to be able to clearly separate high circumferential orders. Therefore in this thesis we will mainly deal with the low circumferential order modes.

2.4 Choice of waveguide modes for testing

In a defined structure many different modes can potentially propagate at any frequency and in order to obtain simple signals that can be reliably interpreted, it is important to choose an appropriate mode and frequency of the test for each specific application. Both the practicality of the choice and the quality and quantity of the information which can be obtained are important to decide the best test configurations.

The basic factors which influence the choice of wave mode and frequency to use were defined by Wilcox et al. [29]:

1) Dispersion

2) Attenuation

3) Sensitivity

4) Excitability

5) Detectability

6) Mode selectivity.

Obviously in a practical implementation of a testing technique some other factors must be considered:

1) Speed of single test

2) Testing tool design

3) Level of difficulty in analyzing the data.

The attenuation factor of propagating modes is not treated in this thesis because only lossless single layer structures in vacuum are considered. Many researchers have reported on the excitability and detectability of modes in plates [21, 47, 48, 49, 29] and pipes [46, 47, 50, 51, 52, 53, 54]. Mode selection for the optimization of plate and pipe testing has also been investigated [55, 49, 56, 57]. In this section we explain the effect of dispersion.

2.4.1 Dispersion

The dispersion phenomenon is due to frequency-dependent velocity variations. In 1877 Lord Rayleigh [58] had already observed that the velocity of a group of waves could be different from the velocity of the individual waves. He was describing the concept of phase and group velocity. The group velocity, V_{gr}, is the velocity at which a guided wave packet will travel at a given frequency while the phase velocity is the speed at which the individual peaks within that packet travel. Phase and group velocities are related to each other through the following equation (see Rose [59] and Graff [60] for more details):

$$V_{gr} = V_{ph} + k\frac{\partial V_{ph}}{\partial k} \tag{2.17}$$

where k is the wavenumber.

Figure 2.9 shows the group velocity for a 3 inch pipe schedule 40 (5.5 mm wall thickness) when the surrounding medium is a vacuum (the related phase velocity

dispersion curves were shown in Figure 2.8). As is clear from Figures 2.8 and 2.9 cylindrical waves are generally dispersive (as are SH and Lamb waves in plates).

The physical manifestation of dispersion is that when a particular mode is excited by a signal of finite duration, the signal is distorted in time and space as it propagates away from the source. Figure 2.10(a) shows an example (calculated using Disperse [35]) of a 5 cycle toneburst with a centre frequency of 70 kHz monitored after 2 metres of propagation (L(0,2) in a 3 inch steel pipe). At this frequency value the signal is almost non-dispersive and there is minimal distortion of the signal, whereas when the frequency is changed to 35 kHz, the signal is dispersive and the wave packet spreads out in time as shown in Figure 2.10(b). Quantitative prediction of the dispersion effect and a general operating method to optimize the tests are discussed in detail in Wilcox et al. [29]. Moreover dispersion compensation techniques have been developed [61, 62].

2.5 FE modelling of guided waves

The solutions to the modal problem provide a great deal of information on how guided waves will propagate; however, they cannot provide all of the information that is needed to create an effective non-destructive testing technique for a given system.

For some difficult geometries the modal problem is difficult to solve. Also the boundary conditions that are specified for the wave propagation model require that the geometry of the system remains invariant in the direction of propagation. Therefore in order to understand the wave propagation in a real structure an additional modelling method is needed.

Many modelling tools have been used to model wave propagation in structures:

1) Finite difference [63, 64]

2) Boundary element [65, 66]

3) Finite element [10, 9, 67, 68, 69, 70, 71, 72, 73]

The finite difference method [74] simplifies the problem of the solution of the differential equations of wave motion for a continuum by discretizing them into a set of algebraic equations in which the field variables are defined at the nodal

intersections of the grid. A practical problem of this formulation is the difficulty in defining stress-free boundaries which are very common in NDT testing (see Alleyne [75] for more details).

The Boundary Element (BE) method [76] converts volume integrals to surface integrals with the aid of the Green's functions. In the BE method, elements are placed over the boundary of the solid under investigation and over defects within the structures. In the Finite Element (FE) method [77] the structure is divided into a finite number of elements of finite size which are connected with the rest of the structure at the boundary of the single element. The wave equation is solved by dividing the continuum into finite elements (characterized by an interpolation function) and solving in terms of field variables at the nodal points.

When comparing the BE method with the FE method it is clear that the BE method has the advantage that just the surface of the structure needs to be discretized but there is generally the need to develop a BE code. On the other hand, the FE method has the advantage that there are many commercial FE codes available which can be used for the purpose of wave modelling and those have built-in options for pre and post-processing of data.

Thus the FE method was used in this thesis to model the propagation of guided waves. The modelling work presented in this thesis was conducted using the general purpose program Finel [78]. Using the FE method, Equation 2.8 can be discretized and the governing equations for the unrestrained system are given by:

$$\overline{\mathbf{M}}\ddot{\mathbf{u}} + \overline{\mathbf{k}}\mathbf{u} = 0 \tag{2.18}$$

in the most general case. We refer to $\overline{\mathbf{k}}$, $\overline{\mathbf{M}}$ as the system stiffness and mass matrices respectively. The system mass matrix $\overline{\mathbf{M}}$ is positive definite but $\overline{\mathbf{k}}$ is singular due to the rigid body degrees of freedom. If rigid body motion of the system is eliminated, it is possible to simplify the equations. Therefore the governing equation reduces to:

$$\mathbf{M}\ddot{\mathbf{u}} + \mathbf{k}\mathbf{u} = 0 \tag{2.19}$$

where both $\mathbf{M}$ and $\mathbf{k}$ are positive definite. In this thesis the FE method has been used mainly for simulation of wave propagation using a time marching procedure.

2.5.1 Time marching procedure

The time domain Finite Element model enables the wave propagation along a structure to be simulated. The temporal discretization may be obtained using a finite difference approximation. Both implicit and explicit schemes could potentially be used for this purpose. In implicit schemes the dynamic equilibrium is satisfied at the end of each time step and the displacements are obtained by solving Equation 2.19. The main disadvantage of using this procedure is that the inversion of a matrix of the order of the number of displacements is needed. On the other hand large time steps are allowed.

Explicit schemes solve the wave equation only at the beginning of the increment. In this scheme the mass matrix is diagonalized, thus the accelerations at time zero are calculated quite simply by using the net mass and force acting on each element. Therefore this scheme does not require any large matrix inversion. The accelerations are then integrated twice to obtain the displacement after a time step Δt. Since the method integrates constant accelerations exactly, for the method to produce accurate results, the time increments must be quite small so that the accelerations are nearly constant during the increments.

The spatial and temporal discretisation of the Finite Element model must be carefully assigned in order to ensure the convergence to the correct solution [75]. In order to adequately model a wave it is necessary to have at least 7 elements for the shortest wavelength, within the bandwidth of the signal, of any waves which may travel in the waveguide:

$$\Delta x \leq \frac{\lambda_{min}}{7} \tag{2.20}$$

For the FE model to have a convergent solution, the time step must be chosen according to the rule:

$$\Delta t \leq 0.8 \frac{\Delta x}{V_{max}} \tag{2.21}$$

where V_{max} is the velocity of the fastest wave.

When modelling wave propagation explicit schemes are preferable because these are less computationally expensive (see reference [79] for more details). In the FE tests reported in this thesis the Explicit scheme was used. Details and a compre-

hensive list of references on FE time marching procedures can be found in Alleyne [75].

2.6 Conclusions

The fundamental concepts related with bulk and guided wave propagation have been introduced.

Two types of wave can travel in a free isotropic plate: Shear Horizontal and Lamb waves. Both the method of potentials and the partial wave technique can be used to find the dispersion relations for a simple plate structure. The characteristics of both propagating and non-propagating modes have been explained for the simple case of SH waves in plates. In a cylinder three types of waves can exist: longitudinal, torsional and flexural.

The concept of dispersion and basic information on guided wave testing optimization have been reported. A brief introduction on guided wave modelling showed the suitability of Finite Element method for the purposes of this investigation.

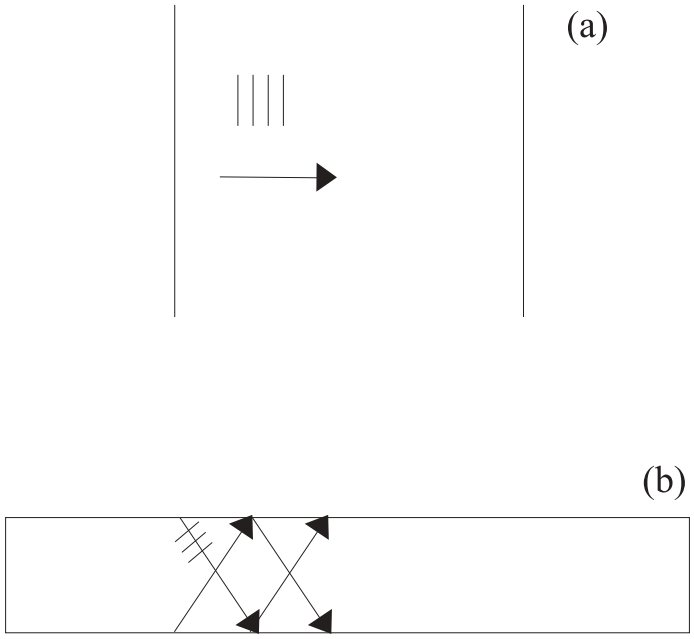

Figure 2.1: Schematic of bulk wave (a) and guided wave (b) propagation.

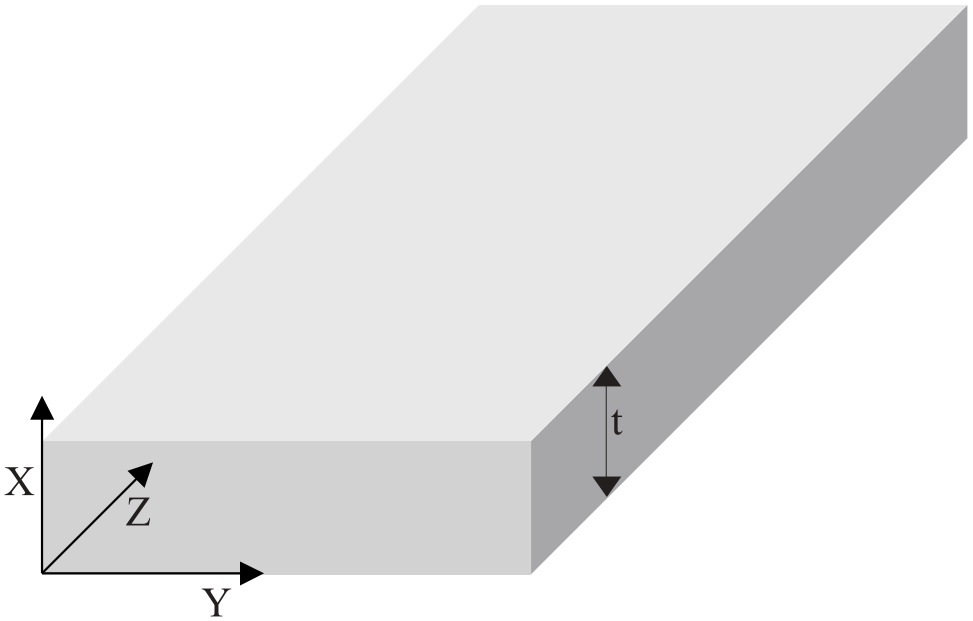

Figure 2.2: Schematic of plate and coordinate system.

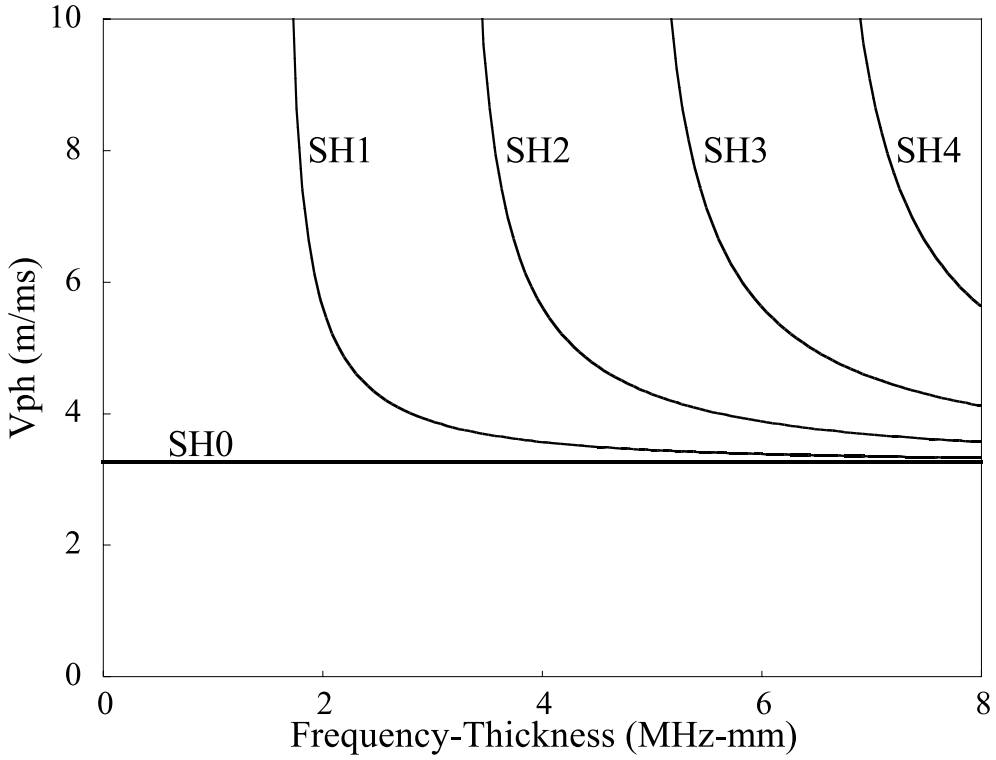

Figure 2.3: Phase velocity dispersion curves for a plate in a vacuum. Only shear horizontal propagating modes are traced.

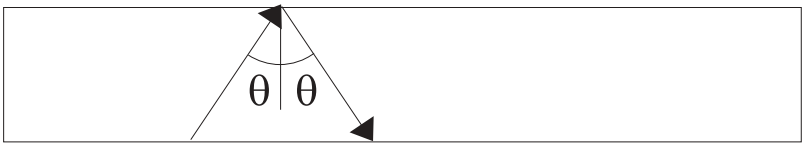

Figure 2.4: Schematic of partial wave solution.

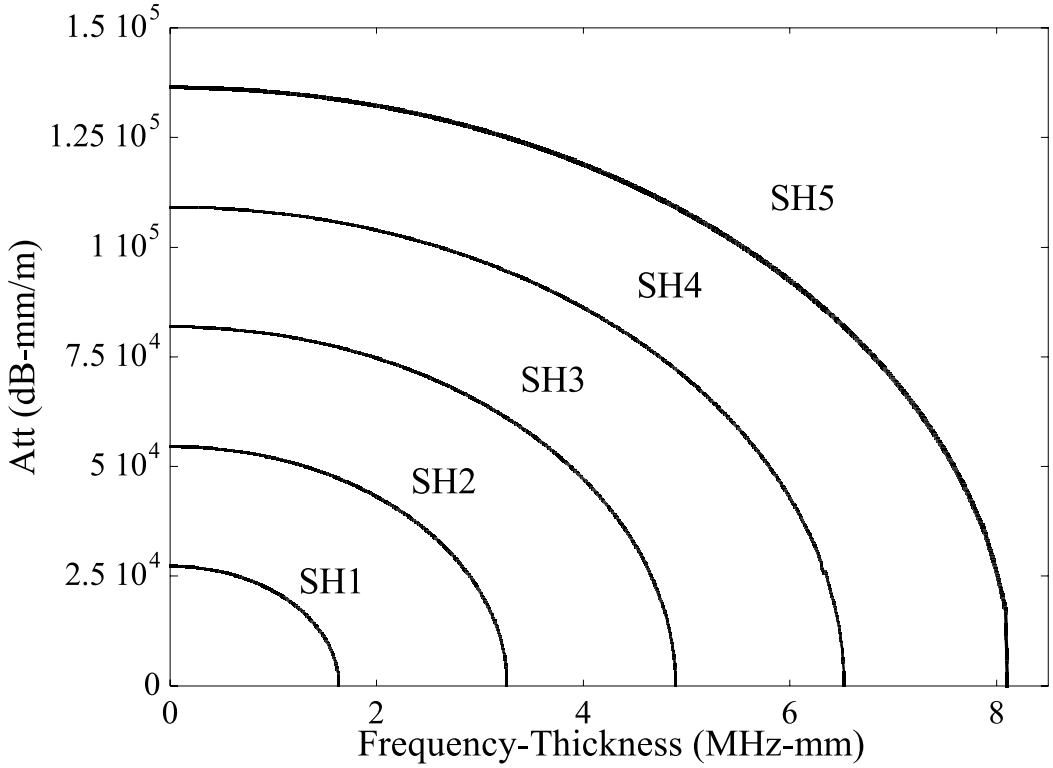

Figure 2.5: Attenuation curves for a plate in a vacuum. Only shear horizontal non-propagating modes are traced.

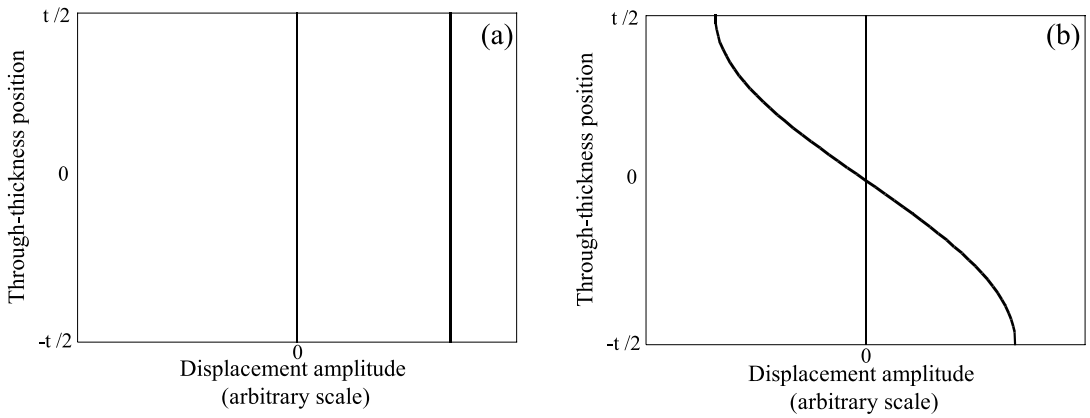

Figure 2.6: Displacement mode shapes in a plate for SH0 (a) and SH1 (b).

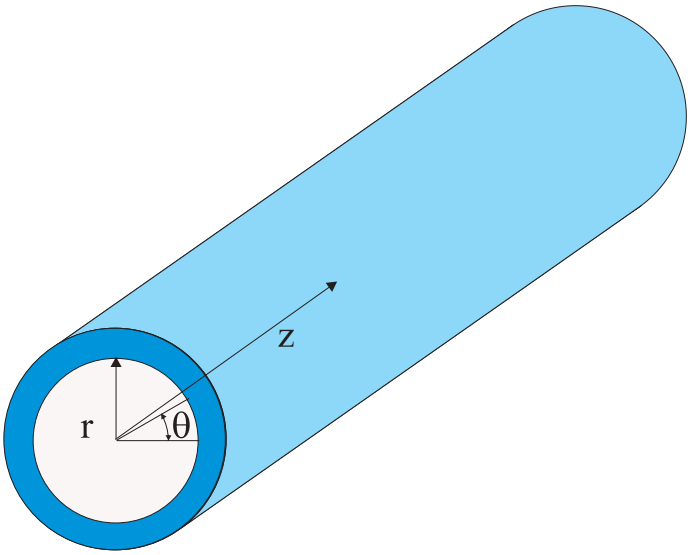

Figure 2.7: Schematic of the pipe and coordinate axis.

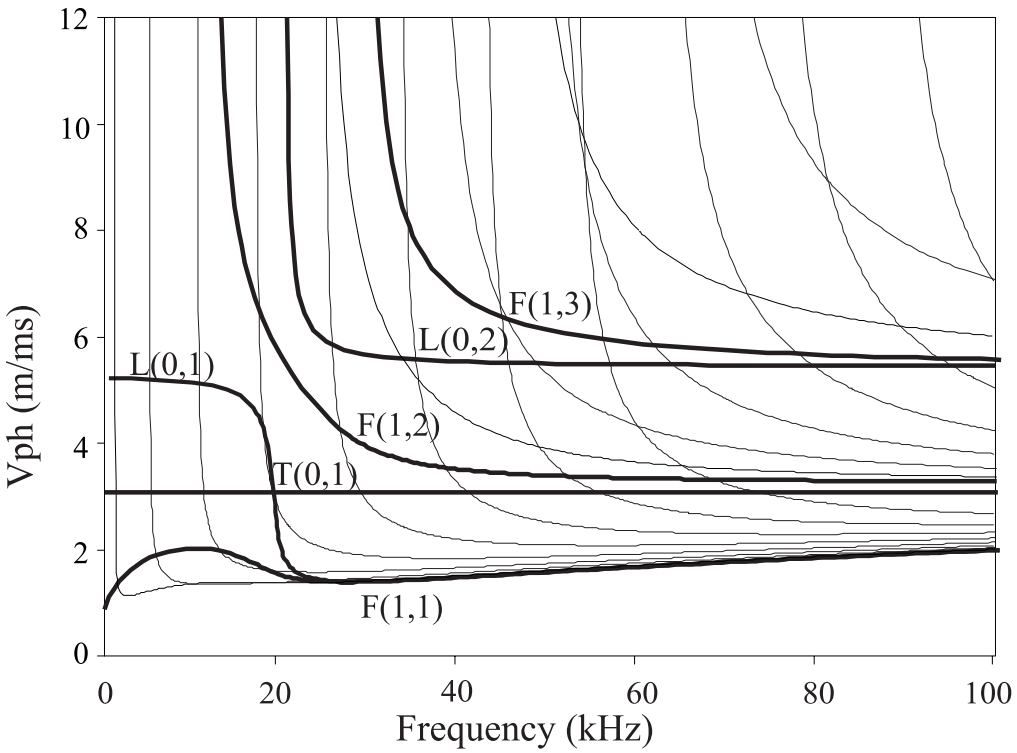

Figure 2.8: Phase velocity dispersion curves for a 3 inch schedule 40 (5.5 mm thickness) in a vacuum.

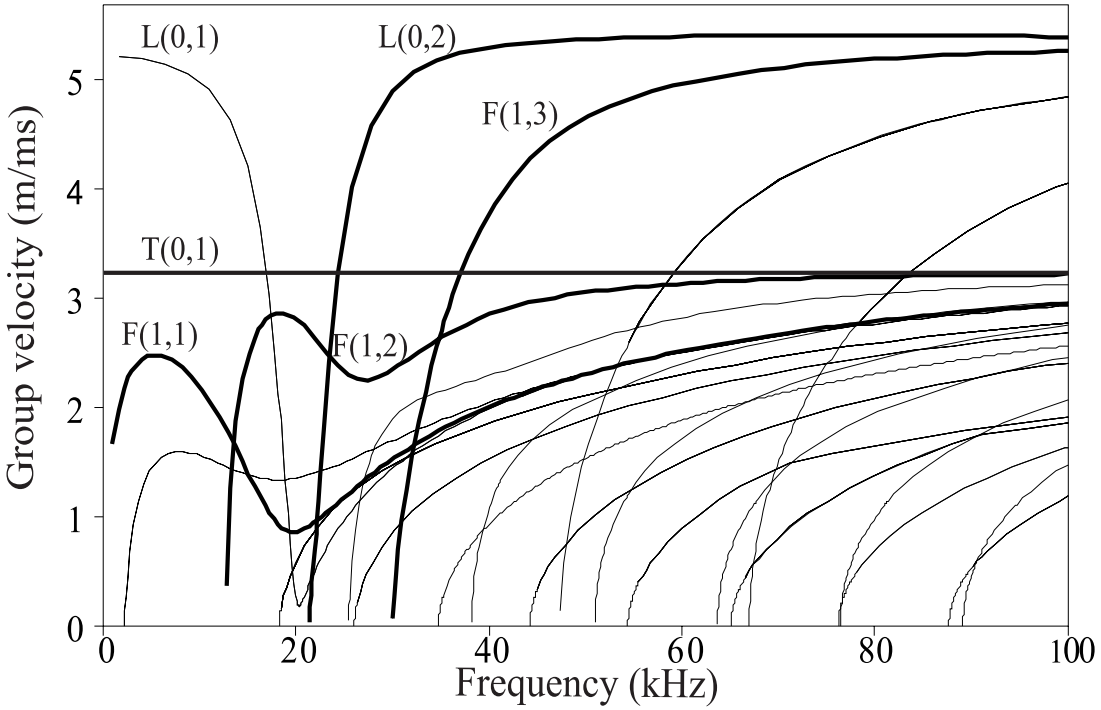

Figure 2.9: Group velocity dispersion curves for a 3 inch schedule 40 (5.5 mm thickness) in a vacuum.

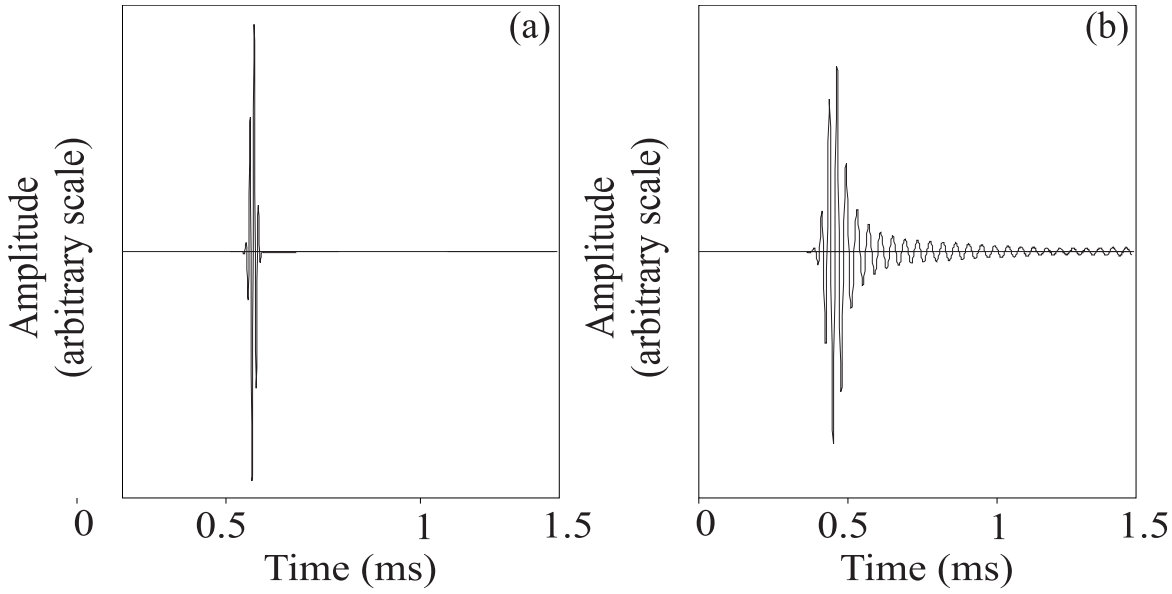

Figure 2.10: Example of dispersion in a 3 inch pipe where L(0,2) is excited and propagates along 2 metres of pipe. (a) shows the case when the excited signal is a 5 cycle 70 kHz toneburst ; (b) shows the case when the excited signal is a 5 cycle 35 kHz toneburst.

Chapter 3

SH wave interaction with discontinuities in plates

3.1 Introduction

This Chapter examines the reflection of the fundamental SH0 mode from thickness changes, notches and cracks in plates. The interaction of guided elastic waves in plates and pipes with discontinuities such as thickness steps has been already studied [70, 80, 81]. Koshiba et al. [70] proposed a combined Finite Element and analytical technique for the analysis of the scattering of SH waves by steps in plates. Ditri [80] studied the scattering of guided SH waves from steps in plates in terms of energy reflection and he also explained the multimode reflection when more than one propagating mode can potentially travel along the waveguide. Engan [81] investigated the torsional wave scattering from diameter changes in a circular solid rod using the modal decomposition method. Several researchers have studied the reflection characteristics of guided waves from notches in plates and pipes [73, 82, 70, 83, 9]. Both Lamb waves [73, 82] and SH waves [70, 83] have been investigated in terms of their interaction with notches in plates. The examination of the reflection coefficient as a function of the notch width has identified the important phenomenon of the interference between the reflection from the two sides of a notch [73, 82].

The aim of this work is to investigate the possibility of predicting the reflection from a notch by superimposing the reflections from a thickness step down (start of the notch) and a thickness step up (end of the notch). The significance

of non-propagating modes in the reflection from discontinuities and the relationship between crack and notch reflections are also discussed.

In this investigation both Finite Element and modal decomposition methods are used to investigate the effect of a thickness step on the propagation of the fundamental shear horizontal mode, the modal decomposition enabling a fuller understanding of the effect of non-propagating modes on the scattering characteristics. In all cases this study considered an incident SH0 mode and the region under examination was 0-0.55 MHz-mm (e.g. 0-100 kHz for a 5.5 mm plate). This relatively low frequency range is of particular interest because of the immediate generalization of this study to the case of pipes with notches where a low frequency torsional wave is used in order to have a long range for a single test (from 10 to 100 metres depending on the application) [11]. Moreover it is of general interest to study the effects of non-propagating modes on the reflection from defects and this is best viewed when only one propagating mode can exist in the wave guide.

The modulus and phase of the reflection coefficient at a step-down (when the thickness decreases) and step-up (when the thickness increases) were used to simulate the signal reflected from a rectangular notch. Therefore the interference phenomenon between the reflection from a step-down and a step-up was reproduced, and the predictions were compared with the Finite element results obtained for notch cases with varying axial extent. The effect of frequency on the reflection from geometrical discontinuities in plates has also been considered.

Finally, the limits of the method proposed to predict the reflection coefficient from notches have been examined. In particular, a study of the reflection from notches when the axial extent tends to zero (crack-like case) has been performed, and a verification of the convergence of the notch case to the crack case as the axial extent decreases has been shown.

3.2 Finite Element models

The Finite Element (FE) method has been extensively and successfully used to study the interaction between guided waves and defects in structures [10, 9, 67, 68, 69, 70, 71, 72, 73]. In general a three-dimensional (3-D) solid model is required to

perform a numerical analysis of the interaction between guided waves and discrete defects. However 3-D models are computationally expensive so when possible we use simplified models [10].

Many studies have been done on Lamb wave interaction with defects using two-dimensional models with the assumption of plane strain [67, 73, 82]. However, plane strain elements model displacements which are solely in the assumed plane of strain. In the case of SH waves, the displacement is normal to the plane, so such an approximation cannot be taken. Nevertheless, an approximate approach using an axisymmetric idealization has been found to work very satisfactorily. The implementation of the approximate method assumes a two-dimensional (2-D) axisymmetric model of a pipe with large diameter (a pipe with infinite diameter approximates a plate). The waves travel in the axial direction and the displacements are in the circumferential direction. The advantage is that the axisymmetric analysis allows displacements in the direction normal to the element (the circumferential direction); this degree of freedom is included in most implementations of axisymmetric elements in order to allow analyses of problems with non-zero circumferential harmonics. Therefore a standard Finite Element program can be used without the need to write specific code. Both the axial extent and the depth through the thickness of a defect can be varied using this model. The axisymmetric nature of the model implies that the defects extend over the full circumference of the pipe so they are equivalent to notches in a plate that are infinitely long in the direction normal to the propagation.

In all cases a finite length of the system was modelled and a geometrical discontinuity was introduced at some distance along it. The input wave signal was excited by prescribing time-varying tangential (u_y) displacements at one end of the model. Since the SH0 mode shape is constant with frequency, pure mode excitation was obtained by simply imposing the mode shape at the center frequency [45]. The displacement distribution was constant through the thickness in this case (see Figure 2.6a). Identically-sized linear (four-noded) quadrilateral axisymmetric elements were used. Using Finite Element analysis we needed to model a plate with a specific thickness but the results obtained from the Finite Elements can be generalized in terms of frequency-thickness product. We modelled a pipe with 5.5 mm wall thickness and 1.5 m radius and performed a convergence test to verify that this

radius was large enough for the system to approximate a plate; it was found that the reflection coefficient from a notch in the 1.5 m radius case was the same as that from a notch of the same depth in a pipe with 4.5 m radius, so confirming that the reflection coefficient had converged to that for a plate.

Three different types of discontinuity were modelled:
1) thickness step (see Figure 3.1a). This was used to study the scattering behavior when there is a change in the thickness of the waveguide. From this model we derived modulus and phase of both reflection and transmission at a thickness step. We modelled both the case in which the thickness decreases (step down) and the case in which the thickness increases (step up). The information derived from this set of models was further used to simulate the reflection from a rectangular notch.
2) rectangular notch (see Figure 3.1 b). This model was employed to study the effect of both frequency and axial extent on the reflection from notches. The results obtained from this model were also used to validate the reconstruction of the reflection from a rectangular notch superimposing the reflections from down and up steps.
3) V-notch (see Figure 3.1 c and 3.1 d). This model was used to study the relationship between crack and notch reflections, the rectangular notch having the limitation of being impractical to use to simulate notches with very small axial extent (this is explained further below).

We now present two subsections in which we describe the FE model for thickness steps and notches respectively.

3.2.1 FE model for thickness step

The thickness step was modelled by creating two regions with different thickness but keeping the dimensions of the elements constant. Only rectangular steps were modelled. The models represented a 1 m length using 2000 elements along the length and 10 elements through the thickness. A convergence study showed that the discretization used was satisfactory. A summary of the FE models that we studied for the step cases is in Table 3.1. The steps were placed at 0.6 m from the excitation point and the monitoring points were at 0.4 m and 0.8 m from the excitation point so the total path of the reflected (1st monitoring point) and transmitted signal (2nd monitoring point) was 0.8 meters in all cases. The excitation was a 10 cycle, Hanning

windowed, linear chirp at a center frequency of 100 kHz where the carrier signal $u(t)$ of duration T, centre frequency ω_c and amplitude A can be described by:

$$u(t) = A\sin(\frac{2\pi\omega_c t^2}{T})[1-\cos(\frac{2\pi t}{T})] \tag{3.1}$$

This gave more energy at low frequency (see typical spectrum signal in Figure 3.2) compared to a similar windowed toneburst. A typical time record from the simulation is also shown in Figure 3.3. This shows the incident signal on its way towards the step defect and then the reflected SH0 mode. The time trace in Figure 3.3 is for the 50% step down model.

Both modulus and phase of the reflected and transmitted signals were calculated. The modulus was obtained by dividing the amplitudes of the reflected and transmitted signals by the amplitude of the incident signal in the frequency domain. An extra FE model was run to obtain a phase reference. This was a model of a 1 m long, 5.5 mm thick plate without defects which was excited as in the case of the plate with a step defect. The signal was monitored at 0.8 meters from the excitation point so we had a reference signal that had travelled along the same path length as the reflected and transmitted signals in the plate with a step. Using a simple FFT algorithm it was possible to obtain the phase of the signals in the frequency domain. The phase of the reference signal was subtracted from the phase of the signals reflected and transmitted at a step so giving the phase shift caused by the scattering at the step.

3.2.2 FE model for notch

In both rectangular notch and V-notch models, a length of the plate was modelled and a notch was introduced at some distance along it. The input wave was excited by prescribing a 10 cycle, Gaussian windowed toneburst with 100 kHz centre frequency at one end of the plate (in this case Gaussian window was used because there was no need to simulate the low frequency behaviour). The tangential displacements (u_y) were monitored at a location between the excitation end and the defect, so both the incident wave and the reflected wave from the discontinuity were detected.

The models represented a 2.4 m long 5.5 mm thick plate using 2000 elements along the length and 10 elements through the thickness. A finer mesh with 20

elements through the thickness and 6000 elements along the length was also studied and gave almost identical results, indicating that convergence was satisfactory. Only the modulus of the reflection was calculated for the notch case and this was done exactly as in the step case. As already mentioned, two types of notch were studied:
1)rectangular notch
2) V notch.

The rectangular notches (see Figure 3.1 b) were created by removing elements. We studied two different defect depths (20% and 50% of the thickness). Several FE models with different axial extent have been studied to investigate the effect of axial extent on the reflection. The axial extent of the elements (inside and outside the notch) was kept constant in order to avoid numerical impedance differences. Therefore a fine mesh was needed to obtain the reflection coefficient at relatively small notch axial extent. Zero-length notches (crack case) were also modelled and this was done by disconnecting adjacent elements; thus although the elements on each side of the notch had nodes at coincident locations, they were not connected [9]. We also wanted to verify the convergence of the notch to the crack when the axial extent is small. A reduction of the axial extent of the notch using the mesh for the rectangular notch implies the use of elements with shorter length and consequently a refinement of the mesh. This is computationally expensive and can become simply impossible at very small defect axial extents. Therefore, in order to verify the convergence of the notch to the crack case, we used a V-notch model.

Using the V-notch model, we reduced the axial extent of the notch by simply decreasing the distance between the opposite faces of the notch. The V-notch was modelled with a 50% defect depth and varying axial extent L (see Figure 3.1c). In this case we used the same number of elements along the length and through the thickness in all of the models, the shape and dimension of each element depending on the extension of the V-notch. The shape change of each element from one model to another was small enough to neglect its effects on the accuracy of the results (see Figure 3.1d). We investigated the effect of changing the axial extent L of the head of the notch, and we checked the convergence of this model to the crack case when the axial extent was decreased.

3.3 Modal decomposition

The presence of a step (up or down) in the thickness of a plate causes scattering and consequent reflection and transmission of the incident signal. In this work we considered a case in which SH0 was incident on a step discontinuity and only SH0 could potentially propagate in the plate (SH0 excited at a frequency lower than the SH1 cut-off). If we made the assumption that only the incident SH0 contributes to the reflection and transmission of the wave, the magnitude of the reflection coefficient would be constant with frequency (up to the frequency at which SH1 appears). The value of reflection obtained at a step down in a plate in this case would be:

$$R_{A1} = \frac{1-\alpha}{1+\alpha} \tag{3.2}$$

in which $\alpha = \frac{t_2}{t_1}$, where t_1 is the thickness of the plate before the step and t_2 is the thickness after the step. The transmission coefficient past the step would be:

$$T_{A1} = \frac{2}{1+\alpha} \tag{3.3}$$

From a step up in a plate we would have:

$$R_{B1} = \frac{\alpha-1}{1+\alpha} \tag{3.4}$$

$$T_{B1} = \frac{2\alpha}{1+\alpha} \tag{3.5}$$

Clearly, only the magnitude of the reflection and transmission has been considered here. Equations (3.2-3.5) are the ratios between the amplitude of the signal after the interaction with the step discontinuity and the amplitude of the incoming signal. When the signal is transmitted through a step discontinuity, the thickness of the waveguide changes so a power normalization procedure is required to obtain a power normalized transmission coefficient (this is not necessary in the reflection case because the thickness of the waveguide does not change). In the case described above, the power normalized transmission coefficients can be obtained by multiplying the transmission coefficients in (3.3) and (3.5) by $\sqrt{\alpha}$ and $\frac{1}{\sqrt{\alpha}}$ respectively. In this simplified theory, the phase of the reflection and transmission coefficient is zero in all cases except in the step up reflection case where there is a π phase shift which is accounted for by the sign reversal in the numerator between (3.2) and (3.4).

However, the assumption that only one mode contributes to the scattering phenomenon at a step does not fulfill the boundary conditions and, in order to obtain an exact solution of the scattering problem, all of the propagating and non-propagating modes should be included in the solution. In practice this is impossible but it has been demonstrated that it is possible to obtain accurate solutions for scattering problems when considering a finite (and reasonable) number of modes [84, 85, 81]. Castaings et al. [84] used modal analysis to investigate the interaction of the A_0 and S_0 Lamb waves with vertical cracks in plates. Vogt et al. [85] applied the modal solution to the scattering of longitudinal and torsional waves at a point when a free waveguide enters an embedding material. Engan [81] used modal decomposition to study the scattering of torsional waves in a circular rod with a free surface that has an abrupt diameter change. The problem discussed by Engan is very similar to the problem of steps in plates when SH0 is incident. Therefore in this Chapter we used the approach proposed by Engan to tackle our scattering problem.

We here consider a plate with a discontinuity in thickness, changing from t_l on the left side to t_r on the right side (see Figure 3.1a). In this paper the subscripts l and r will be used to refer to left and right side of the waveguide. In the most general case SH waves are propagating in both directions on either side of the step. The incident modes have amplitude a and the scattered propagating and non-propagating modes have amplitude b. It is then possible to define the scattering problem using matrix notation:

$$\begin{bmatrix} b_l \\ b_r \end{bmatrix} = \begin{bmatrix} S_{1\,1} & S_{1\,2} \\ S_{2\,1} & S_{2\,2} \end{bmatrix} \begin{bmatrix} a_l \\ a_r \end{bmatrix} \tag{3.6}$$

If we consider n modes, the scattering matrix can be described by:

$$\begin{bmatrix} b_{l1} \\ b_{l2} \\ \vdots \\ b_{ln} \\ b_{r1} \\ b_{r2} \\ \vdots \\ b_{rn} \end{bmatrix} = \begin{bmatrix} [S_{1\,1}] & [S_{1\,2}] \\ [S_{2\,1}] & [S_{2\,2}] \end{bmatrix} \begin{bmatrix} a_{l1} \\ a_{l2} \\ \vdots \\ a_{ln} \\ a_{r1} \\ a_{r2} \\ \vdots \\ a_{rn} \end{bmatrix} \tag{3.7}$$

where the [S] terms are n*n matrices and, for example, a_{lj} is the amplitude of the jth incident mode on the left side of the waveguide. We here considered the most general case when there are incoming waves from both sides; the equations were further simplified for the practical implementation.

As already indicated, to solve the scattering problem we need to fulfill the boundary conditions at the step. These are that the stress is zero at the free surface of the discontinuity and both velocity and stress are continuous functions across the interface. As mentioned in section (2.2.3), the only component of stress which is relevant in our study is the τ_{yz} and this can be derived from the u_y displacement when we know the characteristics of the material (see equation (2.14)). The velocity can also be derived from the expression for the u_y displacement:

$$v = \frac{du_y}{dt} \tag{3.8}$$

Since only one component of stress and displacement will be considered from now on, we omit the subscripts y and z. Therefore the expressions for displacement, stress and velocity of the incoming wave will be:

$$\begin{aligned} u_l^a &= \sum_j a_{l,j} u_{l,j} e^{i(\omega t - k_{l,j} z)} \\ \tau_l^a &= -ic_{44} \sum_j k_{l,j} a_{l,j} u_{l,j} e^{i(\omega t - k_{l,j} z)} \\ v_l^a &= i\omega \sum_j a_{l,j} u_{l,j} e^{i(\omega t - k_{l,j} z)} \end{aligned} \tag{3.9}$$

where $a_{l,j}$ is the amplitude of the incoming mode of order j in the left part of the structure, $u_{l,j}$ is the power-normalized displacement, ω is the circular frequency and $k_{l,j}$ is the complex wavenumber. The expressions for u_l^b, τ_l^b and v_l^b (outgoing wave in the left part) are the same as those for u_l^a, τ_l^a and v_l^a respectively except for the sign in front of the wavenumber, because they are travelling in the opposite direction from right to left after the scattering (see Engan [81] for more details). By using the same procedure, it is possible to derive expressions for displacement, stress and velocity in the right part of the waveguide. Therefore, the boundary conditions mentioned above can be written as:

$$i\omega u_l^a + i\omega u_l^b = i\omega u_r^a + i\omega u_r^b, \quad x < t_r \tag{3.10}$$

$$\begin{aligned} \tau_l^a + \tau_l^b &= \tau_r^a + \tau_r^b, \quad x < t_r \\ \tau_l^a + \tau_l^b &= 0, \quad x > t_r \end{aligned} \tag{3.11}$$

Expansion in eigenmodes yields:

$$i\omega \sum_j a_{l,j} u_{l,j} + i\omega \sum_j b_{l,j} u_{l,j} = i\omega \sum_j a_{r,j} u_{r,j} + i\omega \sum_j b_{r,j} u_{r,j}, \quad x < t_r \tag{3.12}$$

$$\begin{aligned} -ic_{44} \sum_j k_{l,j} a_{l,j} u_{l,j} + ic_{44} \sum_j k_{l,j} b_{l,j} u_{l,j} = \\ ic_{44} \sum_j k_{r,j} a_{r,j} u_{r,j} - ic_{44} \sum_j k_{r,j} b_{r,j} u_{r,j}, \quad x < t_r \\ -ic_{44} \sum_j k_{l,j} a_{l,j} u_{l,j} + ic_{44} \sum_j k_{l,j} b_{l,j} u_{l,j} = 0, \quad x > t_r \end{aligned} \tag{3.13}$$

These equations already contain the solution for the scattering problem but we need to simplify the expressions in order to obtain a simple matrix form which can easily be implemented in a computer algorithm. In particular, since the modes considered in the computation were power normalized, it is wise to obtain an explicit expression for the power flow [81].

From equation (3.12), taking the complex conjugate, multiplying by $\frac{1}{2} i c_{44} k_{r,m} u_{r,m}$ and integrating through the thickness of the plate, we obtain:

$$\begin{aligned} \frac{1}{2} \sum_j \omega c_{44} k_{r,m} a_{l,j}^* \int_0^{t_r} u_{l,j} u_{r,m} dt + \frac{1}{2} \sum_j \omega c_{44} k_{r,m} b_{l,j}^* \int_0^{t_r} u_{l,j} u_{r,m} dt = \\ \frac{1}{2} \sum_j \omega c_{44} k_{r,m} a_{r,j}^* \int_0^{t_r} u_{r,j} u_{r,m} dt + \frac{1}{2} \sum_j \omega c_{44} k_{r,m} b_{r,j}^* \int_0^{t_r} u_{r,j} u_{r,m} dt \end{aligned} \tag{3.14}$$

Introducing the normalized wavenumber $Q_{r,m} = \frac{k_{r,m}}{k_0}$ and simplifying the expression, we obtain:

$$Q_{r,m}^* \sum_j L_{j,m} a_{l,j} + Q_{r,m}^* \sum_j L_{j,m} b_{l,j} = P_{r,m}^* a_{r,m} + P_{r,m}^* b_{r,m} \tag{3.15}$$

where k_0 is the wavenumber of the SH0 mode, $L_{j,m} = \frac{c_{44}}{2} \omega k_0 \int_0^{t_r} u_{l,j} u_{r,m} dt$ and $P_{r,m}$ is the power flow which is equal to one for propagating modes and (-i) for non-propagating modes [81].

From equation (3.13) after multiplying by $\frac{1}{2}i\omega u_{l,m}$ and integrating over the total cross section we can write:

$$-\sum_j \frac{1}{2}\omega c_{44} k_{l,j} a_{l,j} \int_0^{t_l} u_{l,j} u_{l,m} dt + \sum_j \frac{1}{2}\omega c_{44} k_{l,j} b_{l,j} \int_0^{t_l} u_{l,j} u_{l,m} dt = \sum_j \frac{1}{2}\omega c_{44} k_{r,j} a_{r,j} \int_0^{t_r} u_{r,j} u_{l,m} dt - \sum_j \frac{1}{2}\omega c_{44} k_{r,j} b_{r,j} \int_0^{t_r} u_{r,j} u_{l,m} \tag{3.16}$$

Again, introducing the quantity P, we obtain:

$$\sum_j Q_{r,j} L_{m,j} a_{r,j} - \sum_j Q_{r,j} L_{m,j} b_{r,j} = -P_{l,m} a_{l,m} + P_{l,m} b_{l,m} \tag{3.17}$$

In order to derive the S-parameters [15] for the defined problem, we write equations (3.15) and (3.17) as:

$$|Q_{r,m}| \sum_j L_{j,m} b_{l,j} - b_{r,m} = -|Q_{r,m}| \sum_j L_{j,m} a_{l,j} - a_{r,m} \tag{3.18}$$

$$P_{l,m} b_{l,m} + \sum_j Q_{r,j} L_{m,j} b_{r,j} = P_{l,m} a_{l,m} + \sum_j Q_{r,j} L_{m,j} a_{r,j} \tag{3.19}$$

It is then possible to obtain a simple matrix in which we separate the inputs (a) from the unknown values (b):

$$\left[M_b\right] \begin{bmatrix} b_l \\ b_r \end{bmatrix} = \left[M_a\right] \begin{bmatrix} a_l \\ a_r \end{bmatrix} \tag{3.20}$$

with solution:

$$\begin{bmatrix} b_l \\ b_r \end{bmatrix} = \left[M_b^{-1}\right] \left[M_a\right] \begin{bmatrix} a_l \\ a_r \end{bmatrix} \tag{3.21}$$

The scattering matrix will then be:

$$\left[S\right] = \left[M_b^{-1}\right] \left[M_a\right] \tag{3.22}$$

Using Disperse [35] it was possible to obtain the mode shapes and wave numbers for each of the computed modes in the frequency-thickness range 0-0.55 MHz-mm. The mode shapes were extracted using 201 points through the thickness of the left side of the waveguide and we verified that the number of points was satisfactory by performing a convergence study. Subsequently the modes were power normalized according to Engan [81] and the coefficients of the scattering matrix were calculated.

The input vector was in this case a vector with all zeros except the element accounting for the SH0 excitation in the left side of the waveguide. In order to estimate the accuracy of the method, we performed convergence tests by increasing the number of modes considered in the computation and we also verified the conservation of energy. The energy check was done by estimating the error:

$$\varepsilon = 1 - (|b_{l,SH0}|^2 + |b_{r,SH0}|^2) \tag{3.23}$$

where $b_{l,SH0}$ and $b_{r,SH0}$ are respectively the reflection and transmission coefficients for the SH0 mode (only propagating modes can carry energy).

3.4 Results

The numerical results are presented below. We have investigated various cases describing the scattering phenomenon in plates with defects. The section is divided in two subsections in which we describe the results for the thickness step and the notch cases.

3.4.1 Plate with thickness step

Using the results of the FE simulations we studied the effect of up and down steps in a plate where the SH0 mode was incident. A relatively low frequency range (0-0.55 MHz-mm) was investigated (e.g. 0-100 kHz in a 5.5 mm plate). Figures 3.4a and 3.5a show the modulus of the reflection and transmission coefficients respectively when there is a down step of 50% (the dots show the FE results). In this frequency range the modulus is almost constant with frequency in both cases (note the very narrow range on the y axis of Figure 3.4a). The value of the reflection and transmission modulus can be approximated using equations (3.2) and (3.3) respectively. A power normalization procedure was executed when the signal was transmitted through the step (because of the thickness change in the waveguide) in order to be able to compare the results obtained from the Finite Element analysis with the results obtained from the modal decomposition method (see Section 3.3). Figures 3.6a and 3.7a show the modulus of the reflection and transmission coefficients respectively

when there is an up step of the thickness (the reflection and transmission modulus are power normalized).

Figures 3.4b and 3.5b show the phase shift of the reflected and transmitted signal respectively when there is a down step of 50% of the thickness. It is clear that the phase shift is frequency dependent in both cases and it varies monotonically with frequency. At zero frequency the value of phase shift tends to zero for both the transmitted and the reflected waves. In the case of the up step, the phase shift at zero frequency is zero for the transmitted signal (see Figure 3.6b) and π for the reflected signal (see Figure 3.7b).

The numerical results of the modal decomposition method are also shown. The modal decomposition method using only SH0 leads to the same results as those obtained using the simplified theory (see Section 3.3). The reflection coefficient obtained using equation (3.2) is constant with frequency and, at low frequency-thickness, it is reasonably close to the reflection behavior predicted using Finite Elements, diverging at high frequency-thickness values (dashed line in Figure 3.4a). It is clear from Figure 3.4a that the modulus of the reflection coefficient obtained from the Finite Element prediction can be approximated by simply using the SH0 and SH1 modes and neglecting the higher order non-propagating modes in the computation. The reflection modulus is also shown for the case in which 5 non-propagating modes were considered, confirming the good agreement between the Finite Element and the modal decomposition results.

The results for the information of the reflection when there is a step down (see Figure 3.4b) clearly shows that this varies with the number of modes included in the computation. As already mentioned in section 3.3, the phase shift is zero if we take into account only the SH0 mode (see dashed line in Figure 3.4b). The phase shift obtained from the Finite Element predictions is approximated quite well by using two modes (SH0 and SH1) in the modal decomposition algorithm. A convergence test for the phase of the reflection and transmission was performed and its value converged when 5 non-propagating modes were considered in the modal decomposition algorithm. The calculations showed that more modes tend to be required for the phase calculation to converge than for the amplitude to converge. The phase angles predicted introducing 5 non-propagating modes in the modal decomposition

algorithm matched very well with the results obtained from the FE models. The good agreement between the FE predictions and the modal decomposition method when introducing 5 non-propagating modes in the computation was confirmed for the transmission through a down step (Figure 3.5) and both reflection and transmission in the up step case (Figures 3.6-3.7).

The energy criterion described in Section 3.3 was satisfied even when only a few modes were included in the computation. The ε value was always less than 10^{-4} in the cases plotted in Figures 3.4, 3.5, 3.6 and 3.7.

Tests were also done on 20% up and down steps but for brevity these are not shown here. Again good agreement between the results obtained using FE and the results from the modal decomposition were obtained. The number of modes to be included in the computation depended on the specific case being studied. More than 10 non-propagating modes were needed to obtain the convergence of the algorithm when studying a 20% thickness step. It would be interesting to investigate ways of predicting the number of non-propagating modes required in the analysis, but that has not yet been pursued.

3.4.2 Plate with rectangular notch

In this section, Finite Element predictions for the rectangular notch case are compared with superposition of the up and down step predictions.

The geometry of the notch is such that there will be a series of consecutive reflections from the notch decreasing in modulus with the number of times the wave travels back and forth inside the notch. If the effect of the non-propagating modes is neglected, it is possible to use the simplified theory explained in section 3.3. The first reflection is given by equation (3.2). The reflection R_{B1} described by (3.4) is time delayed by L/V compared to the reflection R_{A1} defined by (3.2) where L is the axial extent of the notch and V is the velocity of the SH0 wave, therefore the total phase shift between the two reflections is $\pi + 2fL\pi/V$, where the addition of π takes into account the sign reversal in the numerator between (3.2) and (3.4), and f is the frequency of the wave. The transmission coefficient at the end of the notch, T_{B1} is also time delayed by L/V compared to T_{A1}. The second reflection is due to the signal transmitted through the down step (start of notch), reflected at the up step

(end of notch) and transmitted through the up step (start of notch). The amplitude of the second reflection is:

$$R_{A2} = T_{A1} \cdot R_{B1} \cdot T_{B1} \tag{3.24}$$

and its time delay is $2L/V$ where L is the axial extent of the notch and V is the SH0 velocity. The third reflection is:

$$R_{A3} = T_{A1} \cdot (R_{B1})^3 \cdot T_{B1} \tag{3.25}$$

with time delay $4L/V$; The amplitude of the j^{th} reflection is given by:

$$R_{Aj} = T_{A1} \cdot (R_{B1})^{2j-3} \cdot T_{B1} \tag{3.26}$$

with time delay $j \cdot 2 \cdot L/V$. The total reflection is:

$$R_{TOT} = R_{A1} + R_{A2} + .. + R_{Aj} + ... \tag{3.27}$$

If we do not consider the phase shift due to the contribution of the non-propagating modes, the behavior of the total reflection coefficient from a 50% depth rectangular notch with varying axial extent is described by the dashed line in Figure 3.8. In this prediction, the reflection coefficient has minima when the axial extent is $(\frac{n\lambda}{2})$ and it has maxima when the axial extent is equal to $(\frac{n\lambda}{2} + \frac{\lambda}{4})$, where λ is the wavelength and n is an integer.

It is also possible to take into account the phase shift caused by the up and down steps. If we do this using the Finite Element or modal decomposition predictions from down and up steps in an algorithm which adds up the first four reflections with their modulus and phase, we obtain the solid curve in Figure 3.8. This was traced at a frequency-thickness product of 0.55 MHz-mm (100 kHz for a 5.5 mm plate). This curve is shifted to the left with respect to the curve obtained by neglecting the phase shifts at the steps.

In order to verify the accuracy of the prediction and identify its limits, we studied the reflection from rectangular notches with varying axial extent using Finite Element analysis and the results are also shown in Figure 3.8 for comparison. Clearly there is very good agreement between the predictions using the amplitude and phase information obtained from the step models and the notch cases studied using FE. In

contrast, the reflection coefficient predicted neglecting the phase information does not match the results obtained from the FE model, demonstrating that the phase shift must be considered in this frequency regime. However, it is clear from Figures 3.4a, 3.5a, 3.6a and 3.7a that the simplified theory (no phase shift), can be a relatively good approximation at very low frequency where the phase shift is small enough to be neglected.

Figure 3.9 shows similar results for 20% notch depth, very good agreement between the FE results for the notches and the predictions using the phase shift information again being obtained.

The effect of frequency on the reflection from notches is shown in Figure 3.10. The reflection coefficient was plotted for a 20% depth notch with varying axial extent at three different frequencies (0.44 MHz-mm, 0.55 MHz-mm and 0.66 MHz-mm). It is clear from this plot that the effect of increasing the frequency (if working at relatively low frequency) is a shift of the curves towards the ordinate axis. This is due to the fact that the amplitude of the reflection and transmission coefficients are almost constant with frequency and the phase shift changes monotonically with frequency.

The result obtained for the crack case (zero axial extent) is highlighted on Figure 3.8. The prediction for the crack is below the solid curve; this is the only point that does not match well with the curve. In order to verify the predictions for the crack case, we studied the effect of changing the axial extent of a V-notch. Figure 3.11 shows the modulus of reflection plotted versus V-notch opening (L on Figure 3.1c) on a logarithmic scale. The reflection coefficient decreases monotonically with the axial extent and, when the axial extent is less than 0.001% of the wavelength, it settles to the value of reflection coefficient obtained for the crack case on Figure 3.8 (shown as a dashed line in Figure (3.11)). Therefore the convergence of the notch case to the crack case at low axial extent of the notch was verified.

Figures 3.8 and 3.9 show that the crack case cannot be approximated using the predicted curve for the notch case. This is due to the presence of the non-propagating modes. After the scattering of the incoming signal (SH0) on the left side of the notch (step down), both propagating (SH0 only in our case) and non-propagating modes are present. If the axial extent of the notch tends to zero (crack case), the local

vibration generated on the left side interacts with the right side and vice versa. A different interference pattern than the one depicted for a notch case (at relatively large axial extent) is to be expected in the crack case. In theory, for a rigorous analysis of the crack case using the approach proposed in this paper, the input signal at the second step discontinuity should be written considering both propagating and non-propagating modes. In practice, the input of the modal decomposition was SH0 in all cases so the effect of non-propagating modes generated on one side of the crack and interacting with the opposite side was not taken into account. This indicates that it will be very difficult to model the reflection due to cracks in this way and it would be better to adopt the approach used by Castaings et al. [84].

From Figure 3.8 it is also evident that the notch cases characterized by relatively low axial extent are reasonably well approximated using our algorithm. It would be expected that, as the axial extent diminishes, the non-propagating modes generated at the down step interact with the up step and vice versa. This is because the discontinuities are not far enough apart for the non-propagating wave field to be considered to be completely attenuated. Moreover, as the axial extent reduces, the number of non-propagating modes interacting with both discontinuities increases. This suggests that the reflection coefficient at very low axial extent of the notch cannot be approximated using our algorithm. However, in practice, the lowest axial extent case that was studied for the rectangular notch (1.25% of wavelength) was still reasonably well approximated using our method, suggesting that the non-propagating modes only become significant at lower axial extents. In fact at 1.25% of the wavelength the first non-propagating mode has already decayed by 25% of its maximum value (at zero distance) and the higher order modes are effectively completely attenuated due to their higher attenuation values (as shown in Figure 2.5).

3.5 Conclusions

The scattering of the fundamental SH wave from discontinuities in plate waveguides has been discussed. Both the Finite Element and the modal decomposition methods have been used to study the effect of thickness steps in plates, and the Finite

Element method has also been used to study the reflection from cracks and notches in plates. An alternative method for predicting the reflection from notches has also been proposed. This is based on the superposition of the reflections from a down step (start of the notch) and an up step (end of the notch). The limits of the proposed method have been investigated. The convergence of the notch case to the crack case as the axial extent of the notch decreases has also been verified.

The modulus of reflection and transmission coefficients from a step in a plate when SH0 is incident at relatively low frequency is almost constant with frequency-thickness product and it can be approximated by simply considering SH0. The phase of the reflection and transmission coefficient varies monotonically with the frequency-thickness product and it is necessary to consider the effect of non-propagating modes in the modal solution to reproduce its frequency-dependent behavior. Very good agreement between the Finite Element and modal solutions has been shown.

The reflection from a rectangular notch can be approximated by superimposing the reflection from a down step followed by an up step, the phase information of the reflection and transmission at the steps being very important to reproduce the interference phenomenon at the notch.

The superposition of the reflections from down and up steps cannot be used with the same success to approximate the reflection from cracks, because the interaction of non-propagating modes with both sides of the notch has not been taken into account (the non-propagating modes generated at one side of the notch are assumed to decay before reaching the opposite side of the notch). However, the results obtained at notch axial extent as low as 1.25% of the wavelength still agreed very well with the Finite Element solution, indicating that the interaction of non-propagating modes with the sides of the notch is only significant at very small axial extents.

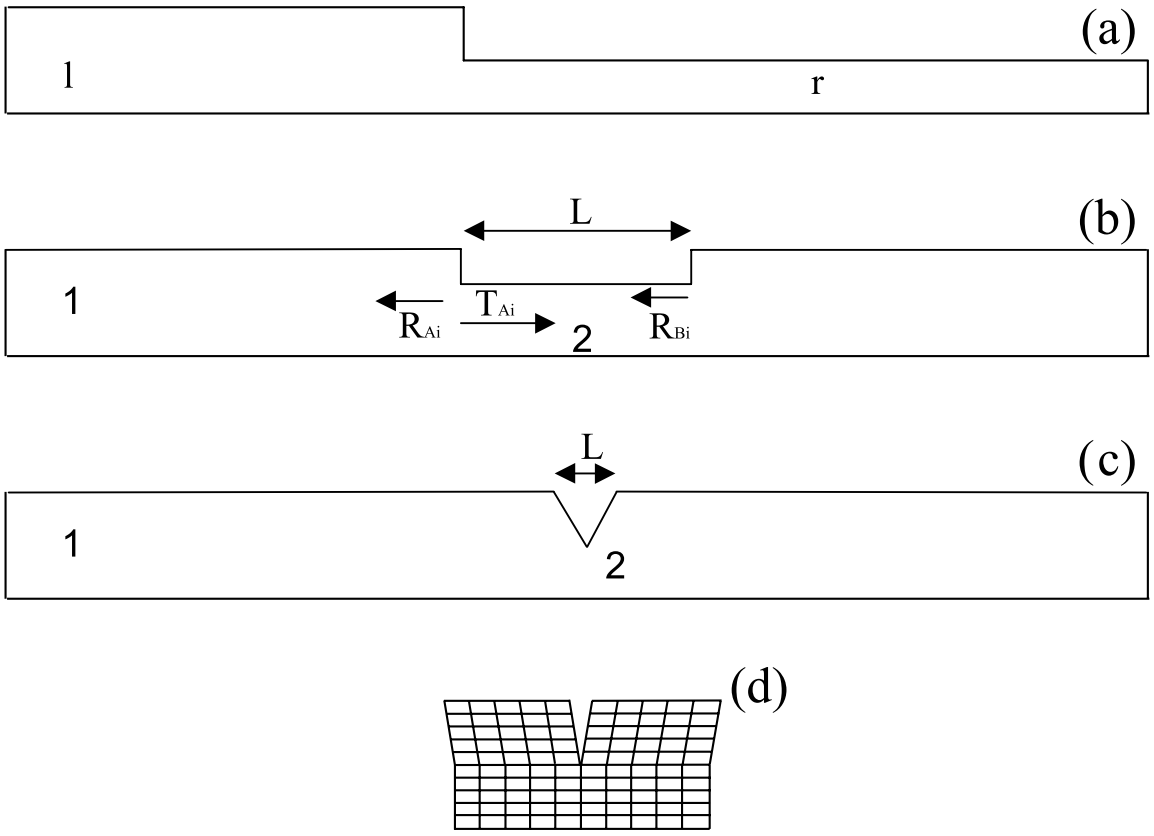

Figure 3.1: (a) Schematic of step; (b) rectangular notch; (c) V-notch; (d) detail of Finite Element mesh for V-notch.

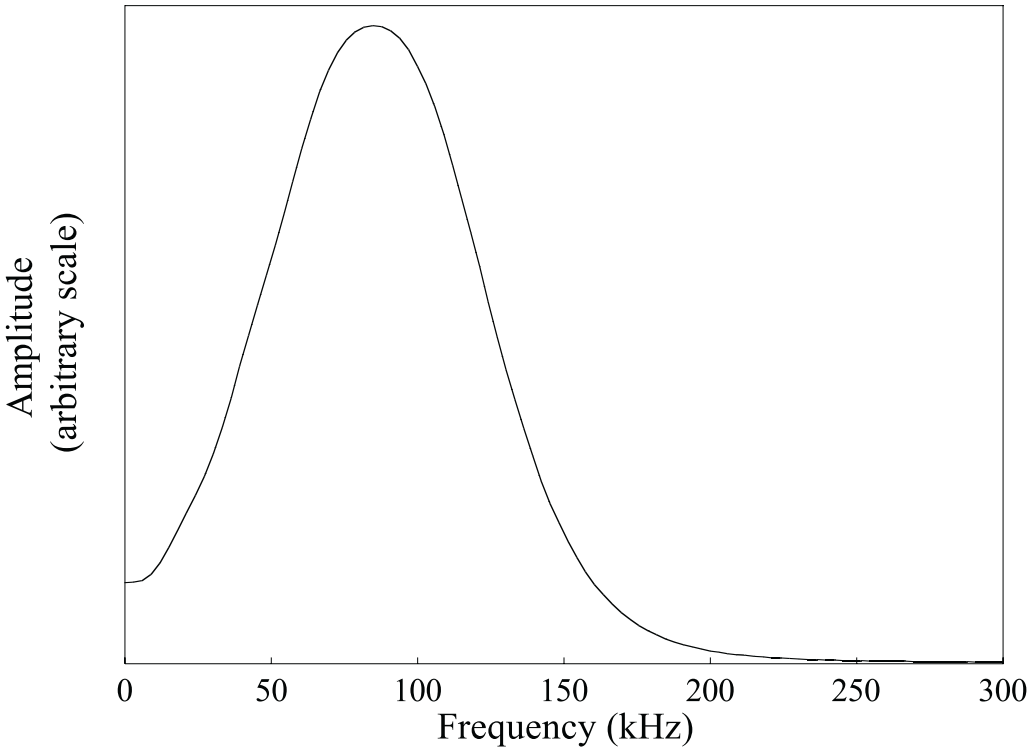

Figure 3.2: Frequency spectrum of Hanning windowed linearly chirped toneburst at 100 kHz center frequency.

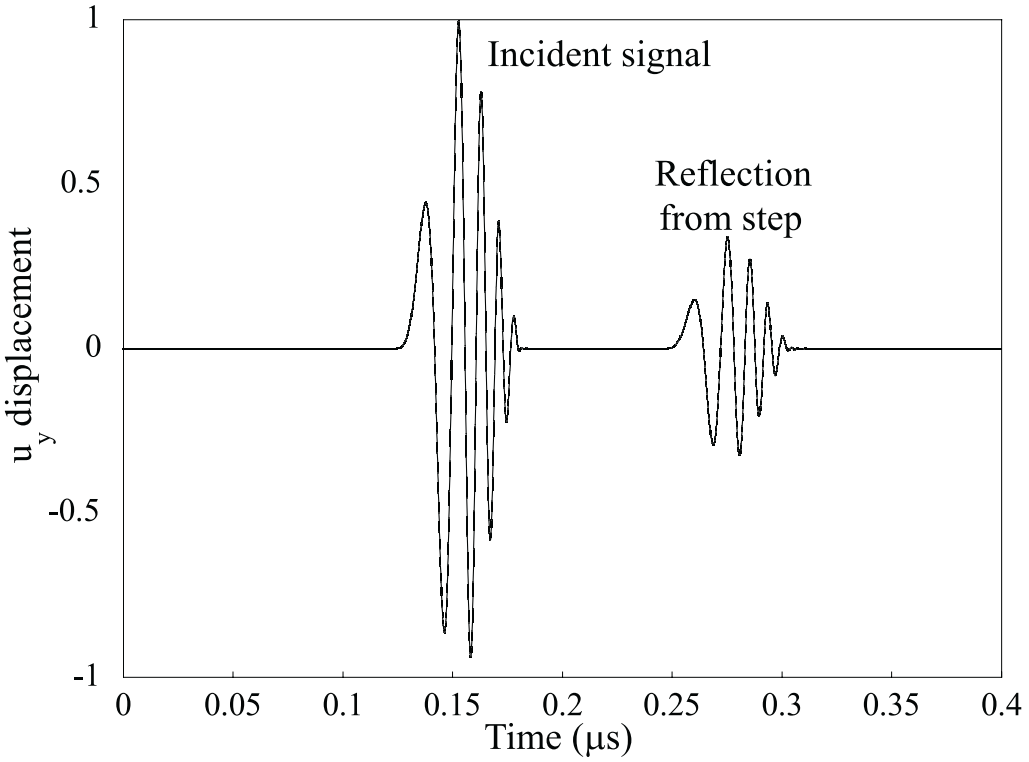

Figure 3.3: Predicted time record for a 5.5 mm plate with 50% thickness step and SH0 mode incident at 100 kHz center frequency.

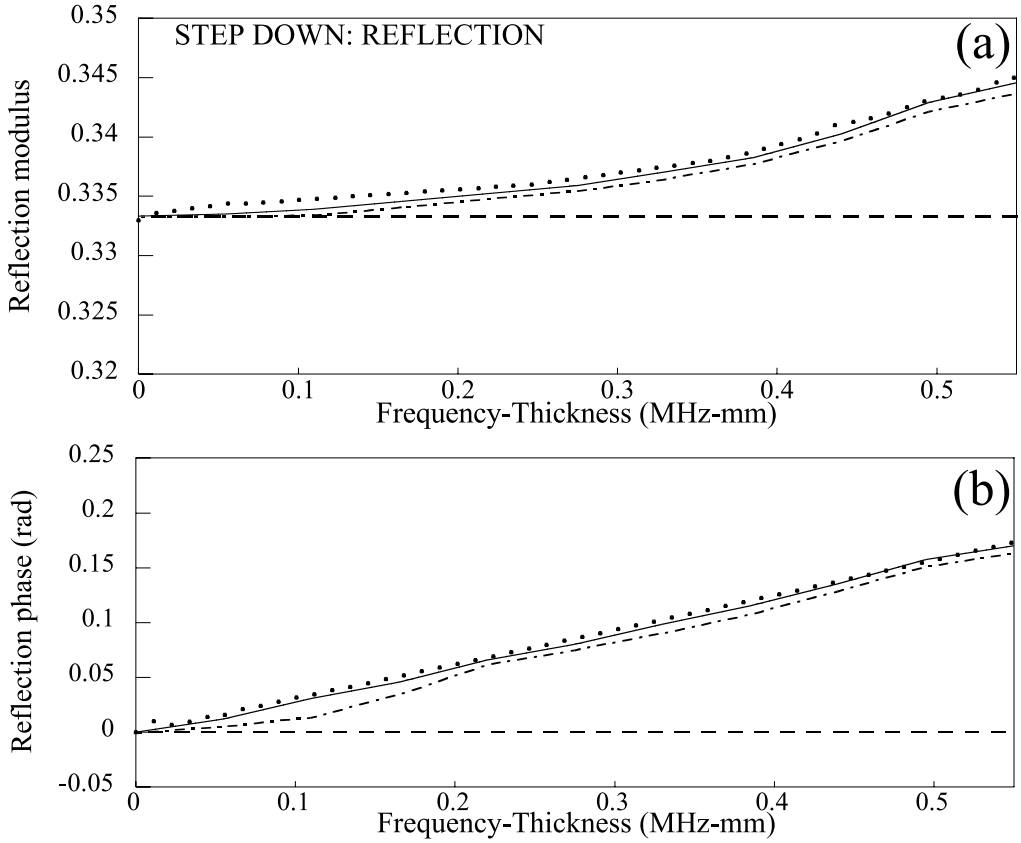

Figure 3.4: Modulus (a) and phase angle (b) of reflected fundamental SH0 mode from a thickness step down of 50% of total thickness. The plot shows the results obtained with FE (dots) and modal decomposition using only SH0 (dashed line), SH0 and the first non-propagating mode (double dashed line), SH0 and the first 5 non-propagating modes (solid line).

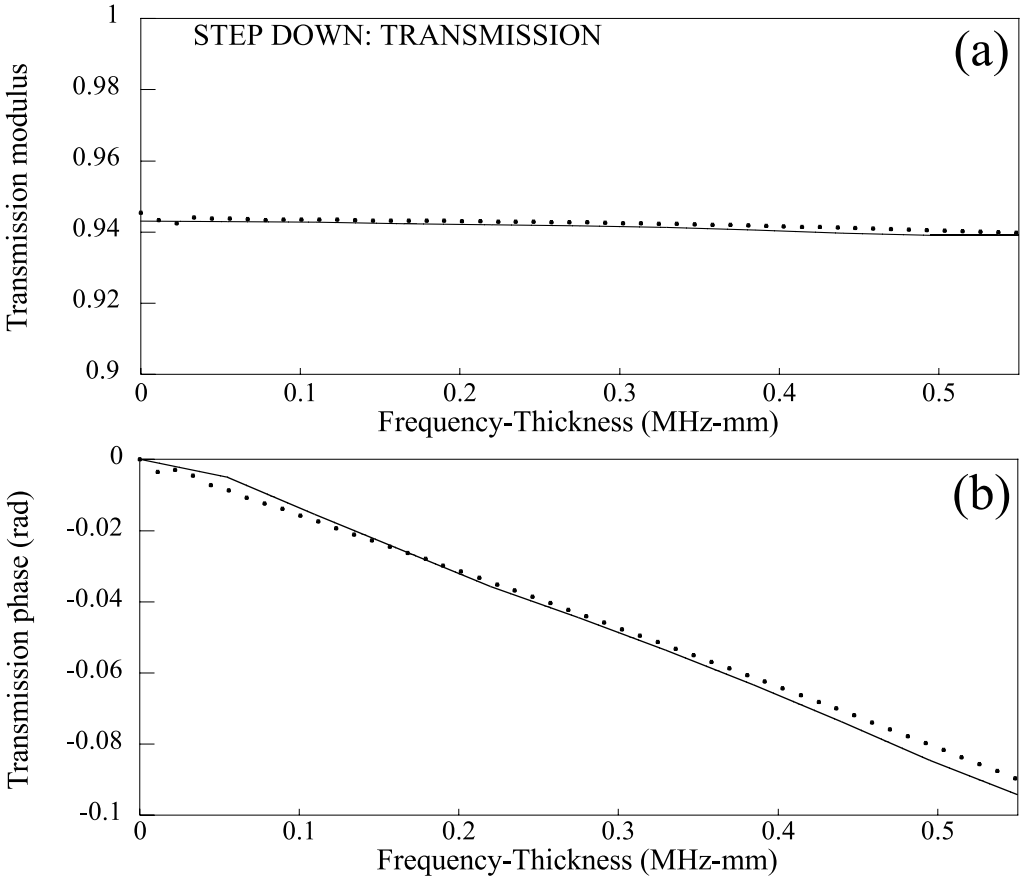

Figure 3.5: Modulus (a) and phase angle (b) of transmitted fundamental SH0 mode from a thickness step down of 50% of total thickness. The plot shows the results obtained with FE (dots) and modal decomposition using SH0 and 5 non-propagating modes(solid line).

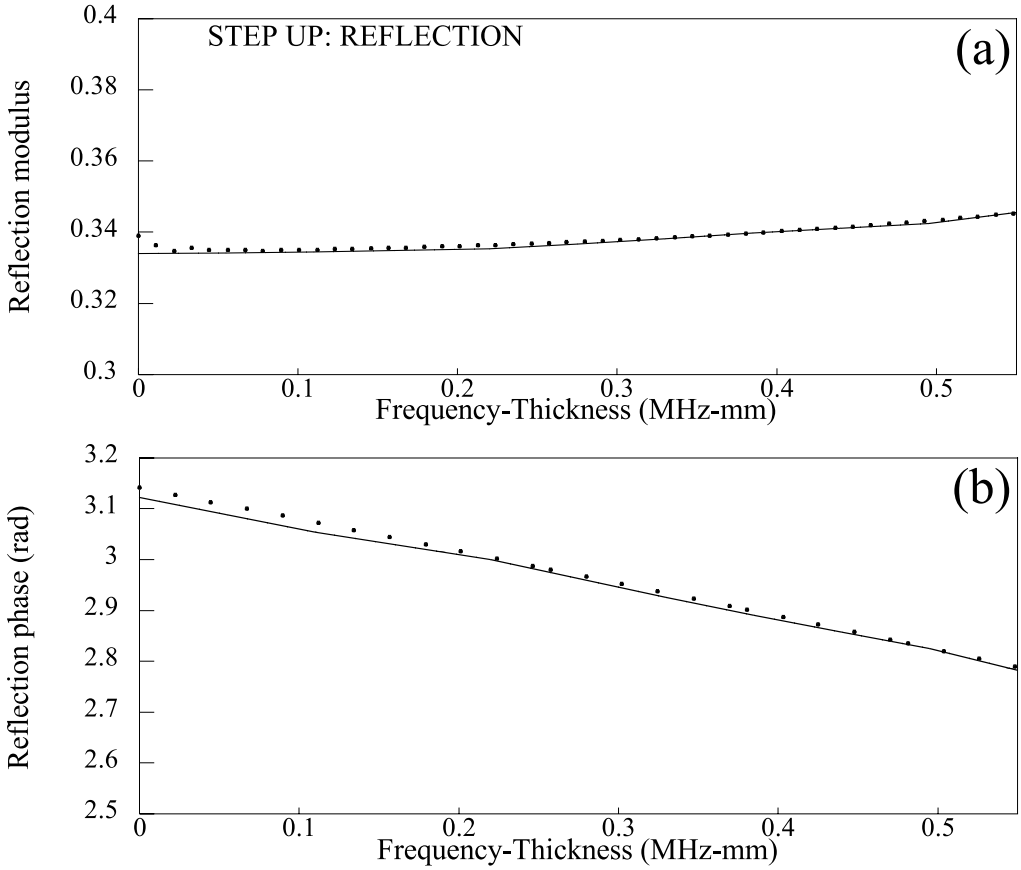

Figure 3.6: Modulus (a) and phase angle (b) of reflected fundamental SH0 mode from a thickness step up of 50% of total thickness. The plot shows the results obtained with FE (dots) and modal decomposition using SH0 and 5 non-propagating modes(solid line).

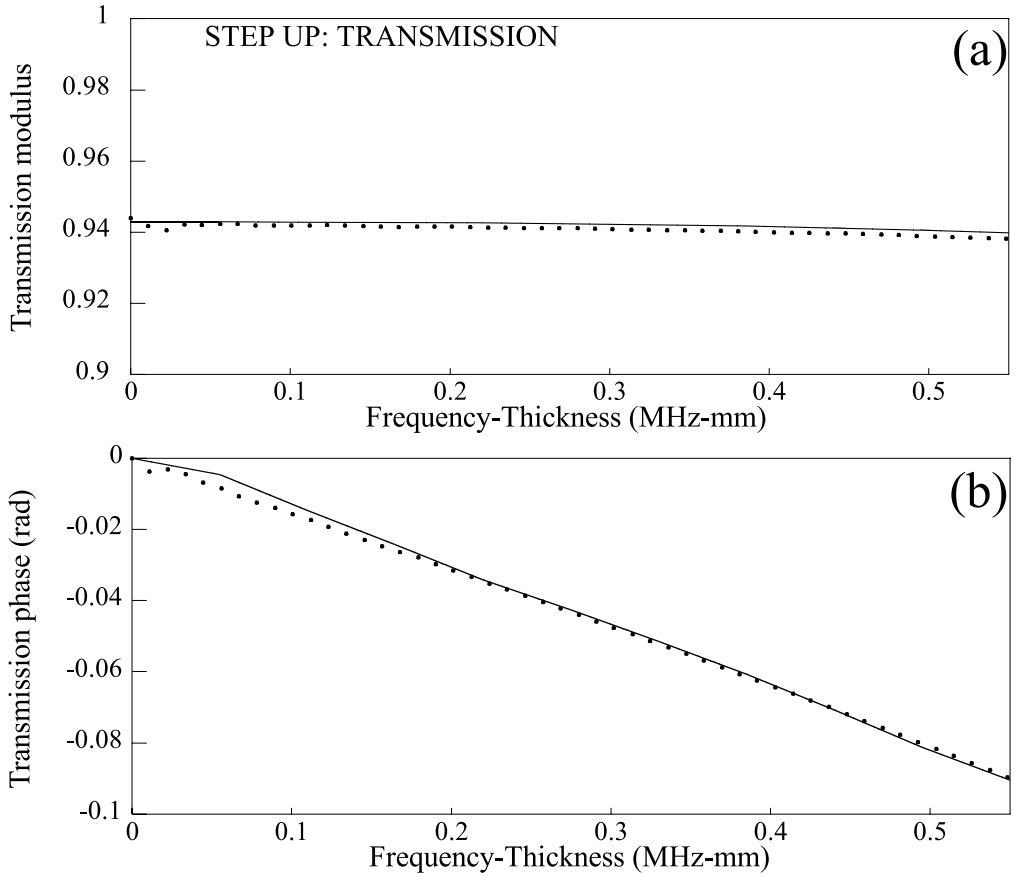

Figure 3.7: Modulus (a) and phase angle (b) of transmitted fundamental SH0 mode from a thickness step up of 50% of total thickness. The plot shows the results obtained with FE (dots) and modal decomposition using SH0 and 5 non-propagating modes(solid line).

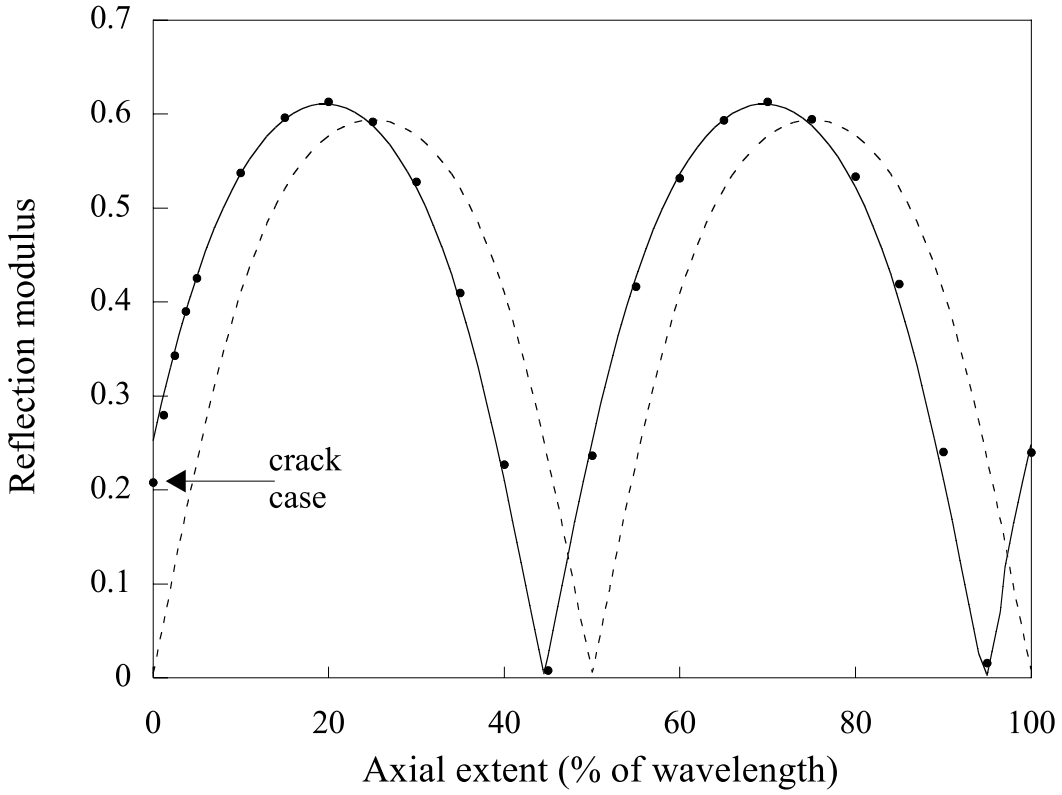

Figure 3.8: Variation of reflection ratio with axial extent of the notch. Results are for a plate with SH0 at 0.55 MHz-mm incident on a notch with 50% thickness depth. The dots indicate the FE results obtained for the rectangular notch case. The dashed line predicts the notch behavior using the simplified theory (no phase shift) and the solid lines reproduce the notch reflection behavior using the complete theory with the phase shift information.

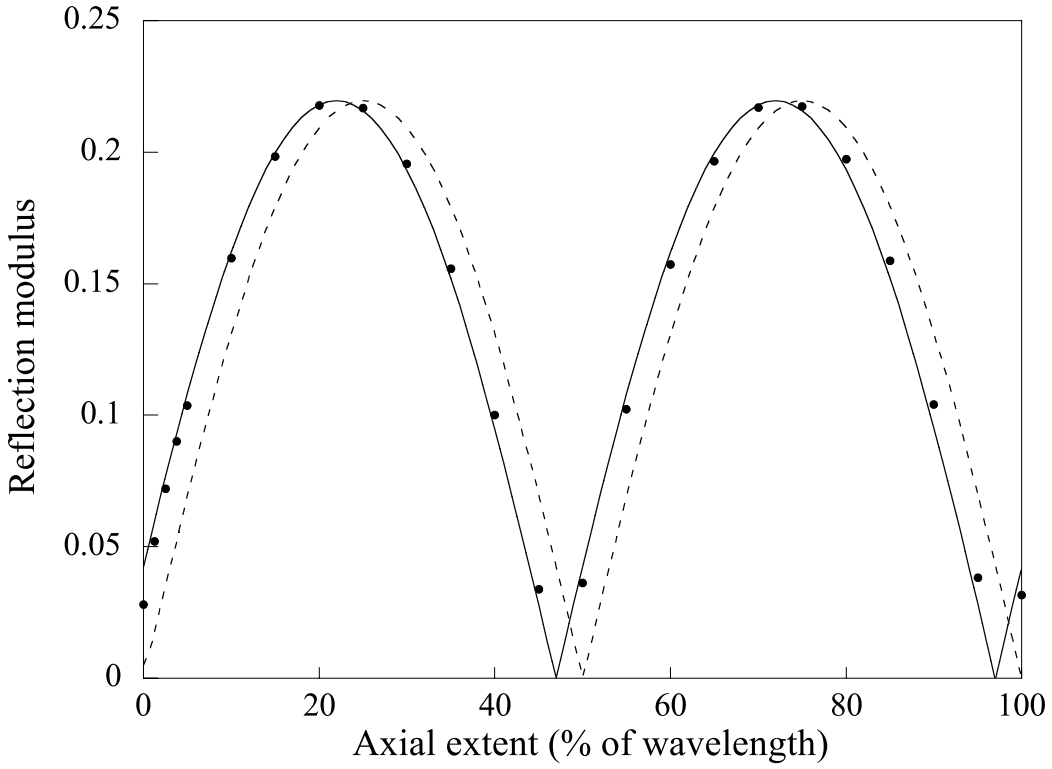

Figure 3.9: Variation of reflection ratio with axial extent of the notch. Results are for a plate with SH0 at 0.55 MHz-mm incident on a notch with 20% thickness depth. The dots indicate the FE results obtained for the rectangular notch case. The dashed line predicts the notch behavior using the simplified theory (no phase shift) and the solid lines reproduce the notch reflection behavior using the complete theory with the phase shift information.

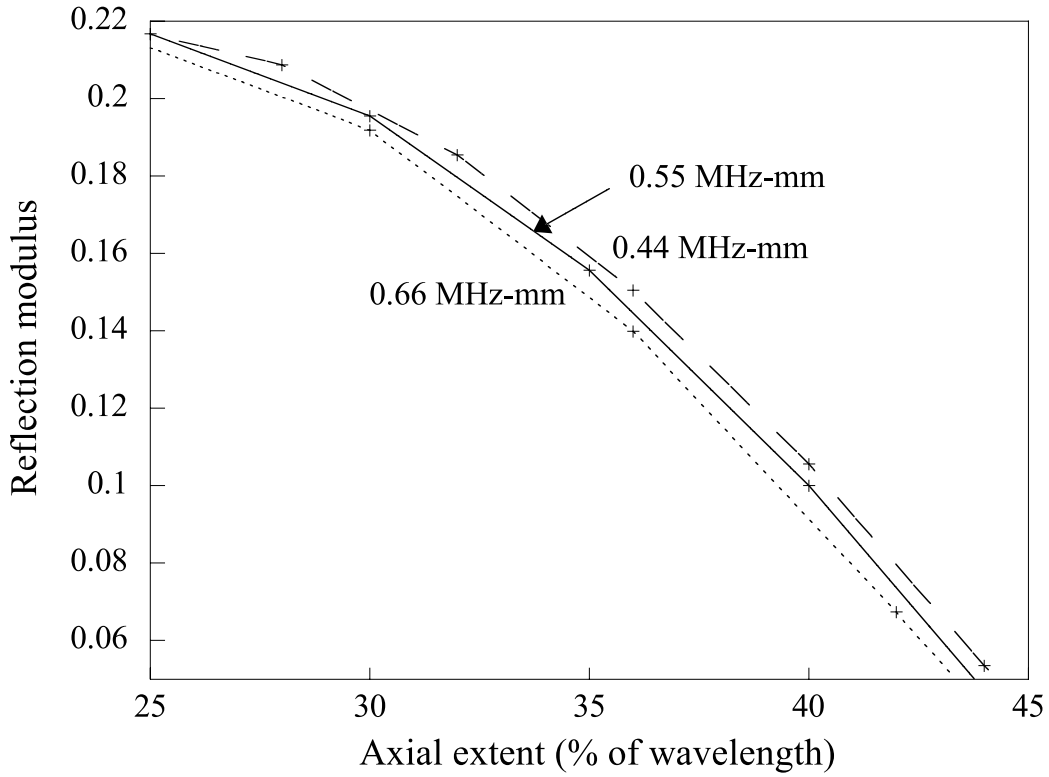

Figure 3.10: Variation of reflection ratio with axial extent of the notch. Results are for plate with SH0 incident on a notch with 50% thickness depth. The dotted, solid and dashed lines indicate the FE results obtained for a rectangular notch case at 0.66 MHz-mm, 0.55 MHz-mm and 0.44 MHz-mm respectively. The crosses indicate the values at which the reflection coefficients were computed using the FE analysis.

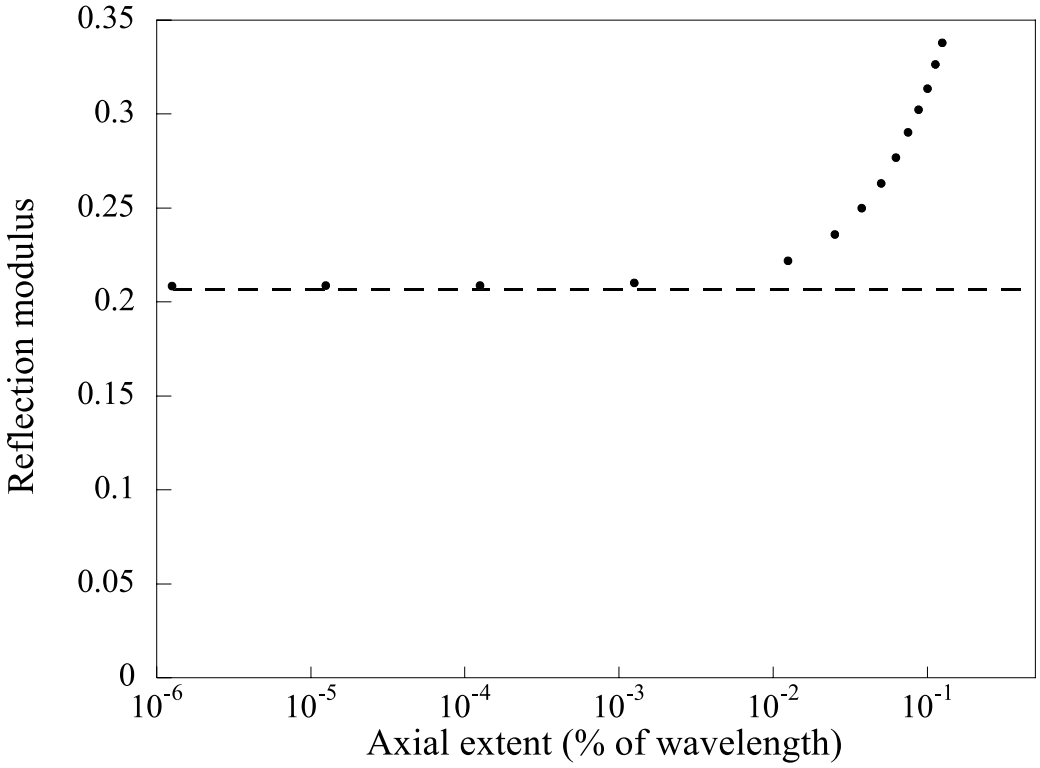

Figure 3.11: Variation of reflection ratio with axial extent L of the V-notch. Results are for a 5.5 mm plate with SH0 incident at 100 kHz on a notch with 50% thickness depth. The dashed line is the crack prediction in Figure 3.8 and the dots are the FE predictions.

Model	thickness of left region (mm)	number of elements through thickness left region	thickness of right region (mm)	number of elements through thickness right region
Step down 20%	5.5	10	4.4	8
Step up 20%	4.4	8	5.5	10
Step down 50%	5.5	10	2.75	5
Step up 50%	2.75	5	5.5	10

Table 3.1: Summary FE models for thickness step.

Chapter 4

The reflection of the torsional mode T(0,1) from defects in pipes

4.1 Historical Background

The foundation of guided wave propagation in hollow cylinders presented in Chapter 2 opened a new perspective for the ultrasonic testing of cylindrical structures. Thereafter the interaction of cylindrically guided waves with discontinuities in the geometry of the waveguide is a topic that has received a great deal of interest [86, 87, 46, 52, 53, 88, 10, 9, 67, 11]. The ability of guided waves to locate cracks and notches in pipes has been documented [86, 87, 46, 52, 53]. Furthermore the effect of defect size on the reflection and transmission characteristics has been investigated by many researchers [88, 10, 9, 67, 57, 11]. There are some exact closed-form analytical solutions to elastodynamic scattering problems in the case of bulk waves. Closed form solutions for scattering of bulk waves can be obtained at high frequencies or at low frequencies [89] but in the mid-frequency range numerical methods are necessary.

The guided wave scattering problem presents an enhanced complexity of the solution compared with bulk waves due to the presence of at least two modes at any given frequency. The large number of possible wave modes in a pipe is illustrated in the group velocity dispersion curves for a 3 inch schedule 40 steel pipe in Figure 2.8. Much of the effort in flaw detection in pipes has been concentrated on the optimization of the guided wave technique, as explained in section 2.4. By generating

a single mode it was possible to reduce the difficulty of dealing with many modes [56]. In a long range test it is also convenient to use a mode in a non-dispersive region [68], though compensation techniques for the signal spreading can be used (see Section 2.4.1).

Most of the previous investigators studied the effect of defects with small axial extent on the reflection of longitudinal waves [10, 9, 67, 90]. Quantitative studies of the reflection due to notches [9] examined the correlation between the circumferential and through-thickness extent of notches and the amplitude of the reflected mode when a longitudinal L(0,2) mode is generated in the waveguide. Mode-conversion studies [10] when the L(0,2) mode is launched in the test pipe enabled discrimination between axially-symmetric reflectors such as circumferential welds and non-axially-symmetric defects. Guided wave tuning of non-axisymmetric waves has also been used for defect detection in tubing [57]. Recently, work on crack characterization using guided circumferential waves has been published [91]. Guided circumferential waves have the limitation that they do not propagate along the length of the pipe so the range of the inspection is limited to a small percentage of the pipe.

In principle both axi-symmetric and non-axisymmetric modes can be used for long range inspection. Axisymmetric modes are in general preferable because they are easier to excite and have relatively simple acoustic fields. Initial practical testing was done using the longitudinal L(0,2) mode [10, 9, 67]. However, more recent testing has employed the torsional mode [11]. This has the advantage that, in contrast to the L(0,2) mode, the T(0,1) mode propagation characteristics are not affected by the presence of liquid in the pipe and there is no other axially-symmetric torsional mode in the frequency range, so axially symmetric torsional excitation will only excite the T(0,1) mode, whereas when the L(0,2) is used, the transducer system must be carefully designed to suppress the L(0,1) mode.

No information is currently available on the reflection and mode conversion characteristics when a torsional mode is incident at a defect. The aim of this investigation is to determine the reflection coefficients from cracks and notches of varying depth, circumferential and axial extent when the T(0,1) mode is travelling in the pipe. An experimental and modelling study on the reflection caused by a series of defect geometries in both 3 inch and 24 inch pipes is presented. A generalization of the

findings of this chapter to other pipe sizes and a comparison with the L(0,2) mode are presented in Chapter 5.

4.2 Guided mode properties

Wave propagation properties in pipes are extremely complicated. Figure 2.9 showed the group velocity dispersion curves for a 3 inch, schedule 40 steel pipe. Moreover the dispersion curves of the F(1,2) and F(2,2) modes scale approximately with the frequency-diameter product in the frequency region of interest and the T(0,1) velocity curve remains constant at all frequency values. This is shown in Figure 4.1 which plots the group velocities of these modes as a function of frequency-diameter product for 3 inch (5.5 mm wall thickness) and 24 inch (20mm wall thickness) pipes. The small difference between the curves is due to the fact that the diameter to thickness ratio is different for the two pipe sizes. This study considered an incident T(0,1) mode in all cases, but mode conversion to the non-symmetric modes could occur at non-axisymmetric features. The frequency regions under examination were 10-50 kHz and 40-100 kHz for the 24 inch and the 3 inch pipes respectively. The lowest frequencies of the range were chosen to be the frequencies usually used in practical testing (45-65 kHz for the 3 inch pipe and 10-20 kHz for the 24 inch pipe). It was also of interest to study the sensitivity of the T(0,1) mode at higher frequencies.

The mode shape of the torsional T(0,1) mode is not frequency dependent and it is completely non-dispersive at all frequencies; its group velocity is the bulk shear velocity. No other torsional mode is present in the frequency range which was used for both Finite Element models and experiments. The mode shape of the T(0,1) mode in a 3 inch pipe is shown in Figure 4.2. This shows the profile of the tangential displacement through the thickness of the pipe wall. No axial or radial displacements are present in this mode. It can be seen that the tangential displacements are approximately constant through the wall thickness, indicating that defects will be detectable anywhere in the cross section of the pipe and there may also be potential for defect sizing. Since the T(0,1) mode shape is also constant with frequency, pure mode excitation was obtained by simply imposing the mode shape at the centre frequency [45]. The torsional mode in the 24 inch pipe has a

very similar mode shape so all the comments about the T(0,1) mode in the 3 inch pipe are also valid for the 24 inch pipe.

When an axisymmetric mode is incident at an axisymmetric defect, only the axisymmetric propagating modes existing at the frequency of interest will contribute to the reflected field. Since we worked below the T(0,2) cut off frequency, there was no mode conversion at an axisymmetric defect and T(0,1) was simply reflected or transmitted past the defect. However T(0,1) can convert to the F(1,2), F(1,3) and F(2,2) modes when an asymmetric feature exists in the pipe. The conversion is dependent on the similarity in particle motion of the incident and mode converted modes. Figures 4.3a,b,c show the mode shapes of the F(1,2), F(1,3) and F(2,2) modes respectively at 45 kHz. The F(1,2) and F(2,2) modes have dominant tangential displacement so the conversion to these modes from T(0,1) is strong. Their torsional behaviour becomes even more dominant at higher frequencies as illustrated in Figures 4.4a,b which show the mode shapes at 100 kHz. Both tangential and longitudinal displacements are significant in the case of the F(1,3) mode at 45 kHz so this mode has both torsional and extensional behaviour at this frequency. The torsional behaviour becomes less significant for this mode as the frequency increases (see the mode shape for the F(1,3) mode at 100 kHz in Figure 4.4c). It is also important to understand the mode shape characteristics at low frequency; figure 4.4d shows that the F(1,2) mode shape at 25 kHz is characterized by longitudinal and tangential displacements of the same order.

4.3 Experimental setup

Laboratory experiments were performed on a set of 3 inch schedule 40 steel pipes to determine the reflection sensitivity of the torsional T(0,1) mode to a series of notches with different dimensions. The specimens used were 3.1 metre long pipes and the notches were machined at 2.3 metres from end A using a 3.2 mm diameter slot drill cutter (see Figure 4.5). The pipe was tested horizontally; it was radially clamped at end B using 8 bolts evenly distributed around the circumference and rested on a steel support positioned approximately at the mid point of the pipe. The support produced a negligible reflection of the ultrasonic signal; the reflection

from end B was not monitored so the nature of the clamping there was unimportant. The cutter was aligned along a radius of the pipe so the circumferential extent of the cut was changed by simply rotating the pipe about its axis of symmetry. Two rings of sixteen dry coupled transducers were clamped to the pipe at 0.9 metres from End A and left in place during the cutting so all of the experiments on one pipe were done without removing the transducers. The use of two rings enabled us to distinguish the direction of propagation of the reflected signal (left or right with respect to the ring position) [11]. Using piezoelectric transducers equally spaced to produce tangential displacement, only torsional modes are generated [11]. In order to generate only axially symmetric modes the number of elements in the ring has to be greater than n where F(n,1) is the highest order flexural mode whose cut-off frequency is within the bandwidth of the excitation signal [92]. A Guided Ultrasonics Ltd. Wavemaker 16 instrument was used to generate a 6 cycle Hanning-windowed toneburst at many frequency values from 40 to 70 kHz. The same instrument was also used for signal reception. In order to obtain a reference measurement, reflections from end A were recorded before any machining was done. By doing that we verified that the vibration induced from the cutting left the contact characteristics of the transducer rings on the pipe unchanged. Experiments were conducted on four separate pipes, using the following notches: (a) a through-thickness notch with axial extent equal to about 3.5 mm and varying circumferential extent; (b) a notch extending over the full circumference of the pipe with axial extent equal to about 3.5 mm and varying notch depth; (c) a notch extending over 25 % of the circumference of the pipe with axial extent equal to about 3.5 mm and varying notch depth; (d) a notch extending over the full circumference of the pipe with notch depth equal to 20 % of the thickness and varying axial extent.

4.4 Finite Element models

The Finite Element (FE) method has been extensively and successfully used to study the interaction between guided waves and defects in structures [10, 9, 67, 68, 69, 70, 71, 72, 73]. In general a three-dimensional solid model is required to perform a numerical analysis of the interaction between guided waves and discrete

defects. However 3-D models are computationally expensive so when possible we use simplified models [10]. In some cases it is possible to study a specific 3-D model by using a combination of two 2-D models. Here we considered three types of models:

1. Membrane. This is a three-dimensional analysis in which the pipe wall is represented by membrane elements. These allow defects removing a fraction of the pipe circumference to be modelled, but the defects remove the full wall thickness. The axial extent of the defect can be varied.

2. Axi-symmetric. This is a two-dimensional analysis which can deal with defects which remove part of the wall thickness, but are axially symmetric and so cover the whole pipe circumference. The axial extent of the defect can be varied.

3. Three-dimensional. Previous work [10, 9, 67] had indicated that the L(0,2) reflection coefficient from a defect was linearly proportional to its circumferential extent. The reflectivity of a defect of a given depth and circumferential extent could therefore be predicted from results of the axi-symmetric analysis by obtaining the reflection coefficient for an axi-symmetric defect having the depth of interest and scaling by the fraction of the circumference covered by the defect. The three dimensional models were used to demonstrate the validity of making predictions using combinations of results from the different types of two-dimensional model when the torsional T(0,1) mode is incident.

In each case a length of the pipe was modelled and a notch was introduced at some distance along it. The input wave signal was excited in the model by prescribing time-varying displacements at one end of the pipe. Narrow band signals were used, typically composed of 10 cycles of the desired centre frequency modulated by a Gaussian window. The tangential displacements were then monitored at a location between the excitation end and the notch, thereby detecting both the incident wave on its way to the notch and the reflected wave returning. The reflection ratio was calculated by dividing the amplitude of the reflected mode by the amplitude of the incident mode in the frequency domain.

In both axisymmetric and 3-D models the excitation was achieved by prescribing the displacements to match the exact mode shape at the end of the pipe. The displacement distribution through the thickness was derived using Disperse [35]. In the membrane model the torsional wave was excited by prescribing the displacement

all around one circumference; displacement distribution through thickness is not possible using this model. The cracks (notches with zero length) were introduced either by disconnecting adjacent elements and the notches were introduced by simply removing elements.

4.4.1 Membrane models (full depth, part circumference)

For the membrane models the geometry of the pipes was discretized using membrane Finite Elements. This type of element describes a two-dimensional rectangular region and it models the stresses which lie in the plane: the two orthogonal in-plane direct stresses and the in-plane shear stress. It assumes plane stress conditions, therefore incorporating the capacity of the plate to change thickness when the in-plane stresses are applied. Although it is a two-dimensional element by shape and (local) behaviour, it may be used in a three-dimensional model, meaning simply that it can be orientated arbitrarily in a three-dimensional space. In a three dimensional model its nodes have displacement degrees of freedom in the three coordinate directions and it has mass which participates in any coordinate direction.

The justification for using membrane elements is the nature of the mode shapes of all of the modes which were studied. As already seen in Figures 4.2 - 4.4, the pipe wall shows extensional or torsional behaviour for all of the modes (especially at high frequency). Therefore the modes of interest could be modelled reasonably well by using the membrane elements, each element lying at the center of the pipe wall. It is not possible to use membrane models in order to simulate modes in which there is local bending of the pipe wall, nor to model part-through notches.

Half of the circumferential extent of a length of pipe was modelled as in previous work with the L(0,2) mode [10, 9] but in this case we assumed one plane of anti-symmetry. A wave was excited at the end of the pipe, a defect was simulated and the signals were monitored on a line between the excitation and the defect. A mesh of identically-sized linear (four noded) quadrilateral membrane elements was used. The models of the 24 inch pipe represented a 3.6 m length, using 900 elements along the length and 40 elements around the circumference. As a result each element was about 4 mm long and 24 mm along the circumference. The models of the 3 inch pipe also represented a 3.6 m length, using 900 elements along the length and 40

elements around the circumference. Hence each element was about 4 mm long and 3 mm in the circumferential direction. Convergence studies indicated that the meshes gave reliable results. The zero-length notches were modelled by disconnecting adjacent elements; thus although the elements on each side of the notch had nodes at coincident locations, they were not connected. The notches with non-zero lengths were modelled by removing elements from the model and were therefore rectangular in shape. The notches were introduced adjoining one of the planes of antisymmetry so that the geometric model described half of the pipe and half of the notch, and the centre of the notch was therefore at the plane of antisymmetry.

The excitation of the axially symmetric modes (circumferential order 0 modes) was achieved by prescribing identical tangential displacement histories at all of the nodes at the end of the pipe. On reception of the multi-mode reflected signal, the order 0 modes were extracted simply by adding the tangential displacements at all of the monitoring nodes around the circumference of the pipe. For the order 1 modes, a phase delay of $\frac{\theta}{2 \cdot \pi}$ was added to each signal before summing them [10, 9], where θ is the angular distance from the centre of the notch. Thus a separate processing calculation was performed in order to extract the amplitude of each type of mode. In principle three order 0 modes (L(0,1), L(0,2), T(0,1)) and three order 1 modes (F(1,1), F(1,2), F(1,3)) can exist in the high frequency range. However L(0,1) and L(0,2) are both longitudinal and are not excited, and F(1,1) does not propagate in the membrane model because it is characterized by through-wall bending behaviour. In most cases the processing already described was therefore sufficient to identify separately the remaining T(0,1), F(1,2) and F(1,3) modes. At some frequencies the F(1,2) and F(1,3) modes have very similar group velocity so it was not possible to separate them in the time domain. Since the signals were rather narrow-band, the processing could reasonably have been performed directly on the raw time records. However, for better accuracy, the calculations were performed in the frequency domain.

Typical time records from the simulations are shown in Figures 4.6a,b. Both of these records are for the 24 inch pipe with a notch which extends around 25 % of the circumference, and for the T(0,1) mode incident at 50 kHz; the difference between them is in the processing. Figure 4.6a shows the signal with processing for order 0.

This shows clearly the incident signal on its way towards the notch and then the reflected T(0,1) mode. Figure 4.6b shows the signal when the same raw results are processed to extract the order 1 modes. This now shows the reflection of the F(1,2) mode. Also, the incident mode has vanished in this plot because it is order 0 and is therefore not detected by the order 1 processing.

4.4.2 Axisymmetric models (full circumference, part depth)

The axi-symmetric elements describe a two-dimensional region representing a radial-axial section through an axially symmetric structure. Thus in application to the pipe models they represent a section through the pipe wall on a plane which contains the axis of the pipe. They model the three in-plane stresses (the radial and axial direct stresses and the radial-axial shear stress) and also the circumferential stress. Thus radial displacements of the elements are correctly coupled to circumferential stresses. It follows that any geometric shape which is modelled must be axially symmetric. Therefore, although it is possible to model notches which extend part-way through the pipe wall (unlike the membrane models which only represent through-wall notches), any notch is assumed to extend around the full circumference. Since the geometry is axially symmetric, there is no mode conversion between modes of different circumferential orders, so only modes of the same order as the excitation signal can propagate. In our models only the T(0,1) torsional mode can be reflected from the axisymmetric notch because this is the only torsional mode existing in the working frequency range.

The excitation, monitoring and notch locations were arranged along the pipe similarly to the membrane models discussed earlier. Identically-sized linear (four noded) quadrilateral axi-symmetric elements were used. The wall thickness of the 24 inch and 3 inch pipes were taken to be 20 mm and 5.5 mm respectively. The models of the 24 inch pipe represented a 2.4 m length, using 1000 elements along the length and 10 elements through the thickness. Therefore each element was 2.4 mm long and 2 mm in the thickness direction. The models of the 3 inch pipe with the T(0,1) mode represented a 2.4 m length, using 2000 elements along the length and 10 elements through the thickness. Therefore each element was 1.2 mm long and 0.55 mm in the thickness direction. Again convergence studies showed that this

discretization was satisfactory. Two other FE models of the 3 inch pipe with an 80% defect depth were run at 150 kHz and 240 kHz center frequency in order to obtain the reflection coefficient at high frequencies. A finer mesh was needed in the 240 kHz case according to the practical rule of having at least 8 elements per wavelength of the smallest wavelength of the excitation signal. The ratio between the frequency spectrum of the reflected signal and the spectrum of the input was then derived for each FE run. Using four FE models with different center frequencies (40 kHz, 100 kHz, 150 kHz and 240 kHz) we covered the frequency bandwidth from 15 kHz to 270 kHz. Higher frequencies were not considered because of the presence of the second torsional mode T(0,2) (the cut off frequency for the T(0,2) torsional mode is 300 kHz in a 3 inch pipe).

The effect of the axial extent of the notch on the reflection coefficient of an axisymmetric notch was also studied. Several FE models with 20% defect depth and different axial extent have been studied. The notches were created in the FE simulations by simply removing elements in the mesh. When the axial extent was long enough, the reflection of the start of the notch was separated from the reflection from the end of the notch.

4.4.3 3D-models (part circumference, part depth)

The three dimensional modelling used 8-node "brick" elements to discretize a length of pipe fully in three dimensions. The brick elements are cuboid in shape and are used to represent, piecewise, the whole volume of the structure. Potentially this offers the advantage of being able to model notches which have limited extent both in the circumferential and the through-wall directions. However, there is a heavy computational penalty because of the large numbers of elements which are necessary for three dimensional models. We here modelled a pipe with a part-circumference and part-thickness notch. The purpose was to compare the reflection coefficient obtained with the one derived by combining the results of membrane and axisymmetric models in order to confirm the assumption which has been made that the reflectivity from such notches can be inferred from the combined results of the membrane and axi-symmetric models.

Half of the circumferential extent of a 2.4 m length of the 3 inch pipe was mod-

elled, assuming one plane of antisymmetry. The excitation, notch and monitoring locations were arranged similarly to the membrane models. The pipe was modelled with 600 elements along the length, 40 elements around the circumference and 3 elements through the 5.5 mm wall thickness. The T(0,1) mode at 100 kHz was excited and monitored. The excitation was achieved by prescribing the displacements to match the exact mode shape at the end of the pipe. The T(0,1) mode was monitored by adding the circumferential displacements at all of the nodes around one circumference at the monitoring location.

Before tackling the problem of the notch with limited extent in both circumferential and depth directions, some analyses of an axially symmetric part-depth notch and a through-wall part-circumference notch were studied using the 3-D model and compared with the related 2-D models. The results from the 3D mesh compared well with those obtained from the 2D models, so validating the discretization.

A 3D model of a part-depth (33%), part-circumference (25%) notch was analyzed using 100 kHz T(0,1) excitation. A notch axial length of 180 % of the wavelength ($\lambda = 32.6$ mm) was chosen, so the defect was a square patch (60 mm x 60 mm) 1.8 mm deep.

4.5 Study of parameters affecting reflection and mode conversion

The numerical results are presented below. We study separately the influence of parameters such as pipe dimension, frequency of the excitation, circumferential extent of the defect, depth of the defect and axial extent of the notch. The section is divided into three subsections in which we describe the results for the three different FE models.

4.5.1 Through thickness defects with zero axial extent (membrane model)

Using the results of the membrane models we studied the effect of the circumferential extent of a defect on the backscattering of the torsional wave at different frequencies.

We first present the results of the simulation for the 3 inch pipe case and later offer a comparison with the 24 inch case.

Practical testing of 3 inch pipes using torsional excitation is usually performed at relatively low frequency (45-65 kHz)[11]. We start by presenting the results at higher frequency (100 kHz) because of the simplicity of this case and we will focus later on the frequencies used in practical testing. The reflection coefficient on the 3 inch pipe with T(0,1) input at 100 kHz is shown in Figure 4.7, the computed points being joined by straight lines.

The T(0,1) reflection coefficient is approximately linear with circumferential extent, the F(1,2) reflection coefficient has a maximum at 50% of the circumferential extent and the F(2,2) has a maximum at 25 % of the circumferential extent and a minimum corresponding to 50% of the circumferential extent. The results obtained in this case are very similar to the results obtained in previous work on the L(0,2) reflection coefficient in a 3 inch pipe at 70 kHz [10]. No significant presence of the F(1,3) mode is noticeable at this frequency.

The variation of the T(0,1) reflection coefficient with circumferential extent at 100 kHz shown in Figure 4.7 indicates some divergence from the overall linear trend; this is probably due to numerical problems. In principle a finer mesh could be used to investigate this but the model which was used here is close to the limits of the available resources so this has not been pursued. In any case the extent of the scatter is small in absolute terms, and is not important from the point of view of practical application.

The interpretation of the 3 inch FE simulation at lower frequencies is more complicated than at high frequency because of changes in the mode shapes of the relevant modes. In the intermediate frequency range (from 30 to 70 kHz) F(1,3) is seen in the reflected signals along with the other modes. This is because there is significant circumferential motion in its mode shape over this frequency range as shown in Figure 4.3b, whereas this displacement component is small at higher frequency (see Figure 4.4c). Figure 4.8 shows the results at a frequency of 45 kHz. At all circumferential extents the amplitude of the F(1,3) reflection is about 20% of that of the F(1,2) mode. Figure 4.9 shows the T(0,1), F(1,2) and F(1,3) reflection coefficients at frequencies from 25 kHz to 100 kHz for the 25% circumferential extent case. As

expected from the mode shapes, the ratio between the F(1,3) and F(1,2) reflection coefficients becomes smaller at higher frequencies. At low frequency (25kHz) the T(0,1) reflection coefficient is small. Figure 4.9 also shows that the F(1,2) mode reflection coefficient at low frequency is very small compared with the other results at higher frequencies. This is due again to the F(1,2) mode shape at low frequency. From Figure 4.4d it can be seen that at 25 kHz the F(1,2) mode has a longitudinal displacement bigger than the tangential displacement so this mode does not have predominantly torsional behaviour at low frequency.

In the case of a 24 inch pipe the general behaviour of the reflection coefficient seen in the 3 inch pipe at 100 kHz case is confirmed (see Figure 4.10). No presence of the F(1,3) mode was observable in the 24 inch FE simulations that were run.

4.5.2 Part thickness axisymmetric defects (axisymmetric model)

The results of the axi-symmetric FE modelling are plotted in Figures 4.11 - 4.13. Since the defect is axi-symmetric, there is no mode conversion between the axi-symmetric (T) modes and the flexural (F) modes. Figure 4.11 shows the trend of the T(0,1) reflection coefficient for both 3 inch and 24 inch pipes as a function of defect depth at different excitation frequencies. If we consider one pipe dimension at one frequency value we observe that the reflection coefficient increases with defect depth in a non-linear manner. The shape of the curves is similar to that predicted for a 3 inch pipe at 70 kHz using the L(0,2) mode in earlier published work [9]. If we now consider one pipe dimension at different frequencies of excitation, we can see that as the frequency decreases, the curves become increasingly 'concave', the reflectivity at low defect depths decreasing markedly. It therefore becomes more difficult to detect shallower defects as the test frequency is decreased. It is also of interest to observe that when the frequency-thickness product is similar, the reflection is similar. Specifically, the reflection coefficients for a 3 inch pipe with 5.5 mm wall thickness at 40 kHz (frequency-thickness product 220 kHz-mm) are similar to the reflection coefficients for a 24 inch pipe with 20 mm wall thickness at 10 kHz (frequency-thickness product 200 kHz-mm). The same observation is valid at high frequency-thickness values; the 3 inch pipe at 160 kHz (880 kHz-mm) has a reflection coefficient similar to that of the 24 inch pipe at 50 kHz (1000 kHz-mm).

Figure 4.12 shows the reflection coefficient in the frequency domain when a 3 inch pipe with various depth notches is excited with the torsional T(0,1) mode. The reflection coefficient increases with frequency at all depth values. In the 80% depth case the rate of change decreases as the frequency increases.

The effect of the axial extent of the defect on the reflectivity of the T(0,1) mode in a 3 inch pipe is plotted in Figure 4.13. The reflection coefficient has a maximum at an axial extent of about a quarter wavelength and a minimum at about half-wavelength. Similar behaviour has been reported for the s_0 mode in a plate [73].

4.5.3 3D models

The results of the 3-D analysis are given in Table 4.1. The results demonstrate excellent agreement between the predictions of the 2D axisymmetric analysis with those of the 3D analysis; for the case of an axisymmetric, 33% depth defect, the predicted reflection coefficients are 23.5% and 23.7% with the 2D axisymmetric and 3D models respectively. Similarly good agreement is shown between the membrane and 3D models for the case of a through wall defect with 25% circumferential extent, the predicted reflection being 21.1% with both models.

Finally, Table 4.1 shows the results for the 3D analysis of a notch with 25% circumferential extent, 33% depth and axial extent of 180% of the wavelength. The 3D analysis predicts a reflection ratio of 5.0% for this case. This is closely matched by the multiplication of the axisymmetric and membrane results which give 5.2%. This confirms the validity of combining the axisymmetric and membrane results to predict the 3D case.

4.6 Experimental validation of numerical modelling

A series of experiments was carried out in order to validate the results obtained from the FE modelling. From previous modelling it was clear that the axial extent can be an important parameter affecting the reflection coefficient from notches, so when simulating the laboratory test cases using FE models it was necessary to introduce a notch with the precise axial extent used in the experiments. Part-thickness, part-circumference defects were modelled using a combination of 2D axisymmetric and

2D membrane models.

Figure 4.14 shows the measured and predicted reflection coefficients at 55 kHz for a series of axisymmetric notches with 3.5 mm axial extent in which the notch depth was varied, together with the prediction for a crack (zero axial extent). The experimental measurements and Finite Element predictions can be seen to agree well. The reflection coefficients for the notch case are higher than those for the crack case. Moreover the concavity of the curve is reduced with respect to the crack case.

Figure 4.15 shows a comparison between experimental and FE results in the case of through-thickness notches with 3.5 mm axial extent and varying circumferential extent when the T(0,1) mode is excited at 55 kHz. Again there is good agreement between the experimental and modelling results.

Figure 4.16 shows the dependence of the reflection coefficient on the frequency in the case of a through-thickness defect with 25% circumferential extent and axial extent equal to 3.5 mm. The reflection coefficient for T(0,1) decreases when the frequency is increased from 50 kHz to 70 kHz in both experiments and predictions. Good agreement between experiments and Finite Elements is also found in this case.

Figure 4.17 shows the behaviour of the reflection coefficient when the axial extent is changed. The results are derived for a 20 % depth defect extending over 25% of the circumference at 55 kHz center frequency excitation. The form of the experimental results agrees with the predictions, the peak of the reflection coefficient occurring when the axial extent is about a quarter wavelength and the minimum at about half wavelength.

4.7 Discussion

A defect in a solid body represents a scatterer for elastic waves and so in principle it can be detected and characterized by its effect on an incident pulse of ultrasonic wave motion. Elastodynamic scattering problems can be solved in closed form in the high frequency regime using either the Kirchoff approximation or the geometrical diffraction theory and at low frequency applying the Rayleigh approximation [89]. In the mid-frequency range these methods are not valid because the wavelength

of the incident pulse is of the same order as the characteristic dimension of the defect and preferable alternatives are numerical methods such as Finite Element, Boundary Element or Finite Difference. Scattering of bulk waves from a crack in an infinite medium has been studied by many investigators and much of this work has been reviewed by Kraut [93] and Datta [94]. Elastodynamic ray theory has been thoroughly studied by Achenbach et al. [95] in order to construct scattering fields generated by cracks.

The interaction of Lamb waves with cracks and notches in plate structures is a topic that has received a great deal of interest in recent years [75, 96, 97, 67, 72, 73]. Wave scattering of guided elastic waves from cracks and notches in isotropic hollow cylinders has also been investigated [88, 90, 67, 10, 9, 57, 98, 91]. The scattering of guided waves is more difficult than the bulk wave case as a consequence of the higher number of modes to be considered and the complexity of the mode shapes. When a single mode in a waveguide encounters the defect there is coupling between the incident mode and all of the propagating and non-propagating modes of the waveguide [15]. If the location of the detector of the wave is placed far enough from the defect, only the propagating modes will have significant amplitude. In fact only a few of the propagating modes contain a significant amount of scattered energy so the problem can be further simplified by only considering these modes [10].

4.7.1 Analysis of the sensitivity of torsional mode to cracks (zero axial extent)

It is well known that three scattering regimes can exist depending on the dimension of the scatterer in relation to the wavelength of the ultrasonic wave [89]. A parameter frequently used to define and distinguish the scattering regimes is ka where a is the characteristic dimension of the defect and k is the wavenumber defined by

$$k = \frac{2\pi f}{V} \tag{4.1}$$

where f is the frequency and V is the phase velocity. This approach, frequently used in the case of bulk waves, has also been used for scattering of Lamb waves [99, 100]. In this investigation the concept of low and high frequency scattering regimes is used to explain the general trends of the results obtained. In the specific

case of the torsional T(0,1) mode propagating in a cylindrical structure, the velocity is constant with frequency so the wavenumber simply increases linearly with frequency. When $ka < 0.1$ the problem is usually approximated using a low-frequency or quasistatic approach. At values for which $ka > 1$ it is possible to use a high frequency approximation (however $ka = 1$ cannot be considered as a strict boundary between the different regimes). For part-thickness, axisymmetric defects the characteristic length is the defect depth, while for through-thickness, part-circumference defects the characteristic length is the circumferential extent. Figures 4.18a,b show the scattering regimes for axisymmetric and through thickness cracks in the case of a 3 inch pipe with 5.5 mm wall thickness. In both figures a rectangular region which is important from the point of view of practical testing is also highlighted. It is evident that in the case of axisymmetric cracks we are in the low-intermediate frequency regime, whereas in the case of through thickness defects we are in the intermediate-high frequency regime.

Discussion on through thickness cracks

The motivation of separately studying the reflection characteristics of the through-thickness, part-circumference and the part-depth axisymmetric defects is the difference in geometry and scattering regime of the two classes of crack. The reflection coefficients of the 24 inch pipe with T(0,1) input at 10 kHz and 50kHz as a function of circumferential extent are shown in Figure 4.19. The circumferential extent is expressed as a percentage of the pipe circumference (1980 mm). The T(0,1) reflection coefficients are very similar at the two frequencies and they increase roughly linearly with circumferential extent, especially at the higher circumferential extents (corresponding to higher ka). A somewhat smaller reflection is obtained for a small defect (5% of circumference) at low frequency (10 kHz). The same behaviour is noticeable in the 3 inch case.

Let us first give an explanation of how the frequency of the test influences the reflection coefficient from through thickness cracks and we will then explain why the dimension of the defect is an important parameter. Lowe et al. [10, 9] showed that the L(0,2) reflection coefficient varies roughly linearly with respect to the circumferential extent of the defect. They presented a calculation in order to discover

whether the reflection coefficients could be estimated from a simple assumption of the opening profile of the crack. The profile of the opening displacement of the FE nodes along the crack face was almost constant in the case of the L(0,2) mode at 70 kHz incident on a crack. Clearly when the Crack Opening Displacement (COD) is constant along the defect, the reflection coefficient of the axisymmetric mode is equal to the extent of the crack as a fraction of the circumference, leading to a linear behaviour of the reflection coefficient as a function of circumferential extent. As they explained, the COD is approximately constant over the crack face when the wavelength of the incoming wave is sensibly smaller than the circumferential extent of the crack (i.e. $ka > 1$). Under such conditions the crack face simply behaves as a free surface which reflects the incoming wave. When ka diminishes, the crack opening displacement (COD) can no longer be considered as constant. The variation of the COD with frequency was observed by Lowe in the case of a s_0 wave incident on a crack in a plate [67]. He showed that the COD changes with frequency and there is a transition between the high frequency COD and the quasistatic COD. From that analysis it is clear that only at relatively high frequency ($ka > 1$) can the COD reasonably be approximated by a constant displacement along the face of the crack.

It is possible to interpret the results at 5% of the circumferential extent for both the 3 inch pipe at 45 kHz and the 24 inch pipe at 10 kHz (see Figure 4.19) by saying that the ka value in these cases is smaller than 1, therefore the reflection coefficient is smaller than its linear approximation. Another explanation of the results at low frequency and small circumferential extent can be proposed. The COD is zero at the boundary points where the crack starts and ends; consequently in the regions of the crack near these boundary points the COD goes from zero to a finite value. When the defect is big enough in terms of circumferential extent, the COD might be considered to be constant and the linear approximation for the reflection coefficient would be valid. However, when the defect is relatively small, the boundary effects described would dominate the COD. In this case the COD cannot be considered as constant over the length of the crack and the reflection coefficient will not be satisfactorily approximated by a linear fit.

Another issue to be tackled is the understanding of mode conversion. Following the analysis of Ditri [88] and Lowe et al. [10], the strength of conversion to each

mode by a circumferential crack may be estimated from the degree to which the crack opening profile matches the stresses in the mode. Let us first consider the simple case in which only one of the modes of a given circumferential order existing at the frequency of interest has a stress profile similar to the incident mode. In this case it is possible to evaluate the reflection coefficient of this mode converted mode by using a spatial Fourier decomposition of the displacement around the circumference at the location of the crack. As shown by Lowe et al. [10] this spatial Fourier transform gives the excitation strengths of the mode converted waves. This is applicable for example to the F(1,2) mode in a 3 inch pipe when the T(0,1) mode is incident at 100 kHz. When more than one mode (or none of the modes) with a given circumferential order has a mode shape similar to the stress profile of the incident mode, the simple spatial Fourier decomposition is no longer valid. Using the spatial Fourier decomposition and supposing that only one of the possible order two modes is involved in the mode conversion, the value of reflection coefficient at a circumferential extent of 50% would be zero, as explained by Lowe et al. [10]. In fact in all of the modelled cases in this Chapter this value is not zero (see F(2,2) at 50% circumferential extent in Figures 4.7, 4.8 and 4.10). This is due to the fact that more than one order two mode is involved in the mode conversion phenomenon.

Discussion on axisymmetric cracks

In the case of axisymmetric cracks the scattering regime in which we are interested is the low-intermediate frequency shown in Figure 4.18b. In Figure 4.12 the amplitude reflection coefficient for a series of crack depths is plotted as a function of frequency, the ka=1 points being indicated with empty circles. We can notice that the curve of reflection coefficient versus frequency is roughly linear until it approaches the value ka =1. It is also interesting to notice that at ka=1 the reflection coefficient is approximately equal to the percentage depth of the defect. We then see a small change in behaviour going from the intermediate to the high frequency scattering regime. The reflection coefficient curve is less steep at high frequency which can be explained by saying that the reflection coefficient tends to a value which is the asymptotic value at high frequency. This behaviour has been encountered in previous work on scattering from cracks in plates [67, 73]. Unfortunately in our case it was not

possible to increase the test frequency in order to derive the value of the reflection coefficient at very high frequency because another torsional mode appears at 300 kHz (T(0,2)).

In Figure 4.11 we showed the amplitude reflection coefficient of the T(0,1) mode for axisymmetric cracks as a function of defect depth at different frequency values. The value at which the high frequency scattering regime is reached is indicated in the figure by an empty circle. Around ka =1 the curve changes its shape from convex to concave. This behaviour can again be attributed to a change in scattering regime.

However, the reflection coefficient is not only ka dependent. Figure 4.11 shows that if we consider one pipe size with two defect depths and the same ka value, a deep defect at low frequency produces larger reflection coefficient than a shallow defect at high frequency. For example, the reflection coefficient for an 80% depth defect at 40 kHz is 31% whereas that from a 20% defect depth at 160 kHz is 5.3%. This is probably because the geometry of the system, and then the stress distribution, is very different for shallow and deep defects; the reflection coefficient would be dependent on ka only at small defect depths (eg below 10%). However, it has not been possible to check this because of limitations on the finite element mesh.

4.7.2 Effect of axial extent

Figure 4.13 shows the amplitude reflection coefficient for a series of axisymmetric notches with 20% defect depth and different axial extent at 100 kHz. The notch case is shown schematically in Figure 4.20. The simplest case to be considered is that in which the notch has an axial extent which is long enough to separate in time the first reflection coming from the start of the notch and the second reflection coming from the end of the notch. The reflection coefficient from a step down in a pipe in which 20% of the thickness was removed is plotted in Figure 4.21 as a function of frequency. It was simply obtained by dividing the FFT of the reflected signal by the FFT of the input signal. It is clear that this reflection is almost independent of frequency. No mode conversion is present in this case since the defect is axisymmetric. Furthermore the T(0,1) mode is not dispersive so there is no change in velocity due to the change in the thickness of the pipe wall. If we consider that the tangential displacement is almost constant through the thickness and that the radius of the pipe is very much

bigger than the thickness, we can approximate the value of reflection coefficient obtained at a step in a pipe by using Equation 3.2, written for the reflection from a thickness step in a plate.

As already seen for the plate case with SH0 excitation, the total reflection coefficient is given by:

$$R_{TOT} = R_{A1} + R_{A2} + .. + R_{Aj}. \tag{4.2}$$

The total reflection coefficient has a maximum when L is equal to a quarter wavelength ($\lambda/4$) and a minimum when L is equal to $\lambda/2$. The maximum is about twice the value of the reflection from a step down of the same depth of the notch. The FE predictions of Figure 4.13 and the experiments of Figure 4.17 confirm that the maximum is obtained at about $\lambda/4$ and the minimum at about $\lambda/2$. In practice, the reflection maxima and minima are not at axial extents of exactly 25% and 50% of the wavelength. This is because the phase delay at a transition between two different thicknesses is not zero or π, as explained in Section 3.3 for the plate case. It should be stressed here that such a large increase in reflectivity when the defect length is a quarter wavelength long is unlikely in practice since real defects would not have a sharp, rectangular profile. Nevertheless, maxima and minima can occur in practical inspection and it is wise to test at more than one frequency.

4.8 Conclusions

A quantitative study of the reflection of the T(0,1) mode from defects in pipes in the frequency range 10-300 kHz has been carried out, finite element predictions being validated by experiments on selected cases. Both crack-like defects with zero axial extent and notches with varying axial extents have been considered. The predictions have largely been done on part-thickness, axisymmetric defects and on full-wall-thickness, part-circumference-defects, both of which can be modelled with two dimensional analyses. However, it has also been shown that it is reasonable to use a combination of these two approaches to predict the reflection from part-thickness, part-circumference-defects.

It has been shown that the reflection coefficient from axisymmetric cracks increases monotonically with depth at all frequencies and increases with frequency at

a given depth. In the frequency range of interest, T(0,1) is the only propagating axisymmetric mode so there is no mode conversion at axisymmetric defects. With non-axisymmetric cracks, the reflection coefficient is a roughly linear function of the circumferential extent of the defect at relatively high frequencies, the reflection coefficient at low circumferential extents falling below the linear prediction at lower frequencies. With non-axisymmetric defects, mode conversion to the F(1,2) mode occurs at all but the lowest frequencies, the amplitude of the mode converted signal being a maximum when the circumferential extent is 50%; at low circumferential extents, the amplitudes of the mode converted and direct reflections are similar. Some mode conversion to F(1,3) as well as F(1,2) is seen at lower frequencies.

The depth and circumferential extent of the defect are the parameters controlling the reflection from cracks; when notches having finite axial extent, rather than cracks, are considered, interference between the reflections from the start and the end of the notch causes a periodic variation of the reflection coefficient as a function of the axial extent of the notch, maxima occurring when the notch width is 25% and 75% of the wavelength, and minima appearing when the width is zero (the crack case), 50% or 100% of the wavelength. This paper has only considered square sided defects; real defects will not have such regular shapes so the interference effects will be less severe. However, some frequency dependence is likely to be seen.

The results have been explained in terms of the wavenumber-defect size product, ka. Low frequency scattering behaviour is seen when $ka < 0.1$, high frequency scattering characteristics being seen when $ka > 1$.

The results demonstrate that the torsional wave is attractive for the practical testing of pipes. The sensitivity to cracks is improved at higher frequencies, but this is not the case for large corrosion patches. Moreover, the use of high frequency conflicts with the desire to use lower frequencies to increase the propagation range, and hence the length of pipe that can be inspected in a single test. When testing for defects that may have significant axial extent, it is wise to test at more than one frequency in order to avoid missing defects due to destructive interference of the reflections from the two ends of the defect.

3 inch and 24 inch pipes have been considered in this Chapter. A generalization of the results here presented to other pipe and defect sizes is presented in the following

Chapter.

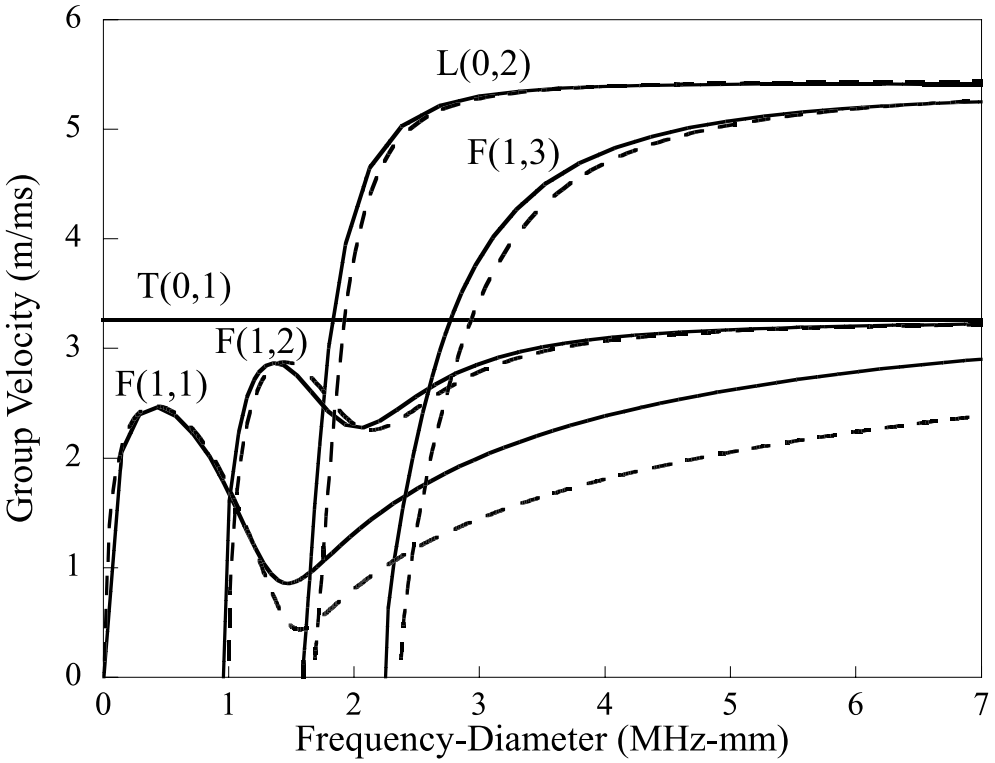

Figure 4.1: Group velocity dispersion curves for L(0,2), T(0,1), F(1,1), F(1,2) and F(1,3) modes in 3 inch (solid lines) and 24 inch pipes (dashed lines) as a function of frequency-diameter product.

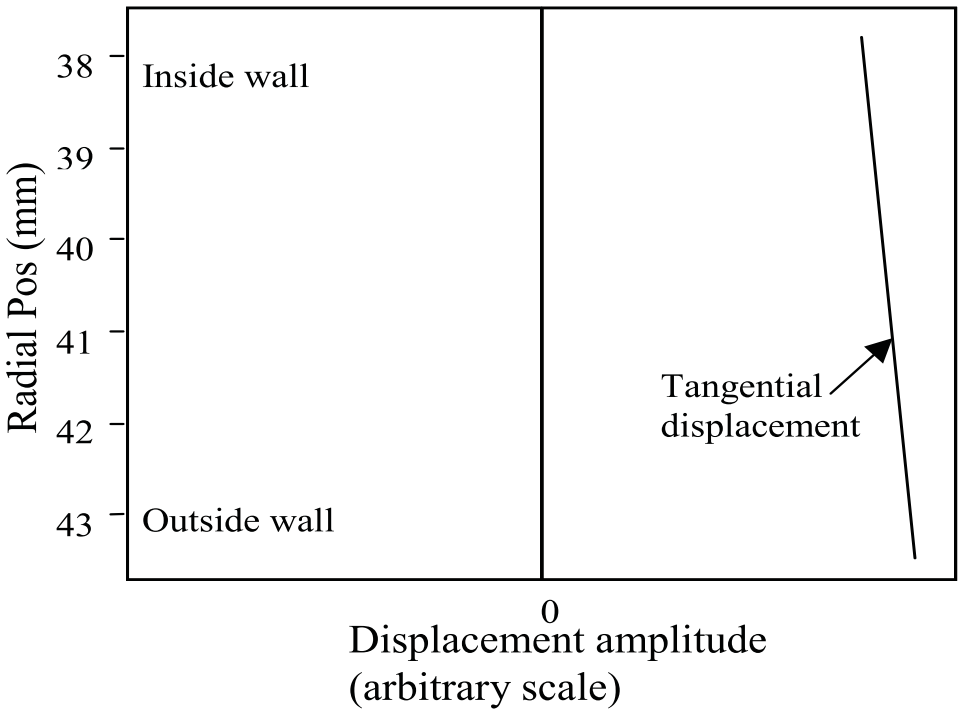

Figure 4.2: T(0,1) mode shape in a 3 inch pipe at 45 kHz. Radial and axial displacements are zero.

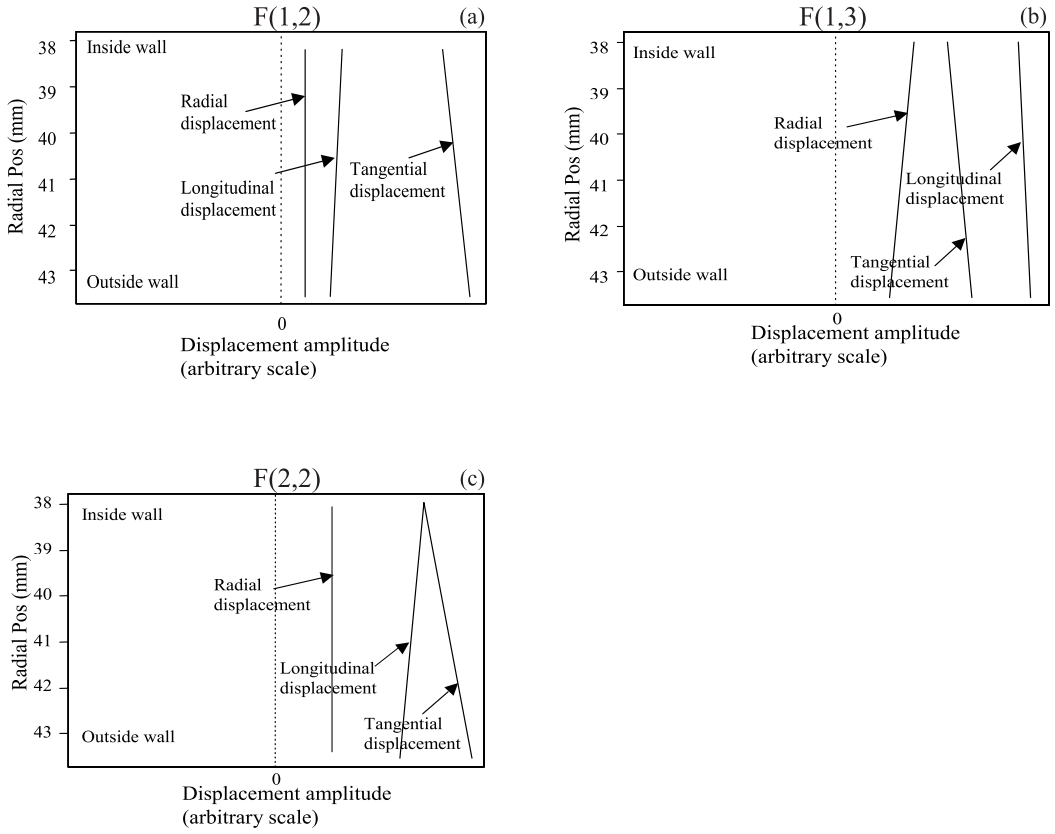

Figure 4.3: Displacement mode shapes in a 3 inch pipe at 45 kHz for F(1,2) (a), F(1,3) (b) and F(2,2) mode (c).

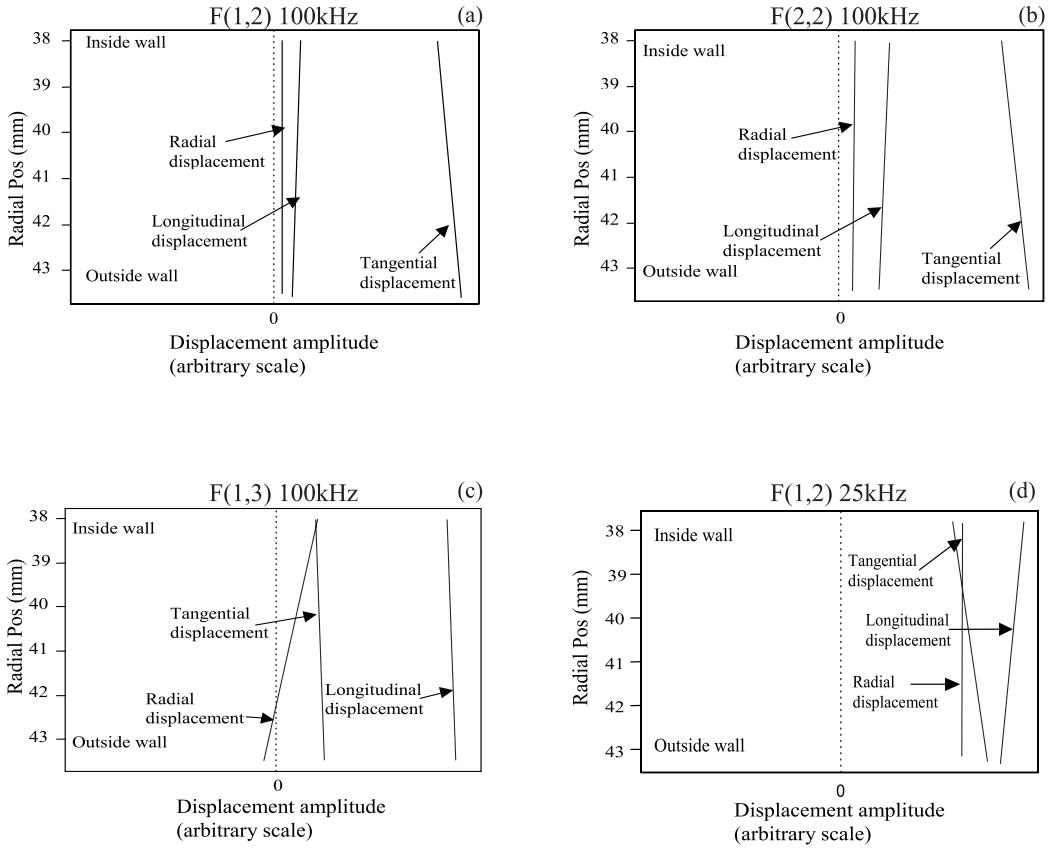

Figure 4.4: Displacement mode shapes in a 3 inch pipe at 100 kHz for F(1,2) (a), F(2,2) (b) and F(1,3) mode (c)and at 25 kHz for F(1,2) mode (d).

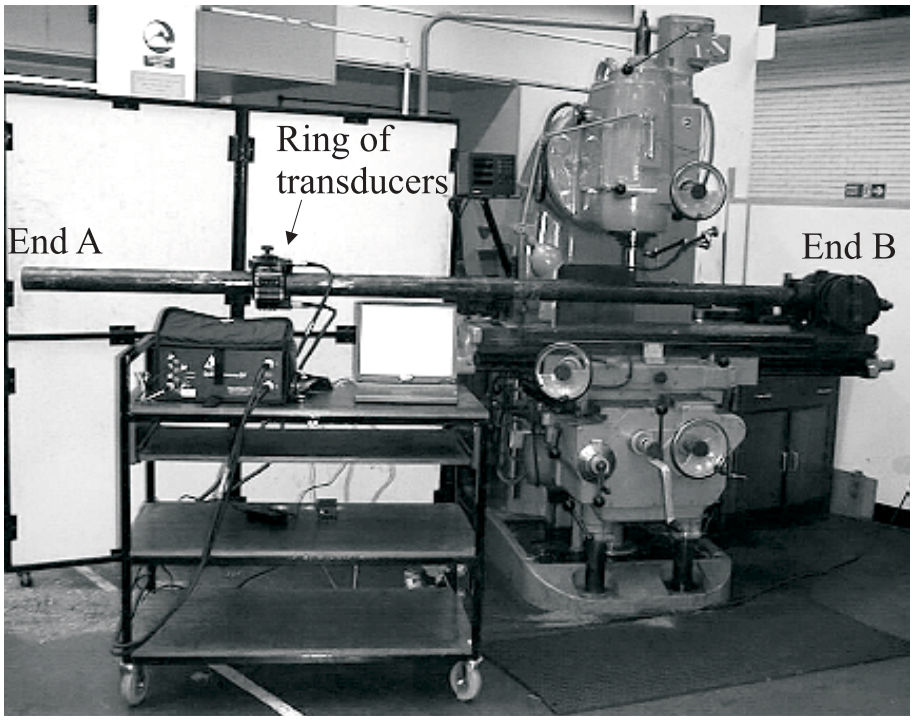

Figure 4.5: Experimental setup.

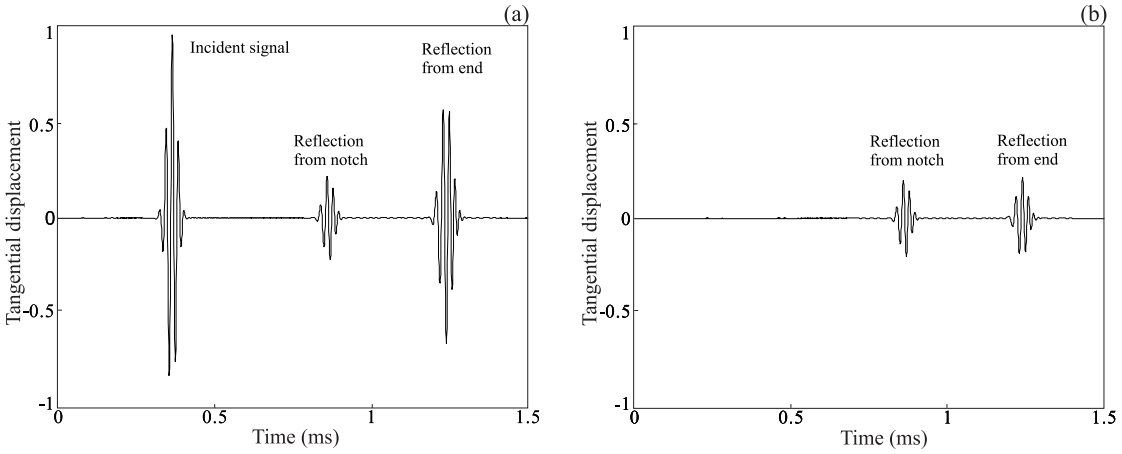

Figure 4.6: Predicted time record for membrane model of 24 inch pipe with notch extending around 25 % of circumference and T(0,1) mode incident. Results processed to show order 0 modes (a) and order 1 modes (b)

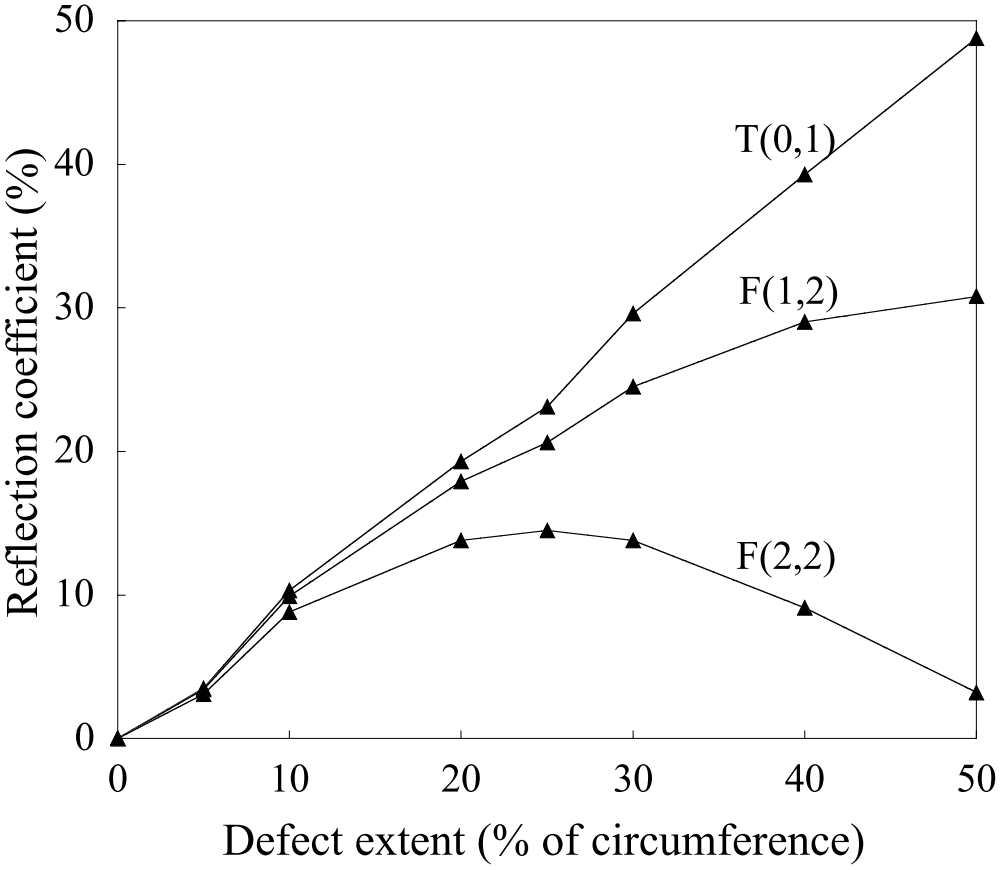

Figure 4.7: Variation of reflection ratio with defect circumferential extent for zero axial length, full wall thickness defect. Results are from membrane model with T(0,1) incident in 3 inch pipe at 100 kHz.

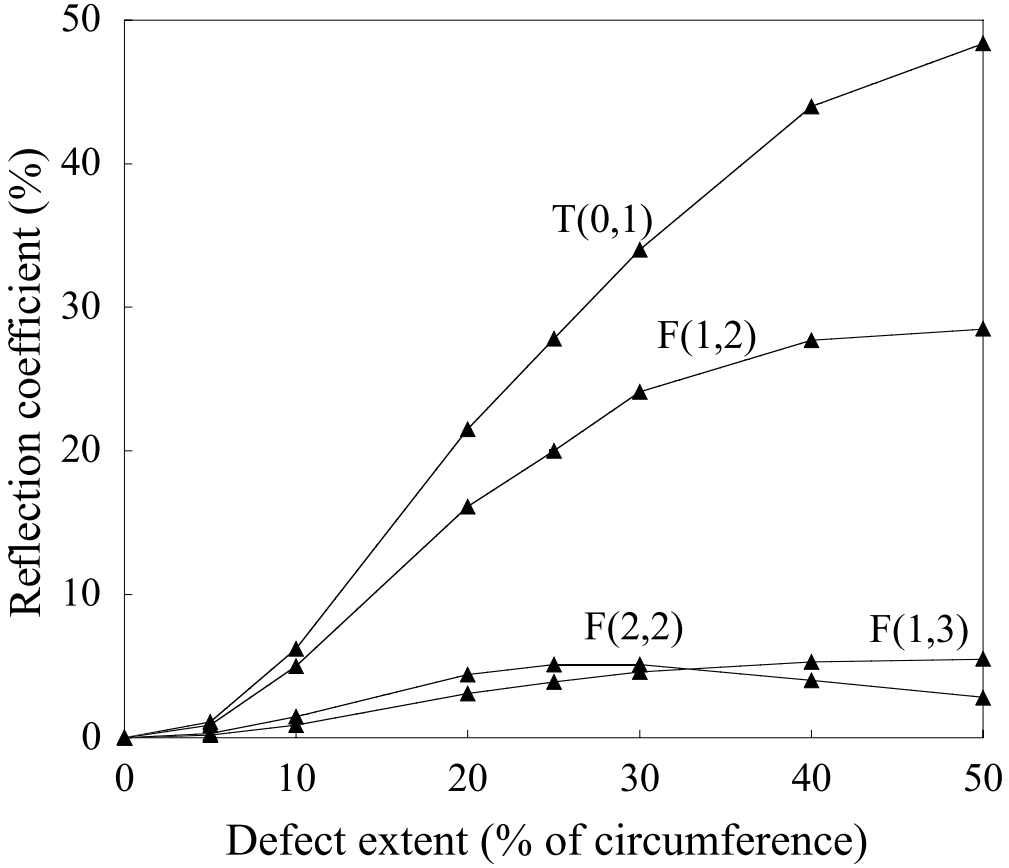

Figure 4.8: Variation of reflection ratio with defect circumferential extent for zero axial length, full wall thickness defect. Results are from membrane model with T(0,1) incident in 3 inch pipe at 45 kHz.

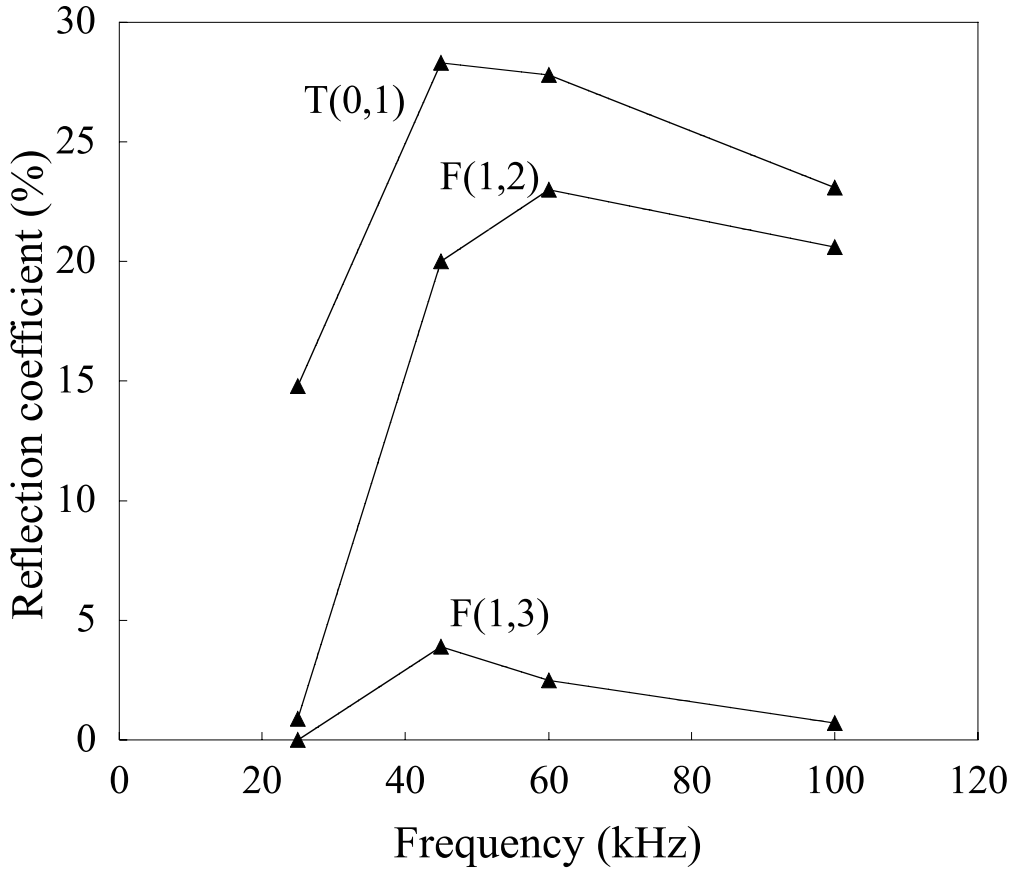

Figure 4.9: Variation of reflection ratio with frequency for T(0,1) mode input in 3 inch pipe using membrane model with 25% notch circumferential extent.

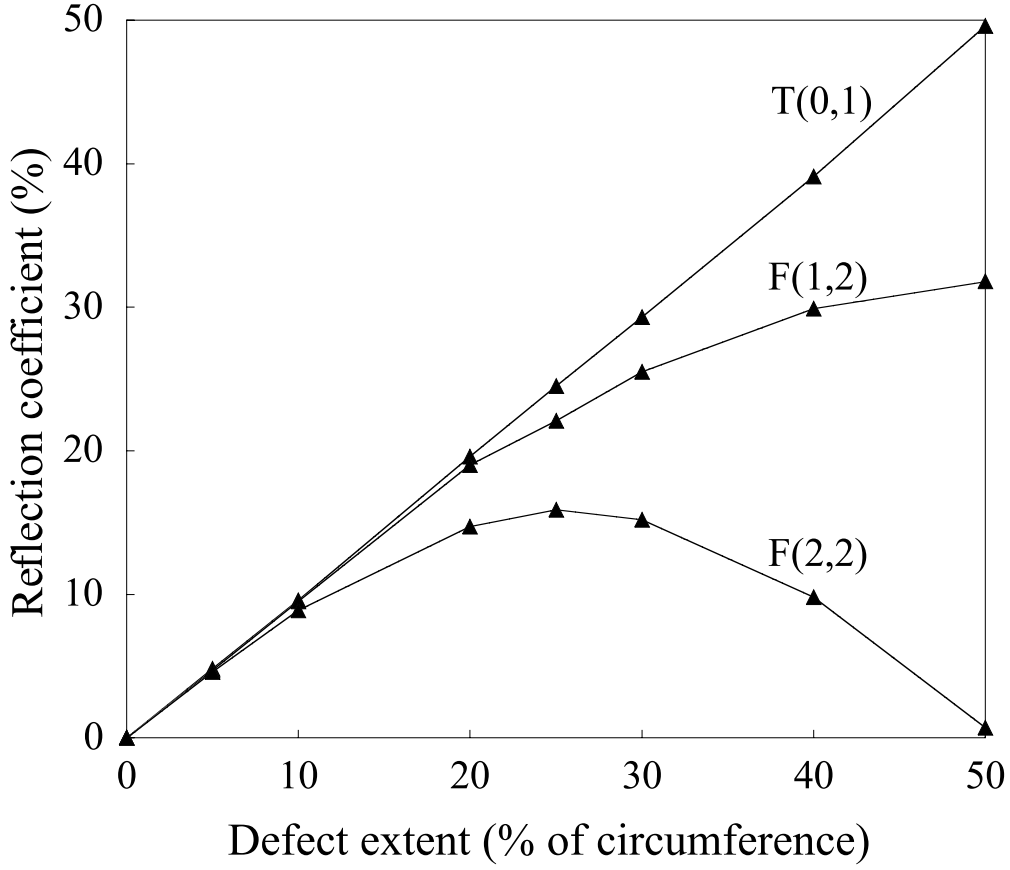

Figure 4.10: Variation of reflection ratio with defect circumferential extent for zero axial length, full wall thickness defect. Results are from membrane model with T(0,1) incident in 24 inch pipe at 50 kHz.

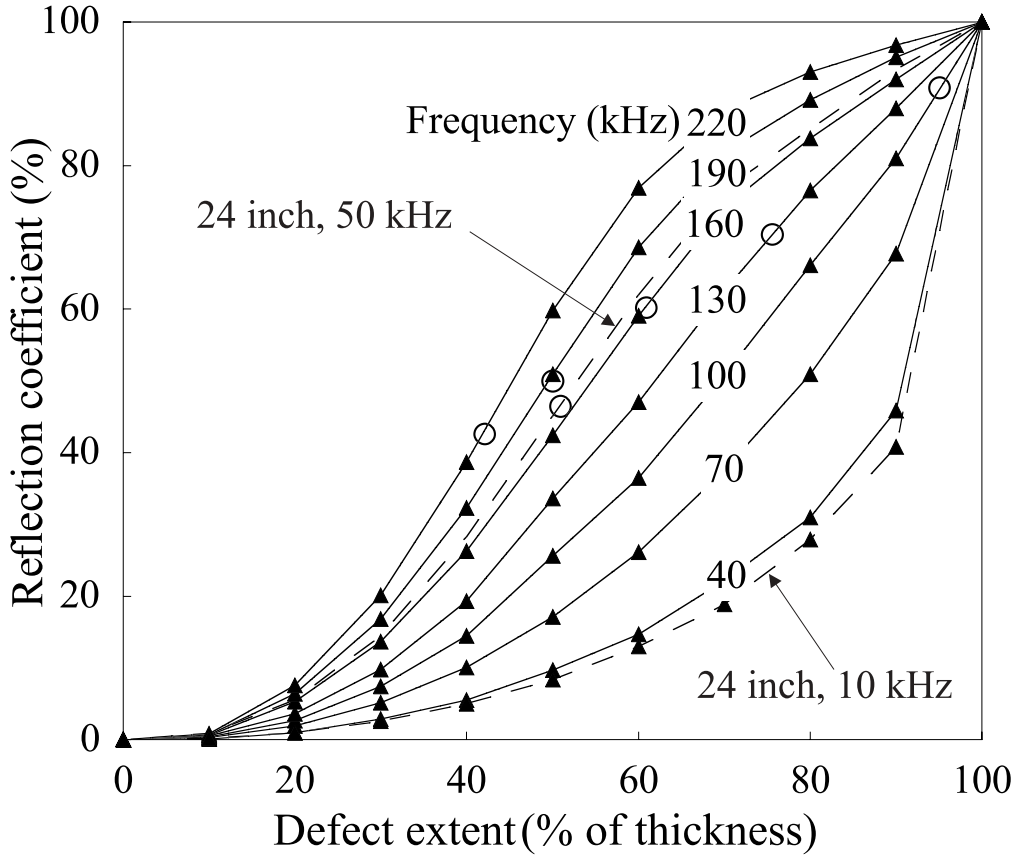

Figure 4.11: Variation of reflection ratio with defect depth for zero axial length at various frequencies, axi-symmetric defect. Results are from axisymmetric model with T(0,1) incident in 3 inch (solid lines) and 24 inch pipes (dashed lines). The empty circles indicate the depth value for which ka=1 at each frequency.

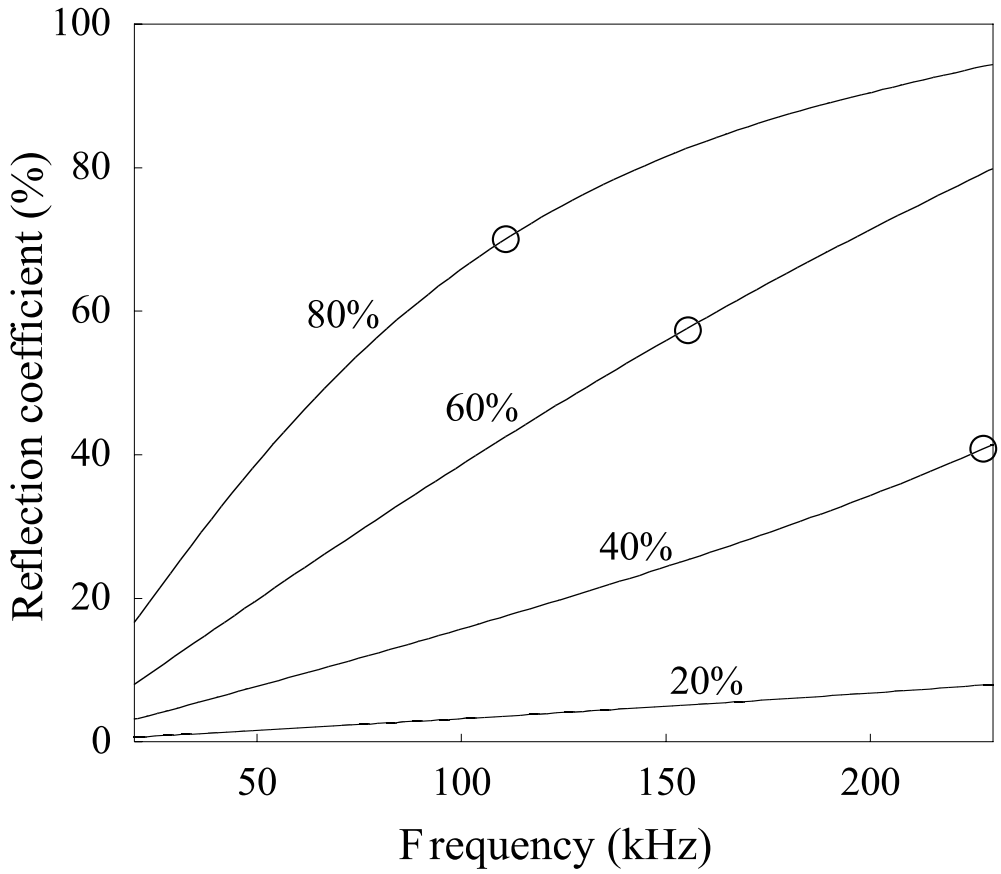

Figure 4.12: Variation of reflection ratio with frequency for zero axial length at various defect depths, axi-symmetric defect. Results are from axi-symmetric model with T(0,1) incident in 3 inch pipe. The empty circles indicate the frequency at which ka=1 for each defect depth.

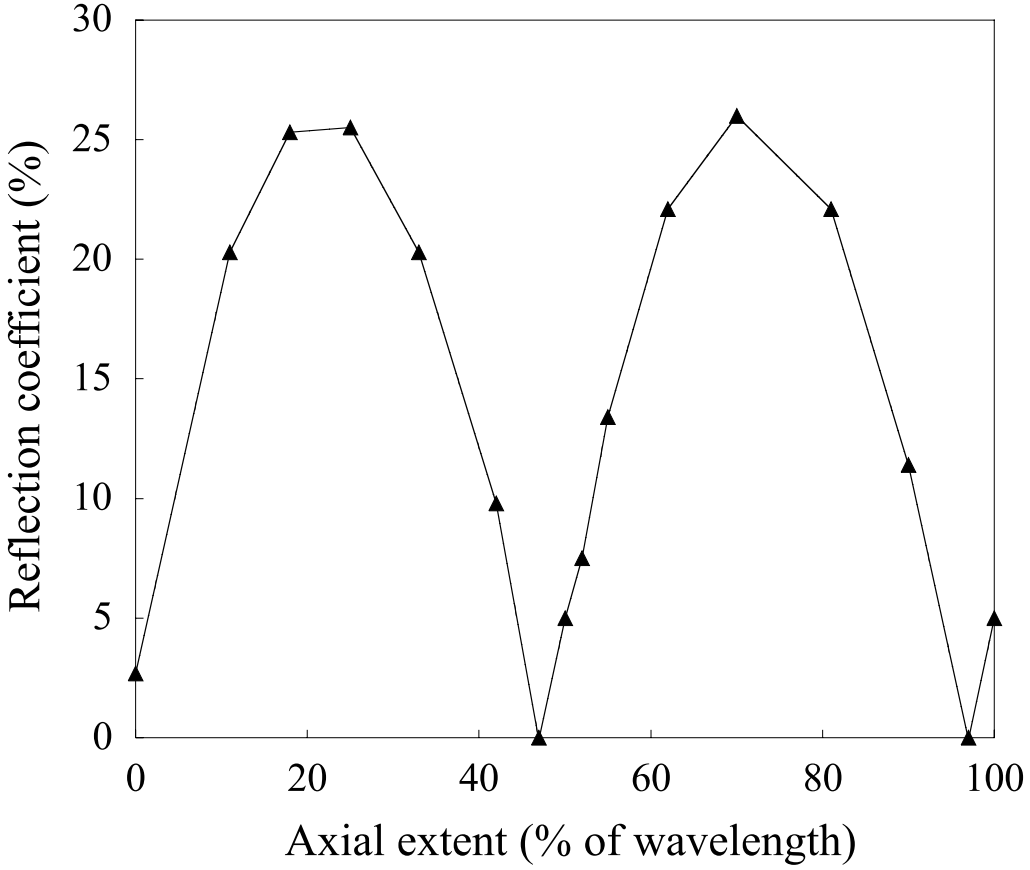

Figure 4.13: Variation of reflection ratio with axial extent when there is an axi-symmetric defect with 20% thickness depth. Results are from axi-symmetric model with T(0,1) incident in 3 inch pipe at 100 kHz.

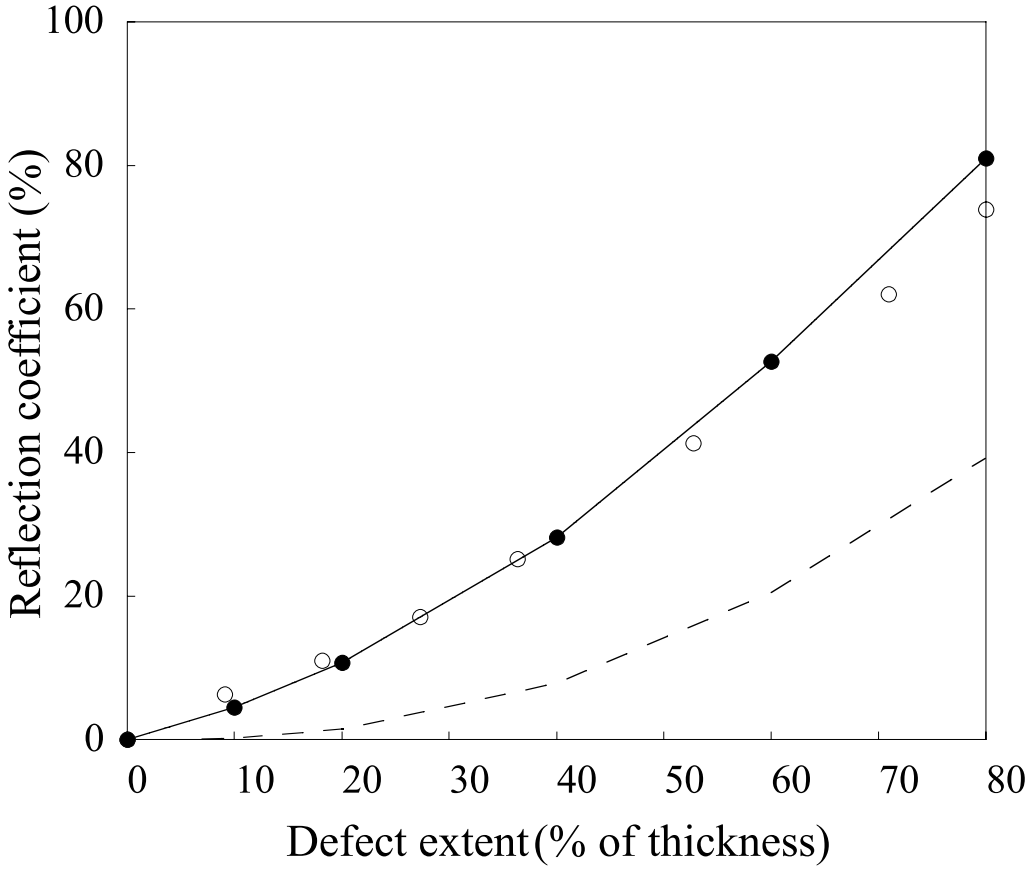

Figure 4.14: Variation of reflection ratio in incident mode with defect depth for 3.5 mm axial length, axi-symmetric defect. FE (-●-) and experimental (○) results are for T(0,1) incident in 3 inch pipe at 55 kHz. The crack case (zero axial extent) is also displayed for comparison (dashed line).

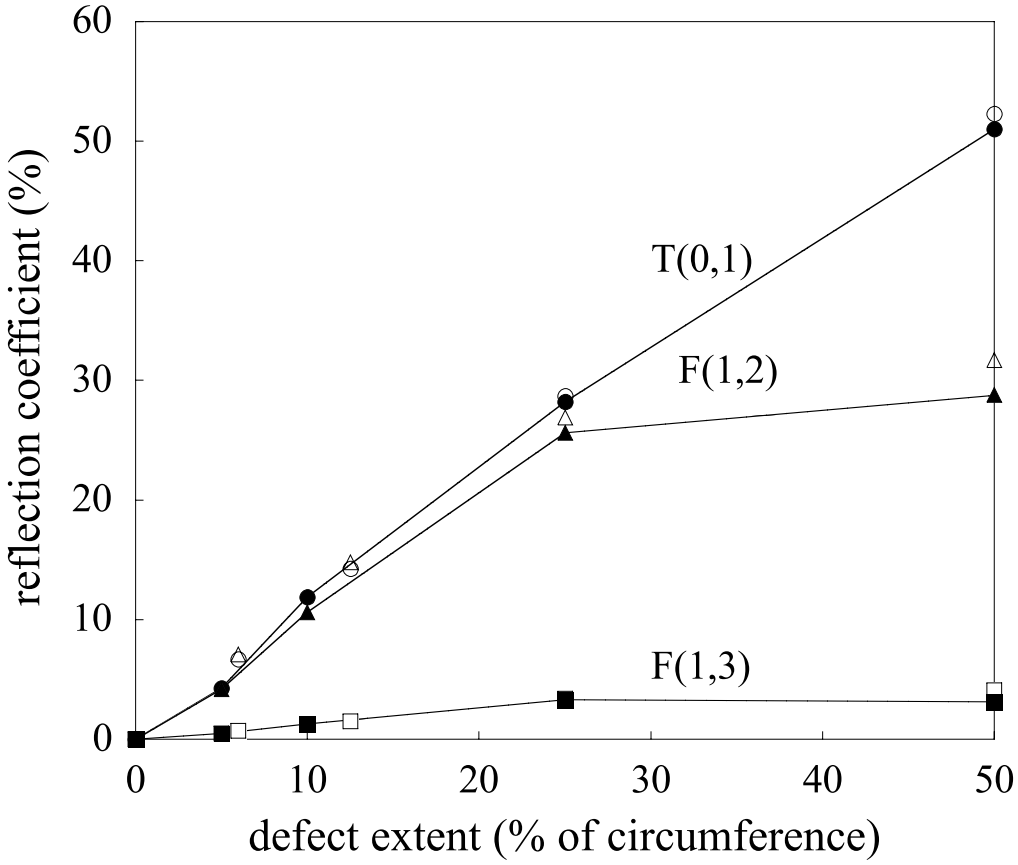

Figure 4.15: Variation of reflection ratio with circumferential extent for 3.5 mm axial length, through thickness defect. FE (lines with solid symbols) and experimental (empty symbols) results are for T(0,1) incident in 3 inch pipe at 55 kHz.

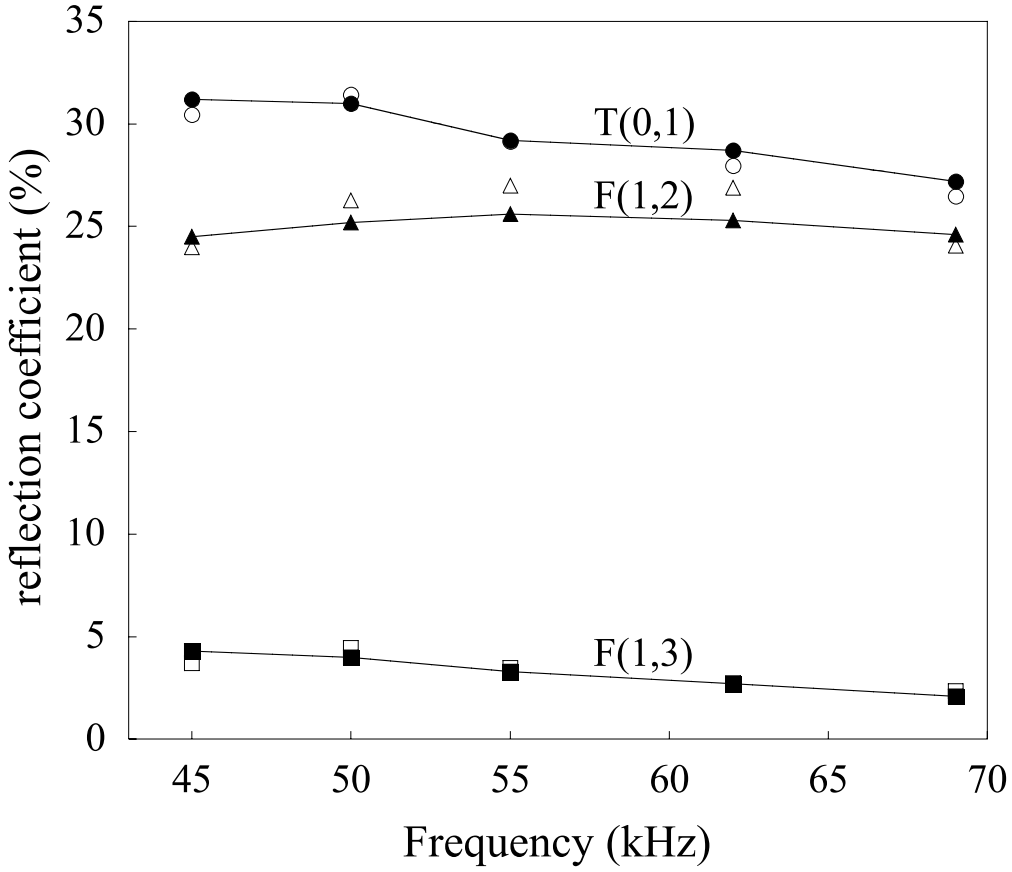

Figure 4.16: Variation of reflection ratio with frequency for 3.5 mm axial length, through thickness defect extending over the 25% of the circumference of a 3 inch pipe . Both FE (lines with solid symbols) and experimental results (empty symbols) are displayed.

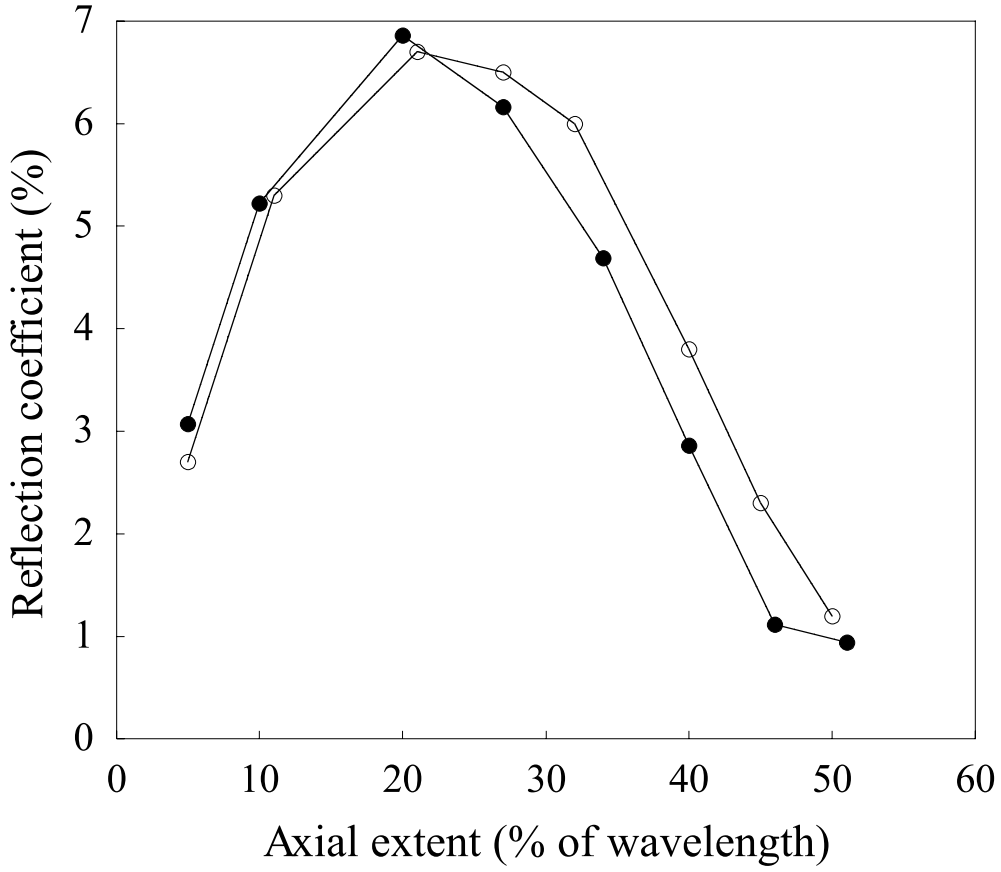

Figure 4.17: Variation of reflection ratio in incident mode with axial extent for a 20% depth, 25% circumferential extent defect. FE (•) and experimental results (○) are for T(0,1) incident in 3 inch pipe at 55 kHz.

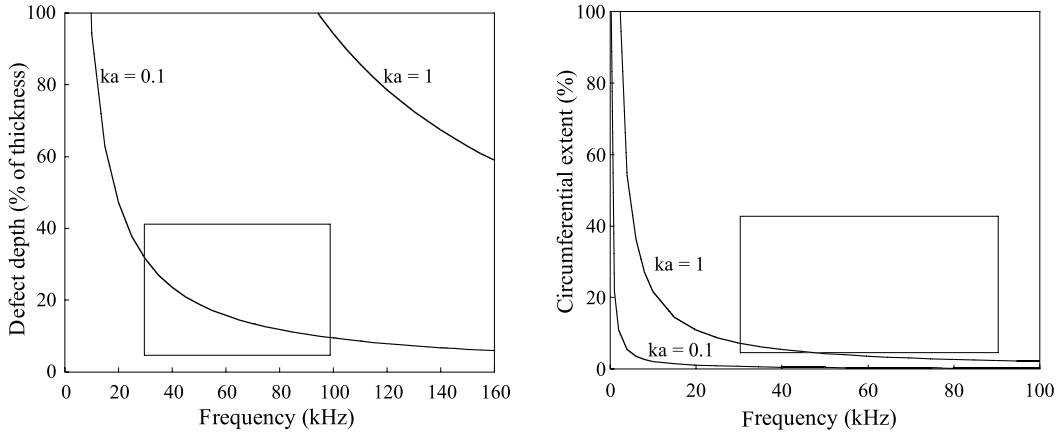

Figure 4.18: Scattering regime regions in the case of the axisymmetric defect in 3 inch pipe with 5.5 mm wall thickness (a) and through thickness defect (b). The boxes indicate the practical testing regions.

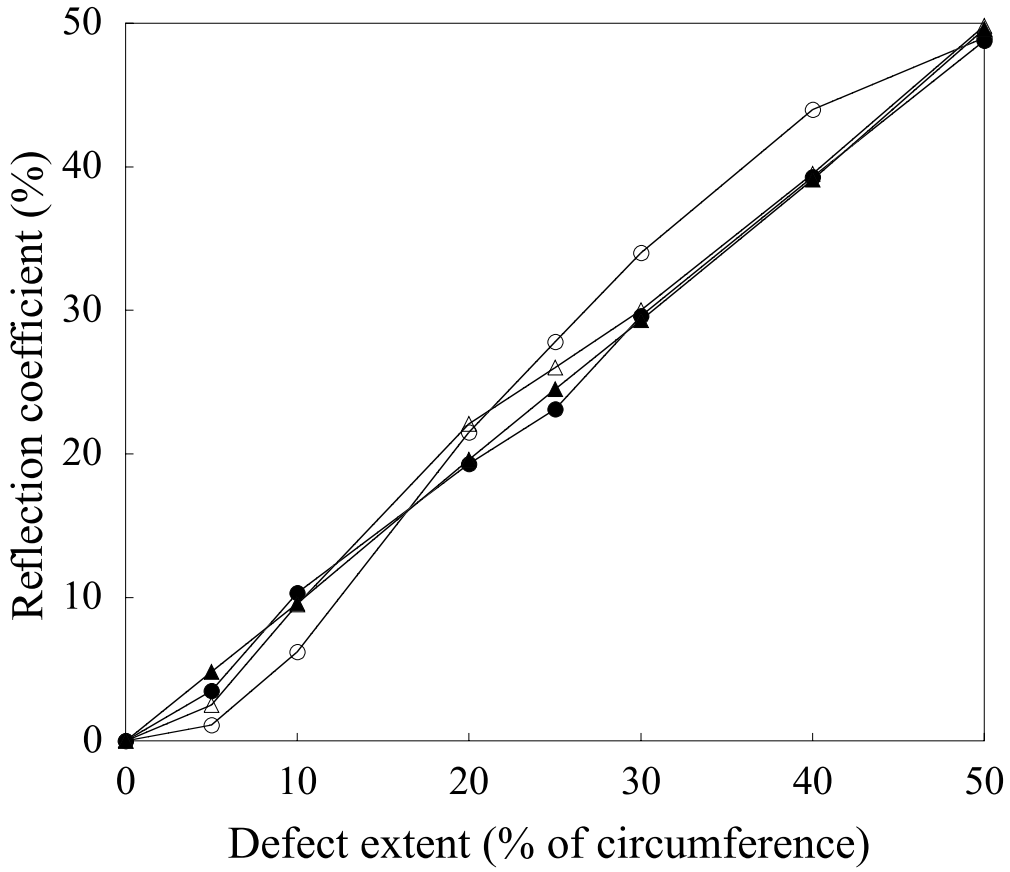

Figure 4.19: Variation of reflection ratio in incident mode with defect circumferential extent for zero axial length, full wall thickness defect. Results are from membrane model with T(0,1) incident in 24 inch pipe at 10 kHz (empty triangle) and 50 kHz (solid triangle) and in 3 inch pipe at 45 kHz (empty circle) and 100 kHz (solid circle).

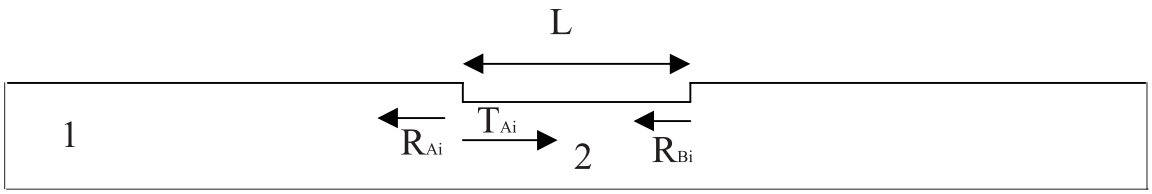

Figure 4.20: Example notch case to explain reflection and transmission characteristics at the start and at the end of the notch.

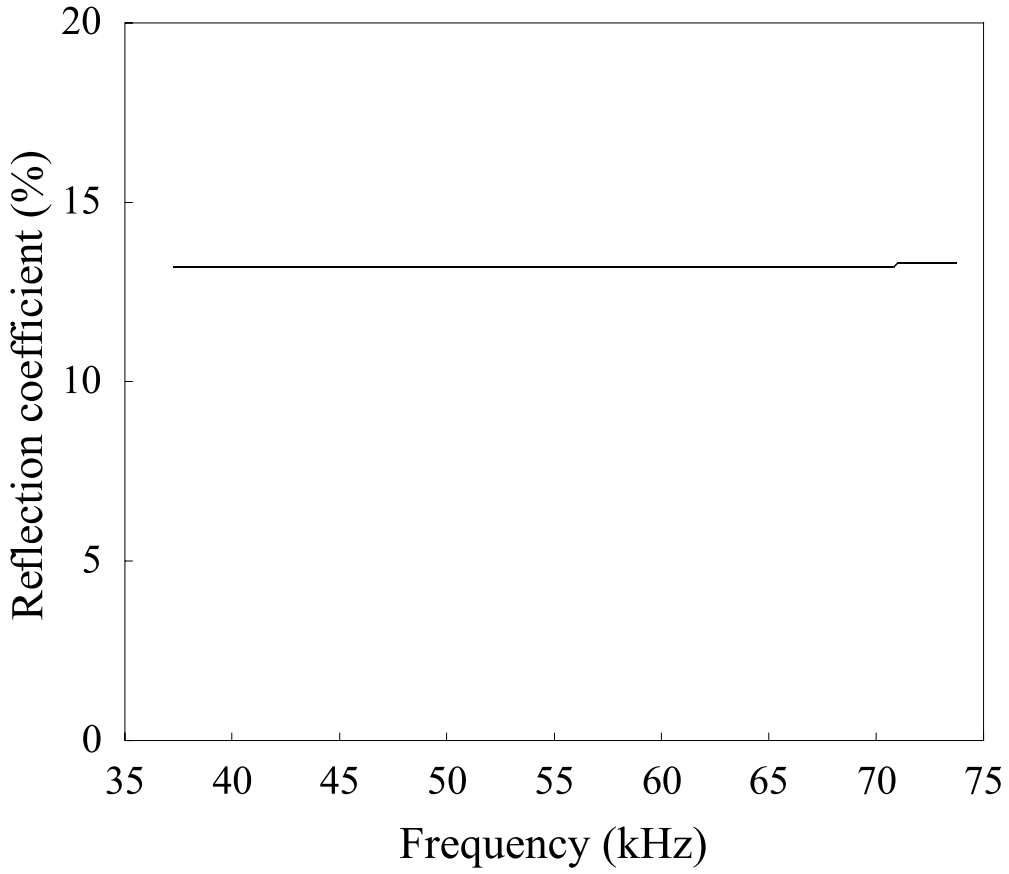

Figure 4.21: Variation of reflection ratio with frequency for a step of 20% of the thickness of the pipe. Results are for T(0,1) incident in 3 inch pipe using signal with center frequency of 55 kHz.

axial extent (% of λ(32.6 mm))	180		
Circumferential extent(%)	100	25	25
through-wall extent (%)	33	100	33
Reflection ratio (%): Axisymmetric model (2D)	23.5		
Reflection ratio (%): Membrane model (2D)		21.1	
Reflection ratio (%): 3D model	23.7	21.1	5.2
Reflection ratio predicted by combining 2-D analyses			5.0

Table 4.1: Comparison of T(0,1) reflection ratio in a 3 inch pipe at 100 kHz from 3D model with combined results from axisymmetric and membrane models.

Chapter 5

Reflection from defects in pipes: a generalization to different testing configurations

5.1 Introduction

As already mentioned in the introduction of this thesis, an ultrasonic guided wave tool for the detection of corrosion in pipes is commercially available. This tool is currently able to classify the severity of a defect by measuring the amplitude of the waves reflected by the defect. A deeper understanding of the interaction of the guided waves with defects is essential for the optimization of the results obtainable with this technique. Moreover, the interaction of guided waves with defects is a very complex phenomenon and it is in the interest of the final users to be able to understand the limits and the potentials of the technique. This can only be achieved when the problem of the scattering from defects is reduced from the many parameters involved to just a few important parameters. Due to the practical interest of this goal a practical approach was used. Nevertheless this investigation offers an accurate scientific analysis of all of the parameters involved in the scattering of guided waves.

5.1.1 Definition of parameters

A quantitative study of the reflection coefficient as a function of the defect size, the dimensions of the pipe, the cylindrical guided wave mode which is used and the frequency at which the wave is excited is difficult to perform because of the number of parameters involved (even when it is an idealized simple rectangular defect). We can identify seven parameters overall: mode excited, frequency (f), pipe diameter(D), pipe thickness (t), axial extent of defect (a), defect depth (b), circumferential extent of defect (c). The geometrical parameters are described in Figure 5.1.

The first step towards a simplification of the problem is the definition of non-dimensional parameters for the defect dimensions. Therefore the non-dimensional axial extent of the defect is defined as a percentage of the wavelength $a\% = \frac{a}{\lambda} \cdot 100$ where $\lambda = \frac{V}{f}$ is the wavelength of the excited wave of phase velocity V at frequency f. The defect depth is non-dimensionalized by using the parameter $b\% = \frac{b}{t} \cdot 100$ (depth as % of wall thickness). The circumferential extent can be described as c% where $c\% = \frac{c}{2\pi R_M} \cdot 100$ and R_M is the mean radius of the pipe (circumferential extent as % of circumference).

5.1.2 Background and new contribution

The interaction of cylindrically guided waves with geometrical discontinuities of the waveguide has been investigated by many researchers [86, 87, 46, 52, 53, 88, 10, 9, 67, 11]. In particular the reflection from cracks when either the L(0,2) mode [10, 9, 101] or the T(0,1) mode (Chapter 4) is incident has been studied. The examination of the reflection as a function of the notch axial extent has identified the important phenomenon of the interaction between the reflections from the two sides of a notch (treated in Chapter 3 and 4). A study on the effect of frequency on the interference phenomenon present in the reflection from rectangular notches was also presented in Chapter 3. Previous work has covered a number of cases for the modes of interest (L(0,2) and T(0,1)). In this Chapter the two modes are addressed and compared and an investigation of the effect of the parameters previously defined (pipe size, frequency and defect size) on the reflection from a notch is performed. In order to have a complete view of the effect of all the different parameters on the reflection

behavior we extended the results obtained in previous investigations by using Finite Element (FE) analysis. The aim of this study is to offer a generalization of the results obtained in previous work by introducing some simple rules for predicting the reflection from notches and so estimating the defect size from a measured reflection coefficient.

This Chapter starts with a brief introduction to the FE models used in this study. Only FE predictions are presented here because all of the model types used have already been validated with experiments in previous papers [9, 10, 102] and in Chapter 4 of this thesis (note that in this investigation, only square sided defects are considered). Then the frequency limits of this investigation are identified. Some observations on the effect of defect size on the reflection coefficient are introduced and the trends of reflection behavior are identified. Some limitations of this investigation in terms of minimum defect extent are defined. A quantitative investigation of the parameters affecting the reflection from axisymmetric notches is performed and the results are presented. The information obtained for axisymmetric notches is then used to predict the reflection behavior of part-thickness, part-circumference defects and conclusions on the capability of defect sizing are presented.

Overall the aim of the work of this Chapter is to provide a basis for estimating the reflection coefficient which may be expected when testing pipes, over a wide range of pipe sizes, defect sizes and frequencies.

5.2 Finite element models

As already mentioned, the Finite Element (FE) tool is employed in this study in order to investigate new cases which were not documented in previous work on the same subject [10, 9, 67, 102] and were not reported in the previous Chapters. In general, a three-dimensional (3-D) solid model is required to perform a numerical analysis of the interaction between guided waves and discrete defects. However 3-D models are computationally expensive so when possible we use simplified models [10]. Here we consider axi-symmetric and three-dimensional models (already described in section 4.4). The three-dimensional model was used to study defects that remove a fraction of circumference and the full wall thickness. In other investigations [9, 10,

102] this geometry was modelled using the less computationally expensive membrane model. In this study a wider frequency range was investigated and not all of the mode shapes at all frequencies could be accurately approximated by membrane elements so solid brick elements were used instead. In all of the three-dimensional models only three elements through the thickness were introduced. The three dimensional analysis could potentially be used to study axisymmetric defects but in this case, due to the number of through-thickness elements required to study the effect of defect depth, the less computationally expensive axisymmetric analysis tool was used.

It was demonstrated in Chapter 4 that it is valid to use a combination of the reflection from a through-thickness, part-circumference defect and an axi-symmetric part-depth defect to predict the response from a part-circumference, part-depth defect. This concept was also applied here.

Most of the modelling work was focused on simulating the effect of a rectangular notch shape (see Figure 5.2a) but a stepped notch case (see Figure 5.2b) was also studied in order to understand the effect of defect shape on the reflection coefficient.

In all cases, a length of the pipe was modelled and a notch was introduced at some distance along it. The input wave signal was excited in the model by prescribing time-varying displacements at one end of the pipe. Narrow band signals were used, typically composed of 8 cycles of the desired centre frequency modulated by a Gaussian window. The displacements were then monitored at a location between the excitation end and the notch, thereby detecting both the incident wave on its way to the notch and the reflected wave returning. The reflection coefficient was calculated by dividing the amplitude of the reflected mode by the amplitude of the incident mode in the frequency domain. In some cases the reflection coefficient was derived by dividing the amplitude of the reflected signal by the amplitude of the input signal in the time domain (Hilbert envelope). This was done when low-frequency excitation was imposed in order to prevent the effect of time signal gating or filtering from affecting the low frequency response. Moreover the Hilbert envelope is used in the practical implementation of the method (see Alleyne et al. [11]).

5.3 Definition of frequency limits

This investigation aims to provide practical guidance to the understanding of the reflection from corrosion in pipes when either L(0,2) or T(0,1) modes are used for rapid screening. Therefore the analysis has been limited to the range commonly used in commercial applications [11], 10-65 kHz.

The lower frequency limits of the two modes are also influenced by the guided wave characteristics. The L(0,2) mode only exists at frequencies for which the frequency-diameter product (fD) is higher than about 1.7 MHz-mm (see Figure 2.9). Furthermore, since L(0,2) is typically used in the non-dispersive region, its use is limited to frequencies for which the product fD is higher than 3 MHz-mm.

On the other hand T(0,1) exists and is non-dispersive at all frequencies, therefore suggesting that there is no limitation to its applicability at low frequency; indeed this is true if there is no need for sizing the defect. However some limitations do appear when defect sizing is attempted since the mode conversion of the excited axisymmetric mode to a flexural mode of the first order enables an estimate of the defect circumferential extent. At relatively low frequency-diameter products, T(0,1) does not convert to F(1,2) because the F(1,2) mode does not have strong 'torsional' behavior at frequency-diameter product lower than 2.1 MHz-mm (see Chapter 4). Therefore it is wise to limit this investigation to the study of the T(0,1) mode at frequency-diameter higher than 2.1 MHz-mm.

To summarize, the low frequency limits of this work, which are shown in Figure 5.3, depend on the pipe size: for small diameter pipes the minimum frequency is given by the guided wave limitations (fD=2.1 MHz-mm for T(0,1) and fD=3 MHz-mm for L(0,2)), while the minimum frequency for large diameter pipes is 10 kHz due to limitations of the transducer design. The high frequency limit of this study is 65 kHz in all cases. Within these frequency limits, the reflection of the T(0,1) mode from through-thickness (100% depth) defects is almost constant with respect to frequency as shown in the example in Figure 5.4 where the reflection from through thickness cracks extending over 25% and 50% in a 3 inch schedule 40 pipe is almost independent of frequency in the frequency range defined above (this is valid also for L(0,2) as shown by Lowe et al. [9]).

5.4 Study of non-dimensional parameters

In this section we describe the effect of defect size in terms of circumferential extent(c%), axial extent (a%) and depth (b%). The general trends are identified using the information given in previous papers [9, 10, 102].

5.4.1 Circumferential extent

The effect of the circumferential extent of the defect (c%) on the reflection from notches has previously been studied for both the T(0,1) (see Chapter 4) and L(0,2) cases [9, 10, 102]. It was found that the reflection coefficient of these axisymmetric modes is linearly dependent on the circumferential extent of the defect provided that the test is performed at relatively high frequency (the low frequency limits were defined in the previous section). The reflection from a through thickness (100% depth) defect is almost independent of frequency. There is a small effect related to the axial extent of a through-thickness defect compared to the wavelength, and hence the frequency [102], but it can be neglected (the difference is of the order of 5-15% of the estimated value for the crack).

Figure 5.5 shows the effect of the circumferential extent of a through-thickness defect on the reflection coefficient of the incident axisymmetric mode and the first order flexural mode which is generated by mode conversion. The data was obtained from a study of the extensional L(0,2) mode incident, with mode conversion to F(1,3) [10], but the same result was found for the torsional T(0,1) mode incident with mode conversion to F(1,2) (see Chapter 4).

The mode conversion to a flexural mode enables the recognition of a non-symmetric feature; if an axisymmetric mode is incident on an axisymmetric feature, only axisymmetric modes will be reflected, whereas flexural modes also appear when the feature is non-symmetric. This, for example, enables a localized corrosion defect in a pipe (typically non-symmetric) to be distinguished from a weld (typically symmetric) [10].

Using the amplitude of the reflected mode converted signal it is possible to estimate the circumferential extent of a defect. This is done by evaluating the ratio between the flexural reflected component (F) and the axisymmetric reflected

component(A) as shown in Figure 5.6. It is clear that at small circumferential extent of defect the F/A ratio is not very sensitive to small changes of the circumferential extent so it is difficult to determine, for example, whether a defect is extending over 5% or 10% of the circumferential extent.

5.4.2 Axial extent

As already mentioned in the previous section, the axial extent (a%) has negligible effect on the reflection from through-thickness defects. However, the axial extent has an important effect on the reflection from part-depth defects. The reflection from an axisymmetric part-depth notch changes cyclically with the axial extent of the notch as illustrated in Figure 5.7. This shows an example where the T(0,1) mode is incident on a 24 inch pipe at 35 kHz and the defect is a 50% depth axisymmetric notch (b=50%). Similar behavior is seen with both T(0,1) and L(0,2) incident modes at all pipe sizes, frequencies and defect depths.

The cyclical behavior shown in Figures 4.13 and 5.7 is the result of interference between the reflections from the start and end of the notch. Depending on the excitation frequency and the axial extent of the notch, the reflections from the opposite faces of the notch can interfere constructively or destructively (see Chapter 4). Figure 5.7 suggests that at an axial extent of about 45% of the wavelength there is no reflection from the notch and it will therefore not be detected. This does not occur in practice because the excitation signal which is used is a Gaussian windowed toneburst which has energy over a range of frequencies. For example, a 5 cycle windowed toneburst has a -6dB bandwidth of about 30% of the centre frequency. Therefore, even if the defect axial extent is 45% of the wavelength at the centre frequency, a reflection will still be seen due to the other frequencies present in the signal. It is also normal practice to test at more than one centre frequency.

Figure 5.7 shows that relatively small reflections are also seen at low defect axial extents, indicating that this low frequency guided wave inspection is less sensitive to cracks than to corrosion patches. The analysis of this paper is limited to axial extents greater than 5% of the wavelength and Table 5.1 shows that even at an inspection frequency as low as 10 kHz this corresponds to a length of 16 mm when T(0,1) is employed and 28 mm if L(0,2) is used. At 20 kHz these lengths are reduced

to 8 mm and 14 mm respectively. The great majority of corrosion patches are larger than this so the analysis presented here covers most practical cases. It is possible to detect shorter defects, but the sensitivity is lower for a constant defect depth.

The use of an excitation signal with a significant bandwidth and testing at more than one centre frequency means that even if the defect axial extent corresponds to 45% of the wavelength at one test centre frequency, a reflection will be seen that is at least as large as that obtained from a 5% axial extent defect of the same depth and circumferential extent. This is shown as Rmin in Figure 5.7; it should be stressed that the value of Rmin varies with the defect depth and circumferential extent.

5.4.3 Defect depth

The effect of defect depth (t%) has been studied in previous work on the reflection from axisymmetric defects when L(0,2) [9] and T(0,1) (Chapter 4) are incident. The results obtained from these studies clearly showed that the reflection coefficient increases monotonically with defect depth. This behavior is illustrated in Figure 5.8 which shows the reflection coefficient of the T(0,1) mode at 55 kHz from a rectangular axisymmetric notch with varying depth and constant axial extent (a=25%) in a 3 inch pipe. This trend is generally seen at all pipe sizes, excitation modes, frequencies and axial extents.

5.5 Effect of frequency, pipe size and pipe schedule on the reflection from axisymmetric defects.

A simple model which enables the estimation of the reflection from axisymmetric (part-depth, full-circumference) defects for different sizes of defects and pipes has not previously been published. In this section we examine the influence of a series of parameters (frequency, diameter, thickness) on the reflection from axisymmetric defects and we then propose a simple model of the reflection from axisymmetric notches. This model will be used to propose a procedure for the sizing of part-circumference, part-depth notches.

5.5.1 Frequency

Figure 5.9 shows the effect of axial extent on the reflection coefficient of the T(0,1) mode from a series of 50% depth (b=0.5 t) axisymmetric notches in a 3 inch schedule 40 pipe at three frequencies (10 kHz, 35 kHz and 65 kHz). In Figure 5.9 the value of reflection at constant a% and varying frequency is given by the intersections of a vertical line at constant a% and the curves at different constant frequencies. It is important to notice that in a practical application we deal with a fixed axial extent of defect (not non-dimensionalized). Thus to find the reflection coefficient at constant absolute axial extent (a) for two different frequencies it is necessary to move to a different frequency curve and different percentage axial extent a% (which is dependent on the frequency).

As already mentioned in section 5.4, the reflection coefficient from axisymmetric notches depends on the axial extent of the notch. In Figure 5.7 we have shown that at a given frequency the reflection coefficient increases with the percentage axial extent a% (in the range for which a% is less than 25% of the wavelength λ). Figure 5.9 shows that the reflection coefficient at a fixed axial extent (a%) increases with frequency. However the effect of frequency on the reflection coefficient is small in the frequency range of interest when considering an axial extent (a%) range of 5%-25% of the wavelength. It is therefore reasonable to say that the reflection coefficient values obtained at an intermediate frequency (e.g. 35 kHz) closely approximates the reflection coefficient at any frequency in the range 10-65 kHz. This approximation of using the 35kHz results to represent the full frequency range of the investigation is valid for all pipe sizes and schedules and for both T(0,1) and L(0,2); it will be used throughout this Chapter. As a result, the effect of changing the frequency of a practical test is simply described by the change of non-dimensionalized axial extent (a%).

5.5.2 Pipe size, pipe schedule and defect location in cross section

In this subsection we evaluate the effect of the geometry of the pipe on the reflection from axisymmetric defects and we propose a simple formula for the reflection and

transmission from thickness steps in pipes. This is relevant to our investigation on reflection from notches because a notch can be considered as a thickness step down followed by a thickness step up as demonstrated for the plate case (see Chapter 3).

Figure 5.10 shows the effect of pipe schedule on the reflection from notches. Both schedule 40 (5.5 mm wall thickness) and schedule 80 (8 mm thickness) 3 inch pipes were modelled. A rectangular notch of varying axial extent was introduced on the outer surface of the pipe and T(0,1) at 35 kHz was excited at one end of the pipe. It is clear that the reflection coefficient increases with pipe thickness. Figure 5.11 shows the effect of pipe diameter on the reflection from notches. A rectangular notch was modelled on the outer diameter of a 3 inch schedule 40 pipe and a 24 inch schedule 40 pipe; the T(0,1) mode was excited at one end of the structure. It is clear that the reflection for a given % depth of notch increases when the pipe diameter decreases. The effect of defect location was studied by Zhu [103] who suggested that defects on the outer wall of a pipe produce a bigger reflection than defects on the inner wall.

The trends of reflection coefficient noted above are valid for both T(0,1) and L(0,2) modes. The dependence of reflection behavior on pipe size, pipe schedule and whether the defect location initiates at the inner or outer wall is due to two effects which are described as follows.

Firstly one can intuitively suggest that defects with the same depth (b%) remove a different fraction of the cross sectional area depending on the pipe size, pipe schedule and initiation side. Therefore, if the cross sectional area was the only parameter, the reflection from a thickness step could be quantified using the following:

$$R_S = \frac{1 - \frac{A_R}{A_L}}{1 + \frac{A_R}{A_L}} \tag{5.1}$$

where A_L is the cross sectional area before the step and A_R is the cross sectional area after the step. However, the Strain Energy Density (SED) varies with the radial position and therefore it must be considered when estimating the reflection from a step discontinuity (see Wilcox et al. [29] for more details on SED). Both for T(0,1) and L(0,2) the SED increases going from the inner to the outer wall therefore suggesting that the radial position of the removed cross sectional area is another important parameter. From these observations we can write an approximate

formula for the reflection from a thickness step in a pipe:

$$R_S = \frac{1 - \frac{A_R \cdot R_{mR}}{A_L \cdot R_{mL}}}{1 + \frac{A_R \cdot R_{mR}}{A_L \cdot R_{mL}}} \tag{5.2}$$

where R_{mL} is the mean pipe radius before the step and R_{mR} is the mean pipe radius after the step. Equation 5.2 was not rigorously derived by exact solution of the scattering problem. This is an intuitive formula which takes into account the effect of pipe diameter and thickness and it also takes into account the position of the defect, that is whether it is on the inside or on the outside of the pipe. This was verified for several cases, and it was found that the difference between the approximation function and the FE results was always less than 5% of the value estimated with FE. The modulus of the transmission coefficient at a step (T_S) can be derived by simply applying the conservation of the energy:

$$R_S^2 + T_S^2 = 1 \tag{5.3}$$

The use of the energy conservation to obtain the transmission coefficient is rigorous for the T(0,1) incident mode because no other torsional axisymmetric mode is present in the frequency range of the investigation. It is also sensibly valid for L(0,2) incident mode because only a small amount of energy is converted into the other longitudinal mode, L(0,1).

5.5.3 Generalization for different geometries.

The approach proposed here for the generalization of the results is to find the reflection coefficients for an axisymmetric notch in a specific defined pipe at all depths and axial extents of the defect using FE, and then to introduce a correction factor to generalize for other pipe sizes, schedules and defect locations in the pipe cross section. The rationale for this is as follows. The maximum reflection coefficient (Rmax in Figure 5.7) can be calculated easily for all pipe sizes and schedules, for any given defect depth (b%), circumferential extent (c%), or position (inside or outside surface). It is reasonable to assume that the curve between 5% and 25% in Figure 5.7 is the same shape for all of these pipes; it differs only in the vertical scale. Therefore the reflection coefficient for any value of axial extent (a%) in a candidate

pipe size may be taken to be the same as that in the reference pipe size, scaled by their respective Rmax values.

In general, the reflection from a notch can be obtained by considering the reflection from a down step followed by the reflection of the signal transmitted through the down step at an up step corresponding to the end of the notch. These initial reflections are followed by reverberations in the notch. In Chapter 3 it was shown that the phases of the reflections from up and down steps are not exactly 0 or π; however this does not affect the maximum reflection that can be obtained since at some axial extent constructive interference will be obtained. Therefore the maximum reflection, Q, can readily be calculated for the simplest case where the phase of the reflection and transmission at up and down steps are either 0 or π. In this case the amplitude of the first reflection from a rectangular notch is

$$R_{N1} = R_S \tag{5.4}$$

The second reflection is

$$R_{N2} = T_S \cdot R_S \cdot T_S = (1 - R_S^2) \cdot R_S \tag{5.5}$$

The j^{th} reflection has amplitude

$$R_{Nj} = T_S \cdot R_S^{2 \cdot j-3} \cdot T_S = (1 - R_S^2) \cdot R_S^{2 \cdot j-3} \tag{5.6}$$

Summing all of the reflection terms it is possible to obtain the maximum reflection coefficient for a notch:

$$Q = R_S + R_S \cdot (1 - R_S^2) - R_S^3 \cdot (1 - R_S^2) + R_S^5 \cdot (1 - R_S^2) - ... \tag{5.7}$$

which can be written as follows:

$$Q = R_S + R_S \cdot (1 - R_S^2) \cdot (1 - R_S^2) \cdot (1 + R_S^4 + R_S^8 + R_S^{12} + ...) \tag{5.8}$$

Using a more compact notation, Equation 5.8 can be written as:

$$Q = R_S + R_S \cdot (1 - R_S^2)^2 \cdot \sum_{j=0}^{\infty} (R_S^{4j}) \tag{5.9}$$

The infinite sum in Equation 5.9 is a converging series and therefore Equation 5.9 yields:

$$Q = R_S + R_S \cdot (1 - R_S^2)^2 \cdot (\frac{1}{1 - R_S^4}) \tag{5.10}$$

Further simplifying Equation 5.10, it is possible to obtain the following formula:

$$Q = R_S \cdot (\frac{2}{1 + R_S^2}) \tag{5.11}$$

which is easy to compute.

Figure 5.12 shows a comparison between the maximum reflection coefficient calculated using FE predictions and the function Q for a 24 inch pipe in which there was a notch with varying depth and T(0,1) incident at 35 kHz. It is clear from Figure 5.12 that the approximation function closely matches the values obtained from the FE simulations. The approximation function derived for T(0,1) can also be used for L(0,2) and this is also shown in Figure 5.12. The results shown in this section are for notches on the outside of the pipe but Equation 5.2 is also valid for notches on the inside of the pipe. Therefore the computed values for the maximum reflection from notches are accurate enough to be used to define a correction factor for pipe size, schedule and defect location in the cross section.

In the following part of the Chapter we will only deal with one frequency (35 kHz) which is used to approximate the reflection in the frequency range 10-65 kHz and we will show the reflection coefficient obtained using FE for one pipe size (3 inch schedule 40) and defects on the outer pipe surface. The results for any other pipe size and defect location can be derived using the results for a 3 inch schedule 40 pipe and a correction factor which takes into account pipe size and defect location.

The correction factor is here defined as $\chi = Q_x/Q_0$ where the subscript 0 refers to a reference pipe and defect location (inside or outside) and the subscript x refers to the pipe under investigation. In our case we have defined Q_0 as the reflection from a 3 inch schedule 40 pipe with defects on the outside wall. The coefficient χ is dependent on the diameter and thickness of the two pipes, on the position of the defect (inside or outside) and on the defect depth (in percent of the thickness), therefore $\chi_{x,0,b\%} = \chi(D_x, t_x, Pos_x, D_0, t_0, Pos_0, b\%)$ where Pos indicates the position (inside or outside). After obtaining the FE reflection coefficients for the reference pipe and defect (here evaluated only in the range 5%-25% axial extent), it is possible to obtain the reflection coefficients at the same axial extent for another pipe and defect position (D_x, t_x, Pos_x) at the same percentage defect depth (b%) by simply

evaluating the following:

$$R_{x,b\%} = \chi_{x,0,b\%} R_{0,b\%} \tag{5.12}$$

where $R_{0,b\%}$ is the reflection coefficient for the reference pipe obtained using FE.

The coefficient $(1-\chi)$ gives an estimate of the difference between the maximum reflection coefficient for the given pipe and the maximum reflection coefficient for the reference pipe. Figure 5.13 shows the $(1-\chi)$ value for a 24 inch pipe where the defects are on the outer surface and a 3 inch pipe with defects on the inner surface (the results shown are obtained using the approximation function for Q). The difference $(1-\chi)$ is relatively high in the case of a 3 inch pipe with the defect on the inside. The coefficient $(1-\chi)$ becomes smaller at deeper defects because R_{mR} tends to R_{mL} in Equation 5.2; it also decreases at large diameter because the pipe tends to the plate case where the position (top or bottom) does not influence the reflection behavior ($R_{mR} \simeq R_{mL}$ in Equation 5.2).

5.5.4 Reflection maps for axisymmetric case

The results shown below are reflection maps for axisymmetric defects in the reference pipe (3 inch schedule 40 with defects on the outer surface of the pipe).

Figure 5.14 shows a 3D plot of the reflection coefficient for T(0,1) at 35 kHz incident on an axisymmetric rectangular notch of varying depth and axial extent (the results are obtained using FE). It is clear from Figure 5.14 that the reflection monotonically increases with axial extent at constant depth and it also increases with depth at constant axial extent.

Figure 5.15 shows a color map of the 3D reflection plot in Figure 5.14. The lines in Figure 5.15 are isolines of constant reflection coefficient as described by the color bar. The isolines in Figure 5.15 show that the reflection coefficient obtained at a certain depth and axial extent is also obtained at smaller depth and larger axial extent, therefore suggesting that it is important to know the axial extent of the defect in order to interpret the reflection from corrosion patches (the depth of a defect is of course more critical than its axial extent). However, it is possible to give an interpretation even though the axial extent is unknown (as always in practical applications) and this will be explained in the next section.

The same behaviour noticed when using T(0,1) is observed when L(0,2) is incident on an axisymmetric defect. This is described in Figure 5.16. In fact, to a first approximation the reflection from axisymmetric notches of the same depth (b%) and axial extent (a%) is the same for T(0,1) and L(0,2). However it is important to stress that the phase velocity of the two axisymmetric modes considered here is rather different (3.3 m/ms for T(0,1) and 5 m/ms for L(0,2). Since for a given absolute defect size the axial extent a% is inversely proportional to the wavelength of the excited wave ($a\% = \frac{a}{\lambda} \cdot 100$), a defect (constant a) tested at constant frequency has an axial extent (a%) which decreases with the velocity of the excited mode. Therefore if we test a localized corrosion defect and we compare the sensitivity of L(0,2) and T(0,1) at the same frequency, the reflection from L(0,2) is smaller because the axial extent a% of the defect is smaller. In order to obtain the same sensitivity to corrosion defects using L(0,2) and T(0,1), it is necessary to use L(0,2) at higher frequency ($f_{L(0,2)} \sim 1.8 f_{T(0,1)}$).

5.6 Effect of non-dimensional parameters on the reflection from part-depth part-circumference notches.

The effect of axial extent (a%), defect depth (b%) and circumferential extent (c%) has been reported in section 5.4. The circumferential extent of a defect can be estimated from the ratio of the first order flexural mode reflection to that of the axisymmetric mode as described in Figure 5.6. As already mentioned in 5.4, the limit of this criterion to quantify the circumferential extent of a defect is the low sensitivity to changes of the circumferential extent at small circumferential extents.

The effect of defect depth and axial extent has also been analyzed, the reflection from a notch increasing at constant depth with axial extent (from 5% to 25%) and at constant axial extent with depth.

It was shown earlier that the minimum reflection coefficient from a notch is obtained at about 5% axial extent at each depth of defect (Rmin in Figure 5.7) and the maximum reflection coefficient is obtained at about 25% axial extent (Rmax

in Figure 5.7). It was also shown that the maximum reflection coefficient of an axisymmetric defect is only dependent on the depth of the defect (provided that a wide frequency range is used). Figure 5.17 shows the minimum and maximum value of reflection coefficient with varying defect depth when T(0,1) is excited a 35 kHz in a 3 inch schedule 40 pipe. Clearly the difference between minimum and maximum is considerable and if performing only single tests, any value in between could potentially be obtained. Thus a criterion to distinguish between a deep short defect (severe corrosion) and a shallow and long defect (medium corrosion) is needed. This is proposed later in this section after showing the reflection maps for part-circumference, part-depth notches.

5.6.1 Reflection maps for part-depth, part-circumference case

Figure 5.17 can be simply scaled with the circumferential extent to obtain the trend of minimum and maximum of reflection with varying defect depth and circumferential extent. The results are shown in Figures 5.18 and 5.19 respectively. Figure 5.18 shows a colour map of the minimum reflection of T(0,1) for rectangular notches when T(0,1) is excited at 35 kHz in a 3 inch pipe. Figure 5.18 shows that the same reflection coefficient can be obtained at small circumferential extent for a deep defect or at large circumferential extent for a shallow defect. In this case, it is possible to discriminate between the two example cases because the information on the circumferential extent can be obtained independently using Figure 5.6. Figure 5.19 shows the color map of the maximum reflection coefficient when T(0,1) is excited at 35 kHz on a 3 inch pipe. The same observations as for Figure 5.18 apply to this case.

Therefore if we assume that a wide frequency bandwidth can be used, the maximum reflection coefficient may be obtained and consequently Figure 5.19 would be enough to classify the severity of a defect. If the frequency range of the test is limited, it is wise to use the graph in Figure 5.18 even though we risk overestimating the severity of the defect.

It is important to say here that the criterion of using the maximum reflection coefficient at a defined depth and circumferential extent is valid even when the shape is a more realistic stepped notch (see Figure 5.2b). In Figure 5.20 we compare the reflections from a rectangular and a stepped notch in a 3 inch schedule 40 pipe when

the defect is on the outer wall of the pipe and T(0,1) is incident at 35 kHz. The depth of the rectangular notch is 50% of the thickness and the maximum depth of the stepped notch is 50%. The axial extent of the stepped notch is measured at its mean depth. From Figure 5.20 it is clear that in both geometries the constructive interference phenomenon appears and it is also clear that the maximum reflection coefficient obtained for the stepped notch is close the one obtained for the rectangular notch (about 20% difference).

Figures 5.21 and 5.22 show zooms of Figure 5.18 and 5.19 respectively in the low reflection coefficient [0-0.1] range, which is also the region of interest for many real corrosion defects.

An explanatory example is also shown in Figures 5.6 and 5.22. Let us suppose that the measured reflection coefficient of the incident axisymmetric mode is 0.06 and the F/A ratio is 0.95. From the F/A ratio and using Figure 5.6 it is possible to estimate the circumferential extent of the defect as about 15%. From the intersection between the curve at constant reflection 0.06 (in Figure 5.22) and a line at 15% circumferential extent we estimate the depth of the defect to be about 30% of the thickness.

5.7 Discussion.

Using the universal maps of reflection coefficient, it is possible to check what sizes of defect are detectable using this technique. The practical implementation of the screening method enables a reflection coefficient of 2% to be measured reliably in a relatively clean pipe. This value is dependent on the signal to noise ratio for the specific application (site, pipe diameter, pipe condition) and it also depends on the calibration of the system which is done by using reference reflectors such as welds. Therefore the 2% reflection limit is an indicative value rather than an absolute limit.

In practice when it is possible to use a wide frequency range, the map in Figure 5.22 can be used and the minimum 2% reflection is obtained at the circumferential extent - depth combinations shown in Table 5.2. As a first approximation it is possible to neglect the correction due to pipe size and defect location and therefore to utilize Figure 5.22 for any pipe size.

Therefore from Figure 5.22 it can be deduced that a severe defect (depth bigger than 50% of the thickness) can be identified (has reflection bigger than 2%) when it extends at least along 3% of the circumference. The 3% of circumference is a relatively small defect when considering small pipe sizes but it is rather large for large pipe sizes (e.g. 3% of the circumference is about 5 mm in a 2 inch pipe and it is about 60 mm in a 24 inch pipe). On the other hand reflections smaller than 2% can usually be identified in large pipe sizes (coherent noise is usually small due to the fact that roughness due to generalized corrosion is small compared to the large wall thickness) therefore suggesting that defects with a circumferential extent smaller than 3% can be detected.

5.8 Conclusions

A quantitative study has been performed to investigate the effect of defect size on the reflection from guided waves in pipes. Maps of reflection coefficient as a function of the circumferential extent and depth of the defect have been presented for a 3 inch schedule 40 steel pipe with defects on the outer surface of the pipe and T(0,1) incident at 35 kHz and a correction factor for different pipe sizes,location of defect in the cross section, ultrasonic guided wave mode and excitation frequency have been presented.

As already established in practical testing, the information on the circumferential extent of the defect is obtained from the mode conversion using the ratio Flexural/Axisymmetric (F/A).

The reflection coefficient from defects is dependent on the axial extent of the defect compared with the wavelength of the excited mode. However, it is possible to assume that its minimum and maximum values are constant at a given defect depth and circumferential extent (the minimum being the value of reflection at 5% of the axial extent and the maximum being the reflection at 25% of the axial extent).

The use of the maps of minimum and maximum reflection coefficient traced as a function of the circumferential extent and depth of the defect enable an estimate of the depth of the defect.

The map for the maximum reflection coefficient can be used when a wide fre-

quency range is used for a test at a single location. The constructive interference phenomenon which leads to a maximum of the reflection has been proven to appear both in rectangular notch shapes and in more realistic stepped notches which more closely approximate rough corrosion patches. The map of the minimum reflection coefficient can be used when only a narrow frequency bandwidth is allowed, though an overestimation of defect size is typical in this case.

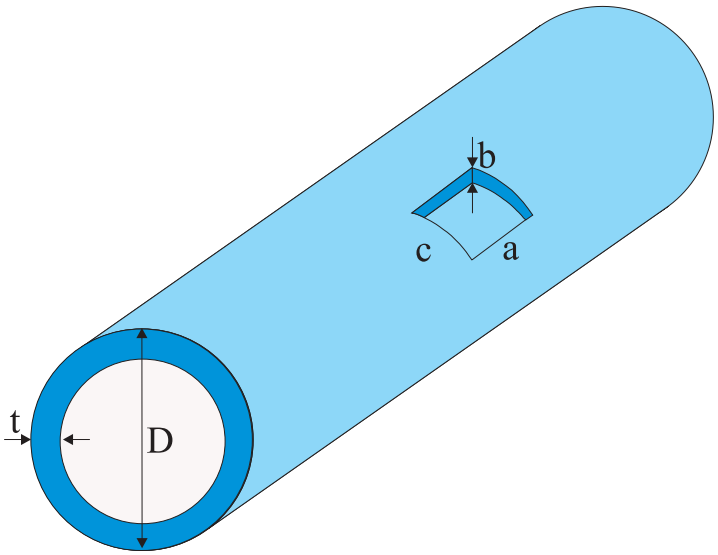

Figure 5.1: Geometrical parameters for pipe and defect size.

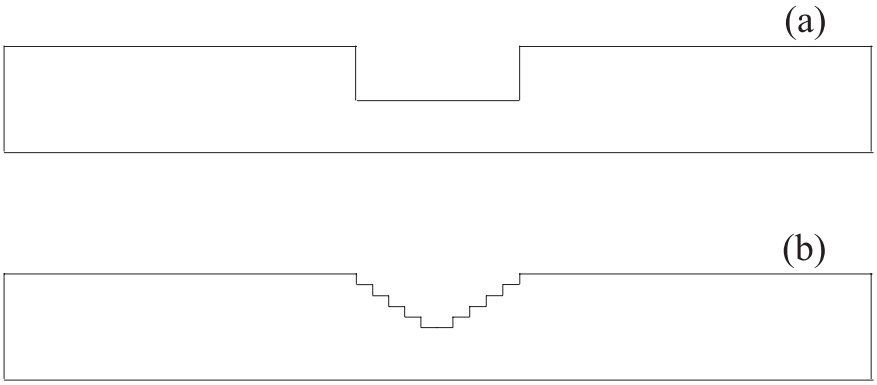

Figure 5.2: (a) Schematic of rectangular notch; (b) Schematic of stepped notch.

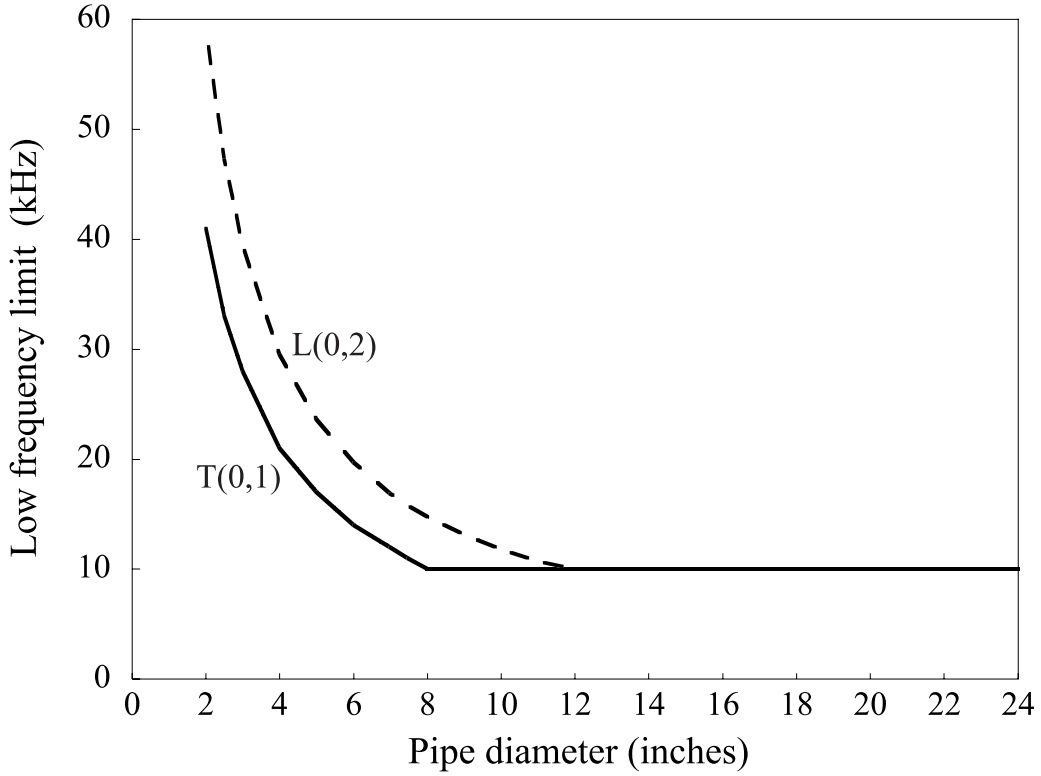

Figure 5.3: Low frequency limits of the investigation.

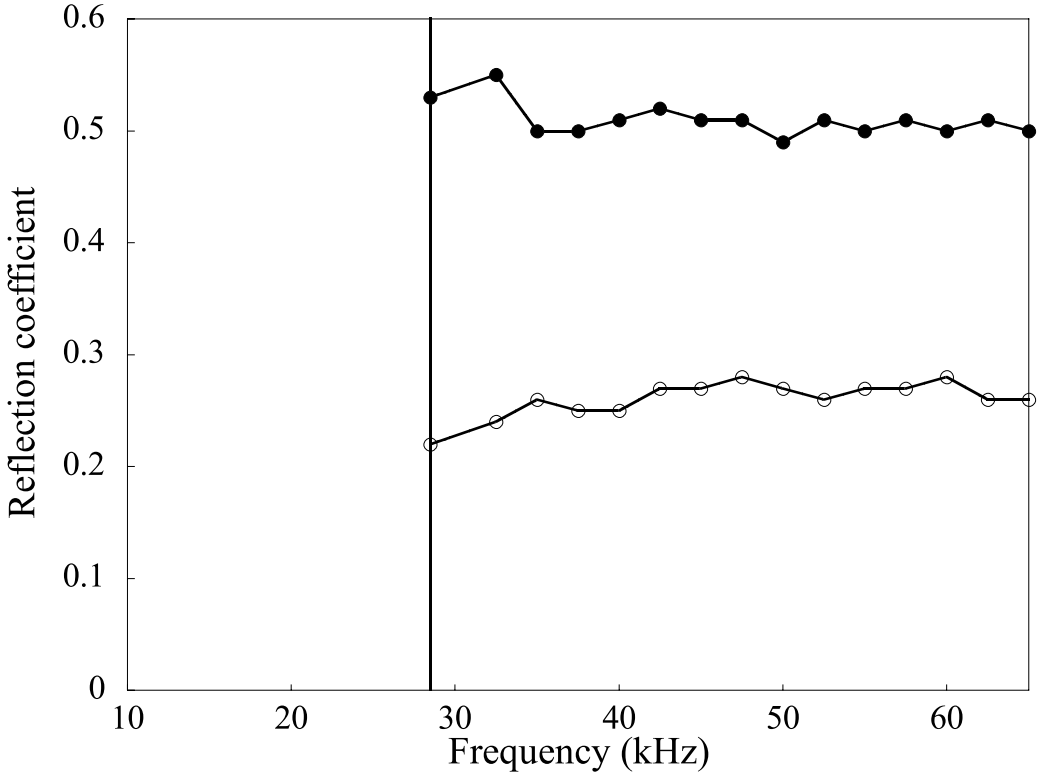

Figure 5.4: T(0,1) reflection coefficient for through thickness cracks in a 3 inch schedule 40 pipe when the crack extends over 25% (empty circles) and 50% (full circles) of the circumference. The vertical solid line indicates the fD limit.

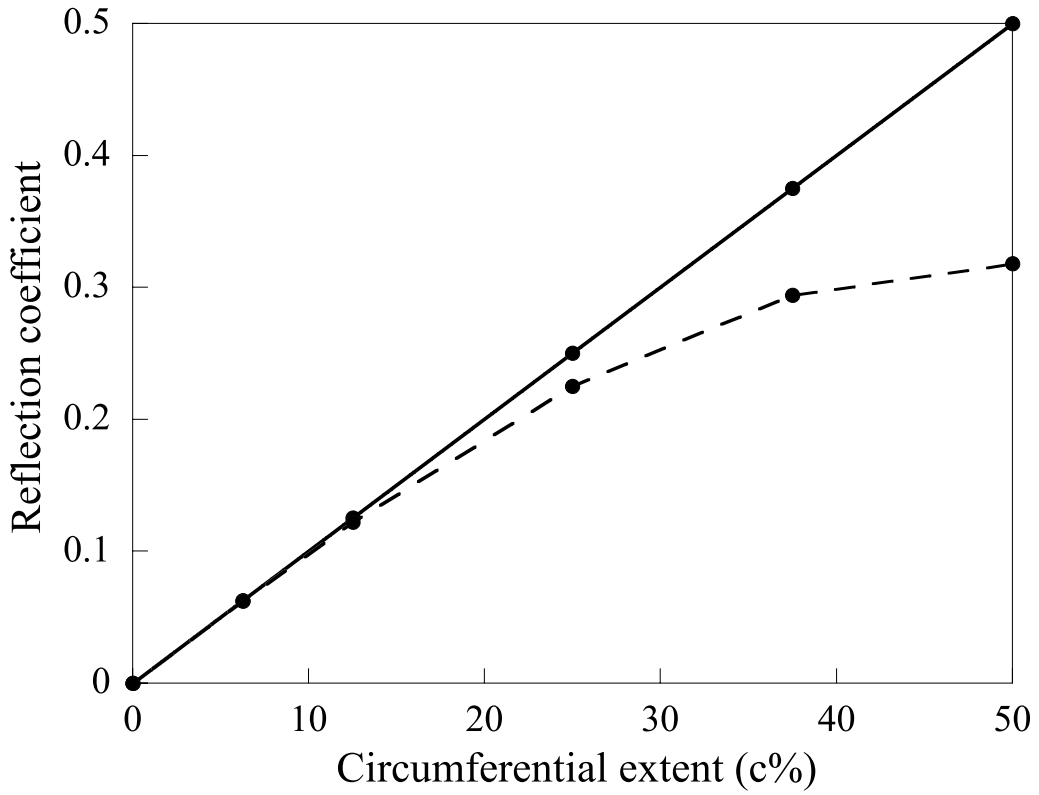

Figure 5.5: Reflection coefficient for axisymmetric (solid line) and flexural mode of the first order (dashed line) as a function of the circumferential extent of a through thickness defect.

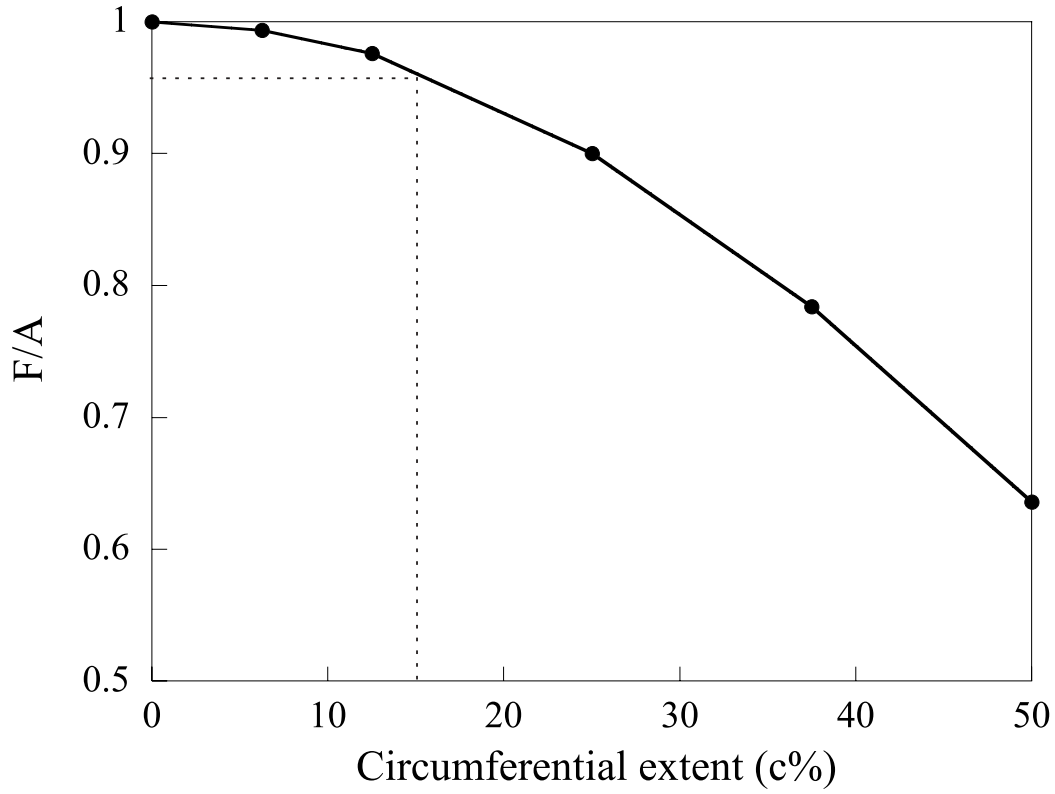

Figure 5.6: Ratio between flexural (F) and axisymmetric (A) mode reflection at varying circumferential extent of defect (c%).

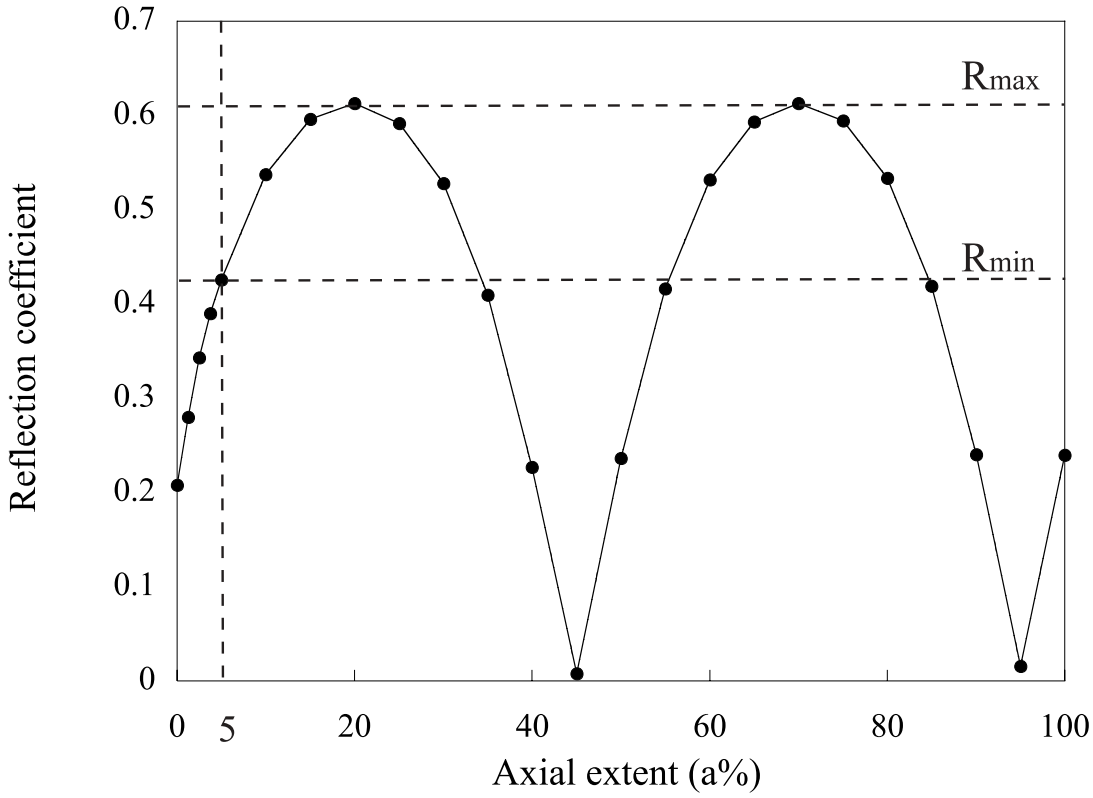

Figure 5.7: Reflection coefficient for axisymmetric notches of varying axial extent. Results are for T(0,1) incident on a 24 inch pipe at 65 kHz and b=0.5t (50% depth notch).

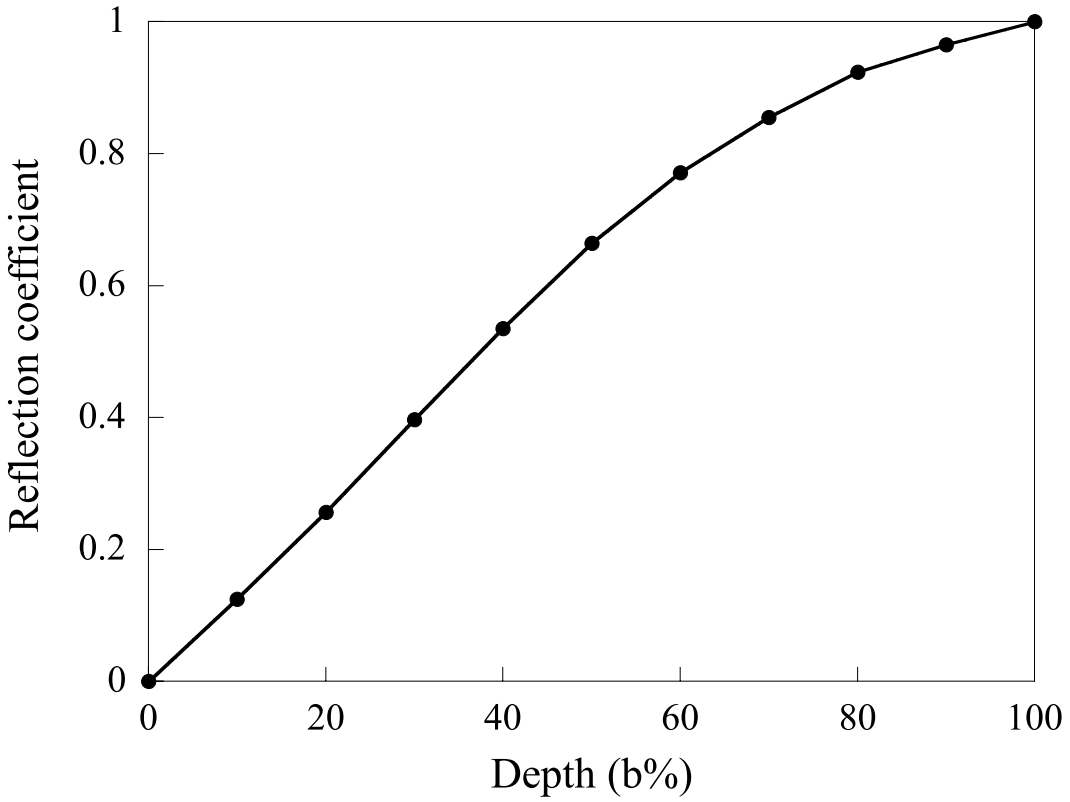

Figure 5.8: Reflection coefficient for axisymmetric notches of varying depth and constant axial extent(25%). Results are for T(0,1) incident on a 3 inch pipe at 55 kHz.

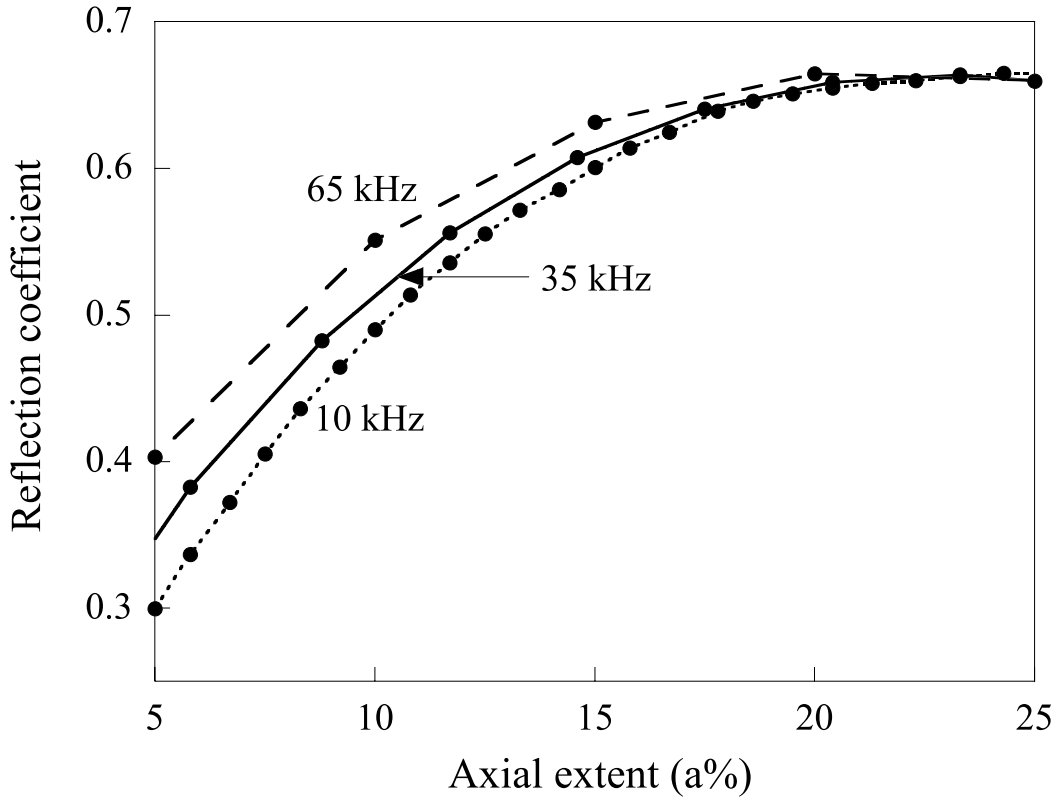

Figure 5.9: Variation of reflection coefficient with axial extent of the notch at different frequencies. Results are for a 3 inch pipe schedule 40 steel pipe with T(0,1) incident on an axisymmetric 50% depth notch. The circles indicate the values at which the reflection coefficients were computed in the FE analysis.

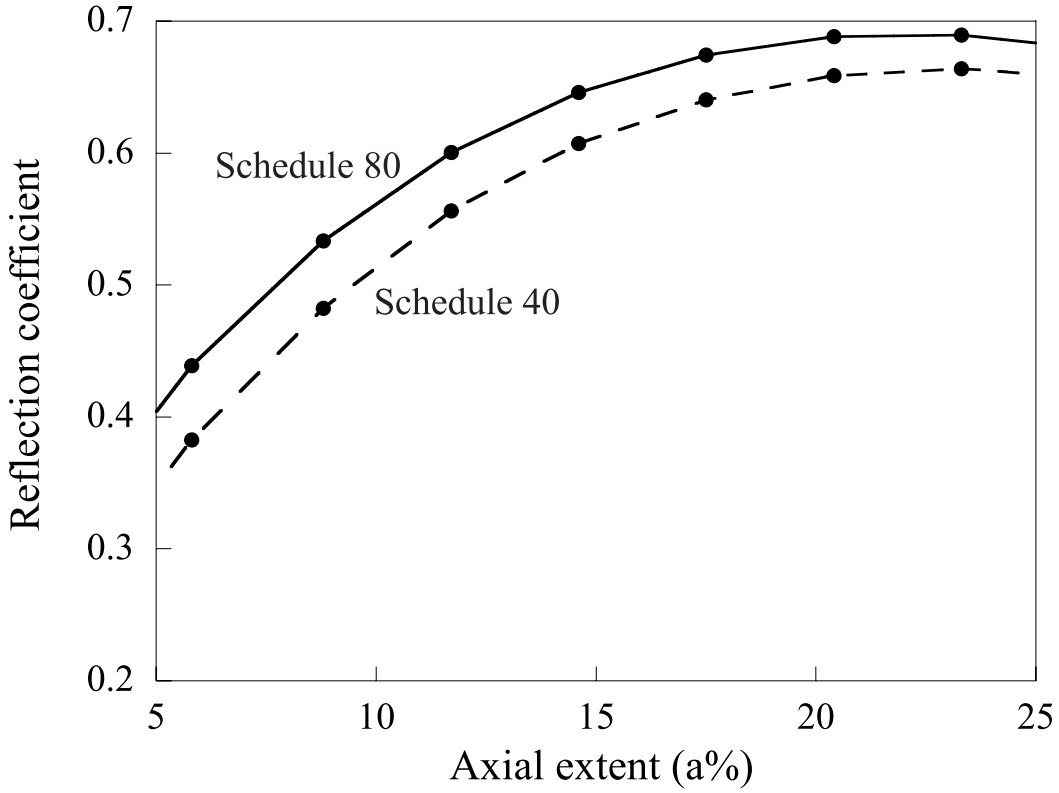

Figure 5.10: Variation of reflection coefficient with axial extent of the notch. Results are for a 3 inch pipe with T(0,1) incident on an axisymmetric 50% depth notch at 35 kHz.

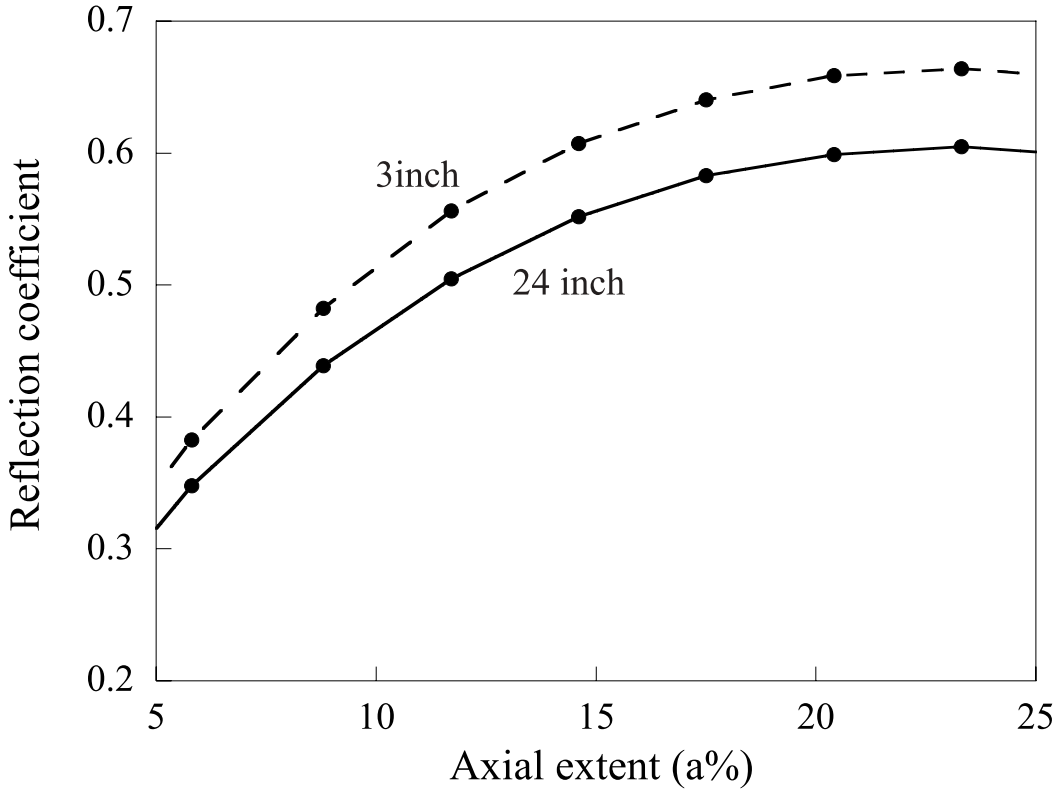

Figure 5.11: Variation of reflection coefficient with axial extent of the notch in different pipe sizes. Results are for T(0,1) incident at 35 kHz on an axisymmetric 50% depth notch.

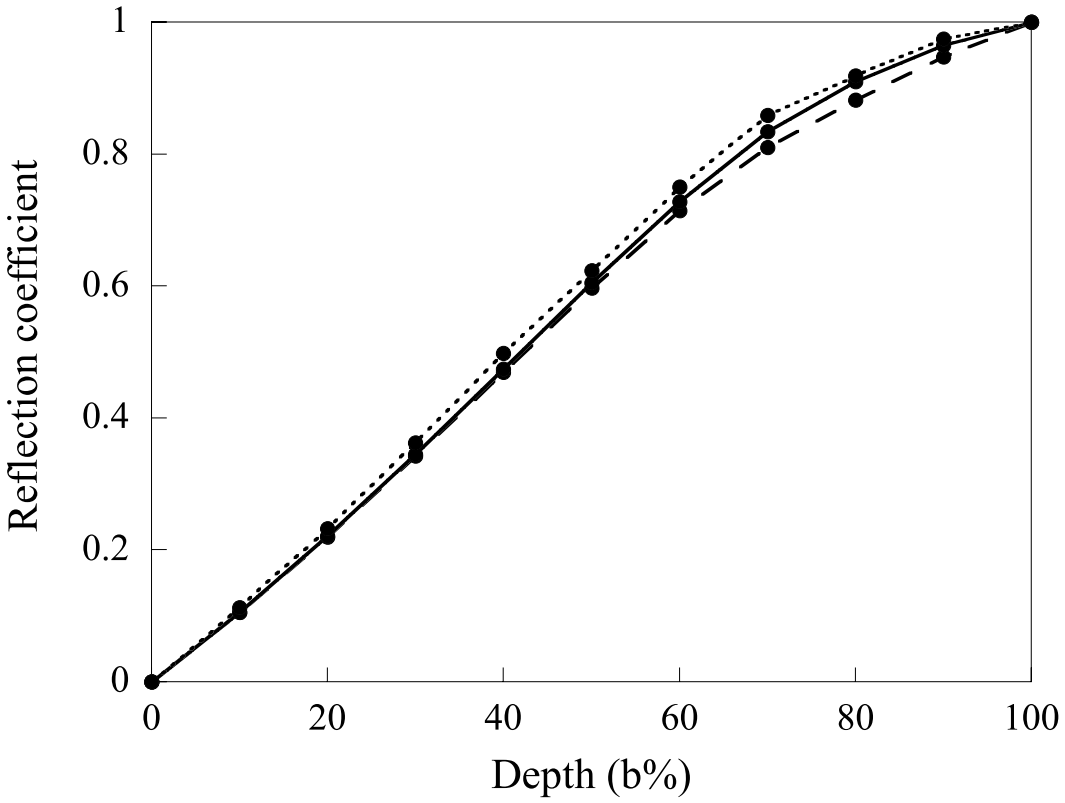

Figure 5.12: Variation of maximum reflection coefficient with depth of the notch. Results are for T(0,1) incident at 35 kHz on a 24 inch schedule 40 pipe with a rectangular notch. The dashed and solid lines indicate the FE results obtained for T(0,1) and L(0,2). The dotted line is our approximation function.

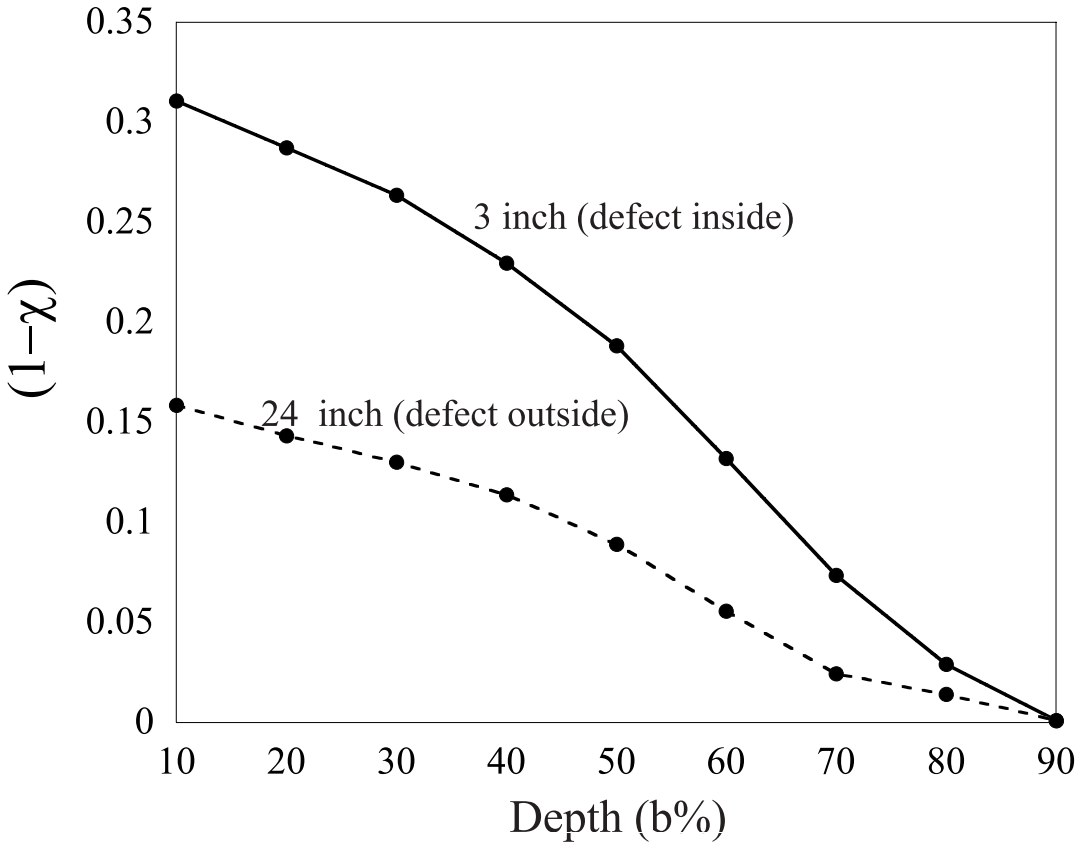

Figure 5.13: Estimate of the difference between Q_0 and Q_x where Q_0 is derived for a 3 inch schedule 40 pipe with defects on the outer surface (reference pipe) and Q_x is derived for a 3 inch schedule 40 pipe with defects on the inner surface (solid line) and also for a 24 inch schedule 40 pipe with defects on the outer surface (dashed line).

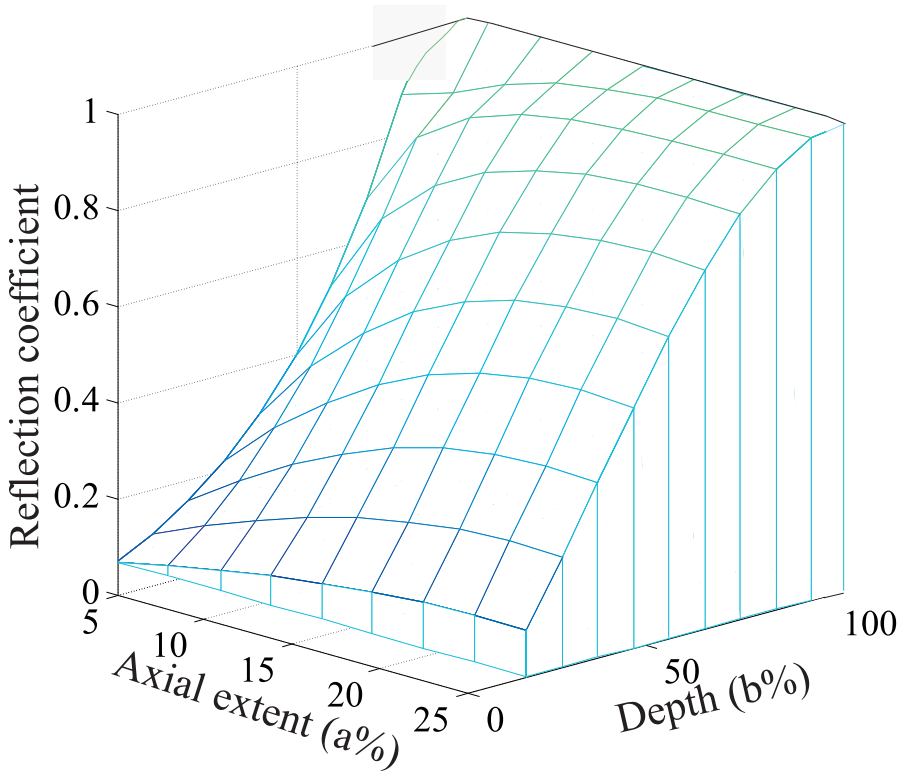

Figure 5.14: 3D graph of reflection coefficient from axisymmetric defects with varying depth and axial extent. Results are for T(0,1) incident at 35 kHz on a 3 inch schedule 40 pipe with a rectangular notch.

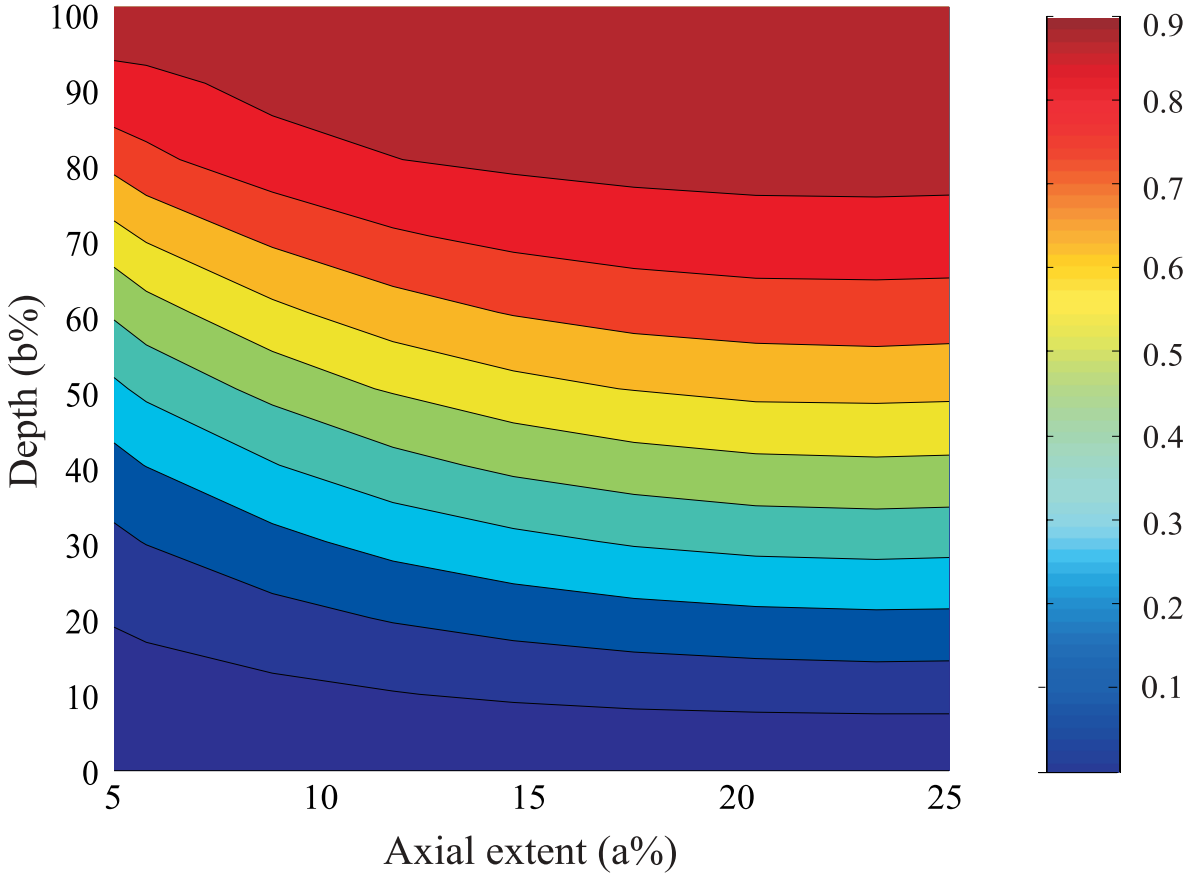

Figure 5.15: Color map of reflection coefficient from axisymmetric defects with varying depth and axial extent. Results are for T(0,1) incident at 35 kHz on a 3 inch schedule 40 pipe with a rectangular notch.

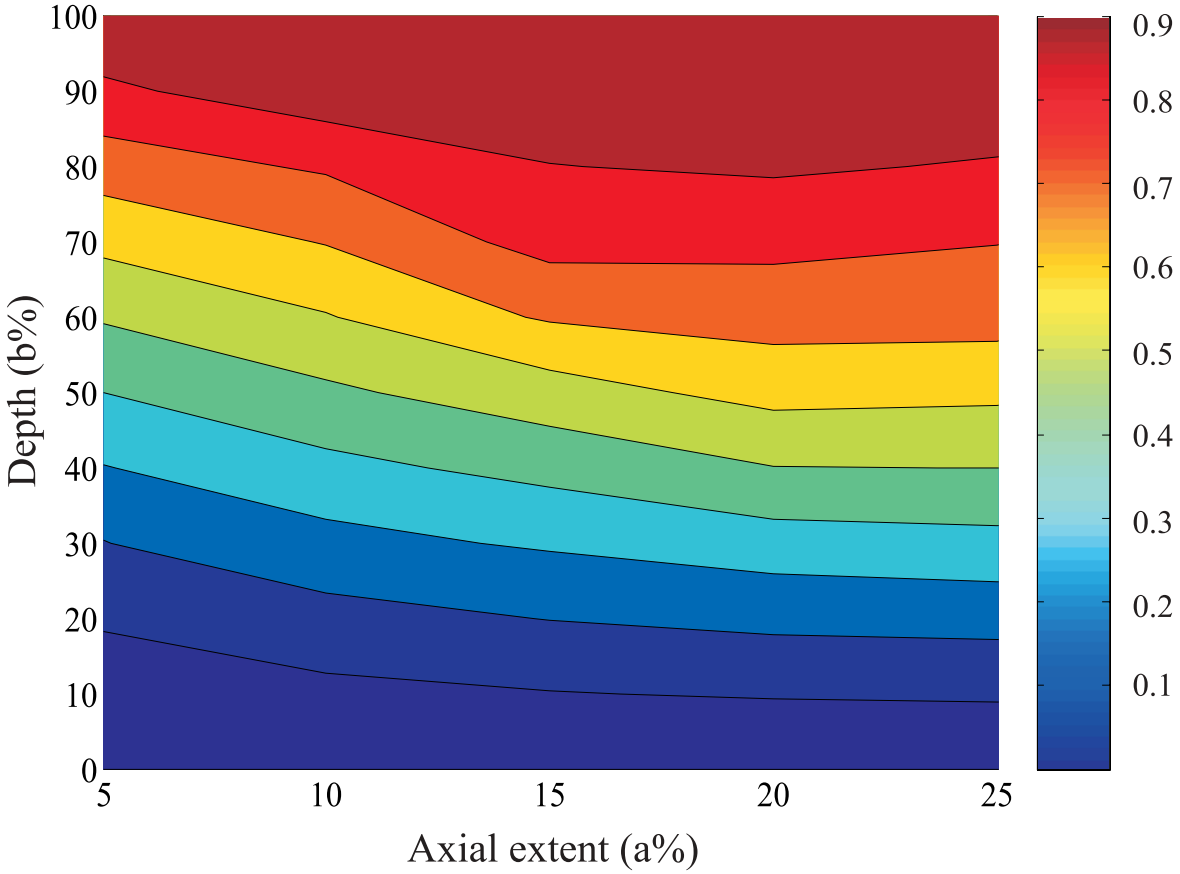

Figure 5.16: Color map of reflection coefficient from axisymmetric defects with varying depth and axial extent. Results are for L(0,2) incident at 35 kHz on a 3 inch schedule 40 pipe with a rectangular notch.

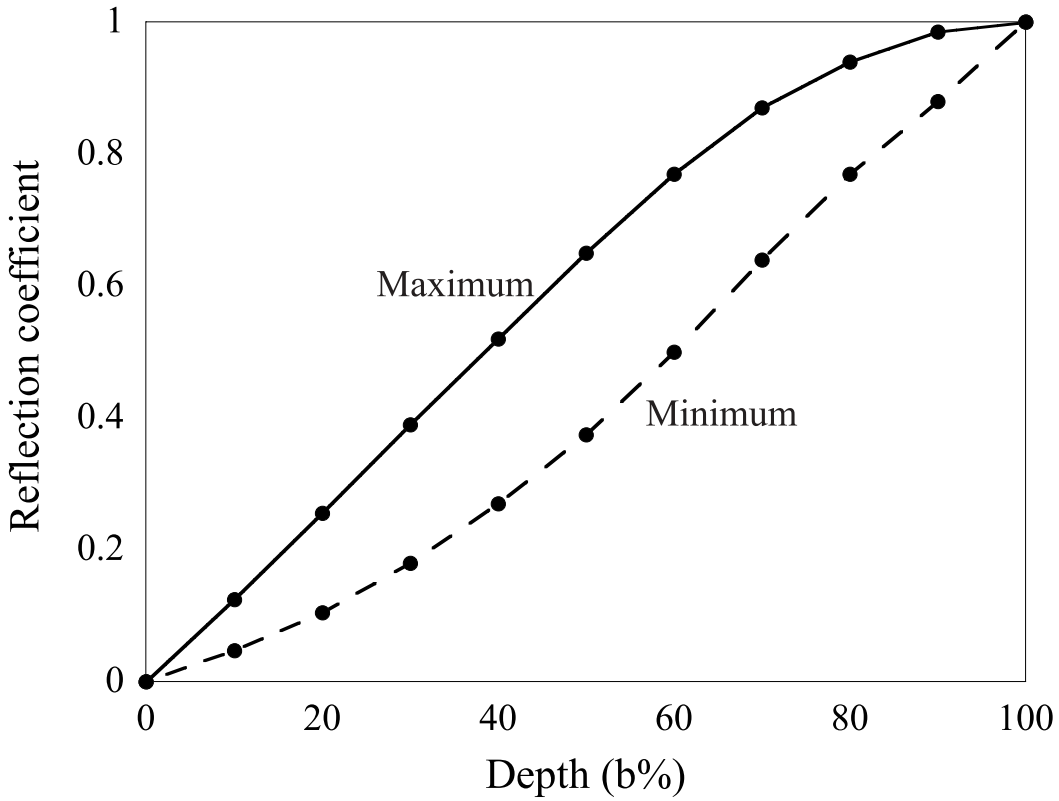

Figure 5.17: Minimum and maximum reflection from axisymmetric defects with varying depth. Results are for T(0,1) incident at 35 kHz on a 3 inch schedule 40 pipe with a rectangular notch.

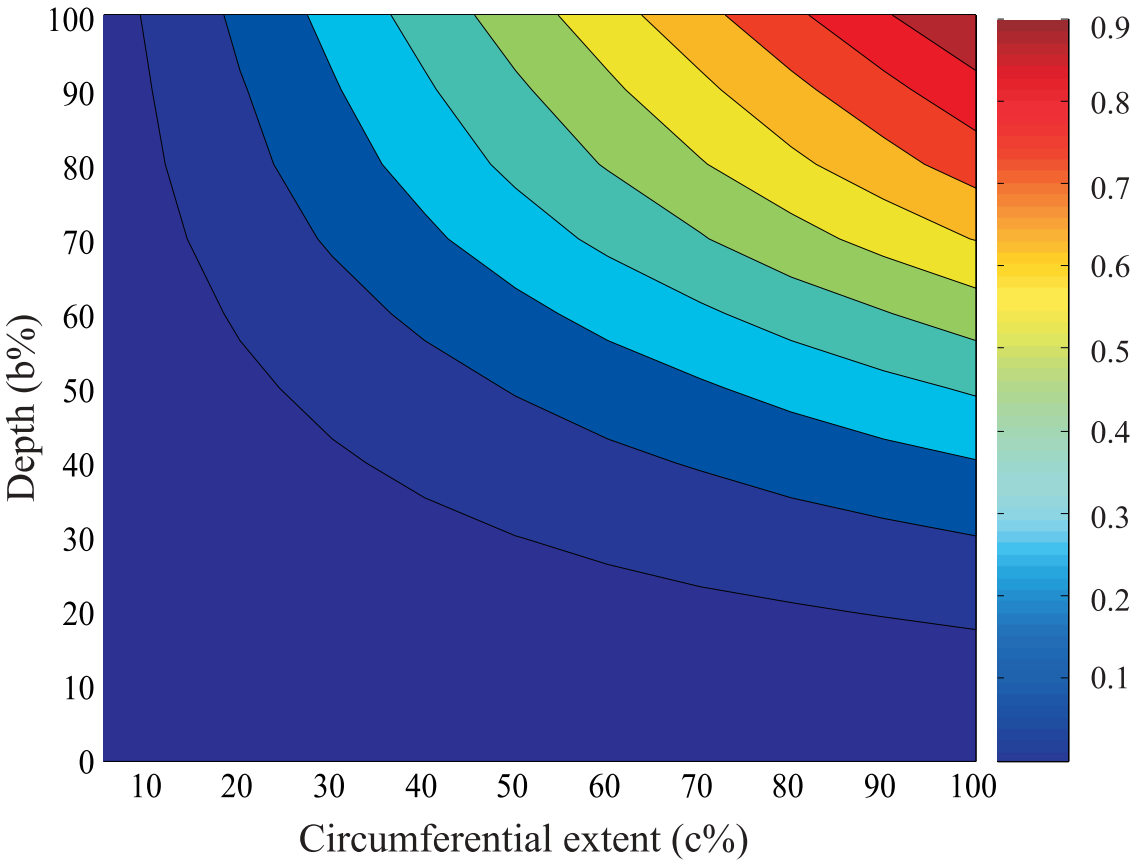

Figure 5.18: Minimum reflection from defects with varying depth and circumferential extent. Results are for T(0,1) incident at 35 kHz on a 3 inch schedule 40 pipe with a rectangular notch.

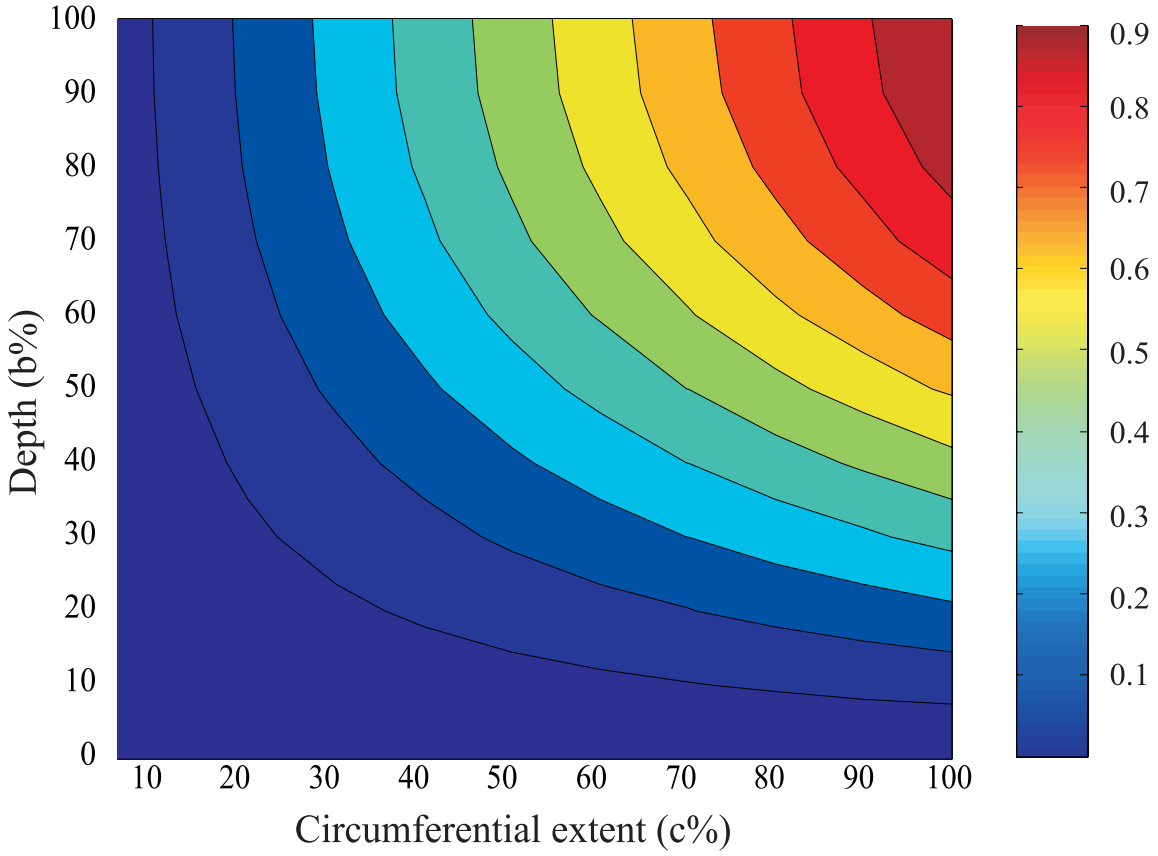

Figure 5.19: Maximum reflection from defects with varying depth and circumferential extent. Results are for T(0,1) incident at 35 kHz on a 3 inch schedule 40 pipe with a rectangular notch.

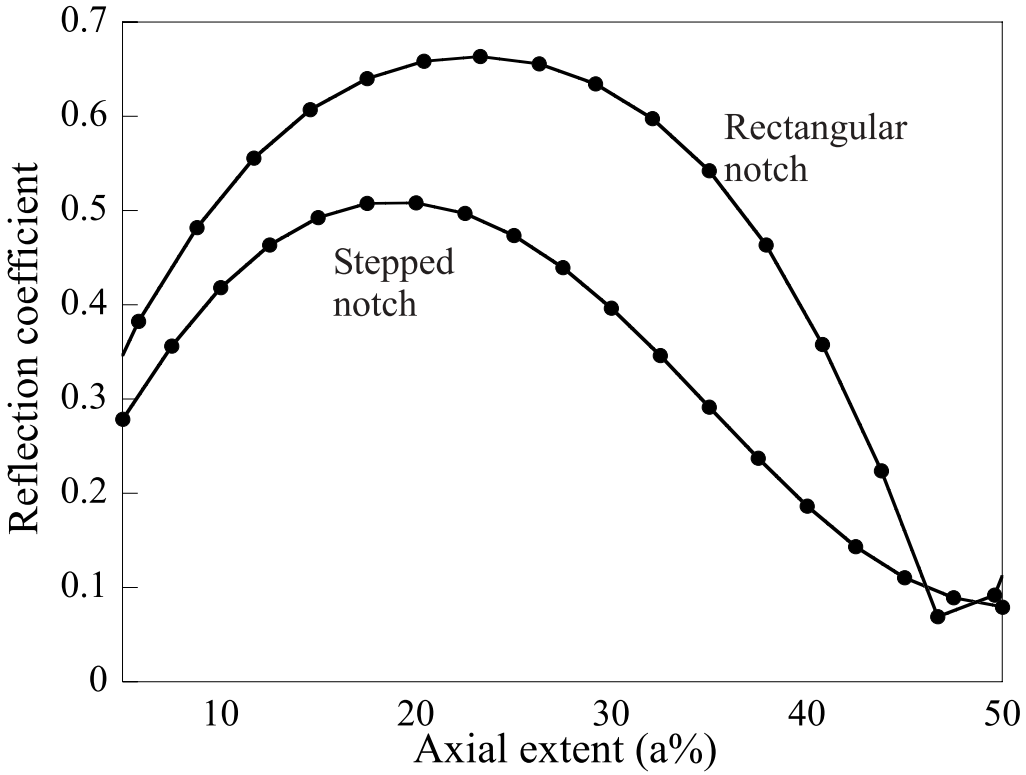

Figure 5.20: Variation of reflection coefficient with axial extent of the notch. Results are for T(0,1) incident at 35 kHz on axisymmetric stepped and rectangular notches with 50% maximum depth. The axial extent a% for the stepped notch is the mean axial extent.

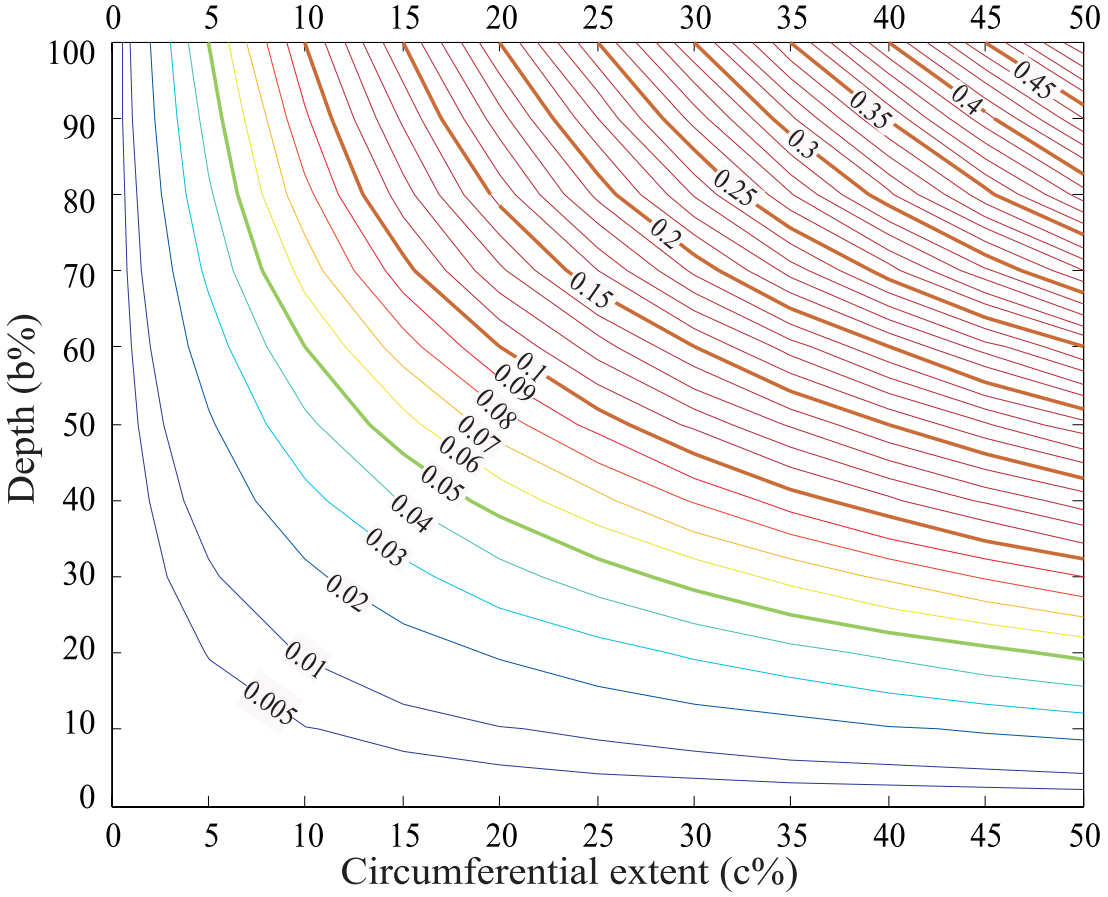

Figure 5.21: Minimum reflection in the low reflection coefficient region [0-0.1] from Figure 5.18. From the reflection of the axisymmetric mode, the curve at constant reflection is defined. From the ratio F/A, the circumferential extent is derived. The ordinate of the crossing point gives an estimate of the defect depth.

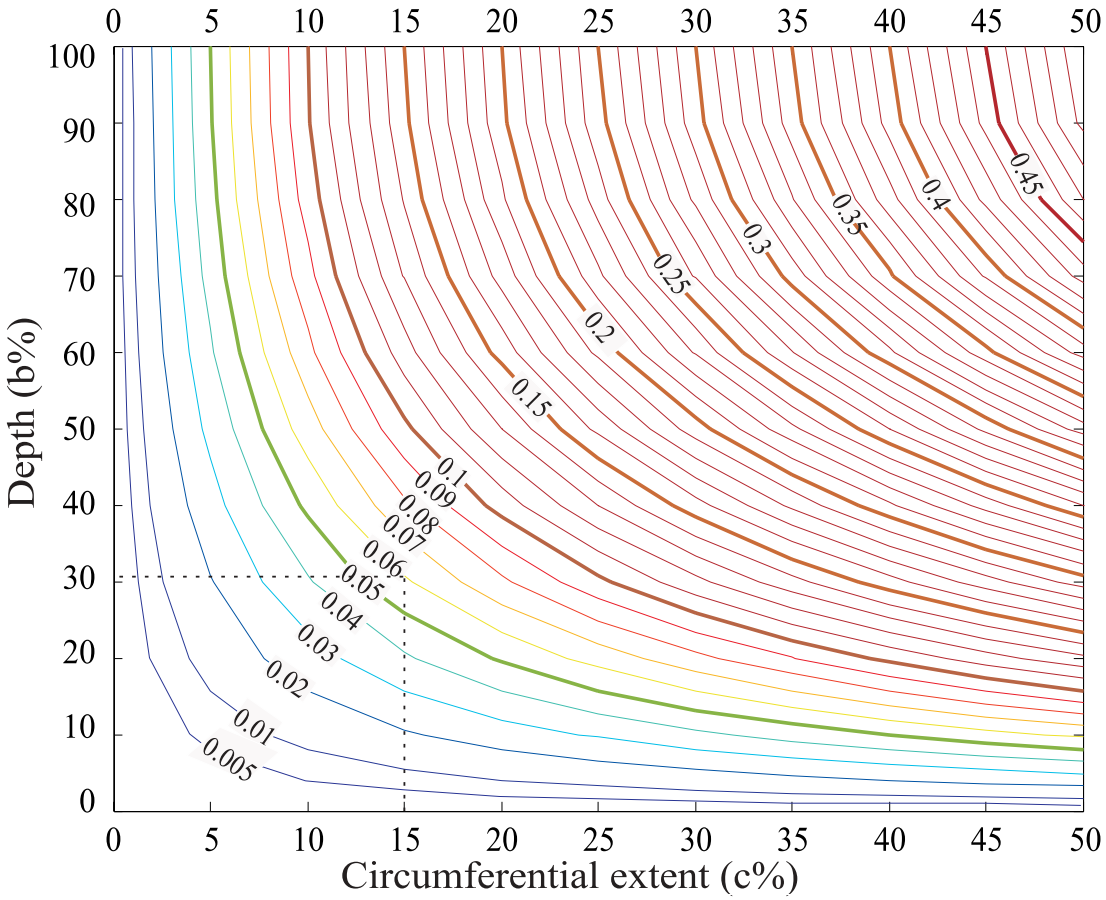

Figure 5.22: Maximum reflection in the low reflection coefficient region [0-0.1] from Figure 5.19. From the reflection of the axisymmetric mode, the curve at constant reflection is defined. From the ratio F/A, the circumferential extent is derived. The ordinate of the crossing point gives an estimate of the defect depth.

	5% of λ (mm)	
Frequency (kHz)	L(0,2)	T(0,1)
10	28	16
20	14	8
30	9	5
40	7	4
50	6	3
60	5	3
65	4	3

Table 5.1: Axial extent (a) of defect at fixed percentage axial extent (a%=5%) as a function of frequency for both L(0,2) and T(0,1) modes.

Circumferential extent (c%)	Depth (b%)
2	100
3	51
4	39
5	31
10	16
20	8
30	6
40	4
50	3

Table 5.2: Circumferential extent-defect depth combinations for which the maximum reflection of the axisymmetric wave is 2%.

Chapter 6

The effect of bends in a pipe network

The practical testing of pipes in a pipe network has shown that there are issues concerning the propagation of ultrasonic guided waves through bends. It is therefore desirable to improve the understanding of the reflection and transmission characteristics of the bend.

Firstly, the dispersion curves for toroidal structures have been calculated using a finite element method, as there is no available analytical solution. Then the factors affecting the transmission and reflection behavior have been identified by studying a straight-curved-straight structure both numerically and experimentally. Finally a generalization of the results obtained is proposed and conclusions are drawn about the behavior of guided waves in curved structures.

6.1 Background on guided waves in curved structures

The study of curved waveguides has been a topic of interest for many years. Lord Rayleigh in 1912 reported on the phenomenon of the "whispering gallery" [104] which effectively was the first and best known experience of propagation in curved waveguides. Thereafter a series of studies followed on the subject of wave propagation in structures with constant curvature [105, 106, 107, 108, 109, 110, 111] and

structures with slowly varying geometry [112, 113]. Most of the work on curved structures has been focused on the study of surface waves since this is of particular interest in geophysical applications but in recent years Wilcox [108] and Liu and Qu [106] have investigated the wave propagation in curved plates starting from the exact formulation of the dispersion relation. Beard [109] continued the work started by Wilcox, presenting for the first time the mode shapes for curved plates. Detailed high-frequency asymptotic analysis of both SH and Lamb-type circumferential waves in an elastic annulus was carried out by Gridin et al. [111]. In this work several types of modes that do not exist in a straight plate were identified and the ray structures of the modes was revealed.

A more practical approach was offered by Drumheller [114] who investigated the attenuation of sound waves in drill strings. In this work the effect of curvature on the attenuation was explained in terms of the interaction of extensional and bending waves.

6.2 Guided waves in toroidal stuctures

The approach of Wilcox [108], Liu and Qu [106] and Beard [109] was to use potential functions to separate the displacement field and subsequently separate the solution of the Helmholtz differential Equations 2.8 into the product of functions of each of the spatial dimensions. This simple approach is not valid when dealing with geometries such as curved pipes where the toroidal geometry of the structure implicitly requires the use of toroidal coordinates (see Figure 6.1). In fact the Helmholtz differential equations are separable only when a conformal transformation of coordinates of 2.8 from (x,y) to a new coordinate system (ξ_1, ξ_2) is such that in defining the complex variables $z = x + iy$ and $w = \xi_1 + i\xi_2$, the condition below is satisfied:

$$(\frac{dz}{dw} \cdot \frac{d\overline{z}}{d\overline{w}}) = f_1(\xi_1) + f_2(\xi_2) \tag{6.1}$$

where f_1 is a function of ξ_1 alone and f_2 is a function of ξ_2 alone and $\overline{z}$ and $\overline{w}$ are the complex conjugates of z and w respectively (see Morse and Feshbach [17] for more details on the separability condition). The condition expressed by equation 6.1 is met when the coordinate system is of a confocal ellipsoidal or paraboloidal system; condition 6.1 is not met in both bispherical and toroidal coordinates [115]. It is

therefore clear that an alternative approach must be used to derive the dispersion relations for toroidal structures.

Since this PhD project was aimed at improving the understanding of guided wave propagation through pipes with bends, we have opted for a computational approach rather than a mathematical approach. An FE modal solution (described in detail in the next paragraph) was used to derive the dispersion curves for toroidal structures and an FE time marching procedure was used to study the straight-curved-straight interaction.

6.3 Use of a Finite Element method to obtain dispersion curves for toroidal structures

The FE method can be used for the purpose of obtaining the dispersion curves for a defined structure. The approach used is very similar to the approach used in computational modal analysis. When the FE method is used to solve the free vibration problem the only assumption which is made is that the external force is zero as in Equation 2.19.

The form of 2.19 suggests that we express the solution as $u = e^{i\omega t}\phi$ where ω is the circular frequency and ϕ defines the displacement pattern. Using this expression for u, 2.19 transforms to

$$(k - \lambda M)\phi = 0 \tag{6.2}$$

$$\lambda = \omega^2 \tag{6.3}$$

This is the classical eigenvalue problem and there are a number of solution schemes available to solve it. In general there are n values (eigenvalues) which satisfy 6.2 and 6.3 and in this case all n values are positive (when both k and M are positive definite). Each eigenvalue represents one of the possible modes. Each eigenvalue corresponds to one eigenvector and one frequency. The values of the elements of the eigenvector are the displacement values at each node of the defined mesh for the studied mode (the one to which the eigenvalue refers).

The vibration analysis of toroidal shells was carried out by many researchers in order to determine the dynamic behaviour of structures such as curved pipes

[116, 117, 118, 119]. These investigations used shell theory to find the vibrational modes of toroidal structures under different boundary conditions.

An FE technique to find the modal properties of structures has been used by Gavric [120] to compute the dispersion curves in a straight waveguide with an arbitrary cross-section. In this technique the displacement field is defined by two terms, the first takes into account the mode shape of the cross section and the second (a complex exponential) prescribes its wave nature in the propagation direction. Therefore the polynomial approximation of the displacement field along the waveguide used in 3D FE analysis is avoided and the 3-D model of a waveguide with finite length can be substituted by a 2D model of the cross section of the waveguide. At each frequency, the modal solution of the Hamiltonian of an infinitesimal element of the waveguide is found and subsequently the dispersion curves are traced. A modification to Gavric's method was introduced by Wilcox et al. [121] who used axisymmetric models to calculate the wave properties of solids with arbitrary shapes. Wilcox created a two-dimensional mesh representing the cross section of the structure and traced the propagating modes for such a structure.

The modal solution was used by both Gavric and Wilcox in order to find the dispersion curves in straight waveguides. The method proposed by Wilcox is essentially easier to apply because it only requires the use of standard FE packages whereas Gavric's method involves the use of a dedicated computational scheme. Moreover, since Wilcox had studied very shallow curved structures to approximate straight waveguides, this method was identified as the most suitable to study the curved waveguides which are the subject of this investigation.

By simply rotating the mesh for a circular disc with a central hole around the axis of symmetry (Figure 6.2a) we can create a toroid (Figure 6.2b). The mesh generation of toroids with different bend radii could be practically achieved by regulating the distance of the centre of the disc from the axis of symmetry. The wave nature of the displacement with respect to the angular coordinate ψ in Figure 6.1 was simply assigned by defining the harmonic number (n) which represents the number of wavelengths along 360 degrees of the coordinate ψ (see Figure 6.1). For more details on the suitability of this model to represent the displacement field in waveguides, refer to Wilcox et al. [121]. Once the mesh was generated and the harmonic number

was defined, the wavelength was implicitly assigned:

$$\lambda = \frac{2\pi R_{BM}}{n} \tag{6.4}$$

where n is the harmonic order and R_{BM} is the bend radius of the toroid.

At each wavelength defined by one harmonic number a series of eigensolutions corresponding to different modes were found using a modal solution FE algorithm. From the frequency value of each eigensolution the phase velocity can be derived using:

$$V_{ph} = \lambda \cdot f \tag{6.5}$$

Therefore one (frequency, phase velocity) value is found for each eigensolution and it describes a point in the phase velocity-frequency plot. Each wavelength (corresponding to one harmonic number) produces solutions which define a straight line in the phase velocity - frequency plot. Small numbers of wavelengths around the toroid (small harmonic number) correspond to larger wavelengths. Increasing the harmonic number, the wavelength decreases and the line rotates as described in Figure 6.3. Each of the aligned points in Figure 6.3 describe different modes at the same wavelength value.

It is important to say here that there are two problems associated with this method of calculating dispersion curves for toroidal structures. Firstly, the number of wavelengths for which solution can be found is limited by the fact that the harmonic number n is a positive integer, therefore the modal solutions are found at different frequency intervals for the different modes. Secondly, the solution at the lowest frequency is limited by the fact that the longest wavelength is obtained for the harmonic number n equal to 1. Clearly from equation 6.4 this limit is severe for tight bend radii.

This method is quantitatively equivalent to the modal solution obtained using Disperse [35]. In order to validate the dispersion curve tracing method previously described, we modelled an "almost-straight" pipe. The pipe modelled was a 2 inch pipe with 1.5 metre bend radius. In this pipe the ratio R_{BM}/D was equal to 25. The circular disc was defined using 4 elements through the thickness and 104 elements around the circumference so the single element was about 1.5 x 1.5 mm. A convergence study confirmed that the number of elements chosen to model the structure

was sufficient to obtain accurate results for low frequency modes. FE77 was used for the modal analysis of the defined structure [78].

Using the modal solution at many wavelengths (harmonic numbers) it was possible to obtain an adequate number of points in the plot (see Figure 6.4). After finding the points it was possible to recognise and distinguish the different modes. Figure 6.5 shows an example mode shape. The circular undeformed shape is the circular disc with hole in Figure 6.2a. From the deformation pattern we can assign the circumferential order to the investigated mode. After classifying each point it was then possible to join the points corresponding to the same circumferential order.

The group velocity dispersion curves and the power normalized mode shapes were derived using a Matlab program provided by Dr. Evans of Guided Ultrasonics Ltd. who implemented the method described by Wilcox [121].

In Figure 6.6 the results obtained using the FE modal solution in the case of a shallow bend (2 inch with 1.5 m bend radius) are compared with the dispersion curve for a straight pipe (2 inch) obtained using Disperse [35]. The excellent match between FE and Disperse validates the use of the method previously explained to find the dispersion curves for a toroidal structure.

6.4 Main features of dispersion curves in toroidal structures

The dispersion curves for toroidal structures present many interesting features not appearing in straight pipes. In this paragraph a comparison between the modes appearing in toroidal and cylindrical pipes is offered. Figure 6.7 shows a comparison between the phase velocity dispersion curves for a 2 inch straight pipe and the corresponding curves for a 2 inch diameter toroid in which the bend radius is 0.45 m. The modes present in a curved pipe have phase velocity close to the one for straight pipe. From Figure 6.7 it is clear that when the radius of curvature decreases, the dispersion curves change. In particular the flexural modes show an interesting phenomenon at small bend radius. A mode which is described by one curve for a straight pipe splits into two curves in the curved pipe. This phenomenon is easy to interpret by considering the mode shapes of the two flexural modes in the curved

pipe corresponding to the F(1,3) mode in a 2 inch straight pipe. These are shown in Figure 6.8 where the undeformed shape describes the original position of the circumference of the circular disc and the line SS is the plane of symmetry of toroid. It is possible to distinguish and classify the two modes by their different mode shapes, which are antisymmetric with respect to the plane of symmetry SS in Figure 6.8a and symmetric with respect to the plane of symmetry SS in Figure 6.8b.

These two different solutions already exist in the straight pipe but they have exactly the same phase velocity and displacement amplitudes due to the axisymmetry of the straight pipe and their mode shapes differ only by a rotation of the reference coordinate axis.

Another interesting characteristic is the loss of the axisymmetric mode shape of the longitudinal and torsional modes in a toroid. A comparison between the L(0,2) mode shape in a cylindrical pipe (Figure 6.9a) and L(0,2) mode shape in a toroid (Figure 6.9b) is shown. The L(0,2) mode shape is axisymmetric because of the geometrical axisymmetry of the structure. Due to the absence of geometrical axisymmetry in the curved case, L(0,2) in a toroid (here named $L(0,2)_T$) has a non-uniform displacement distribution around the circumference and it has a larger displacement on the outside of the toroid.

Given the observations above, a mode present in a toroidal structure can be unequivocally identified using the naming method adopted for cylindrical structures (see Chapter 3) and adding a parameter defining the symmetry of the flexural modes. The flexural modes symmetric with respect to the plane of symmetry are named $F(m,n)_S$ and the modes antisymmetric with respect to the plane of symmetry are named $F(m,n)_A$. The flexural modes plotted in Figure 6.8 are defined according to the above naming convention. Moreover the longitudinal and torsional modes will be indicated as $L(0,n)_T$ and $T(0,n)_T$ where the subscript T gives the extra information that the modes are for toroidal structures and are therefore non-axisymmetric.

A further interesting feature of the dispersion curves for toroidal structures is shown in Figure 6.10. The lines describe the phase velocity dispersion curves for an 8 inch schedule 40 toroid where the ratio between the mean bend radius (see Figure 6.1) and the diameter of the pipe $k = \frac{R_{BM}}{D}$ is equal to 1.5; the points describe a toroid in which the geometrical parameters (D, t, R_{BM}) were simply multiplied

by 3/8 (i.e. the cross sectional geometries were similar; this is not seen in real pipes because for a given schedule the diameter/wall thickness value changes with diameter). From Figure 6.10 it is clear that the dispersion curves scale perfectly with frequency-diameter when both the bend ratio ($k = \frac{R_{BM}}{D}$) and the D/t ratio are kept constant. This result is of significant theoretical importance. The study of waveguides has shown that for geometries such as plates and pipes, the dispersion of a mode is related to the geometry of the structure. If the product between the frequency and the relevant geometrical parameters (thickness for the plate, thickness and radius for the pipe) are kept constant, the dispersion curves are identical (see Viktorov [122] and Pavlakovic [45] for examples). According to the findings on plates and pipes, the rule of the scaling factor applies to toroids the only difference being that there are three relevant geometrical parameters in this case: diameter, thickness and bend radius.

6.5 Testing round bends

A pipe elbow present in a pipe network can either be inserted between two straight pipes and welded to them or simply be obtained by bending a straight pipe (forming a 'pulled bend'). When testing a pipe with a bend the approach can be different depending on whether the part to be tested is the curved part itself or the straight parts after the bend. The testing of a pipe elbow was studied by Rose and Zhao [123] who proposed the use of flexural mode tuning for pipe elbow testing. This thesis focuses on understanding and solving the problems related to testing the straight part of pipe after the bend. This is because, for example, in applications such as road crossings the geometry and accessibility is such that the signal must be transmitted through at least one bend to reach the area to be tested from the position where the transducers ring is located (see Figure 6.11).

In this thesis the transmission through a single pulled bend is studied and some considerations for other testing configurations are discussed.

6.6 Transmission through a bend

The system studied was composed of three regions as shown in Figure 6.12a.

There were two cylindrical pipes, one placed before and one after a section of toroidal pipe. This simple system was studied both numerically (Finite Elements) and experimentally and the results obtained were interpreted using the background information on curved pipes reported in the previous paragraphs of this chapter.

6.6.1 Finite Element Analysis

In all the Finite Element models produced to investigate the transmission through a bend the desired wave was excited at one end of the pipe (end A in Figure 6.12b). The wave travelling along the pipe was monitored at the 1st monitoring line in order to verify the excitation signal and to investigate the reflection from the bend, and it was also monitored at a 2nd monitoring line (see Figure 6.12b) in order to extract the transmitted signals. The excitation input was either a torsional wave (T(0,1)) or a compressional wave (L(0,2)) according to the strategy discussed in Chapter 4.

The first task was to determine an appropriate mesh for the curved structure of Figure 6.12b. A good general reference on the Finite Element analysis of curved members is presented by Ashwell and Gallagher [124]. A Finite Element vibration study of straight-curved-straight hollow shafts was carried out by Wang [125]. Moreover a preliminary Finite Element and experimental study of the propagation of guided waves in straight-curved-straight structures was performed by Aristegui et al. [126]. An accurate Finite Element analysis of the propagation of guided waves in a curved pipe requires a 3-dimensional solid model which is computationally expensive and in general no assumptions can be made on the characteristics of symmetry of the structure. A convergence study showed that a solid model with three elements through the thickness of the pipe could accurately model low frequency modes in the curved structure and it also showed that membrane models can potentially be used for qualitative analysis of trends of transmission coefficients of low order modes.

The system described in Figure 6.12b has one plane of symmetry (which is the plane of symmetry of the toroid). Therefore it is intuitive to expect that symmetric excitation inputs can only convert to symmetric modes and antisymmetric excitation

inputs can only convert to antisymmetric modes. In order to verify this assumption, two solid models of the system described in Figure 6.12b have been investigated. Both models were excited using T(0,1) mode shape at End A of the pipe, the first model being a full model of the system and the second being a half model with the condition of antisymmetry at the plane of symmetry of the toroid. The results clearly showed that the models are equivalent and therefore it is possible to reduce the computational time by using the half pipe model. The same verifications were performed for the L(0,2) mode incident, confirming that the half model can be used also in this case (notice that the plane of symmetry of the toroid is also a plane of symmetry for the displacement in this case).

Therefore in this study only half of the system was modelled. Moreover 2D membrane models were used for the understanding of the general trends and 3D solid analysis was used for quantitative analysis. As already mentioned, this investigation focuses on understanding the interaction of the curved and straight parts when the longitudinal L(0,2) and torsional T(0,1) modes are excited in the straight pipe. Due to the geometry of the toroid, the problem of the straight pipe-curved pipe interaction involves different modes depending on the excitation signal. More specifically, when L(0,2) is excited in the straight pipe it could convert to $L(0,n)_T$ and $F(m,n)_S$ modes only and when T(0,1) is input for the straight pipe it could convert to $T(0,n)_T$ and $F(m,n)_A$ modes only. Nevertheless the problem involved with the transmission through a bend is very similar in the two cases due to the similar mode conversion pattern which is expected. Therefore in the following part of this chapter the transmission through a bend is discussed with reference to both longitudinal and torsional mode inputs.

The size of pipes under investigation were 2 and 8 inches in almost all cases. The 2 inch pipe was chosen to exactly reproduce the size of the samples studied experimentally. The 8 inch pipe size was chosen because most industrial testing is on pipes larger than 2 inch diameter.

Longitudinal excitation results

The objective of the longitudinal FE tests was to predict the effects due to the presence of a bend inserted in a pipe network and to identify the parameters affecting

the transmission.

Typical time traces for longitudinal excitation of a pipe with a bend are shown in Figure 6.13; the mode extraction was carried out using the method already explained in section 4.4. These figures show the FE predictions for the case of a 2-inch pipe with k=6 where k is the ratio of the mean bend radius to the pipe diameter. Before the bend [Figure 6.13a], the order 0 mode was identified from time of flight as being the generated L (0,2) mode. Moreover the amplitude of the order 0, 1 and 2 modes reflected from the bend was negligible [Figure 6.13a-c]. The incident L(0,2) mode, Figure 6.13a, is transmitted through the bend (Figure 6.13d) and mode converted into the F(1,3) (Figure 6.13e) and F(2,3) modes (Figure 6.13(f)). As expected, the F(2,3) component was small, so it could be neglected in a first approximation.

Figure 6.14 shows the frequency analysis of the single transmission predictions for four different values of the bend parameter k. The L(0,2) transmission coefficient was calculated by dividing the spectrum of the transmitted L(0,2) mode by that of the incident L(0,2) mode. From Figure 6.14 it is evident that the bend radius affects the transmission. We expected a shallow bend (large value of R) to be similar to a straight pipe. This was confirmed for very high bend radius (e.g. $k = R_{BM}/D = 25$). However an unexpectedly small transmission coefficient was found in the case of high bend radius (e.g. k=R_{BM}/D=10) at relatively high frequencies (>65 kHz).

Figure 6.15 shows the transmission coefficient for the case of k=R_{BM}/D=10 at two different bend lengths. At small bend length (90 degrees) and relatively high frequency (from 60 to 80 kHz) the transmission coefficient decreased with the frequency, whereas at larger bend length (180 degrees) it decreased from 60 to 65 kHz and then increased again. From this example it is evident that bend length affects transmission.

Explanation of longitudinal results

An interpretation of these results is offered in 6.16. The L(0,2) mode is generated at End A and propagates through the straight pipe before the bend. At the start of the bend there is mode conversion to two modes of a curved pipe, to be called here modes "A" and "B". We also assume that in the case of shallow bends the A and B modes indicated in Figure 6.16 are the $L(0,2)_T$ and $F(1,3)_S$ modes of the toroid

defined in the previous sections of this chapter. After the bend, both mode A and mode B reconvert into L(0,2) and F(1,3) so that the L(0,2) mode after the bend is the result of signal superposition:

$$L(0,2)_{AFTER-BEND} = L(0,2)_I + L(0,2)_{II} \tag{6.6}$$

where $L(0,2)_I$ is reconverted from mode A and $L(0,2)_{II}$ is reconverted from mode B. Since modes A and B have different velocities, a different bend length produces a different time delay between the two L(0,2) components and therefore affects this superposition and produces different frequency dependence. It is also important to observe that mode B is likely to be dispersive in the frequency range used in our simulation, so that the time delay is also frequency dependent for a given bend length and bend radius.

Torsional excitation results

The same analysis executed in the case of the longitudinal excitation has been carried out in the case of torsional excitation. The time domain signal revealed that no significant reflection due to the bend is noticeable (see Figures 6.17a, b). The signal transmitted through the bend was a combination of torsional T(0,1) mode (see Figure 6.17c) and F(1,2) (see Figure 6.17d). The results shown refer to the FE predictions for the case of a 2 inch pipe with k=6.

The explanation offered for the longitudinal excitation case is also valid for the torsional excitation (see Figure 6.16). In this case mode A is the $T(0,1)_T$ and mode B is $F(1,2)_A$ and the modes transmitted through the bend are T(0,1) and F(1,2).

Generalization for different pipe sizes

As already discussed, the problem of the transmission through bends is of particular interest in practical applications were tight bends are often present and these cause increased distortion of the transmitted signal. Moreover all pipe sizes in the range 2-24 inches are usually present in a petrochemical plant. Therefore a generalization of the transmission coefficient for different pipe sizes would be beneficial to the testing operations. In this part of the investigation we focused on the transmission of the torsional T(0,1) mode through tight bends (bend ratio k=1.5). FE solid analysis

was performed to model various pipe sizes in the range from 3 to 24 inches (schedule 40).

The transmission coefficient was obtained by dividing the peak to peak signal of the transmitted T(0,1) mode by the peak to peak signal of the incident mode. This was done to be consistent with the data obtained in real applications. The models were run at 7 different centre frequencies (7.5 kHz, 12.5 kHz, 17.5 kHz, 25 kHz, 35 kHz, 45 kHz, 55 kHz and 65 kHz). The signal excited was a 6 cycle Gaussian windowed toneburst.

The results are plotted in Figure 6.18. It is clear from Figure 6.18 that the transmission coefficient scales almost perfectly with frequency-diameter product. It was explained in section 6.4 that the models perfectly scale when multiplying all dimensions by a constant. Moreover, since the bend ratio is fixed (k=1.5), the bend length depends on the pipe diameter and at constant frequency-diameter products the same number of wavelengths of a specific mode fit in the bend. Therefore the mode interference pattern is also the same. The small differences of transmission coefficient depending on the pipe diameter are due to the fact that the dispersion curves for schedule 40 pipes do not perfectly scale with frequency diameter (thickness effect). As clear from Figure 6.18, since the transmission coefficient is similar at a given frequency-diameter product, the effect of the thickness on the dispersion curves and therefore on the interference pattern at a defined frequency-diameter product, is small enough to be neglected. The results in Figure 6.18 demonstrate that the best transmission condition appears at a frequency-diameter product of 90-110 kHz-inches. Hence, for example, the best transmission frequency for a 4 inch pipe is 25 kHz.

6.6.2 Experiments

Four lengths of 2 inch steel pipe with 90 degrees bends at different bend radii R_{BM} were tested (bend ratio k= 4.5, 5.2, 6.0 9.3). All the pipes were bent using cold bending at room temperature by bending over a former. The cold bending procedure causes a change in thickness distribution in the bent region. We are now making the assumption that the effects due to cold bending are not significantly affecting our study and this will be shown later in this chapter. Only one of the

pipes was tested in through transmission (k=6) but all of the pipes were tested in double transmission experiments (reported in the next section).

The main features of the experimental approach were designed to both excite and receive the T(0,1) mode. Figure 6.19 shows the experimental setup. The excitation of the signal was provided by Guided Ultrasonics Ltd Wavemaker. One ring of twelve dry coupled transducers was used to excite the torsional wave. This was positioned at one end of the pipe. Using piezoelectric transducers equally spaced to generate tangential displacement, only T(0,1) is generated. The detection was achieved using a laser interferometer (Polytec OFV 2700, with dual differential fibre optic lines) to measure the in-plane displacement. The in-plane displacement was measured by using two laser beams at an angle of 30 degrees to the normal; the difference between their two signals is the in-plane displacement. A thin retro-reflective tape was attached to the surface of the pipe to enhance the optical back-scatter.

The measurements were performed at two monitoring locations (at 90 degrees from the plane of symmetry of the structure), one before and one after the bend (see Figure 6.19). Ten measurements at each of the two locations were performed. In the following A_I and A_T indicate the peak-to-peak amplitude of the reference and transmitted signal respectively. The amplitude of the lowest and highest signals of the 10 recorded signal at each of the two locations were considered to calculate the range of the transmission coefficient. The low transmission coefficient in Figure 6.20 was obtained by dividing the lowest A_T by the highest A_I. The high transmission coefficient was obtained by dividing the biggest A_T by the smallest A_I.

The experimental results are compared with the results obtained using a solid FE model of the pipe, reproducing exactly the same geometry and monitoring the transmitted signal at the same location as in the experiment (0.55m after the bend). Clearly from Figure 6.20 there is a very good agreement between the results obtained experimentally and the FE simulations.

6.6.3 Evaluation of error due to cold bending

In order to verify that a pulled bend has approximately the same dispersion characteristics as a perfect cylindrical toroid, a verification was needed. A measurement of the circumferential distribution of the thickness of a pulled bend was carried

out and the dispersion curves and mode shapes for a perfect cylindrical toroid and for a toroid with same thickness distribution as measured in the pulled bend were compared.

The thickness measurement was performed by using a simple pulse-echo ultrasonic test where longitudinal bulk wave was excited at 5 MHz on a pulled bend (k=6) of a 2 inch pipe. The results showed that the thickness variation was relatively small. The original thickness was 5.5 mm. The smallest thickness measured on the outside of the bend was 5.2 mm and the largest thickness measured on the inside of the bend was 5.82mm(about 6% difference).

Subsequently two pipes were modelled, the first being a pure toroid with bend ratio 6 and uniform thickness and the second being a toroid with smaller thickness on the outside and larger on the inside. The thickness variation was in this case overestimated so the inside thickness was 5.9 mm and the outside was 5.1 mm (about 7.5% difference) The dispersion curves and mode shapes for these two structures were found and the computation shows that the phase velocity of the modes is almost unaffected (Figure 6.21).

A comparison of the power normalized mode shapes for $L(0,2)_T$ in the two models is presented in Figure 6.22 which shows that a small difference of the displacement distribution is present. Note that the abscissa axis in Figure 6.22 is the angular coordinate θ of the toroid shown in Figure 6.1 and the ordinate is the displacement in ψ direction (see Figure 6.1) on the outside wall of the toroid. The error introduced by the use of a pulled bend for the experiments can be evaluated using the following expression:

$$\epsilon = \frac{u_T - u_{PB}}{u_T} \tag{6.7}$$

where u_T is the displacement value of the toroid and u_{PB} is the displacement value of the pulled bend. Figure 6.23 shows that the maximum estimated error is smaller than 4%. The same considerations applying for the other mode shapes, it is possible to conclude that the error due to cold bending can be neglected.

6.7 Double transmission through a bend

In practical pipe testing the usual testing configuration is a pulse echo setup and therefore it is important to understand the effect of a bend when the signal is transmitted through the bend itself, reflected back and then transmitted through the bend for a second time. This is obtained for example when using the first monitoring line in Figure 6.12b and detecting the signal coming back from end B.

6.7.1 Finite Elements

The model for an 8 inch schedule 40 pipe with k=1.5 was used to study the double transmission through a bend. T(0,1) was excited at end A (see Figure 6.12b) and the signal was recorded at the first monitoring line to verify the input signal and to measure the double transmitted signal, and at the second monitoring line to measure the initial signal transmitted through the bend and the signal reflected from end B of the pipe.

The double transmission coefficient was obtained by dividing the peak-to-peak amplitude of the double transmitted T(0,1) mode by the peak-to-peak amplitude of the input signal. Figure 6.24 shows a comparison of single and double transmission coefficients in the frequency range 25-65 kHz. From Figure 6.24 it is clear that the double transmission coefficient is smaller than the single transmission coefficient. This is because the wave packet which was excited at one end of the pipe becomes even more distorted as it passes the second bend. It is also clear that the double transmission coefficient is not a simple function of the single transmission coefficient (e.g. single transmission coefficient squared). This is because both T(0,1) and F(1,2) are present after the bend and their time delay is dependent on the length of the second straight pipe after the bend (here called l_2). After passing the bend the two modes propagate in the straight pipe, then they are reflected from End B and propagate a second time along the straight pipe before reaching the bend. Since the two modes have different velocities at a given frequency the time delay between them will depend on the length l_2 of pipe in which they travel. Moreover, due to their dispersion characteristics, T(0,1) arrives unchanged at the pipe bend because it is not dispersive at the working frequency whereas F(1,2) is dispersive in the frequency

bandwidth used for the tests so the wave packet is distorted along the path length. As a result the time delay between T(0,1) and F(1,2) (and therefore the interference pattern) will depend on the l_2 length and on the frequency. This is a critical point in our modelling because only perfect reproduction of the experimental case can lead to same results in the FE modelling.

This is also of great importance from the practical point of view because the typical test is performed in pulse echo and therefore the amplitude of reflection from a feature present after the bend will depend on its location.

6.7.2 Experiments

Figure 6.25 shows the experimental set-up. Two rings of twelve dry coupled transducers were used in pulse echo mode. Using piezoelectric transducers equally spaced to generate tangential displacement, only torsional modes are generated. The torsional T(0,1) mode is the only mode excited when the equally spaced transducers are forced to move circumferentially whereas usually two modes, nominally L(0,2) and L(0,1), are excited by an axial excitation of the transducers. Special care in transducer length may eliminate L(0,1) mode [92]. By simply rotating the transducer orientation by 90 degrees we were able to excite either longitudinal or torsional modes. The received signals were processed using a similar logic to that of Equation 4.3 to give the signals corresponding to zero (axi-symmetric) and order 1 modes.

In all the tests the transducers were placed about 1 metre away from end A. The signal coming back from end A was used as a reference signal in order to have a calibration of the transducer ring. The signal coming back from end B passed twice the bend before arriving (double transmission). The excitation and reception of the signal was done using a Guided Ultrasonics Ltd. Wavemaker 16 instrument.

Torsional experiment results

In the case of the torsional excitation for the double transmission experiments, only one of the samples was used (k=6). In this experiment a relatively wide frequency range could be used, due to the fact that the torsional wave is not dispersive at any frequency. Both torsional and flexural modes were propagating in the straight pipe after twice passing the bend. It was verified that the torsional and flexural

velocities were similar to the Disperse predictions for the T(0,1) and F(1,2) modes respectively. The double transmission coefficients from the experiment are shown in Figure 6.26. The same configuration was studied computationally; clearly there is a quite good agreement between the experimental results and the FE simulations.

Longitudinal experiment results

In the longitudinal case the excitation signal was a 6-cycle tone burst at 65 kHz centre frequency modified by a Hanning window. Only one frequency was used during the longitudinal experiment. Lower frequencies are not suitable because of the L(0,2) cut off (see Figure 2.9). Higher frequencies were not used because of the transducer design limits.

Order 0 and 1 modes were propagating in the straight pipe after reflection at end B. Figure 6.27 shows a typical result obtained during the tests. Here the envelope of the received time trace for the case of a 2 inch pipe with 9 inch bend radius is shown (this is the typical automatic output of the Wavemaker software). Position 0 in figure represents the position where the transducer ring was located. The signal on the right side is the signal travelling towards end B (here called forward direction). The signal on the left side travels in the opposite direction (backward direction). The black curve represents the longitudinal signal and the red one represents the first order circumferential mode. The signals immediately close to the position of the ring are inside the dead zone of the signals (the same channels are used for transmission and reception). Group velocity evaluation of the order 0 and 1 modes detected showed good agreement with Disperse predictions for the L(0,2) and F(1,3) modes respectively. It was verified that no L(0,1) was generated by mode conversion at the bends.

Moreover another post-processing method was used in order to get the orientation of the F(1,3) signal. As already explained in section 4 of this Chapter, the order one flexural modes can have two different orientations in the pipe. In one, type A, the motion is a maximum at the HH positions (Figure 6.28) and zero at the VV positions, while in the other orientation, type B, the motion is a maximum at VV positions and zero at HH positions. The flexural mode orientation depends on the orientation of the asymmetric feature in the pipe under test. Due to the geometry

of the structure the A orientation was expected in this case. Separating the modes in the two different orientations (using an automatic procedure of the Wavemaker software) it was found (Figure 6.29) that the mode orientation was of type A (larger motion in the HH positions).

Figure 6.30 shows the comparison between experimental data and finite element predictions in the longitudinal case at 65 kHz. The experimental coefficient was simply obtained by dividing the peak of the L(0,2) signal coming from end B by the peak of the L(0,2) signal coming from end A (the reference signal). The numerical value was obtained by dividing the peak of the second L(0,2) signal appearing in the time trace (coming back from end B) by the peak of the first L(0,2) signal (incoming signal). Figure 6.30 shows reasonable agreement between predictions and experiments. The poorer result obtained in the $R_{BM}/D = 4.5$ case was probably due to kinking in the pipe caused by the cold bending.

6.8 Conclusions

In this Chapter the propagation of guided waves in curved pipes was discussed. The modes propagating in toroidal structures have been found using an FE procedure. The axisymmetric modes for cylindrical structures exist in toroidal structures but they have uneven displacement distribution around the circumference. The flexural mode for cylindrical structure split into two modes: one mode is symmetric with respect to the plane of symmetry and the other is antisymmetric. It was also verified that one set of dispersion curves plotted versus frequency-diameter product describes a family of toroidal structures with geometry similar to the geometry for which the curves were derived.

Starting from the knowledge of the dispersion characteristics of toroids, it was possible to interpret the signals seen in interaction straight-curved-straight pipe sections which are very common in practical testing of pipes. The transmission coefficient through bends was found to depend on the geometry of the pipe, the bend diameter and the length of the bend. An additional parameter, the length of the pipe after the bend and before the first reflector, is also important when using a pulse-echo setup (as always in practical applications).

The quantitative results obtained from experimental work and numerical simulations showed good agreement both for single and double transmission configuration. The transmission coefficient through tight 90^o bends (k=1.5), which are typically found in practical applications, was studied and a universal curve valid for different pipe sizes was found.

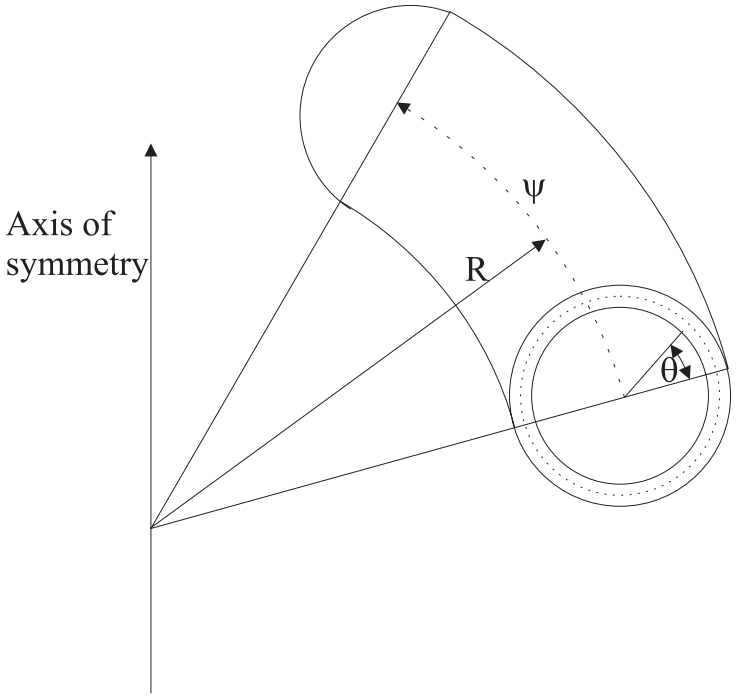

Figure 6.1: Schematic of the toroid and coordinate axis.

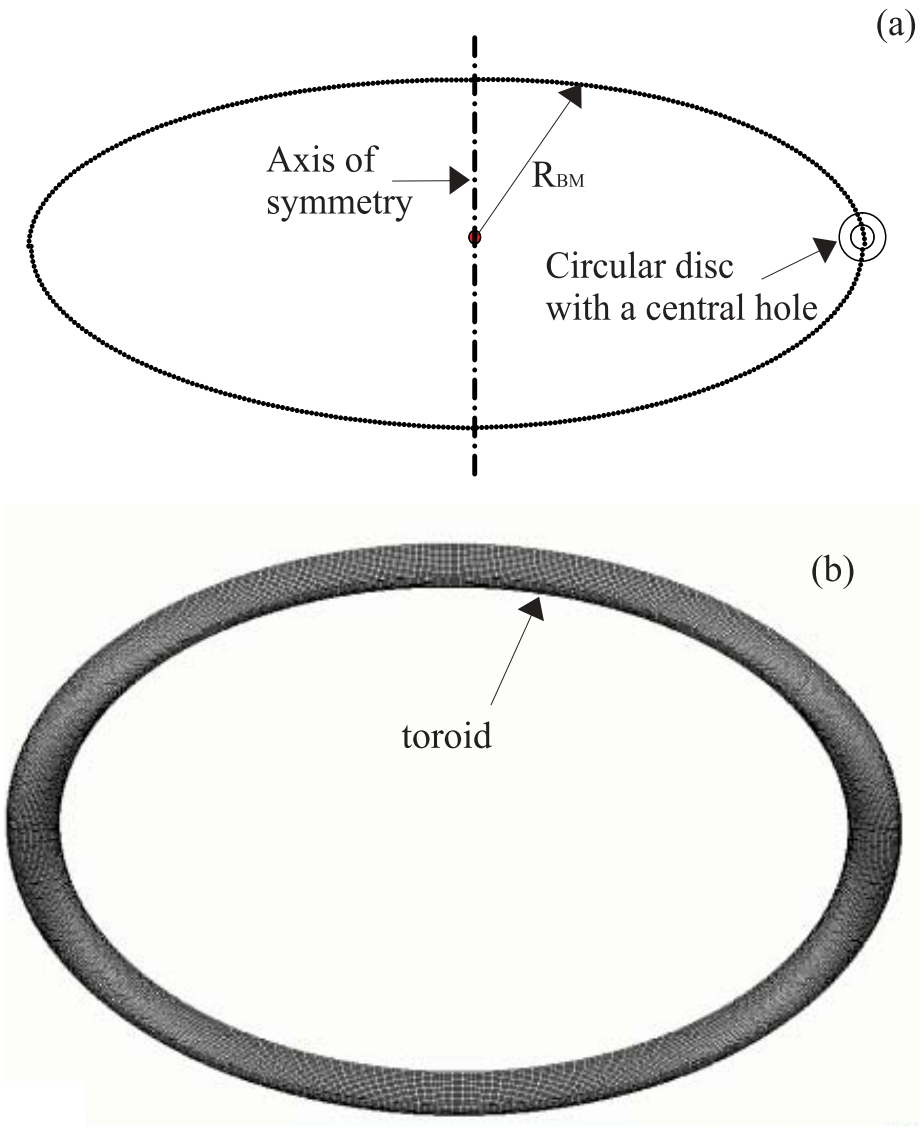

Figure 6.2: Description of the geometry of the FE model used for the modal solution. Two dimensional axisymmetric model of a cross section of the pipe (a) to calculate standing waves in a complete toroid (b).

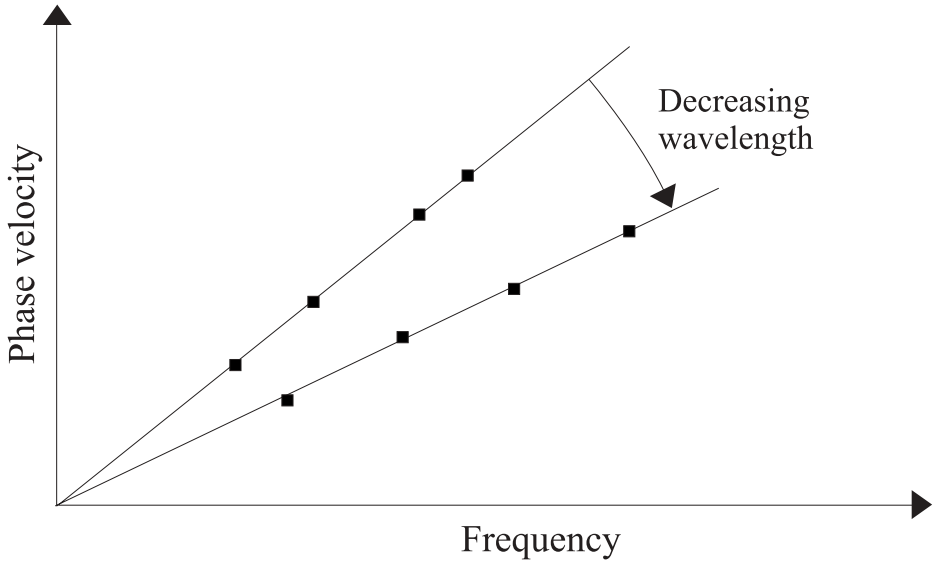

Figure 6.3: Modal solution plot explanation.

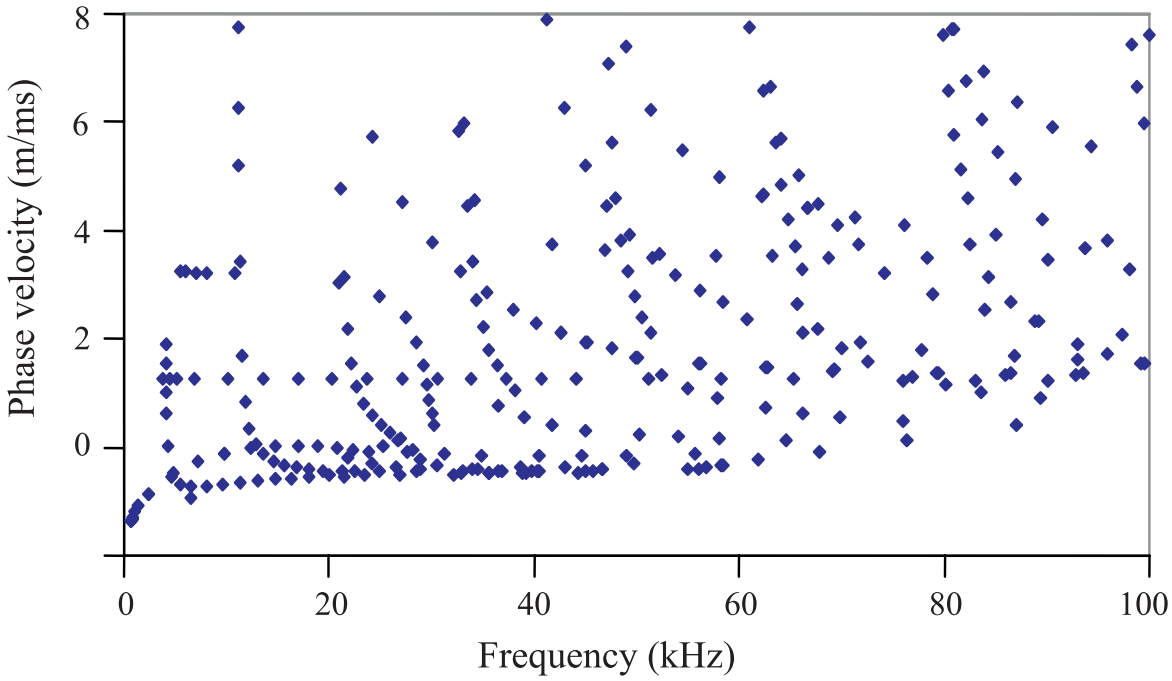

Figure 6.4: Points obtained from the modal solution method for a 2 inch pipe with 1.5 m bend radius.

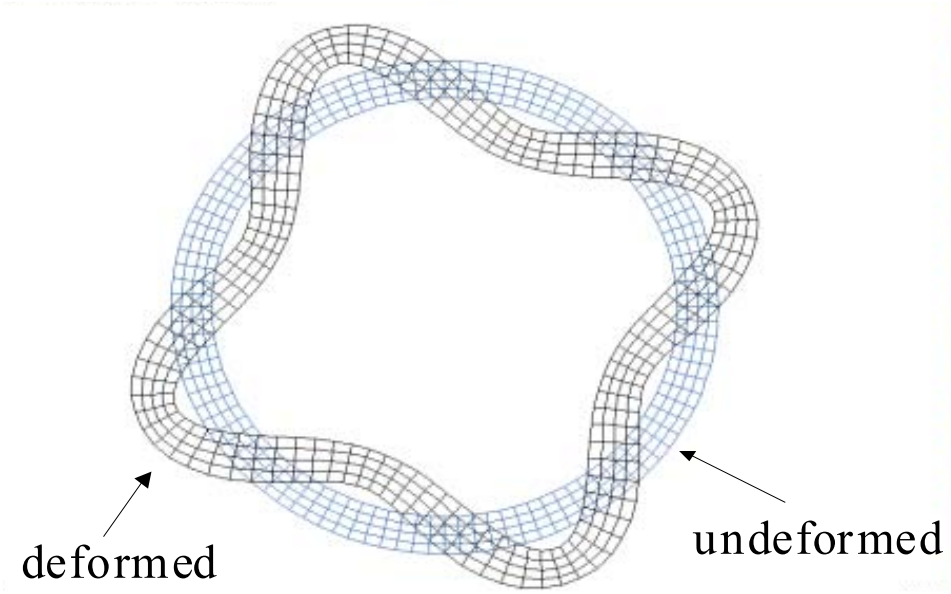

Figure 6.5: Mode shape example. Deformed mesh is for a circumferential order four mode.

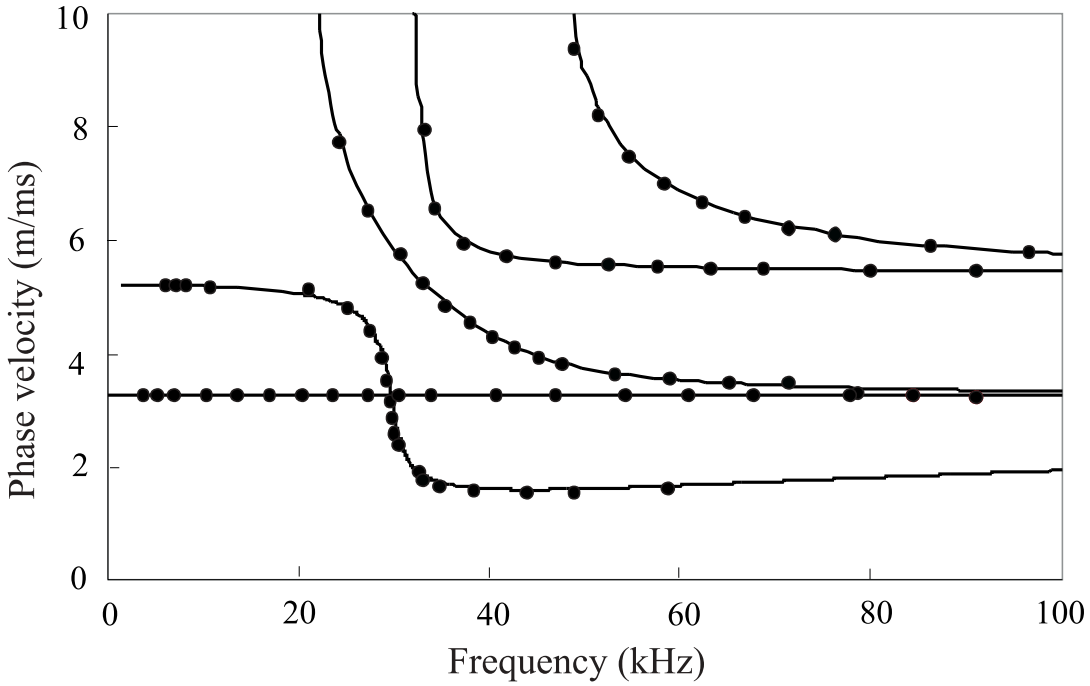

Figure 6.6: Comparison between dispersion curves obtained for a 2 inch straight pipe using the FE modal analysis (points) and Disperse software (solid lines).

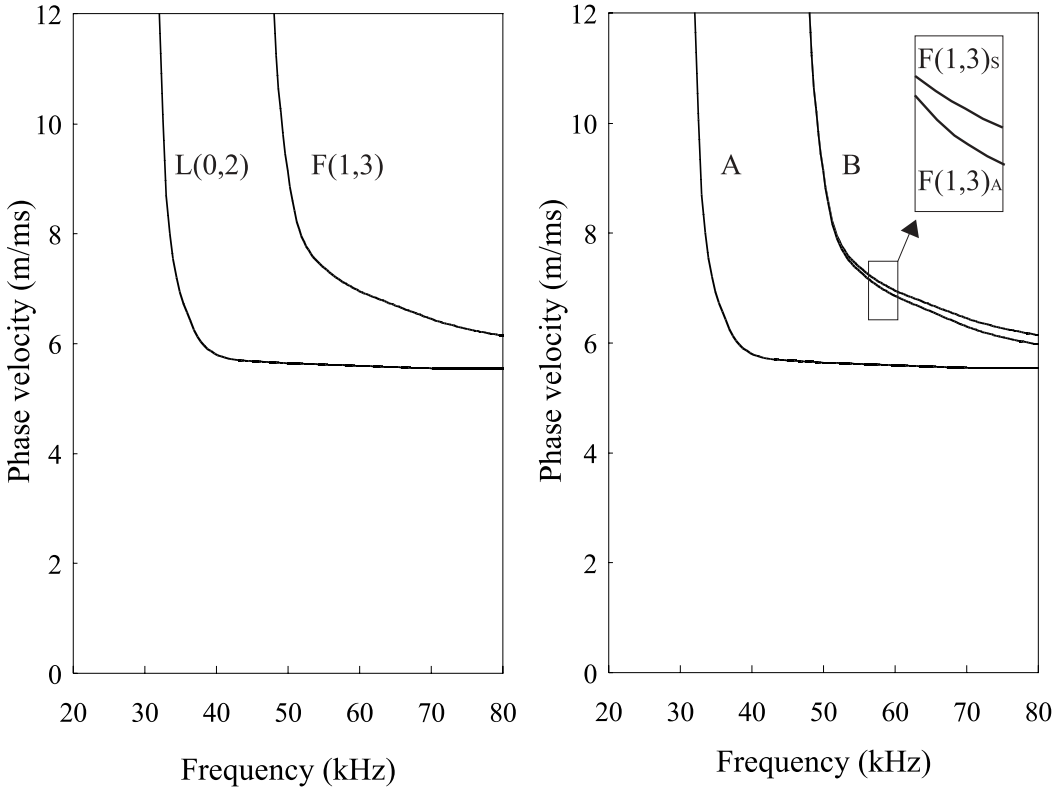

Figure 6.7: Comparison between dispersion curves for (a) a straight pipe and (b) a curved pipe.

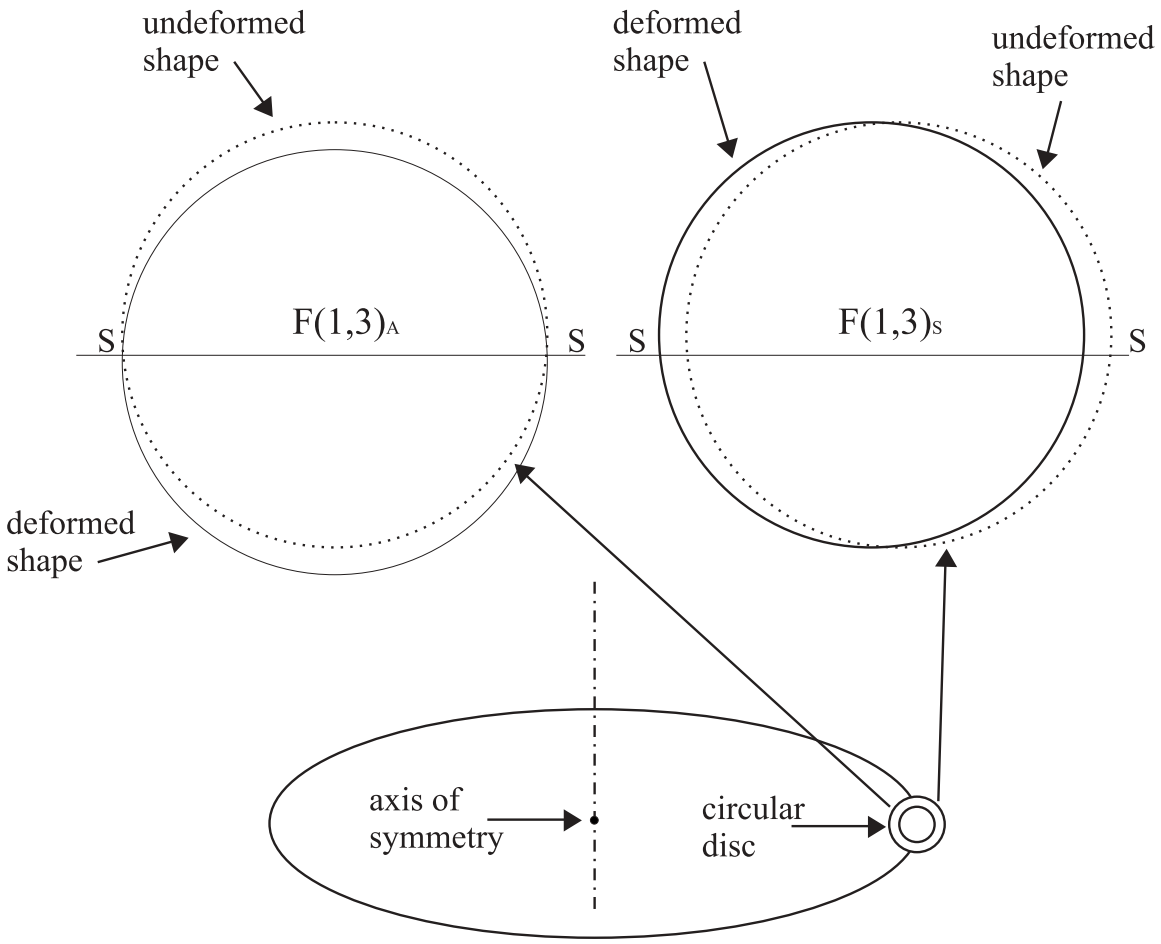

Figure 6.8: Antisymmetric (a) and symmetric (b) mode shape for F(1,3) in a toroidal structure.

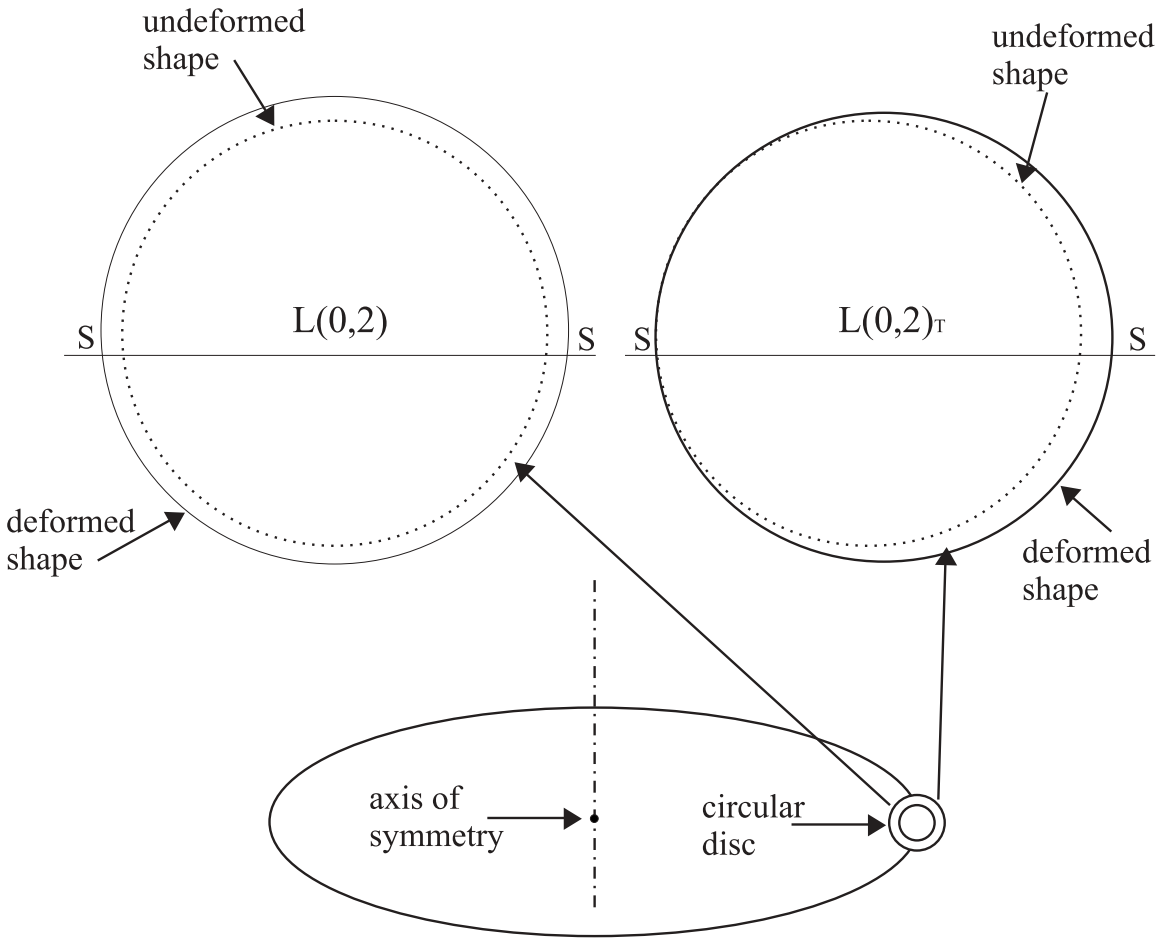

Figure 6.9: Comparison between L(0,2) mode in a straight pipe (a) and L(0,2)T mode in a curved pipe (b).

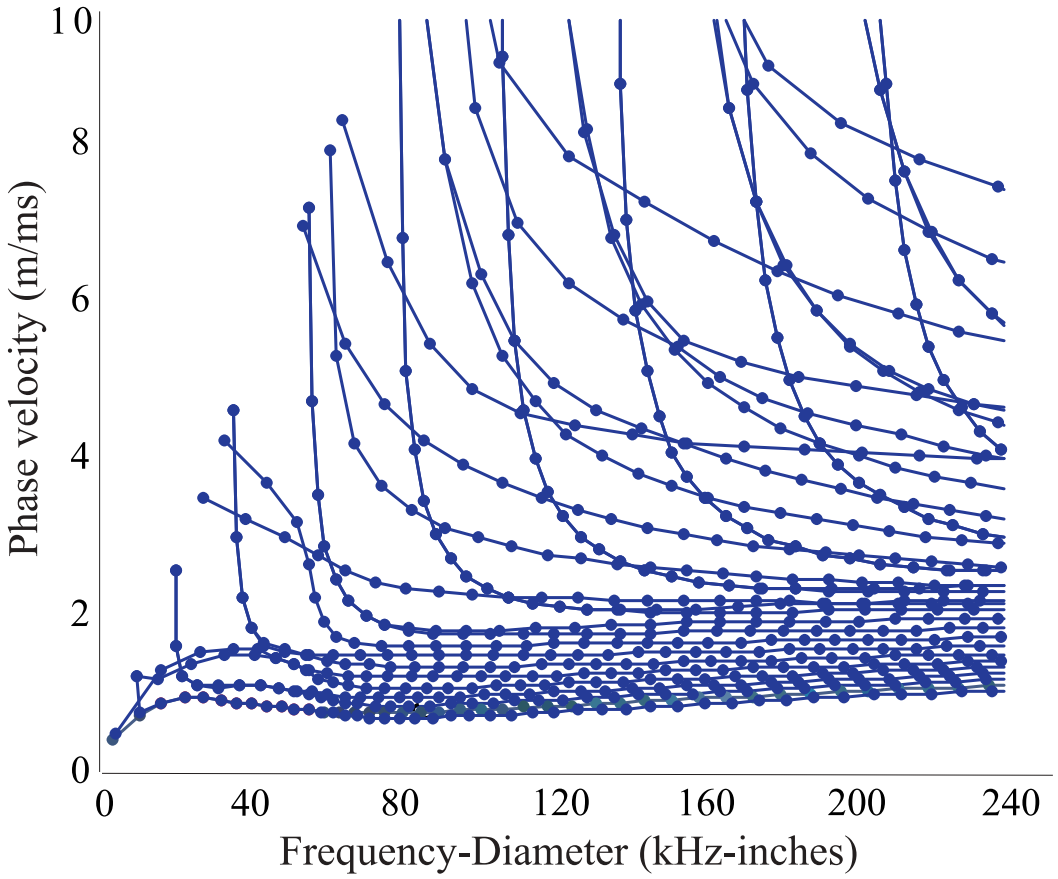

Figure 6.10: Phase velocity dispersion curves for 8 inch schedule 40 toroid with k=1.5 (lines) and for a 3 inch toroid defined as 3/8 of the dimensions of the 8 inch schedule 40 toroid (dots).

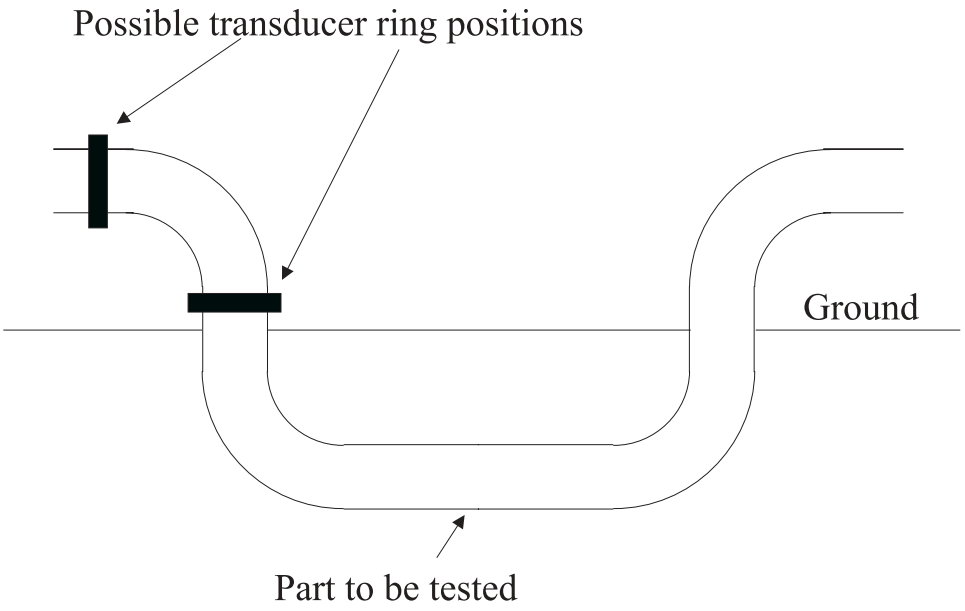

Figure 6.11: Example of road crossing application where it is necessary to test through bends.

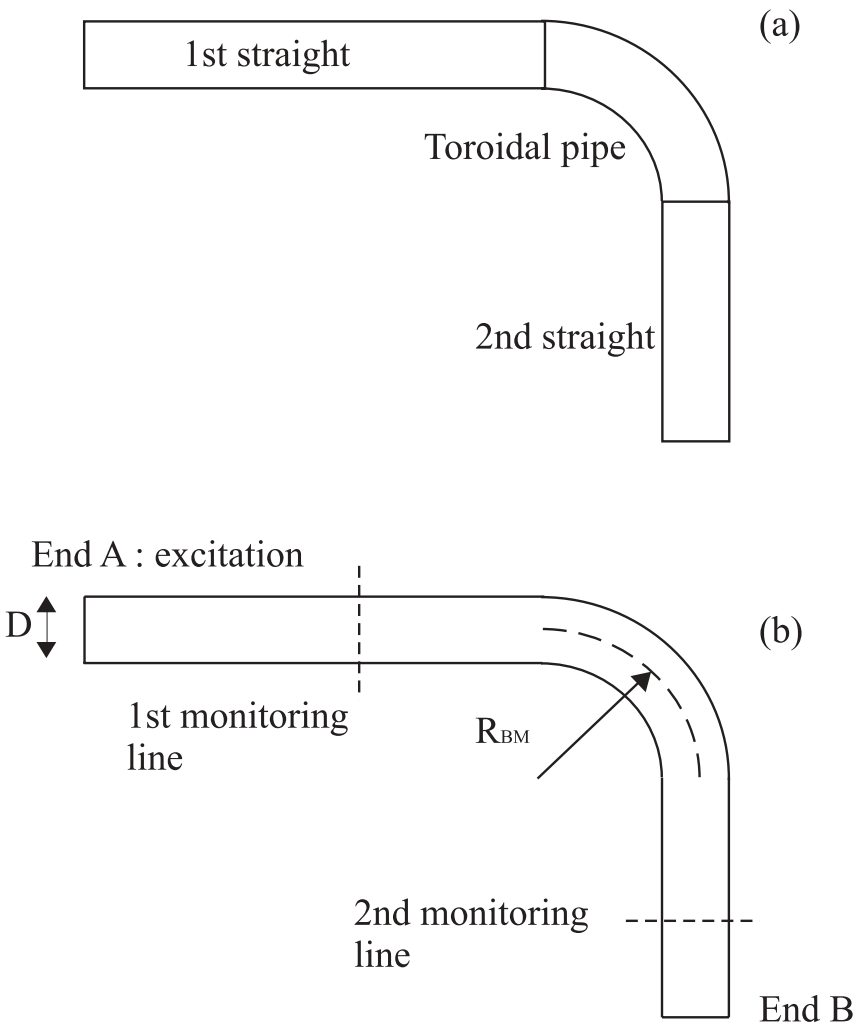

Figure 6.12: Description of the geometry of the model (a) and schematic diagram of the setup used for the FE analysis (b).

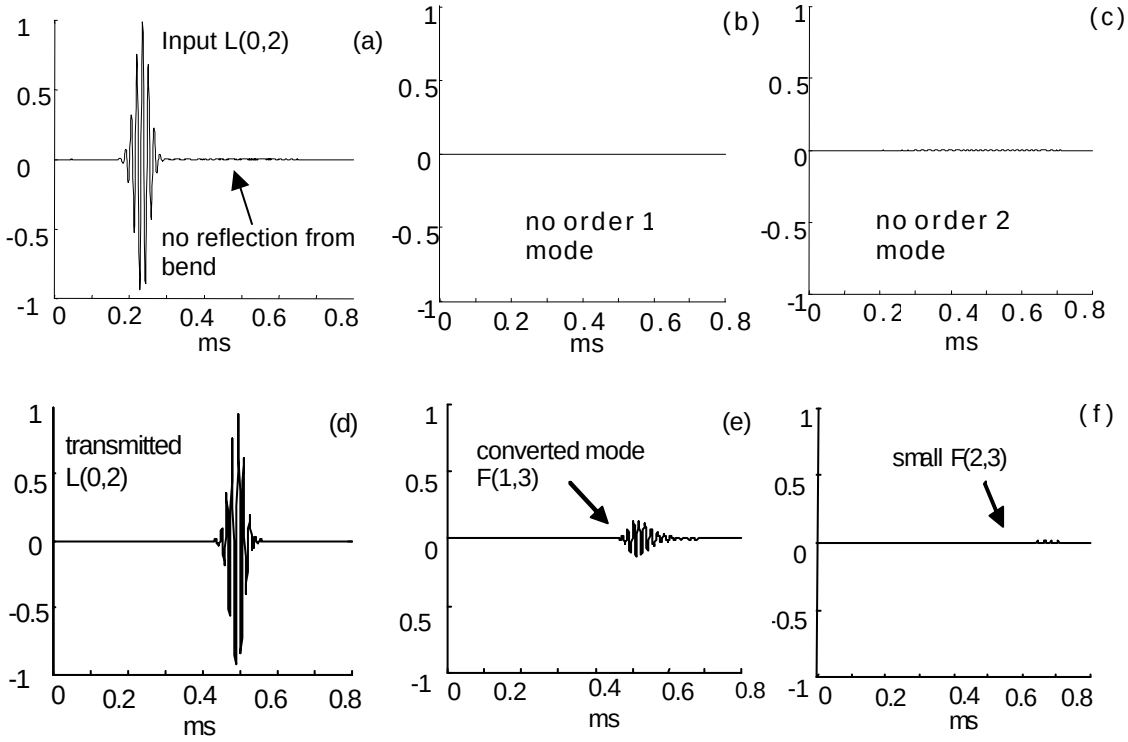

Figure 6.13: Amplitude of the axial displacement calculated from the displacement field at each node of the monitored lines displayed in Figure 6.12b for the k=6 case. The mode extraction has been performed before the bend for the order 0 (a), 1 (b) and 2 (c) modes and after the bend for the order 0 (d), 1 (e) and 2 (f) modes.

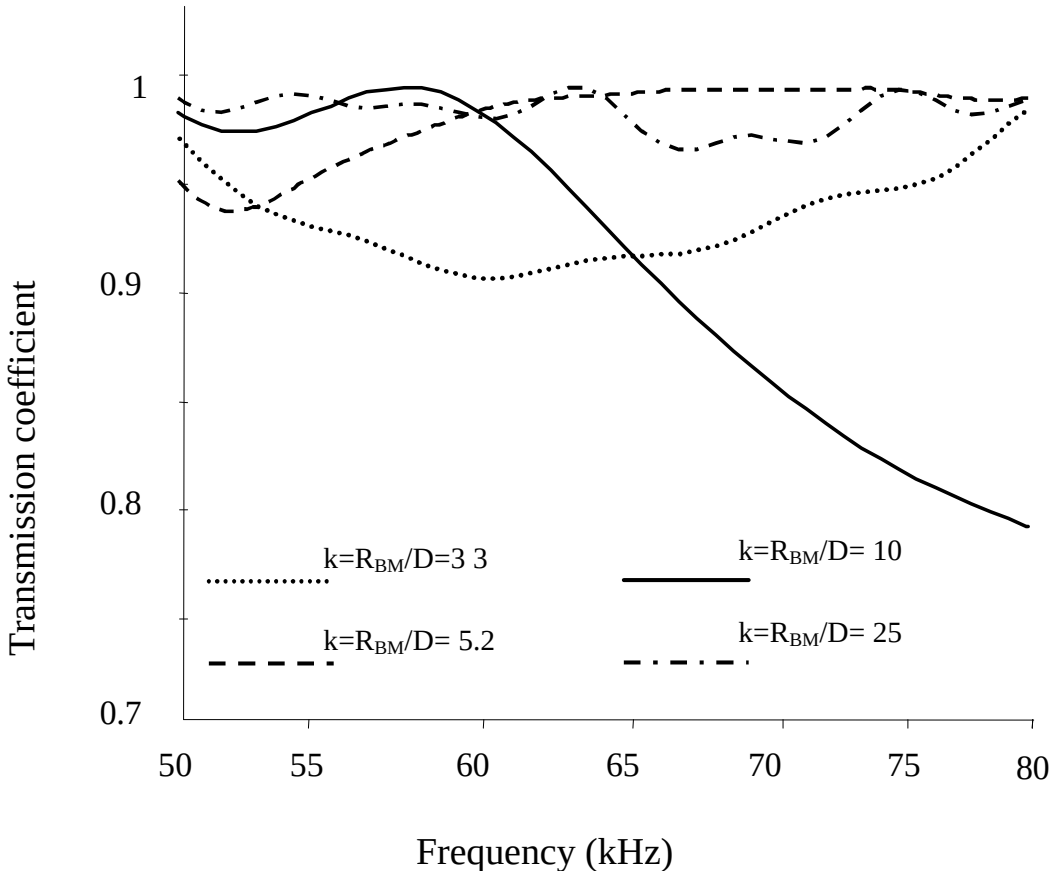

Figure 6.14: Predicted L(0,2) transmission coefficient for different bend radii R_{BM}.

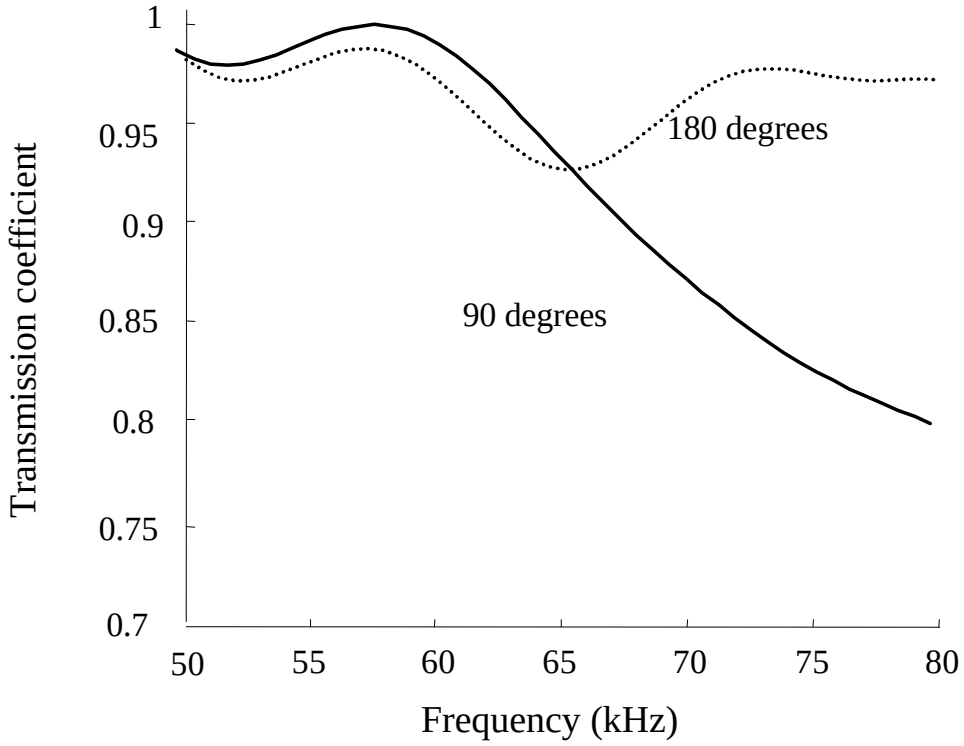

Figure 6.15: Predicted L(0,2) transmission coefficient for different bend lengths (k=10).

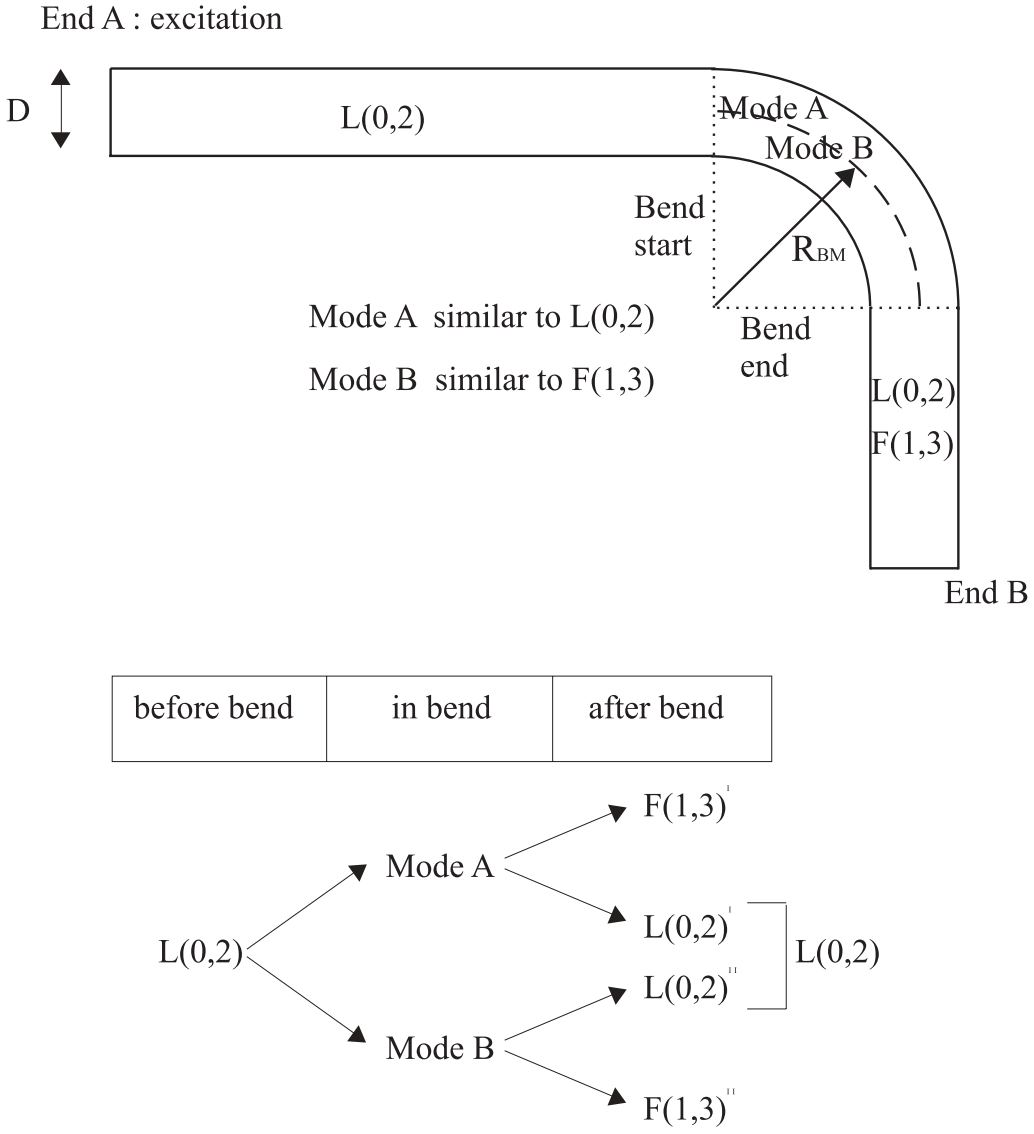

Figure 6.16: Interpretation of mode propagation in pipe with bend.

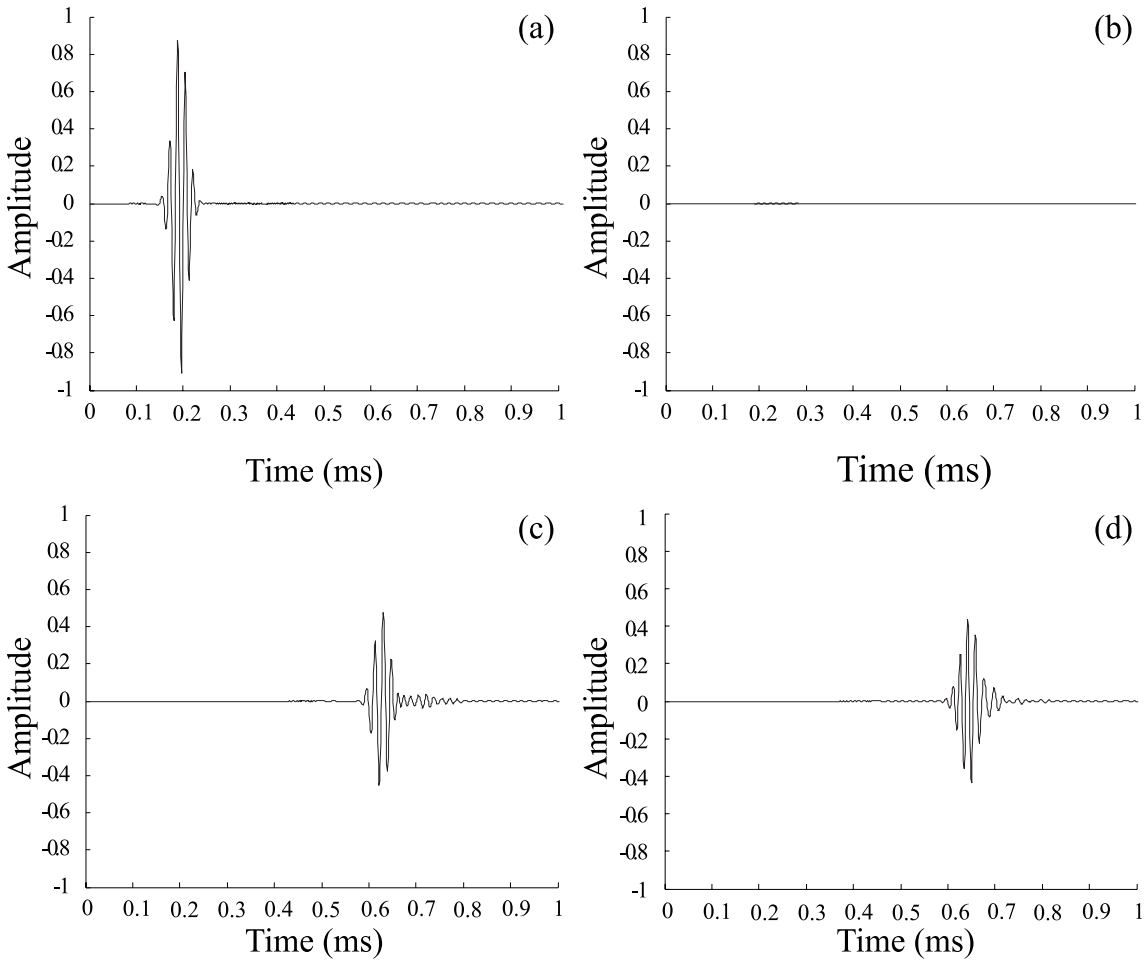

Figure 6.17: Amplitude of the torsional displacement calculated from the displacement field at each node of the monitored lines displayed in Figure 6.12b for the k=6 case. The mode extraction has been performed before the bend for the order 0 (a), and 1 (b) modes and after the bend for the order 0 (c), and 1 (d) modes.

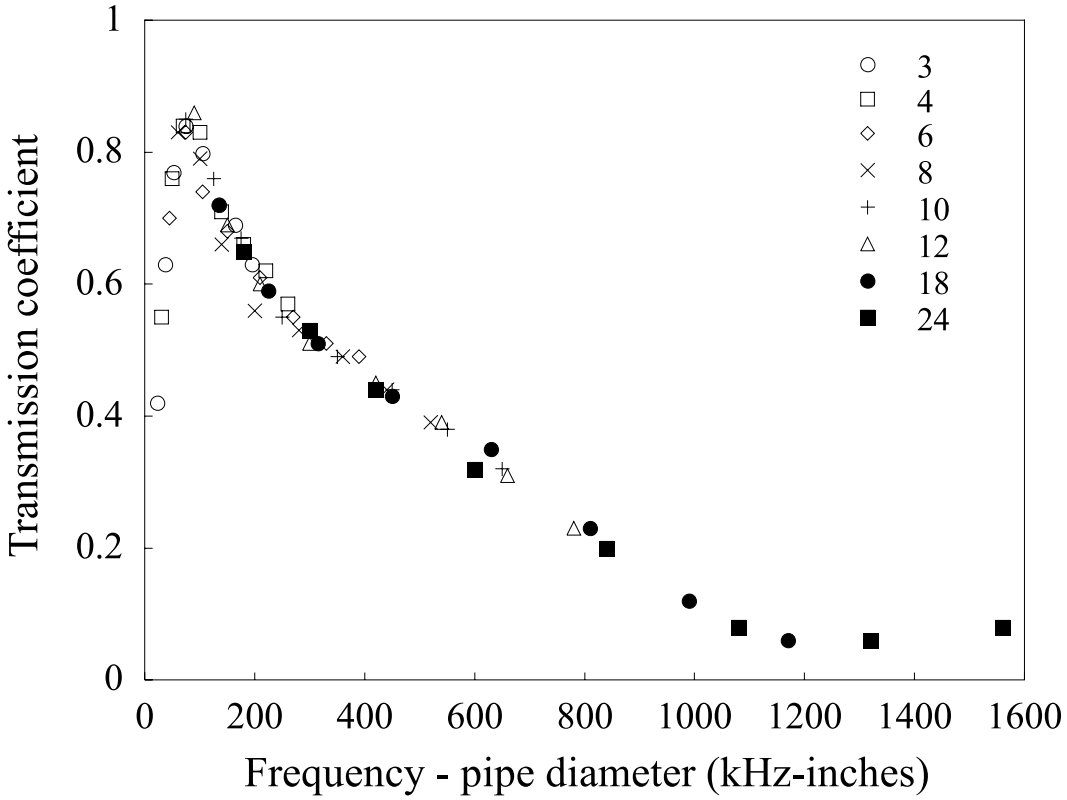

Figure 6.18: Transmission coefficient generalization for different pipe sizes ($k = \frac{R_{BM}}{D}$=1.5; 90 degrees bend; torsion excitation).

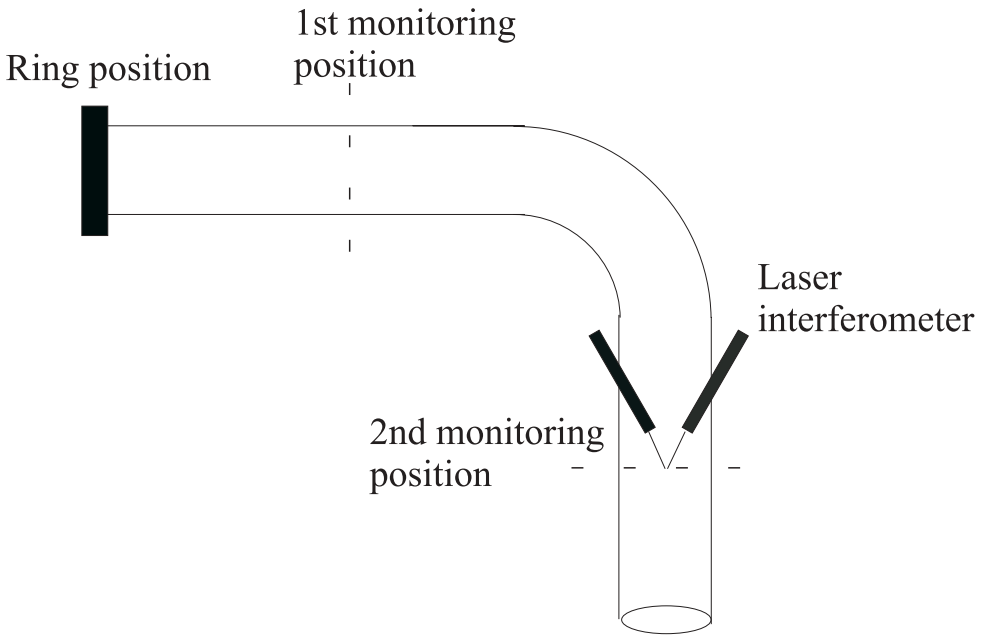

Figure 6.19: Setup of single transmission experiment. The excitation ring was located at one end of the pipe and the laser interferometer was used to receive the signal.

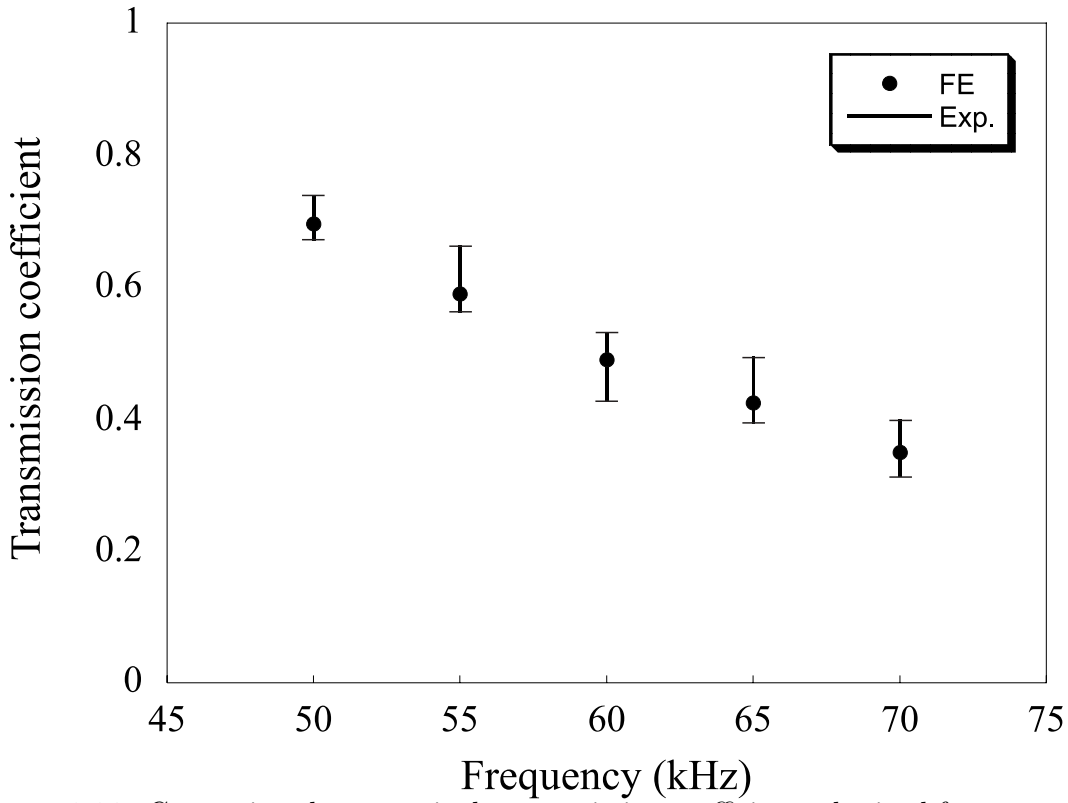

Figure 6.20: Comparison between single transmission coefficients obtained from experiments (highest and lowest value) and using FE. Results are for a 2 inch schedule 40 pipe with a bend with bendratio k=6.

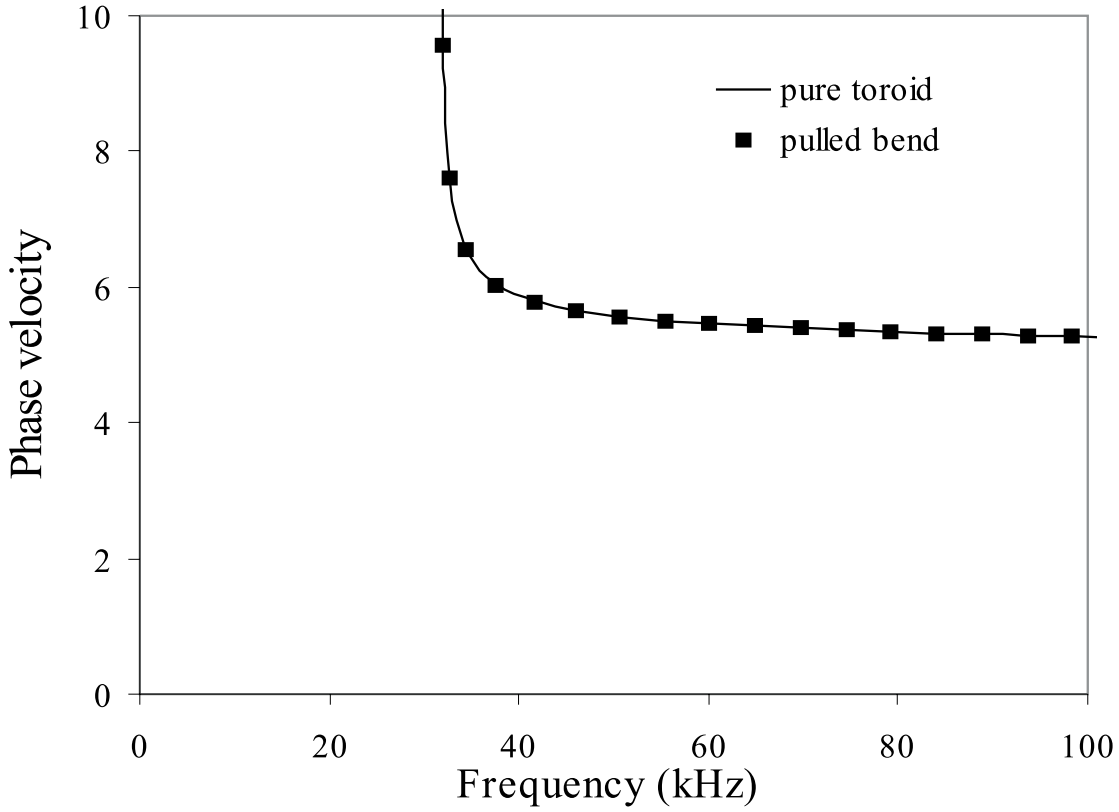

Figure 6.21: Comparison phase velocity for $L(0,2)_T$ in a pure toroid and a pulled bend (k=6). The results are for a 2 inch schedule 40 pipe.

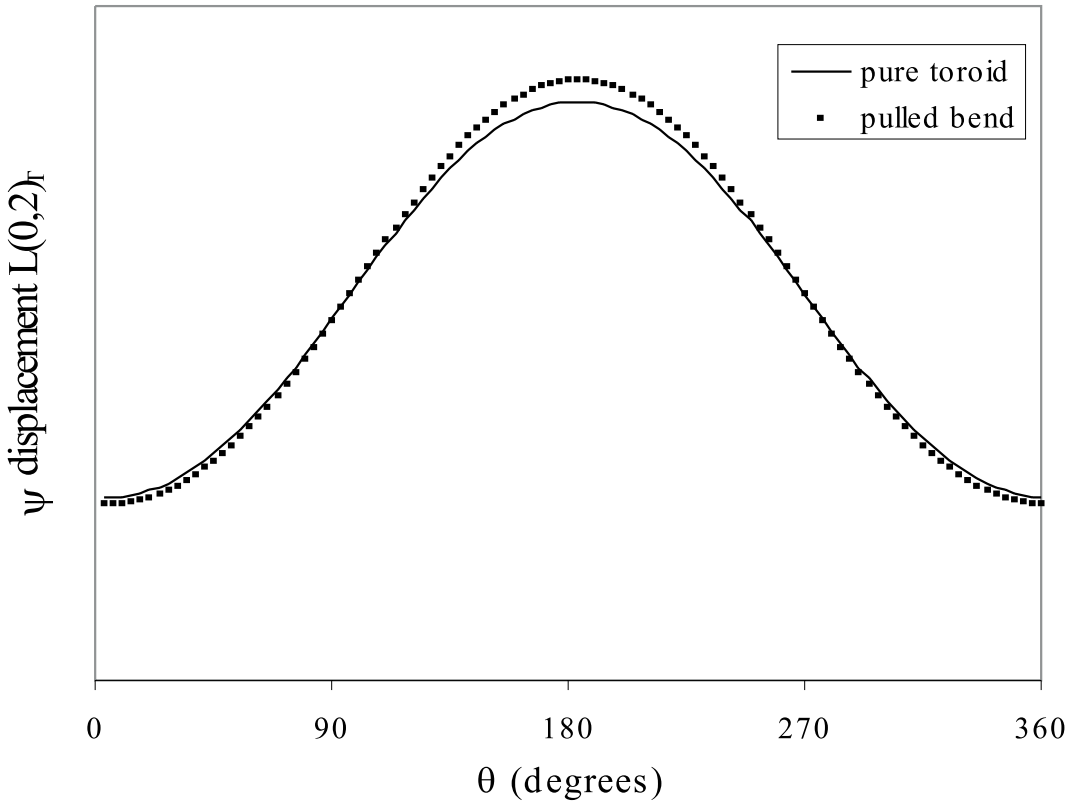

Figure 6.22: Comparison mode shapes for $L(0,2)_T$ in a pure toroid and a pulled bend (k=6). The results are for a 2 inch schedule 40 pipe.

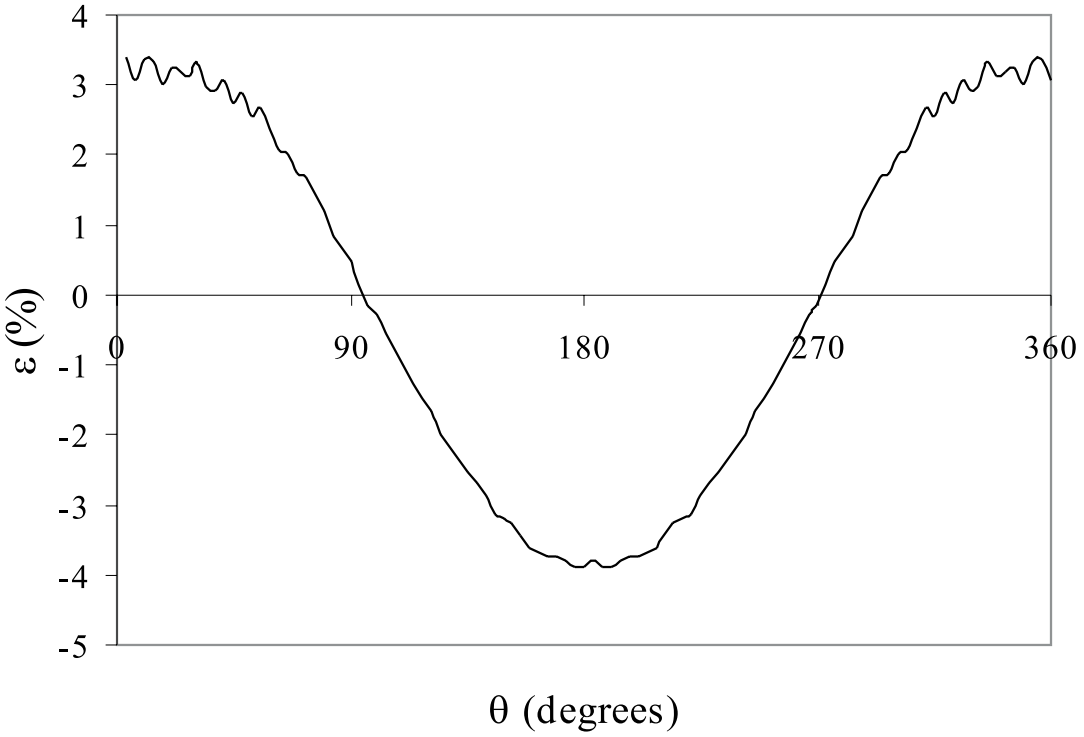

Figure 6.23: Estimated error due to cold bending.

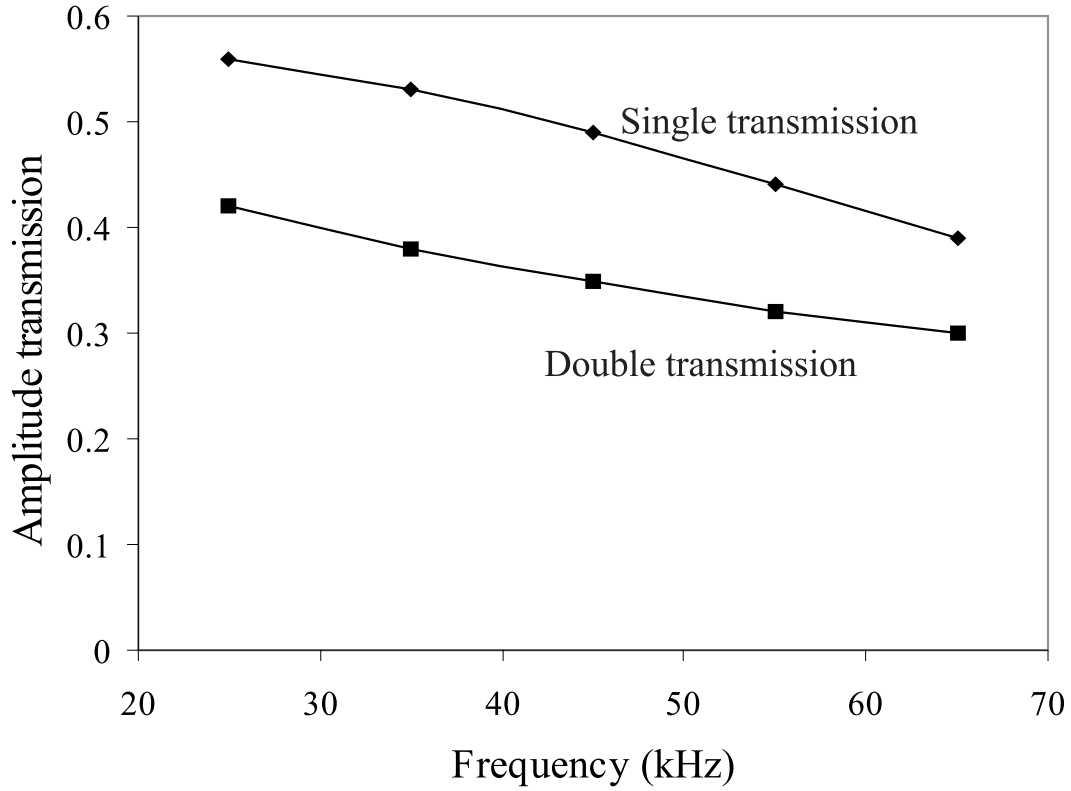

Figure 6.24: Comparison of single and double transmission through a bend when T(0,1) is excited in an 8 inch pipe with a tight bend (k=6).

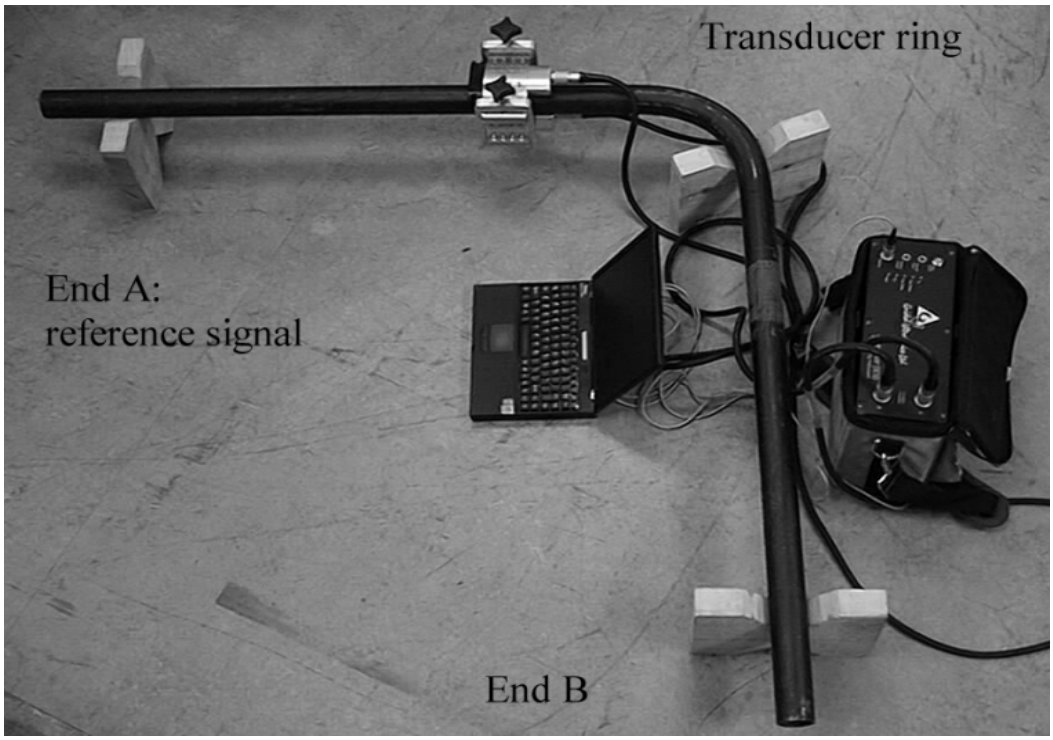

Figure 6.25: Experimental setup for double transmission experiments.

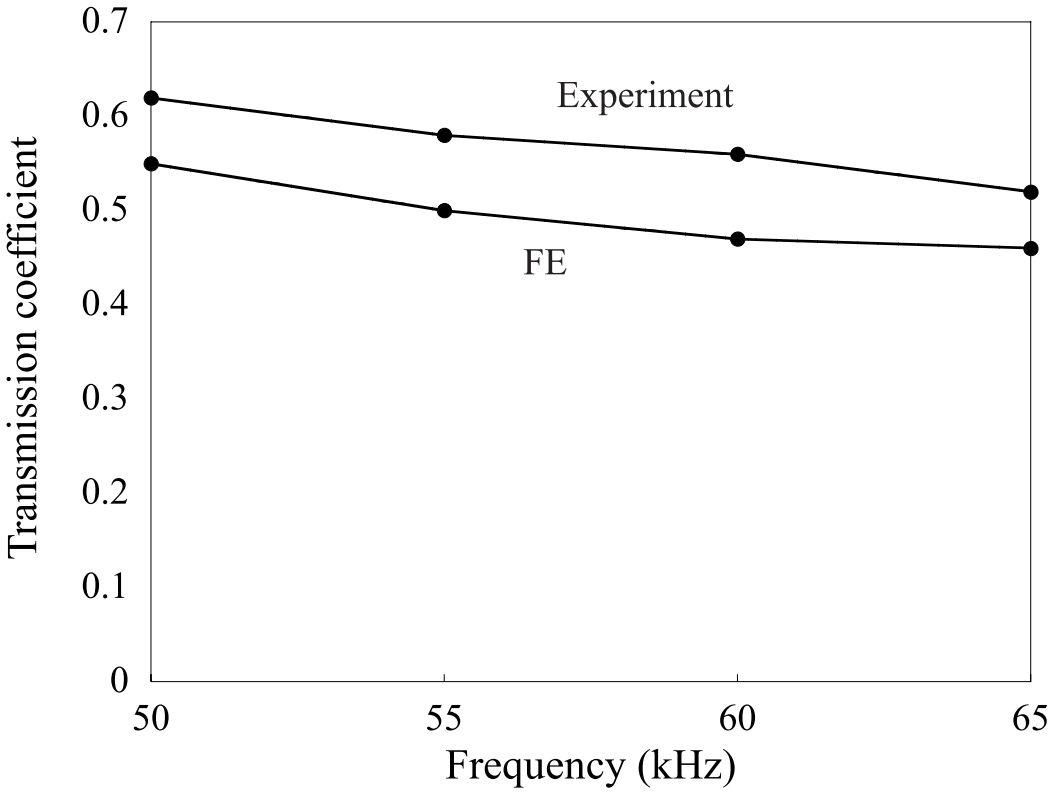

Figure 6.26: Comparison between experimental and FE results obtained in the case of 2 inch pipe with 6 inch radius of bend when T(0,1) mode was excited.

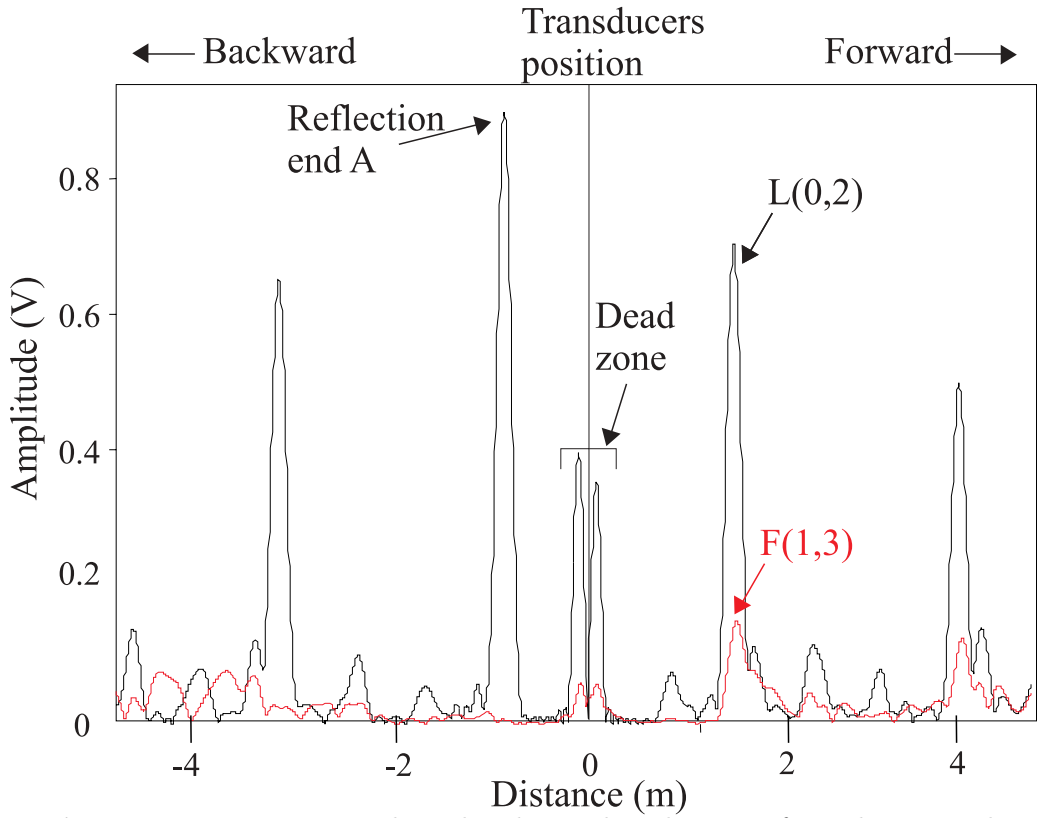

Figure 6.27: Experimental results obtained in the case of 2 inch pipe with 9 inch radius of bend.

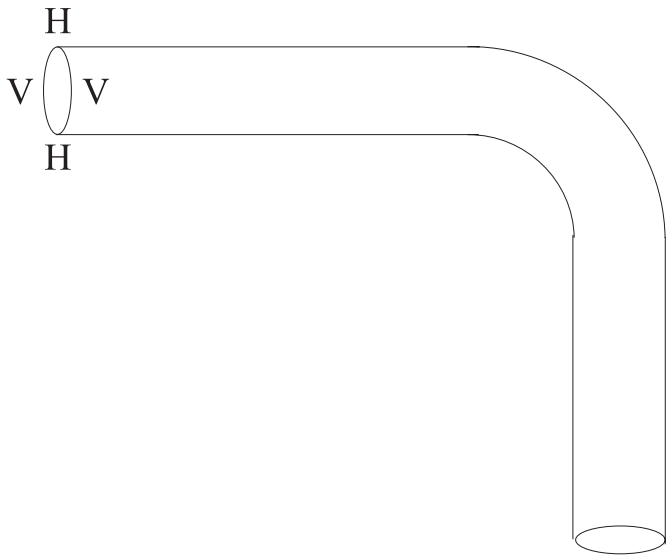

Figure 6.28: Flexural mode orientation explanation diagram

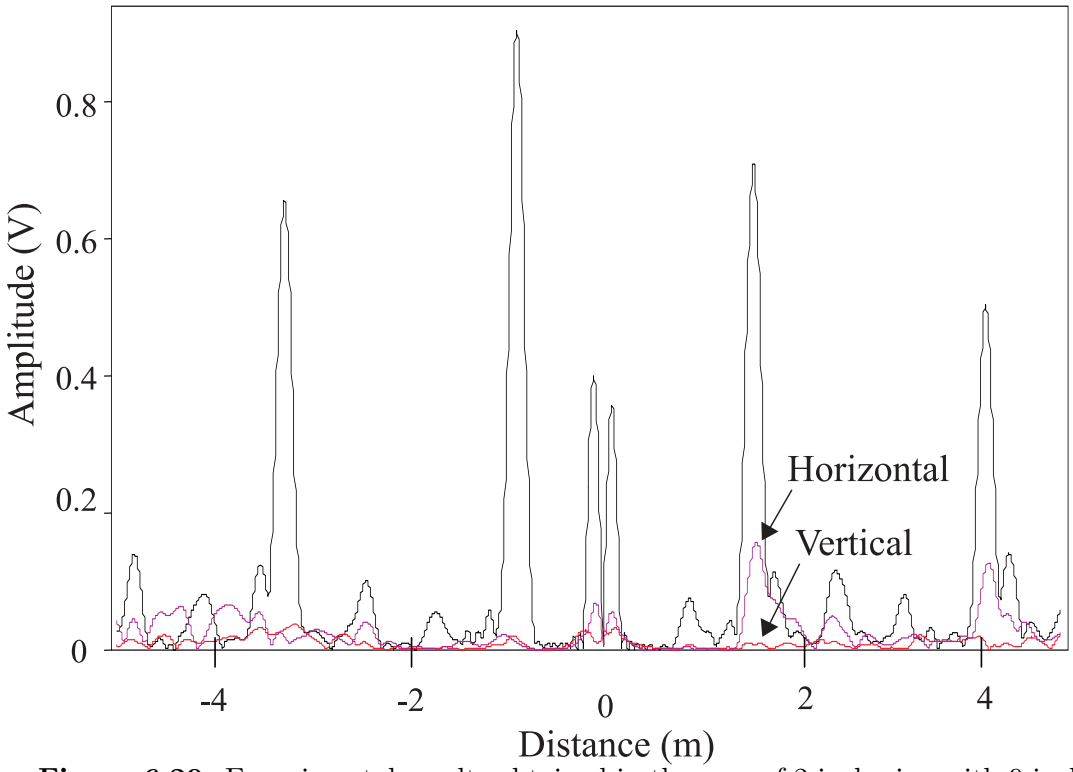

Figure 6.29: Experimental results obtained in the case of 2 inch pipe with 9 inch radius of bend when L(0,2) mode was excited. The horizontal-vertical flexural mode orientation is recognizable in this figure.

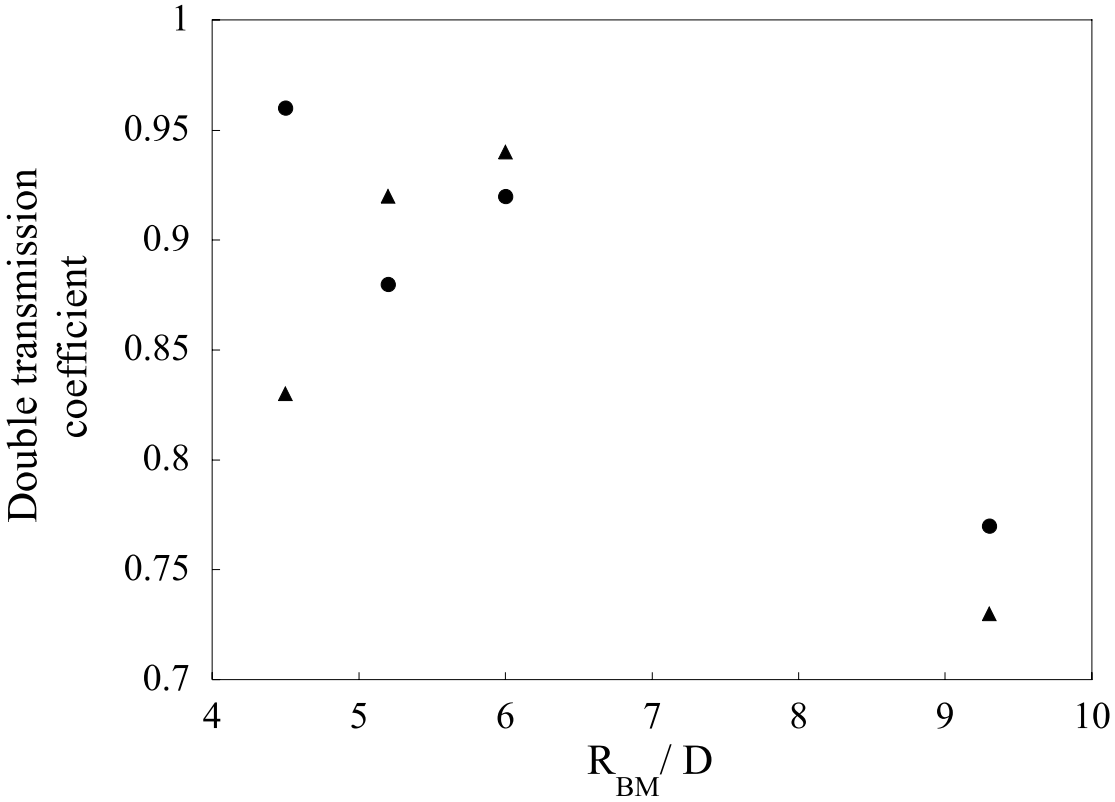

Figure 6.30: Correlation of experiments (triangles) with Finite Element predictions (circles) for L(0,2) double transmission at 65 kHz.

Chapter 7

Conclusions

This thesis studied the effect of geometrical discontinuities on the propagation of guided waves.

Chapter 3 reported on a simple case where the geometrical discontinuity considered was either a thickness step or a notch in a plate. Firstly the interaction between the SH0 mode and a thickness step in a plate was studied using both Finite Element analysis and modal decomposition. The modal decomposition study highlighted the importance of non-propagating modes in the scattering from discontinuities. Knowing the scattering behaviour at thickness steps it was possible to reconstruct the reflection from a rectangular notch (which is effectively a thickness step down followed by a thickness step up). The cyclic behavior of the reflection from a notch as a function of the axial extent was then explained. The study on SH0 in a plate was effectively the starting point for the more complicated analysis of reflection from defect in pipes. In fact the study of a notch in a plate with SH0 incident is equivalent to the case of an axisymmetric notch in a large pipe size when T(0,1) is incident.

A study of the reflection of the T(0,1) mode from defects in pipes was presented in Chapter 4. Part-circumference through-thickness, part-depth axisymmetric and part-circumference, part-depth defects were studied. This study showed that the T(0,1) mode can be used for NDT testing of pipes. This is because T(0,1) stresses 100% of the wall of the pipe and its mode conversion behaviour enables the distinction between axisymmetric and non-axisymmetric features. It was demonstrated that it is possible to use a combination of two (computationally inexpensive) 2D

models in order to model a part-circumference, part-depth defect. The parameter ka was used to understand the trends of reflection from cracks in pipes. This approach explains the difference in behavior of part-circumference, through-thickness cracks and part-depth, axisymmetric cracks.

Chapter 5 presented a systematic analysis of the effect of pipe size, defect size, guided wave mode and frequency on the reflection from defects in pipes. In this Chapter a practical approach was used to reach the goal of producing a new generalization procedure which can account for any case studied. The original 7 parameters involved in the study were reduced to two key parameters: depth (as a function of the thickness of the pipe) and circumferential extent of the defect (as a function of the circumference of the pipe). A defect sizing technique was then proposed. This used the ratio between the flexural mode of the first order and the reflection coefficient for incident axisymmetric mode to obtain information on the circumferential extent of the defect (as already established in practical testing). Then maps of minimum and maximum possible reflection coefficient as a function of circumferential extent and depth of the defect were proposed for the purpose of estimating the depth of the defect. The map for the maximum reflection coefficient can be used when a wide test frequency range is used. The map for the minimum reflection coefficient can be used when only a narrow frequency bandwidth is allowed. The results are of great practical importance since it was verified that the constructive interference phenomenon, always seen in the rectangular notch cases, is also present with a more realistic, stepped notch.

Chapter 6 examines the problem of the guided wave interaction between straight and curved pipes. The dispersion curves for toroidal structures have been derived using an FE procedure. The main characteristics of the modes in toroidal structures have been identified. Two flexural modes with different orientation (symmetric or antisymmetric with respect to the plane of symmetry of the toroid) appear at slightly different phase velocity, whereas two modes at coincident velocity appear for the cylindrical case. None of the modes in the curved pipe presented axisymmetric distribution of displacement. The modes in toroidal structures have been proven to be scaleable with frequency-diameter (at constant pipe diameter/thickness and bend radius/pipe diameter). Knowing the dispersion characteristics in toroidal structures,

an explanation was proposed for the interaction between straight and curved pipes. The parameters affecting the transmission through a bend were identified. The transmission through tight 90 degrees bends (bend radius/pipe diameter=1.5) when T(0,1) is the incident mode was studied at different pipe sizes, the results showing that it is possible to scale the transmission coefficient as a function of the Frequency-Diameter product, the maximum transmission coefficient for this case being obtained at about 100 kHz-inches. The effect of double transmission through a bend was also studied. This showed that in this case the length of the straight pipe after the bend is also an important parameter.

7.1 Future work

The study on the reflection of the SH0 mode from thickness steps and notches in plates, though complete in its own, opened the perspective of studying any defect using the step approximation. It would therefore be of interest to use this approach to study the effect of irregular shaped defects in which the defect is modelled as a superposition of small steps.

The study on the transmission of a wave through bends in pipes has enabled an explanation of the trends seen both in numerical simulations and experiments. Further work is needed to obtain the non-propagating branches of the dispersion curves for toroidal structures. This would enable a modal decomposition study of the interaction between straight and curved pipes, and possibly an easy and practical approach to predict the effect of interaction between straight pipes and any curved geometry.

Bibliography

[1] P.S. Ong, W.L. Anderson, B.D. Cook, and R. Subramanyan. A novel x-ray tachnique for inspection of steel pipes. *J. Nondestruct. Eval*, 13:165–173, 1994.

[2] Y.S Sun, M.X. Qu, T.J. Si, C.T Lu, X.Y. Zhou, and Atherton D.L. Improvement in remote-field eddy current probe structure. *Mater. Eval.*, 50:237–250, 1992.

[3] Y.S Sun, T.J. Si, D. Cooley, H.C. Han, S. Udpa, and W Lord. Effects towards gaining a better understanding of the remote field eddy current phenomenon and expanding its applications. *IEEE Transactions on Magnetics*, 32:1589–1592, 1996.

[4] J.H.J. Stalenhoef and J.A. De Raad. Mfl and pec tools for plant inspection. In *ECNDT Proceedings*, 1998.

[5] D.L. Atherton. Magnetic inspection is key to ensuring safe pipelines. *J. Oil and Gas*, 87:52–61, 1989.

[6] A. Plotnikov and L. Clapham. Stress effects and magnetic nde methods for pipeline inspection: a study of interacting defects. *Insight*, 44:74–78, 2002.

[7] J.L. Cordell. The latest developments in pipeline pigging world-wide,. *Pipes and Pipelines International*, 39:16–21, 1994.

[8] G.C. Williamson and W.M. Bohon. Evaluation of ultrasonic intelligent pig performance: inherent technical problems as a pipeline inspection tool. *Pipes and Pipelines International*, 39:29–34, 1994.

[9] D.N. Alleyne, M.J.S. Lowe, and P. Cawley. The reflection of guided waves from circumferential notches in pipes. *J. Appl. Mech*, 65:635–641, 1998.

[10] M.J.S. Lowe, D.N. Alleyne, and P. Cawley. The mode conversion of a guided wave by a part-circumferential notch in a pipe. *J. Appl. Mech*, 65:649–656, 1998.

[11] D. Alleyne, B. Pavlakovic, M.J.S Lowe, and P. Cawley. Rapid, long range inspection of chemical plant pipework using guided waves. *Insight*, 43:93–96, 2001.

[12] P.D. Wilcox, M.J.S. Lowe, and P. Cawley. An emat array for the rapid inspection of large structures using guided waves. In D.O. Thompson and D.E. Chimenti, editors, *In press in Review of Progress in Quantitative NDE*. American Institute of Physics , New York, 2002.

[13] J. Szilard. *Ultrasonic Testing*. John Wiley and Sons, 1980.

[14] J. Krautkramer and H. Krautkramer. *Ultrasonic testing of materials*. Springer-Verlag, 1983.

[15] B.A. Auld. *Acoustic Fields and Waves in Solids*, volume 2. Krieger Publishing Company, Malabar, Florida, 1990.

[16] B.A. Auld. *Acoustic Fields and Waves in Solids*, volume 1. Krieger Publishing Company Malabar, Florida, 1990.

[17] P.M. Morse and H. Feshbach. *Methods of Theoretical Physics*. McGraw-Hill Book Company, 1953.

[18] L.E. Malvern. *Introduction to the mechanics of a continuous medium*. Prentice-Hall, 1969.

[19] H. Lamb. On waves in an elastic plate. In *Proc. R. Soc. London, Ser. A*, pages 114–128, 1917.

[20] D. Worlton. Experimental confirmation of Lamb waves at megacycle frequencies. *J. Appl. Phys.*, 32:967–971, 1961.

[21] I. A. Viktorov. *Rayleigh and Lamb waves*. Plenum Press, New York, 1970.

[22] A.H. Nayfeh and D.E. Chimenti. Propagation of guided waves in fluid-coupled plates of fibre-reinforced composite. *J. Acoust. Soc. am.*, 83:1736–1743, 1988.

[23] B.T. Khuri-Yakub, J.H. Kim, C.-H. Chou, P. Parent, and G.S. Kino. A new design for air transducers. In *Proceedings of the 1987 IEEE Ultrasonic Symposium*, pages 503–506, 1988.

[24] Y. Bar-Cohen and A.K. Mal. Characterisation of adhesive bonding using leaky lamb waves. In D.O. Thompson and D.E. Chimenti, editors, *Review of Progress in Quantitative NDE*, pages 1271–1277. Plenum Press, New York, 1990.

[25] A. Mal and S.-S. Lih. Characterisation of the elastic properties of composite interfaces by ultrasonic nde. In D.O. Thompson and D.E. Chimenti, editors, *Review of Progress in Quantitative NDE*. Plenum Press, New York, 1992.

[26] D.N. Alleyne and P. Cawley. Optimization of Lamb wave inspection techniques. *NDT & E Int.*, 25:11–22, 1992.

[27] J.J. Ditri, J.L. Rose, and G. Chen. Mode selection criteria for defect optimization using Lamb waves. In D.O. Thompson and D.E. Chimenti, editors, *Review of Progress in Quantitative NDE*, pages 2109–2115. Plenum Press, New York, 1992.

[28] T. Ghosh, T. Kundu, and P. Karpur. Efficient use of Lamb modes for detecting defects in large plates. *Ultrasonics*, 36:791–801, 1998.

[29] P.D. Wilcox, R.P. Dalton, M.J.S. Lowe, and P. Cawley. Mode and transducer selection for long range Lamb wave inspection. *Key Eng. Materials, Proc. DAMAS*, 34:152–161, 1999.

[30] E. Lehfeldt and P. Holler. Lamb waves and lamination detection. *Ultrasonics*, pages 255–257, 1967.

[31] T.L. Mansfield. Lamb wave inspection of aluminium sheet. *Mater. Eval.*, 33:96–100, 1975.

[32] D.F. Ball and D. Shewring. Lamb waves for inspection of commercially rolled hot strip material. *Non-Destructive Testing*, pages 13–15, 1976.

[33] P. Fromme and P. Cawley. Remote monitoring of plate-like structures using guided waves arrays. In D.O. Thompson and D.E. Chimenti, editors, *In press in Review of Progress in Quantitative NDE*. American Institute of Physics , New York, 2002.

[34] J.D. Achenbach. *Wave propagation in elastic solids.* North-Holland Publishing Company, Amsterdam, 1984.

[35] B.N. Pavlakovic, M.J.S. Lowe, D.N. Alleyne, and P. Cawley. Disperse: A general purpose program for creating dispersion curves. In D.O. Thompson and D.E. Chimenti, editors, *Review of Progress in Quantitative NDE*, pages 185–192. Plenum Press, New York, 1997.

[36] J. Pochhammer. Uber die fortpflanzungsgeschwindigkeiten kleiner schwingungen in einem unbergrenzten isotropen kreiscylinder. *J fur reine und angewandte Math.*, 81:324–336, 1876.

[37] C. Chree. The equations on an isotropic elastic solid in polar and cylindrical coordinates, their solutions, an applications. *Trans. Cambridge Philos. Soc.*, 14:250–369, 1889.

[38] R. M. Davies. A critical study of the hopkinson pressure bar. *Phil. Trans. Roy. Soc. London A*, 240:375–457, 1948.

[39] Y.-H. Pao and R.D. Mindlin. Dispersion of flexural waves in an elastic, circular cylinder. *J. Appl. Mech*, 27:513–520, 1960.

[40] M. Onoe, H.D. McNiven, and R.D. Mindlin. Dispersion of axially symmetric waves in elastic solids. *J. Appl. Mech*, 29:729–734, 1962.

[41] T. R. Meeker and A. H. Meitzler. Guided wave propagation in elongated cylinders and plates. In W. P. Mason and R. N. Thurston, editors, *Physical Acoustics, Principles and Methods*, volume 1A, pages 111–167, New York, 1972. Academic Press.

[42] D.C. Gazis. Three dimensional investigation of the propagation of waves in hollow circular cylinders. I. analytical foundation. *J. Acoust. Soc. am.*, 31:568–578, 1959.

[43] D. C. Gazis. Three-dimensional investigation of the propagation of waves in hollow circular cylinders. II. numerical results. *J. Acoust. Soc. am.*, 31(5):573–578, may 1959.

[44] A.H. Fitch. Observation of elastic-pulse propagation in axially symmetric and nonaxially symmetric longitudinal modes of hollow cylinders. *J. Acoust. Soc. am.*, 35:706–708, 1963.

[45] B.N. Pavlakovic. *Leaky guided ultrasonic waves in NDT*. PhD thesis, University of London, 1998.

[46] M.G. Silk and K.F. Bainton. The propagation in metal tubing of ultrasonic wave modes equivalent to Lamb waves. *Ultrasonics*, 17:11–19, 1979.

[47] G.A. Alers and L.R. Burns. Emat designs for special applications. *Mater. Eval.*, 45:1184–1189, 1987.

[48] F. L. Degertekin and B. Khuri-Yakub. Single mode lmb wave excitation in thin plates by hertzian contacts. *Appl. Phys. Lett.*, 69:146–148, 1996.

[49] R.S.C. Monkhouse, P.D. Wilcox, and P. Cawley. Flexible interdigital pvdf lamb wave transducers for the development of smart structures. In D.O. Thompson and D.E. Chimenti, editors, *Review of Progress in Quantitative NDE*, pages 877–884. Plenum Press, New York, 1996.

[50] W. Bottger, H. Schneider, and W. Weingarten. Prototype EMAT system for tube inspection with guided ultrasonic waves. *Nuclear Eng. Design*, 102:356–376, 1987.

[51] A.C. Duncumb and D.M. Keighley. Inspection of titanium tubing using ultrasonic Lamb waves generated by an electromagnetic acoustic transducer. In *Euro. Conference NDT*. Pergamon, 1987.

[52] M.V. Brook, T.D. Ngoc, and J.E. Eder. Ultrasonic inspection of steam generator tubing by cylindrical guided waves. In D.O. Thompson and D.E. Chimenti, editors, *Review of Progress in Quantitative NDE*, pages 243–249. Plenum Press, New York, 1990.

[53] J. Ditri, J. Rose, and A. Pilarski. Generation of guided waves in hollow cylinders by wedge and comb type transducers. In D.O. Thompson and D.E. Chimenti, editors, *Review of Progress in Quantitative NDE*, pages 211–218. Plenum Press, New York, 1993.

[54] D. Alleyne, M. Lowe, and P. Cawley. The inspection of chemical plant pipework using lamb waves : defect sensitivity and field experience. In D.O. Thompson and D.E. Chimenti, editors, *Review of Progress in Quantitative NDE*, pages 1859–1866. Plenum Press, New York, 1996.

[55] J.J. Ditri and J.L. Rose. Excitation of guided waves in generally anisotropic layers using finite sources. *J. Appl. Mech*, 61:330–338, 1994.

[56] D.N. Alleyne and P. Cawley. Long range propagation of lamb waves in chemical plant pipework. *Mater. Eval.*, 55:504–508, 1997.

[57] H.J. Shin and J.L. Rose. Guided wave tuning principles for defect detection in tubing. *J. Nondestruct. Eval*, 17:27–36, 1998.

[58] J.W.S. Rayleigh. *The theory of sound*. Dover, New York, 1945.

[59] J.L. Rose. *Ultrasonics waves in solid media*. University Press, Cambridge, 1999.

[60] K.F. Graff. *Wave Motion in Elastic Solids*. Dover Publicaitons inc., New York, 1973.

[61] P.D. Wilcox, M.J.S. Lowe, and P. Cawley. A signal processing technique to remove the effect of dispersion from guided wave signals. In D.O. Thompson and D.E. Chimenti, editors, *Review of Progress in Quantitative NDE*, pages 555–562. American Institute of Physics , New York, 2001.

[62] R. Sinclair, J. Goyette, and D. Zellouf. A numerical dispersion compensation technique for time recompression of lamb wave signals. *Ultrasonics*, 40:727–732, 2002.

[63] L.J. Bond, M. Punjani, and N. Saffari. Review of some recent advances in quantitative ultrasonic ndt. In *Proceedings of the 1983 IEEE Ultrasonic Symposium*, pages 265–273, 1984.

[64] A. Harker. Numerical modelling of the scattering of elastic waves in plates. *J. Nondestruct. Eval*, 4:89–106, 1984.

[65] J.D. Achenbach. Mathematical modelling for quantitative ultrasonics. *Nondestr. Test. Eval.*, 9:363–377, 1992.

[66] Y. Cho and J.L. Rose. A boundary element solution for a mode conversion study on the edge reflection of lamb waves. *J. Acoust. Soc. am.*, 99:2097–2109, 1996.

[67] M.J.S. Lowe. Characteristics of the reflection of lamb waves from defects in plates and pipes. In D.O. Thompson and D.E. Chimenti, editors, *Review of Progress in Quantitative NDE*, pages 113–120. Plenum Press, New York, 1998.

[68] D.N. Alleyne and P. Cawley. The interaction of lamb waves with defects. *IEEE Trans. Ultrason. Ferroelectr. Freq. Control*, 39:381–397, 1992.

[69] D.N. Alleyne. *The Nondestructive Testing of Plates using Ultrasonic Lamb Waves*. PhD thesis, University of London, 1991.

[70] M. Koshiba, H. Hasegawa, and M. Suzuki. Finite-element solution of horizontally polarized shear wave scattering in an elastic plate. *IEEE transactions on ultrasonics, ferro electrics and frequency control*, 34:461–466, 1987.

[71] F. Moser, L. Jacobs, and J. Qu. Modeling elastic wave propagation in waveguides with finite element method. *NDT & E Int.*, 33:225–234, 1999.

[72] N.N. Kishore, I. Sridhar, and N.G.R. Iyengar. Finite element modelling of the scattering of ultrasonic waves by isolated flaws. *NDT & E Int.*, 33:297–305, 2000.

[73] M.J.S. Lowe and O. Diligent. Low frequency reflection characteristics of the s0 lamb wave from a rectangular notch in a plate. *J. Acoust. Soc. am.*, 111:64–74, 2002.

[74] G.D. Smith. *Numerical solution of partial differential equations: finite difference methods*. Oxford University Press, 1985.

[75] D.N. Alleyne and P. Cawley. The quantitative measurement of lamb wave interaction with defects. In *Ultrasonics International*, pages 491–494, 1991.

[76] C.A. Brebbia. *The boundary element method for engineers*. Pentech Press, London, 1978.

[77] J. Zemanek. An experimental and theoretical investigation of elastic wave propagation in a cylinder. *J. Acoust. Soc. am.*, 51:265–283, 1972.

[78] D. Hitchings. Fe77 user manual. Technical report, Imperial College of Science, Technology and Medicine, London, UK, 1994.

[79] "Abaqus". Explicit user's manual. In *Abaqus*. Abaqus, 2001.

[80] J.J. Ditri. Some results on the scattering of guided elastic sh waves from material and geometric waveguide discontinuities. *J. Acoust. Soc. am.*, 100:3078–3087, 1996.

[81] H.E. Engan. Torsional wave scattering from a diameter step in a rod. *J. Acoust. Soc. am.*, 104:2015–2024, 1998.

[82] M.J.S. Lowe, P. Cawley, J.-Y Kao, and O. Diligent. Low frequency reflection characteristics of the a0 lamb wave from a rectangular notch in a plate. *J. Acoust. Soc. am.*, 112:2612–2622, 2002.

[83] J.L. Rose and X. Zhao. Anomaly throughwall depth measurement potential with shear horizontal guided waves. *Mater. Eval.*, 59:1234–1238, 2001.

[84] M. Castaings, E. Le Clezio, and B. Hosten. Modal decomposition method for modelling the interaction of lamb waves with cracks. *J. Acoust. Soc. am.*, 112:2567–2582, 2002.

[85] T. Vogt, M. Lowe, and P. Cawley. The scattering of guided waves in partly embedded cylindrical structures. *Submitted to J. Acoust. Soc. Am.*, 2002.

[86] R.B. Thompson, G.A. Alers, and M.A. Tennison. Application of direct electromagnetic lamb wave generation to gas pipeline inspection. In *Proceedings of the 1971 IEEE Ultrasonic Symposium*, pages 91–94, 1972.

[87] W. Mohr and P. Holler. On inspection of thin-walled tubes for transverse and longitudinal flaws by guided ultrasonic waves. *IEEE Trans. Sonics Ultrason.*, SU-23:369–378, 1976.

[88] J.J. Ditri. Utilization of guided elastic waves for the characterization of circumferential cracks in hollow cylinders. *J. Acoust. Soc. am.*, 96:3769–3775, 1994.

[89] G.S. Kino. *Acoustic waves : devices, imaging and analogue signal processing.* Prentice-Hall Inc, New Jersey, 1987.

[90] W. Zhuang, A.H. Shah, and S.K. Datta. Axisymmetric guided wave scattering by cracks in welded steel pipes. *Journal of Pressure Vessel technology*, 119:401–406, 1997.

[91] C. Valle, M. Niethammer, J. Qu, and L.J. Jacobs. Crack characterization using guided circumferential waves. *J. Acoust. Soc. am.*, 110:1282–1290, 2001.

[92] D. Alleyne and P. Cawley. The excitation of lamb waves in pipes using dry-coupled piezoelectric transducers. *J. Nondestruct. Eval*, 15:11–20, 1996.

[93] E.A. Kraut. Review of theories of scattering of elastic waves by cracks. *IEEE Trans. Sonics Ultrason.*, SU-23:162, 1972.

[94] S.K. Datta. Scattering of elastic waves. *Mechanics Today*, 4:149–208, 1978.

[95] J.D. Achenbach, A.K. Gautesen, and H. McMaken. *Ray methods for waves in elastic solids.* Pitman Books Limited, 1982.

[96] Y.Y. Wang and J. Shen. Scattering of elastic waves by a crack in a isotropic plate. *Ultrasonics*, 35:451–457, 1997.

[97] J.Y. Wang, K.Y. Lam, and G.R. Liu. 'wave scattering of interior vertical crack in plates and detection of the crack. *Engineering Fracture mechanics*, 59:1–6, 1998.

[98] H. Bai, A.H. Shah, N. Popplewell, and S.K. Datta. Scattering of guided waves by circumferential cracks in steel pipes. *J. Appl. Mech*, 68:619–631, 2001.

[99] C.M. Fortunko and R.B. King. Nondestructive evaluation of planar defects in plates using low-frequency shear horizontal waves. *J. Appl. Phys.*, 53:3450–3458, 1982.

[100] Z. Abduljabbar and S.K. Datta. Diffraction of horizzontally polarized shear waves by normal edge cracks in a plate. *J. Appl. Phys.*, 54:461–472, 1982.

[101] H. Bay, A.H. Shah, N. Popplewell, and S.K. Datta. Scattering of guided waves by circumferential cracks in steel pipes. In D.O. Thompson and D.E. Chimenti, editors, *Review of Progress in Quantitative NDE*, pages 188–194. American Institute of Physics, 2001.

[102] P. Cawley, M. Lowe, F. Simonetti, C. Chevalier, and A.G. Roosenbrand. The variaton of reflection coefficient of extensional guided waves in pipes from defects as a function of defect depth, axial extent, circumferential extent and frequency. *J. Mech. Eng. Sc.*, 216:1131–1143, 2002.

[103] W. Zhu. An fem simulation for guided elastic wave generation and reflection in hollow cylinders with corrosion defects. *Journal of Pressure Vessel technology*, 124:108–117, 2002.

[104] L. Rayleigh. The problem of the whispering gallery. In *Scientific papers*, volume 5, pages 617–620. Cambridge University, Cambridge, 1912.

[105] H. Weinberg and R. Burridge. Horizontal ray theory for ocean acoustics. *J. Acoust. Soc. am.*, 55:63–79, 1974.

[106] G. Liu and J. Qu. Guided circumferential waves ina circular annulus. *J. Appl. Mech*, 65:424–430, 1998.

[107] G. Liu and J. Qu. Transient wave propagation in a circular annulus. *J. Acoust. Soc. Am.*, 104:1210–1220, 1998.

[108] P.D. Wilcox. *Lamb wave inspection of large structures using permanently attached transducers*. PhD thesis, University of London, 1998.

[109] M.D. Beard. *Guided wave inspection of embedded cylindrical structures*. PhD thesis, University of London, 2002.

[110] J.G. Harris. Rayleigh wave propagation in curved waveguides. *Wave motion*, 36:425–441, 2002.

[111] D. Gridin, R. V. Craster, J. Fong, and M. J. S. Lowe. The high-frequency asymptotic analysis of guided waves in a circular elastic annulus. *submitted to Wave motion*, 2002.

[112] F.P. Bretherton. Propagation in slowly varying waveguides. *Proc. Roy. Soc. Lond.*, A.302:555–576, 1968.

[113] Y. Desaubies and K. Dysthe. Normal-mode propagation in slowly warying ocean waveguides. *J. Acoust. Soc. am.*, 97:933–946, 1995.

[114] D.S. Drumheller and S.D. Knudsen. The propagation of sound waves in drill strings. *J. Acoust. Soc. am.*, 97:2116–2125, 1995.

[115] L.P. Eisenhart. Separable systems in euclidean 3-space. *Physical Review*, 45:427–428, 1934.

[116] A.Y.T. Leung and N.T.C. Kwok. Free vibration analysis of a toroidal shell. *Thin walled structures*, 18:317–332, 1994.

[117] M. Redekop. Dynamic response of curved pipes. *International Journal of pressure vessels and piping*, 70:167–172, 1997.

[118] D Huang, M. Redekop, and B Xu. Natural frequencies and mode shapes of curved pipes. *Computers and structures*, 18:465–473, 1997.

[119] L Salley and J. Pan. A study of the modal characteristics of curved pipes. *Appl. Acoust.*, 63:189–202, 2002.

[120] L. Gavric. Computation of propagative waves in free rail using finite element technique. *J. Sound Vib.*, 185:531–543, 1995.

[121] P.D. Wilcox, M Evans, O. Diligent, M. Lowe, and P. Cawley. Dispersion and excitability of guided acoustic waves in isotropis beams with arbitrary cross section. In D.O. Thompson and D.E. Chimenti, editors, *Review of Progress in Quantitative NDE*, pages 203–210. American Institute of Physics , New York, 2002.

[122] I. Viktorov. Ultrasonic lamb waves (review). *Soviet Physics - Acoustics*, 11:1–14, 1965.

[123] J.L. Rose and X. Zhao. Flexural mode tuning for pipe elbow testing. *Mater. Eval.*, 59:621–624, 2001.

[124] D.G. Ashwell and R.H. Gallagher. *Finite elements for thin shells and curved members*. Butterworth, Hungary, 1976.

[125] R.T. Wang. Vibration of straight-curved-straight hollow shafts. *Journal of sound and vibration*, 234:369–386, 2000.

[126] C. Aristegui, P. Cawley, and M.J.S. Lowe. Reflection and mode conversion of guided waves at bends in pipes. In D.O. Thompson and D.E. Chimenti, editors, *Review of Progress in Quantitative NDE*, pages 209–216. Plenum Press, New York, 2000.

List of Publications

A. Demma, P. Cawley, M. Lowe. Mode conversion of longitudinal and torsional modes due to pipe bends. In D.O. Thompson and D.E. Chimenti, editors, *Review of Progress in Quantitative NDE*, volume 20, pages 172-179. American Institute of Physics, New York, 2001

A. Demma, P. Cawley, M. Lowe. Guided waves in curved pipes. In D.O. Thompson and D.E. Chimenti, editors, *Review of Progress in Quantitative NDE*, volume 21, pages 157-164. American Institute of Physics, New York, 2002

A. Demma, P. Cawley, M. Lowe. Scattering of the fundamental Shear Horizontal mode from steps and notches in plates. *Journal of the Acoustical Society of America*, in press

A. Demma, P. Cawley, M. Lowe, A.G. Roosenbrand. The reflection of the fundamental torsional mode from cracks and notches in pipes. Submitted to the *Journal of the Acoustical Society of America*, March 2002.

A. Demma, P. Cawley, M. Lowe. Scattering of the SH0 mode from geometrical discontinuities in plates. Submitted for publication in D.O. Thompson and D.E. Chimenti, editors, *Review of Progress in Quantitative NDE*. American Institute of Physics, New York, August 2002

A. Demma, P. Cawley, M. Lowe, A.G. Roosenbrand, B. Pavlakovic. The reflection of guided waves from corrosion defects in pipes: a guide for interpreting measurements. To be submitted.